



**Top-Quark Mass Determinations
in the $e\mu$ Dilepton Channel**

and

**Top-Quark Mass Effects in
Higgs Boson Pair Production**

Ludovic M. Scyboz



Top-Quark Mass Determinations in the $e\mu$ Dilepton Channel

and

Top-Quark Mass Effects in Higgs Boson Pair Production

Ludovic M. Scyboz

Vollständiger Abdruck der von der Fakultät für Physik der Technischen Universität München zur Erlangung des akademischen Grades eines

Doktors der Naturwissenschaften (Dr. rer. nat.)

genehmigten Dissertation.

Vorsitzender:

Prof. Dr. Andreas Weiler

Prüfende der Dissertation:

1. Dr. Stefan Kluth
2. Prof. Dr. Wolfgang Hollik,
Technische Universität München

Die Dissertation wurde am 16.05.2019 bei der Technischen Universität München eingereicht und durch die Fakultät für Physik angenommen.

5 Abstract

6 In the Standard Model (SM) of Particle Physics, the top quark plays the role of a center-
7 piece. It interacts across all sectors and with all gauge fields, and has been successfully
8 used as a portal to precision measurements of the SM parameters. Top quarks are
9 also indirectly related to other SM sectors, for example to Higgs boson production pro-
10 cesses which are induced predominantly by top-quark loops at the Large Hadron Collider
11 (LHC). During Runs I and II of the LHC, a large number of top-quark pair ($t\bar{t}$) and
12 single-top events were recorded. They allowed to reduce the experimental uncertainty on
13 top-quark properties, like the top-quark mass, but also spin correlations and W -boson
14 polarization in $t\bar{t}$ events, the Wtb coupling, or flavor-changing neutral currents. In the
15 case of the top-quark mass, the experimental uncertainties of the latest ATLAS and
16 CMS combination are now competing with theoretical uncertainties: approximations
17 that were previously thought to be appropriate must be reevaluated.

18 In particular, the narrow-width approximation (NWA) for top-quark pair processes
19 assumes the production of an on-shell top and anti-top quark, and is used in Monte-Carlo
20 (MC) predictions for most experimental measurements. Since the actual final-state is
21 composed of the top-quark pair decay products, a more accurate description of the signal
22 should consider $W^+W^-b\bar{b}$ final-states instead. The full final-state includes contributions
23 that cannot be factorized in both top-quark decay legs, or that do not contain a top-quark
24 pair to begin with. These diagrams are called non-factorizing, respectively non-doubly
25 resonant. In cases where measurements rely on phase-space regions sensitive to these
26 contributions, the extracted top-quark mass will be biased.

27 In this work, the 8 TeV ATLAS top-quark mass analysis in the $e\mu$ dilepton channel
28 is taken as an example. It bases on simulated templates to extract the MC top-quark
29 mass by an unbinned likelihood fit. In a setup similar to the experimental analysis, the
30 extracted top-quark mass is compared at parton-level for different theoretical descrip-
31 tions of the $t\bar{t}$ final-state at next-to-leading order (NLO) in production. MC events are
32 produced for three different descriptions of the top-quark decay in the NWA, as well as
33 for the full $W^+W^-b\bar{b}$ process at NLO in production. The top-quark mass m_t^{MC} extracted
34 by the template fit method is compared for each of these theoretical descriptions, and
35 important offsets of up to $\Delta m_t^{\text{MC}} \sim 1 \text{ GeV}$ are underlined. A more realistic assessment,
36 where these predictions are folded to detector-level, is also presented.

37 As mentioned, the top-quark mass also plays an important role in other sectors of the
38 SM. With the example of di-Higgs production with non-SM values of the Higgs couplings,
39 it is shown that the m_t -dependence of QCD NLO corrections introduces sizeable differ-
40 ences with respect to predictions where top-quark degrees of freedom are integrated out.
41 A full-fledged MC event generator (with the possibility of varying the Higgs self-coupling
42 and the Higgs-top Yukawa coupling) is introduced.

⁴³ Zusammenfassung

⁴⁴ Im Standard-Modell (SM) der Teilchenphysik spielt das Top-Quark eine zentrale Rolle.
⁴⁵ Es wechselwirkt mit Teilchen aller Sektoren sowie mit allen quantentheoretischen Eich-
⁴⁶ feldern, und wurde in verschiedenen Zusammenhängen als Grundpfeiler für Präzisions-
⁴⁷ messungen des SM verwendet. Top-Quarks sind auch eng mit anderen Sektoren des
⁴⁸ SM verbunden: Higgs-Bosonen zum Beispiel werden am Large Hadron Collider (LHC)
⁴⁹ überwiegend durch Top-Quark-Schleifen erzeugt. Während Runs I und II des LHC
⁵⁰ wurde eine große Anzahl an Top-Quark-Paar ($t\bar{t}$) und Einzel-Top-Events ermittelt. Diese
⁵¹ haben es ermöglicht, Messungen von Top-Quark-Eigenschaften bedeutend zu verbessern,
⁵² beispielsweise die der Top-Quark-Masse. In diesem Fall sind die von ATLAS und CMS
⁵³ angegebenen experimentellen Unsicherheiten zu dem Punkt gekommen, wo sie mit den
⁵⁴ aktuellen theoretischen Unsicherheiten rivalisieren: das heisst insbesondere, dass früher
⁵⁵ verwendete Näherungen neu abgeschätzt werden müssen.

⁵⁶ Die sogenannte Schmal-Breite-Näherung (NWA), bei der ein Top-Quark-Paar on-shell
⁵⁷ produziert wird, wird üblicherweise in den meisten Monte-Carlo (MC) Analysen ver-
⁵⁸ wendet. Weil der gemessene $t\bar{t}$ -Endzustand aber von den Top-Zerfallsprodukten gebildet
⁵⁹ wird, sollte eine konsistente Beschreibung des Signals eher auf dem intermediären
⁶⁰ $W^+W^-b\bar{b}$ Zustand beruhen. Letzterer beinhaltet Feynman-Diagramme, die entweder
⁶¹ nicht in zwei Top-Zerfall-Kanälen faktorisieren, oder überhaupt keine zwei Top-Propa-
⁶² gatoren aufweisen. Diese Diagramme heissen nicht-faktorisierend, bzw. nicht-doppelt-
⁶³ resonant. Wenn Messungen durchgeführt werden, die sensitiv auf solche Beiträge sind,
⁶⁴ kann sich ein systematischer Fehler in der extrahierten Top-Quark-Masse bilden.

⁶⁵ Wir nehmen als Beispiel die ATLAS Top-Quark-Massenanalyse im $e\mu$ -Dileptonkanal,
⁶⁶ welche auf simulierten Templates basiert zur Bestimmung der Top-Quark-Masse. In
⁶⁷ einem ähnlichen Setup wird die extrahierte Top-Masse verglichen, wo unterschiedliche
⁶⁸ $t\bar{t}$ -Endzustandsbeschreibungen in nächstführender Ordnung der Störungstheorie (NLO)
⁶⁹ in Produktion eingesetzt werden. Genauer werden für drei verschiedene Beschreibun-
⁷⁰ gen des Top-Quark-Zerfalls, sowie für die volle NLO $W^+W^-b\bar{b}$ -Rechnung, Verteilungen
⁷¹ erzeugt. Die mithilfe der Template-Fit-Methode extrahierte Top-Quark-Masse m_t^{MC}
⁷² zeigt erhebliche Unterschiede bis zu $\Delta m_t^{\text{MC}} \sim 1 \text{ GeV}$. Eine realistischere Studie wird
⁷³ eingeführt wo Particle-Level-Vorhersagen auf Detector-Level gefaltet werden.

⁷⁴ Außerdem wirken Top-Quark-Effekte auch im Higgs-Sektor. Anhand des Beispiels
⁷⁵ von Higgs-Paar-Produktion (hh) beim LHC wird gezeigt, dass die m_t -Abhängigkeit
⁷⁶ von hh Produktion auf NLO QCD zu Unterschieden in differentiellen Verteilungen
⁷⁷ führt im Vergleich zu Vorhersagen, wo die Top-Quark-Freiheitsgrade ausintegriert wer-
⁷⁸ den. Ein vollständiges MC-Programm zur Erzeugung von Higgs-Paar-Events (wo die
⁷⁹ trilineare Higgs-Selbstkopplung sowie die Higgs-Top-Yukawakopplung variiert werden
⁸⁰ können) wird präsentiert.

81 Contents

82	Abstract	v
83	Zusammenfassung	vii
84	Contents	ix
85	1 Introduction	1
86	I Theoretical and Experimental Setup	5
87	2 The Standard Model	7
88	2.1 Matter content and gauge interactions	7
89	2.2 The Higgs mechanism	10
90	2.3 Top-Higgs interactions	13
91	2.4 Outstanding issues with the Standard Model	16
92	3 Higher-order perturbative calculations in hadron-hadron collisions	17
93	3.1 Divergences in Quantum-Field Theory	17
94	3.1.1 Regularization	17
95	3.1.2 Renormalization	20
96	3.1.3 Perturbative expansion of Quantum Chromodynamics	20
97	3.2 Infrared divergences	22
98	3.3 The factorization theorem	23
99	4 Monte-Carlo (MC) event generators	25
100	4.1 Matrix-element providers	27
101	4.1.1 GoSAM: MC interfacing of one-loop amplitudes	28
102	4.1.2 Infrared divergence cancellation	29
103	4.2 Parton-shower models	31
104	4.2.1 Altarelli-Parisi splitting functions	31
105	4.2.2 The Sudakov form factor	32
106	4.2.3 Parton-shower matching	32
107	4.3 Hadronization	34
108	4.3.1 Lund string model	34
109	4.3.2 Cluster model	34

Contents

110	5 The LHC and the ATLAS detector	37
111	5.1 The Large Hadron Collider	37
112	5.2 The ATLAS detector	38
113	5.2.1 The Inner Detector	39
114	5.2.2 Calorimeters	41
115	5.2.2.1 The Liquid Argon (LAr) Calorimeter	42
116	5.2.2.2 The Tile Calorimeter (TileCal)	42
117	5.2.3 The Muon Spectrometer	43
118	5.2.4 Trigger and Data acquisition	43
119	5.2.4.1 Data formats	44
120	5.2.4.2 MC simulation and event reconstruction	45
121	II Top-Quark Mass Determinations	49
122	6 Theoretical predictions for $t\bar{t}$ final-states	51
123	6.1 The narrow-width approximation (NWA)	52
124	6.2 $W^+W^-b\bar{b}$ production: review of existing calculations	54
125	6.3 $W^+W^-b\bar{b}$ calculation setup at NLO QCD	55
126	6.4 Event requirements	57
127	6.5 Total cross-section results	58
128	7 NWA versus $W^+W^-b\bar{b}$: Top-quark mass uncertainties at parton-level	59
129	7.1 The template fit method	59
130	7.2 Definition of the observables	60
131	7.3 Comparison of the different theoretical descriptions	62
132	7.4 Template fit results	67
133	8 Experimental resolution and bin migration	73
134	8.1 Inverse problems	73
135	8.2 Folding setup in ATLAS	74
136	8.3 Theoretical descriptions and MC samples	76
137	8.4 The AnalysisTop setup	78
138	9 Determination of the top-quark mass at detector-level	79
139	9.1 Differential results at particle- and detector-level	79
140	9.2 Statistical and systematic cross-checks	84
141	9.3 Folded results and template parametrization	86
142	9.4 Numerical result for top-quark mass uncertainties	86

143	III Top-Quark Mass Effects in Higgs Pair Production	89
144	10 Top-mass dependence in Higgs pair production at NLO	91
145	10.1 Theoretical descriptions of hh production	92
146	10.1.1 Approximations in the heavy-top limit ($m_t \rightarrow \infty$)	93
147	10.1.2 Two-loop contribution in the SM	94
148	10.2 The Electroweak Chiral Lagrangian	94
149	10.3 Total cross-sections for BSM benchmark points	96
150	10.4 Differential cross-sections and HTL approximations	102
151	11 Variations of the triple Higgs-coupling and parton-shower effects	105
152	11.1 The Powheg-BOX framework	105
153	11.2 Interfacing two-loop contributions	106
154	11.3 Total and differential cross-sections at fixed-order	107
155	11.4 Parton-shower matched predictions at NLO	109
156	12 Conclusion and Outlook	113
157	Bibliography	117
158	A Further template fit plots	136
159	B Template fit parameters at detector-level	140
160	C BSM benchmark points in hh production	141
161	D Hardness definitions in matching Powheg to Pythia	144
162	Acknowledgments	145

¹⁶³ 1 Introduction

¹⁶⁴ The Standard Model (SM) of Particle Physics is one of the most successful physical
¹⁶⁵ theories to date. While it still begs some unanswered questions that are outlined in
¹⁶⁶ Chapter 2, the precision to which its predictions were tested by high-energy colliders,
¹⁶⁷ but also in low-energy experiments, large-scale universe phenomena, neutrino and other
¹⁶⁸ experiments is extremely convincing. In particular, the SM bases on mathematical
¹⁶⁹ concepts that allow for a significant predictive power. Considering that physicists tend to
¹⁷⁰ like a theory that contains the least amount of free parameters and a maximal predictive
¹⁷¹ power, the SM fares rather well: it contains only 19 parameters, namely the angles of the
¹⁷² Cabibbo-Kobayashi-Maskawa mixing matrix and its CP-violating phase (3+1), the gauge
¹⁷³ couplings corresponding to the model's underlying symmetries (3), the lepton and quark
¹⁷⁴ masses (9), the QCD vacuum angle (1), and the Higgs mass and vacuum expectation
¹⁷⁵ value (2). Since most of these parameters have been measured to an excellent precision,
¹⁷⁶ efforts have largely concentrated on the less well-measured parameters, one of these being
¹⁷⁷ the top-quark mass.

¹⁷⁸ Because the top quark is the heaviest known elementary particle, with a mass from
¹⁷⁹ the world combination measured at $m_t = 173.0 \pm 0.4$ GeV [1], physicists had to wait
¹⁸⁰ until 1995 for its discovery by the CDF [2] and DØ [3] experiments at Fermilab, 23
¹⁸¹ years after it was predicted. Only then did the last missing piece of the three quark
¹⁸² generations fall into place. Nowadays, abundant production of top quarks with the
¹⁸³ Large Hadron Collider (LHC) at CERN allows for a variety of accurate measurements
¹⁸⁴ of its properties. Of particular interest, the precise determination of its mass is a key
¹⁸⁵ to a deeper understanding of modern quantum-field theory (QFT). Most notably, the
¹⁸⁶ top-quark mass enters global electroweak fits which are important for consistency testing
¹⁸⁷ of the SM; it also strongly affects corrections to the Higgs quartic coupling, thus having
¹⁸⁸ a large impact on the stability of the SM vacuum. Finally, being the only quark with a
¹⁸⁹ lifetime surpassing the hadronization scale, it is the only *bare* colored particle produced
¹⁹⁰ in SM processes. In general, one has to choose an appropriate mass definition, be it a
¹⁹¹ QFT-consistent definition like the pole mass (on-shell renormalized) and the $\overline{\text{MS}}$ mass
¹⁹² (renormalized after the short-distance $\overline{\text{MS}}$ scheme), or the so-called Monte-Carlo (MC)
¹⁹³ mass.

¹⁹⁴ Recently, the ATLAS and CMS experiments, using innovative approaches and analysis
¹⁹⁵ techniques, have been able to reduce the uncertainty of the measured MC top-quark
¹⁹⁶ mass to about $\Delta m_t \approx 0.5$ GeV in their respective combinations [5, 6] (see Fig. 1.1 for
¹⁹⁷ measurements at the LHC). Achieving a more precise determination of m_t constitutes
¹⁹⁸ a significant challenge for both the experimental and theoretical communities. While
¹⁹⁹ on the one hand, experimentalists have to find new ideas to drive down the mostly
²⁰⁰ systematics-dominated uncertainties, theorists need to improve precision calculations by

1 Introduction

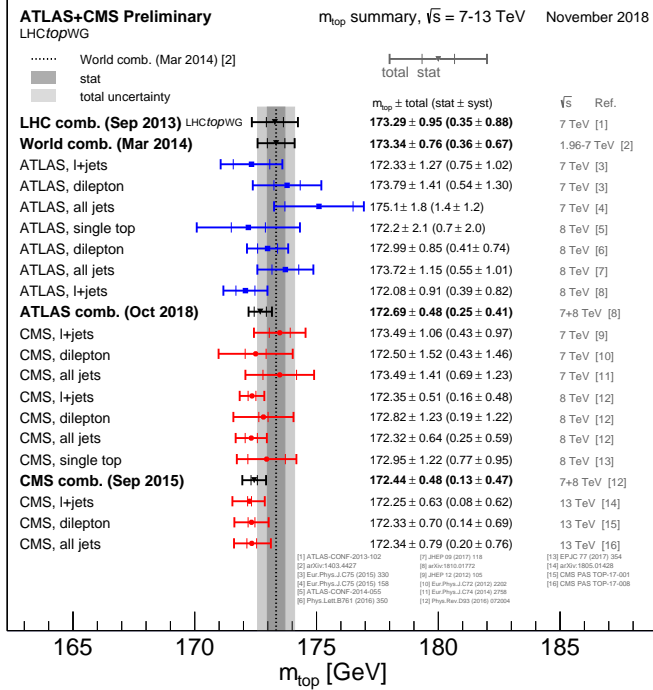


Figure 1.1: ATLAS and CMS combination of $\sqrt{s} = 7, 8, 13 \text{ TeV}$ data for measurements of the top-quark mass m_t . Figure taken from Ref. [4].

going to higher-order predictions and beyond formerly accepted approximations. The computation of higher-order corrections for on-shell top-quark pair ($t\bar{t}$) production has been a major success during the LHC era. The production of a pair of on-shell top quarks is referred to as the narrow-width approximation (NWA). Because the corrections to NWA calculations are expected to be small, of order $\mathcal{O}(\Gamma_t/m_t) < 1\%$ for inclusive cross-sections, most fixed-order predictions aim at computing higher-order QCD and EW corrections to top-quark pair production in this approximation.

The experimentalists, though, reconstruct the top-quark pair from their decay products, either from the dilepton, lepton+jets or all-hadronic final-states, depending on the decay channel of the top and anti-top quarks. The fixed-order prediction of a fully-decayed $t\bar{t}$ final-state is computationally demanding: instead of a $2 \rightarrow 2$ process, the final-state phase-space becomes that of a $2 \rightarrow 4$ (for $pp \rightarrow W^+W^-b\bar{b}$) or a $2 \rightarrow 6$ process (including W -boson decay products). The full final-state prediction at next-to-leading order (NLO) comprises Feynman diagrams that are not present in the NWA: some do not contain doubly-resonant top quarks, and others include internal lines between the top-quark decay legs, which means the latter do not factorize. In fact, the additional interference terms can be of importance to distributions that are sensitive to higher-order and off-shell effects, for example in phase-space regions populated first at higher-order in QCD. The qualitative differences between NWA and full $W^+W^-b\bar{b}$ predictions shall be investigated later on.

221 Another issue concerns the theoretical definition of the top-quark mass. Indeed, rela-
222 tions between different renormalization schemes are known at 4-loop order [7]. This rela-
223 tion suffers from an infrared (IR) so-called renormalon singularity, which is associated to
224 an intrinsically non-perturbative ambiguity in the definition of the top-quark pole mass.
225 This inherent uncertainty was estimated to be of the order $\mathcal{O}(250 \text{ MeV})$ [8–11]. More-
226 over, analyses that rely on simulated distributions (like the template fit method studied
227 in the next chapters) measure the MC top-quark mass, not the pole mass. Although the
228 discussion on the exact relation of the MC to the pole top-quark mass is still ongoing, the
229 difference between both values is expected to be of the order $\mathcal{O}(300 – 500 \text{ MeV})$ [12, 13].

230 In this work, the foundations of the SM are briefly presented, including the Higgs
231 mechanism and the relation between the Higgs sector and the top quark, in Chapter 2. In
232 Chapter 3, the basics of higher-order calculations are summarized: the appearance of UV
233 and IR divergences in loop corrections and the way to deal with them, the perturbative
234 expansion for QCD at high energies from the running of the strong coupling α_s , and the
235 factorization theorem for hadron-hadron collisions are laid out in some detail. Finally,
236 the focus point is set on MC event generators in Chapter 4 and the ingredients needed
237 for particle-level event generation are explained. Switching to the experimental side, the
238 LHC and in particular the ATLAS detector are presented in Chapter 5. After having
239 sketched out these fundaments, the different theoretical descriptions of top-quark pair
240 production are discussed in Chapter 6. With the example of top-quark pair predictions
241 in the $e\mu$ dilepton channel, it is shown how higher-order and off-shell effects can have a
242 sizeable impact on an experimental MC top-quark mass extraction in Chapter 7. There,
243 four different theoretical descriptions are compared with respect to an experimentally
244 realistic top-quark mass extraction for $pp \rightarrow W^+(\rightarrow e^+\nu_e)W^-(\rightarrow \mu^-\bar{\nu}_\mu)b\bar{b}$. In the NWA,
245 top-quark pairs are produced at NLO QCD, where the top-decay is described at different
246 accuracies: LO, respectively NLO QCD, as well as operated by a parton-shower. The
247 NWA results are compared to a full $W^+W^-b\bar{b}$ computation at NLO QCD. Taking into
248 account detector reconstruction efficiencies and bin migration effects, which is the subject
249 of Chapter 8, the shift in the extracted top-quark mass is quantified in an exact ATLAS
250 framework in Chapter 9, where distributions are folded up to detector-level.

251 Looking at another sector entirely, top quarks also play an important role in calcu-
252 lations for the production of one or several Higgs bosons at the LHC. Because the top
253 quark is the heaviest SM particle and since the Higgs boson’s coupling to fermions is
254 proportional to their mass, higher-order corrections to Higgs processes mainly happen
255 through top-quark loops. For instance, single Higgs production at the LHC is domi-
256 nated by gluon-fusion with a top-quark loop intermediate state (so-called loop-induced
257 production), i.e. higher-order corrections to $gg \rightarrow h$ start at two-loop level already. The
258 same holds for the production of a pair of Higgs bosons: this process is of particular
259 interest, since di-Higgs production is the main channel for probing the trilinear Higgs self-
260 coupling. Although the Higgs couplings to heavy fermions and gauge bosons are currently
261 nicely constrained, as shown in Fig. 1.2, the best limit set on the Higgs self-coupling’s
262 ratio κ_λ to the SM-predicted value is given by ATLAS at $-5.0 \leq \kappa_\lambda \leq 12.1$ [16]. In
263 general, the Higgs sector is one of the more poorly explored experimentally, and it is
264 important to have precise (at best model-independent) theoretical predictions for the

1 Introduction

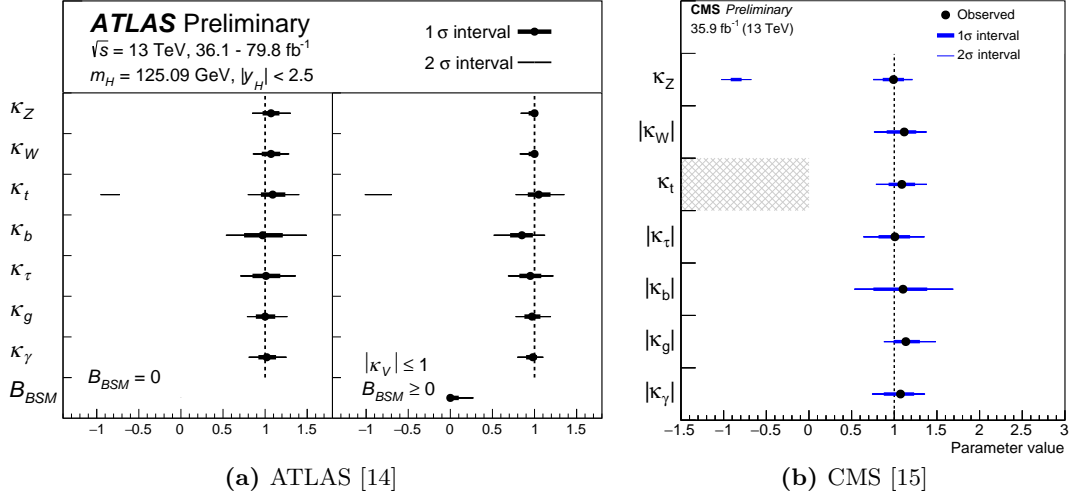


Figure 1.2: Fit values of the Higgs coupling modifiers with respect to the SM-predicted coupling strength (in the κ -framework).

case where the Higgs couplings are not SM-like. It is shown, within a non-linear Effective Field Theory (EFT) framework allowing to vary the Higgs couplings, that the full m_t -dependence of di-Higgs production at NLO QCD has important effects, especially on differential cross-section predictions. In Chapter 10, the EFT framework is introduced under the form of the electroweak chiral Lagrangian (EWChL). The results for NLO di-Higgs cross-sections and differential distributions with variations of the Higgs couplings are presented at a center-of-mass energy of 14 TeV for several benchmark points. Finally, the implementation of the full m_t -dependent NLO corrections for di-Higgs production into the POWHEG-BOX-V2 [17–19] event generator is the subject of Chapter 11. In this package, variations of the trilinear Higgs self-coupling and the top-Higgs Yukawa coupling are now possible. Studies comparing differential distributions for fixed-order NLO to parton-shower matched predictions are presented. Parton-shower related uncertainties are also discussed. Finally, the current state of the SM is summarized and future, potentially interesting developments in both top quark and Higgs physics are outlined.

280

Part I

²⁸¹ Theoretical and Experimental Setup

²⁸² 2 The Standard Model

²⁸³ The SM was developed and supplemented over five decades, and describes all elementary
²⁸⁴ particles and their interactions via three of the four fundamental forces in a quantum-field
²⁸⁵ theoretical framework: the electromagnetic, weak and strong interactions. Although it
²⁸⁶ is known that the SM suffers from some theoretical shortfalls that are briefly described
²⁸⁷ at the end of this chapter (like non-zero neutrino mass measurements [20]), there is, to
²⁸⁸ date, no experimental evidence that directly contradicts it.

²⁸⁹ At the core, the discovery by Glashow, Salam and Weinberg [21–23] that the electro-
²⁹⁰ magnetic and weak interactions could be embedded in a unified theory constitutes the
²⁹¹ first stone of the SM edifice. What if all known forces and particles could be described
²⁹² by the same, unique theory? Later, the quantum chromodynamics (QCD) sector, which
²⁹³ describes the strong interaction, was correctly theorized to rely on a (non-Abelian) gauge
²⁹⁴ symmetry group by Wilczek, Gross and Politzer [24, 25], which leads to asymptotic free-
²⁹⁵ dom of color-charged particles. The addition of the Higgs mechanism, that generates
²⁹⁶ mass terms for the fermions and gauge bosons, culminated in what is known today as the
²⁹⁷ SM Lagrangian. The SM is one of the most successful theories up-to-date, and has been
²⁹⁸ extensively tested against experimental data. A comprehensive comparison of computed
²⁹⁹ cross-sections for SM processes to values measured by ATLAS, shown in Fig. 2.1, makes
³⁰⁰ for a compelling argument in favor of the SM’s predictive power.

³⁰¹ 2.1 Matter content and gauge interactions

³⁰² The SM is a quantum-field gauge theory: the known elementary particles are interpreted
³⁰³ as the excitations of quantized fields, and their interactions are described by the exchange
³⁰⁴ of gauge bosons. Both matter and gauge fields obey certain rules under the corresponding
³⁰⁵ gauge transformations: that is, they transform according to different representations of
³⁰⁶ the underlying gauge group. The SM builds on the

$$SU(3)_C \times SU(2)_L \times U(1)_Y$$

³⁰⁷ gauge group. It is the product group of the QCD group $SU(3)_C$, and its corresponding
³⁰⁸ color quantum number C , and the electroweak group $SU(2)_L \times U(1)_Y$, that distinguishes
³⁰⁹ left- from right-handed particles as doublets, respectively singlets under the group trans-
³¹⁰ formation. The $U(1)_Y$ group’s quantum number is the so-called hypercharge Y . The
³¹¹ fermionic matter fields are classified into left-handed leptons and quarks, both transform-
³¹² ing as doublets under the $SU(2)_L$ group, and their singlet right-handed counterparts.
³¹³ There are furthermore three distinct copies, called generations, or families:

2 The Standard Model

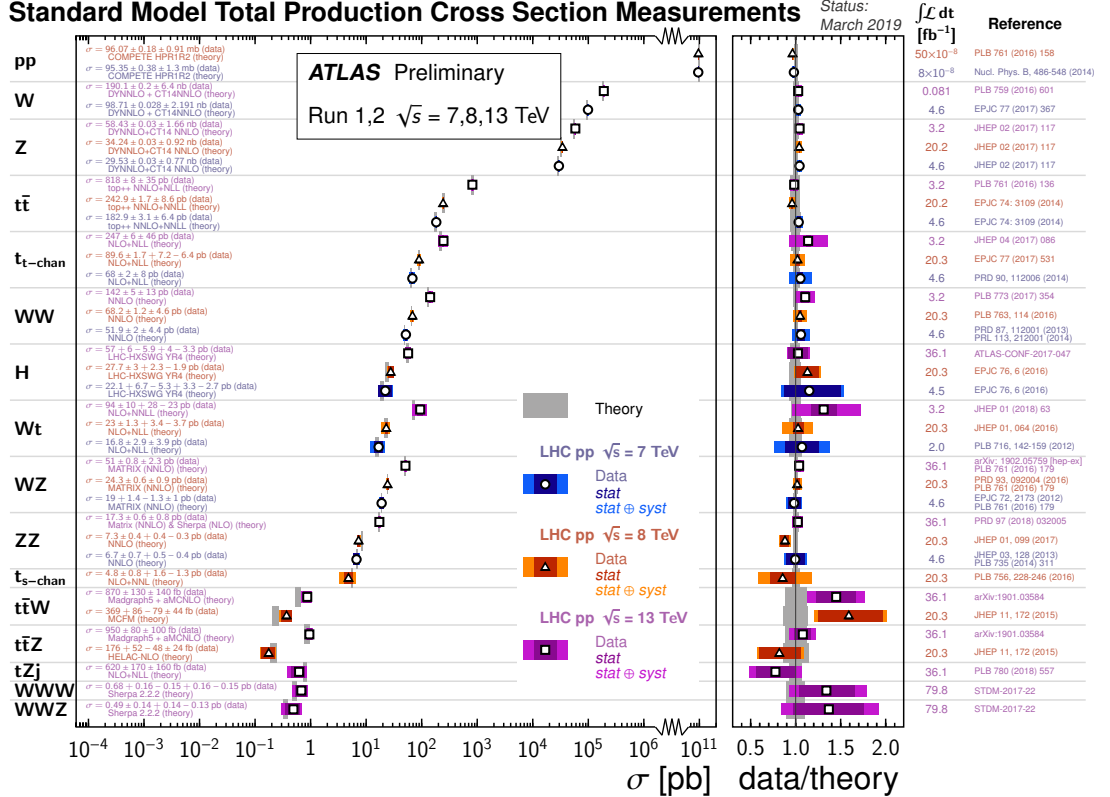


Figure 2.1: The predicted cross-sections (in gray, where bands represent the theoretical uncertainty) for SM production processes at LHC center-of-mass energies of $\sqrt{s} = 7, 8, 13$ TeV are compared to their measured values at the ATLAS experiment (in color) [26]. The ratio of data to theory is shown to be compatible with 1.

$$\begin{pmatrix} \nu_e \\ e^- \end{pmatrix}_L, \quad \begin{pmatrix} u \\ d' \end{pmatrix}_L, \quad \begin{pmatrix} \nu_\mu \\ \mu^- \end{pmatrix}_L, \quad \begin{pmatrix} c \\ s' \end{pmatrix}_L, \quad \begin{pmatrix} \nu_\tau \\ \tau^- \end{pmatrix}_L, \quad \begin{pmatrix} t \\ b' \end{pmatrix}_L,$$

$$e_R^-, \quad u_R, \quad d'_R, \quad \mu_R^-, \quad c_R, \quad s'_R, \quad \tau_R^-, \quad t_R, \quad b'_R,$$

and their corresponding antiparticles. Here, e, μ, τ are the three lepton (ℓ) generations and their corresponding neutrinos ν_ℓ . The particles u, c, t , and d', s', b' are the up-type, respectively down-type quark weak eigenstates. The down-type eigenstates mix via the unitary Cabibbo-Kobayashi-Maskawa (CKM) matrix to give the physical mass eigenstates d, s, b :

$$\begin{pmatrix} d' \\ s' \\ b' \end{pmatrix} = \begin{pmatrix} V_{ud} & V_{us} & V_{ub} \\ V_{cd} & V_{cs} & V_{cb} \\ V_{td} & V_{ts} & V_{tb} \end{pmatrix} \begin{pmatrix} d \\ s \\ b \end{pmatrix}.$$

2.1 Matter content and gauge interactions

319 The quarks are the only matter fields carrying color charge, and live in the triplet **(3)**,
 320 respectively anti-triplet **(̄3)** representations of the $SU(3)_C$ group. The color quantum
 321 numbers are defined as red, blue and green, respectively anti-red, anti-blue and anti-
 322 green. That is, for the up- and down-quark:

$$\begin{pmatrix} u_r \\ u_b \\ u_g \end{pmatrix}, \quad \begin{pmatrix} d_r \\ d_b \\ d_g \end{pmatrix} \in SU(3)_C .$$

323 Governing the interactions, the gauge bosons corresponding to each subgroup couple
 324 with a separate strength to the matter fields. There are:

- 325 • three W_μ^a , $a = (1, 2, 3)$, bosons belonging to $SU(2)_L$, coupling with strength $\propto g$,
- 326 • one B_μ boson belonging to $U(1)_Y$, coupling with strength $\propto g'$,
- 327 • eight gluon fields G_μ^a , $a = (1, \dots, 8)$, belonging to $SU(3)_C$, with coupling $\propto g_s$.

328 By the principle of gauge covariance, the interaction terms between gauge bosons and
 329 the rest of the particle fields are given by promoting the 4-derivatives in the kinetic terms
 330 of the corresponding sector to covariant derivatives:

$$\partial_\mu \rightarrow D_\mu = \left[\partial_\mu + ig \frac{\sigma_a}{2} W_\mu^a + ig' \frac{Y}{2} B_\mu \right] \quad (\text{EW}) , \quad (2.1)$$

331

$$\partial_\mu \rightarrow D_\mu = \left[\partial_\mu + ig_s T_a G_\mu^a \right] \quad (\text{QCD}) , \quad (2.2)$$

332 where σ_a are the three Pauli matrices (the generators of the Lie algebra of $SU(2)_L$),
 333 and T_a are the eight generators of the Lie algebra of $SU(3)_C$. The replacement by a
 334 covariant derivative also induces gauge boson self-coupling interactions.

335 Finally, analogously to the quarks, the electroweak gauge bosons mix to give rise to
 336 the physical charged- and neutral-current interaction bosons:

$$W^\pm = \frac{1}{\sqrt{2}} (W^1 \mp iW^2) , \quad (2.3)$$

$$\begin{pmatrix} \gamma \\ Z \end{pmatrix} = \begin{pmatrix} \cos(\theta_W) & \sin(\theta_W) \\ -\sin(\theta_W) & \cos(\theta_W) \end{pmatrix} \begin{pmatrix} B \\ W^3 \end{pmatrix} , \quad (2.4)$$

337 where θ_W is the Weinberg angle.

338 2.2 The Higgs mechanism

339 If one writes down the most general, renormalizable Lagrangian for the model above,
 340 two problems appear:

- 341 • the usual Dirac mass terms one can introduce in the fermionic sector are not
 342 invariant under $SU(2)_L$,
- 343 • mass terms for the W^\pm, Z bosons are not gauge-invariant.

344 So, in order to generate masses for the aforementioned particles, an external contrap-
 345 tion is needed. The Brout-Englert-Higgs [27–29] mechanism proposed in 1964 introduces
 346 a new spin-0 fundamental $SU(2)_L$ doublet, called the Higgs field:

$$\phi(x) = \begin{pmatrix} \phi^+(x) \\ \phi^0(x) \end{pmatrix}. \quad (2.5)$$

347 It is colorless, and is charged under the electroweak $U(1)_Y$ symmetry. The $SU(3)_C \times$
 348 $SU(2)_L \times U(1)_Y$ Lagrangian gets completed by a (gauged) Higgs sector, where the
 349 covariant derivative D_μ is given by Eq. (2.1):

$$\mathcal{L}_h = (D_\mu \phi)^\dagger (D^\mu \phi) + V(\phi) \quad (2.6)$$

$$= (D_\mu \phi)^\dagger (D^\mu \phi) + \mu^2 \phi^\dagger \phi - \lambda (\phi^\dagger \phi)^2, \quad \lambda > 0. \quad (2.7)$$

350 Similarly to the case of superconductivity [30], the underlying $SU(2)_L \times U(1)_Y$ sym-
 351 metry can be spontaneously broken if the Higgs potential $V(\phi)$ has a non-zero ground
 352 state. This is the case for the *Mexican-hat* potential given above, which is pictured in
 353 Fig. 2.2. When the Higgs field assumes one of the degenerate ground states with a vac-
 354 uum expectation value at the minimum of the potential around $v = \mu/\sqrt{\lambda} \sim 246$ GeV,
 355 it spontaneously breaks the $SU(2)_L \times U(1)_Y$ symmetry of the Lagrangian.

356 Expanding the Higgs field from Eq. (2.5) around the vacuum and taking the EW
 357 covariant derivative from Eq. (2.1),

$$\phi(x) = \frac{1}{\sqrt{2}} \begin{pmatrix} 0 \\ v + h(x) \end{pmatrix}, \quad (2.8)$$

$$D_\mu \phi(x) = \frac{1}{\sqrt{2}} \begin{pmatrix} -\frac{ig}{2} (W_\mu^1 - iW_\mu^2) (v + h(x)) \\ \partial_\mu h(x) - \frac{i}{2} (g'B_\mu - gW_\mu^3) (v + h(x)) \end{pmatrix}, \quad (2.9)$$

358 the Higgs field naturally couples to the gauge bosons. Then, computing the squared
 359 gauged kinematic term of the spontaneously broken Higgs field from Eq. (2.7), and
 360 replacing the gauge fields with their physical rotated states from Eqs. (2.3), (2.4) gives:

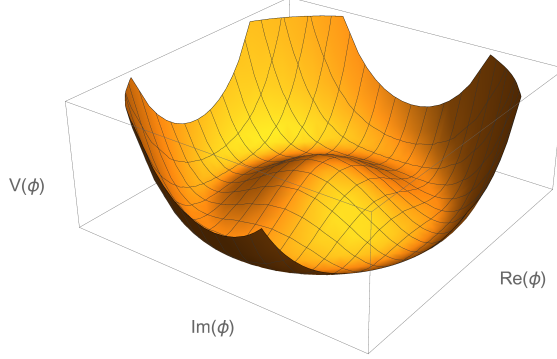


Figure 2.2: The $SU(2) \times U(1)$ symmetric Higgs Mexican-hat potential has a degenerate non-zero ground state at $v^2 = \langle \phi_0^\dagger \phi_0 \rangle \sim (246 \text{ GeV})^2$.

$$\begin{aligned} \mathcal{L} \supset & \frac{1}{2} (\partial_\mu h)(\partial^\mu h) + \underbrace{\frac{g^2 v^2}{4}}_{m_W^2} W_\mu^+ W^{-\mu} + \frac{1}{2} \underbrace{\left(\frac{(g^2 + g'^2)v^2}{4} \right)}_{m_Z^2} Z_\mu Z^\mu \\ & + \underbrace{\frac{1}{2} (2\lambda v^2)}_{m_h^2} h^2 + \lambda v h^3 + \frac{\lambda}{8} h^4. \end{aligned} \quad (2.10)$$

361 So, the dynamic EW spontaneous symmetry breaking (EWSB) of the Higgs potential
 362 generates masses for the W^\pm , Z gauge bosons and identifying the mass terms in the
 363 Lagrangian leads to the following leading-order boson mass relations¹:

$$\begin{aligned} m_H &= \sqrt{2\lambda}v, \\ m_W &= \frac{gv}{2}, & \cos(\theta_W) &= \frac{g}{\sqrt{g^2 + g'^2}}, \\ m_Z &= \frac{\sqrt{g^2 + g'^2}v}{2}, & \sin(\theta_W) &= \frac{g'}{\sqrt{g^2 + g'^2}}. \\ m_\gamma &= 0, \end{aligned}$$

365 The W and Z boson masses are related (at tree-level):

$$m_W = m_Z \cos(\theta_W),$$

366 with the experimentally measured values $m_W = 80.385 \text{ GeV}$, $m_Z = 91.1876 \text{ GeV}$ and
 367 the Weinberg angle $\theta_W = 0.2223$. Finally, considering the last two terms in Eq. (2.10),
 368 the Higgs couples to itself to produce the Feynman diagrams shown in Fig. 2.3.

¹The introduction of the Higgs mechanism also allows for a fermionic gauge-invariant mass term, e.g. by the Yukawa coupling of fermions to the Higgs boson $\mathcal{L} \supset \frac{m_f}{2v} \bar{\psi}_f \psi_f h \xrightarrow{(h \rightarrow v)} \frac{1}{2} m_f \bar{\psi}_f \psi_f$.

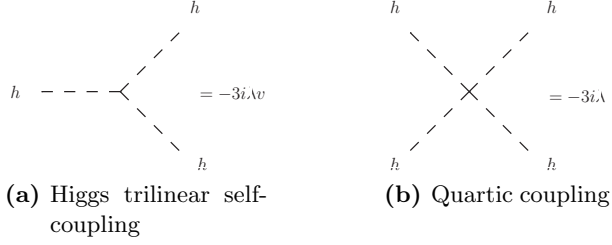


Figure 2.3: The physical Higgs field couples to itself after EWSB. The Feynman rules are given for (a) the triple vertex and (b) the quartic vertex.

369 As a side note, expressing Eq. (2.5) with all available degrees of freedom would give,
370 in polar coordinates,

$$\phi(x) = \frac{1}{\sqrt{2}} e^{\frac{i}{v} \chi_a(x) \sigma^a} \begin{pmatrix} 0 \\ v + h(x) \end{pmatrix}, \quad (2.11)$$

371 where the three real fields χ_a are the massless Goldstone bosons associated with the
372 EWSB of $SU(2) \times U(1)$. Because they will anyhow disappear from the theory (their
373 respective degrees of freedom are sacrificed to the W - and Z -boson longitudinal polar-
374 izations), they are not explicitly considered in the following. Combining the matter and
375 gauge terms with the Higgs sector yields the final form of the SM Lagrangian:

$$\begin{aligned} \mathcal{L}_{\text{SM}} = & -\frac{1}{2} \langle G_{\mu\nu} G^{\mu\nu} \rangle - \frac{1}{2} \langle W_{\mu\nu} W^{\mu\nu} \rangle - \frac{1}{4} B_{\mu\nu} B^{\mu\nu} \\ & + \sum_{\psi=q_L,l_L,q_R,l_R} \bar{\psi} i \not{D} \psi + \text{h.c.} \\ & + Y_l \bar{\psi}_L \phi \psi_R + Y_d \bar{q}_L \phi d_R + Y_u \bar{q}_L \phi u_R + \text{h.c.} \\ & + (D_\mu \phi)^\dagger (D^\mu \phi) + \mu^2 \phi^\dagger \phi - \lambda (\phi^\dagger \phi)^2, \end{aligned} \quad (2.12)$$

376 where $\langle \cdot \rangle$ represents the trace and $\not{D} = \gamma^\mu \partial_\mu$. The first line contains the field-strength
377 tensors of the corresponding gauge bosons, e.g. for a gauge group with structure func-
378 tions f^{abc} defined by the generators $[T_a, T_b] =: i f^{abc} T_c$ of the corresponding Lie algebra,
379 and general coupling strength \tilde{g} :

$$F_{\mu\nu}^a = \partial_\mu A_\nu^a - \partial_\nu A_\mu^a + \tilde{g} f^{abc} A_\mu^b A_\nu^c.$$

380 For the three SM subgroups:

- $SU(3)_C$
 - $A_\mu^a := G_\mu^a$ the gluon fields in the adjoint representation,
 - $\tilde{g} := g_s$ the strong coupling constant,
 - $[T_a, T_b] =: if^{abc}T_c$ with the generators given in Eq. (2.2).

- $SU(2)_L$
 - $A_\mu^a := W_\mu^a$ the gauge fields defined in Eq. (2.1),
 - $\tilde{g} := g$ the $SU(2)_L$ coupling constant,
 - $[\sigma_a, \sigma_b] =: 2i\epsilon_{abc}\sigma_c$ with the Pauli matrices σ_i and the Levi-Civita symbol ϵ_{abc} .

- $U(1)_Y$
 - $A_\mu^a := B_\mu$ the last gauge field appearing in Eq. (2.1),
 - $\tilde{g} := g'$ the $U(1)_Y$ coupling constant,
 - $f^{abc} = 0$ since the group is Abelian.

383 The second line of the SM Lagrangian in Eq. (2.12) contains the kinetic and interaction terms for the fermion fields. The third line contains the Yukawa interaction of all fermions with the Higgs boson for mass generation, and the last line is the unbroken SM Higgs boson sector.

387 The addition of just one Higgs doublet to the SM, like in Eq. (2.5), is a minimal choice. One could legitimately introduce further Higgs fields, as in the two-Higgs doublet model (2HDM) [31] or the Minimal Supersymmetric SM (MSSM) [32], which predict five physical scalar Higgs particles and which can assimilate the discovered Higgs boson at $m_h = 125$ GeV. These extensions of the SM predict in general different coupling strengths of the Higgs boson(s) to other particles and to itself, and precise experimental measurements of these couplings (and of the Higgs decay branching ratios) are needed in order to differentiate between models.

395 2.3 Top-Higgs interactions

396 Intrinsically, the top quark is tightly linked to the Higgs boson properties and has generally strong phenomenological implications for the Higgs sector. Because it is the heaviest SM elementary particle, and since the Yukawa coupling of the Higgs boson to fermions is proportional to their masses, the Higgs couples strongest to the top quark (in comparison, bottom-quark effects in inclusive Higgs observables are of the order of $m_b/m_t = 2.8\%$). 401 It is especially important for Higgs production at the LHC: the predominant production mechanism is gluon-fusion via a triangle top-quark loop, as shown in Fig. 2.4. In comparison, other associated production modes have cross-sections that are more than one order of magnitude smaller. The Feynman diagrams for the main production channels at LHC are also depicted in Fig. 2.5.

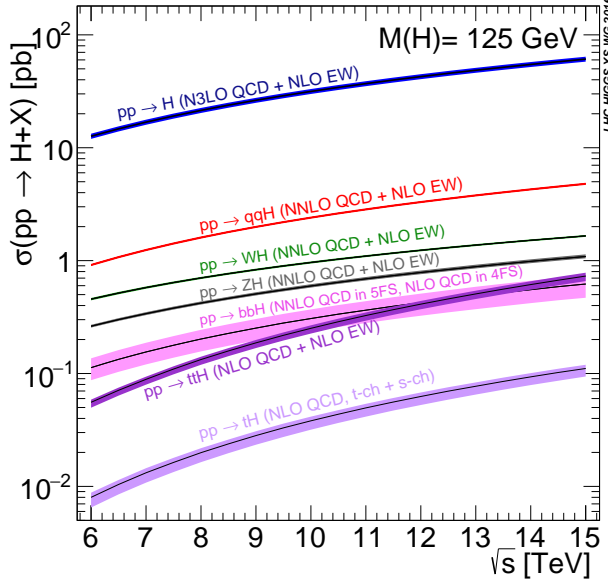


Figure 2.4: Theory prediction for $pp \rightarrow h + X$ production cross-sections as a function of the center-of-mass energy \sqrt{s} . Single Higgs production at the LHC is dominated by gluon fusion mediated by a top-quark loop. Figure taken from Ref. [33].

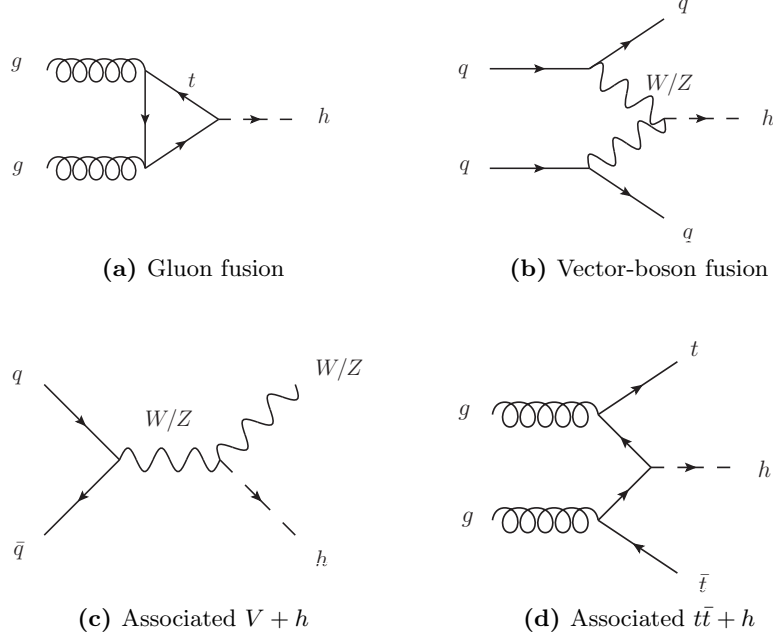


Figure 2.5: Leading-order diagrams for Higgs production by (a) gluon fusion, (b) vector-boson fusion, (c) associated vector production and (d) associated $t\bar{t}$ production.

2.3 Top-Higgs interactions

In relation to both the measurement of the Higgs triple self-coupling and the importance of top-mass effects in Higgs production, the reader is referred to the extensive discussion laid out in Chapter 10. Not only do top quarks influence Higgs process cross-sections at collider experiments, but they also have a deeper connection to the Higgs potential. Indeed, the β -function of the Higgs quartic coupling (which governs the evolution of the coupling's value at different resolution scales, see Chapter 3) is sensitive to renormalization counterterms stemming from top-quark loops.

Eq. (2.13) gives the one-loop β -function for the Higgs quartic coupling [34]:

$$\mu^2 \frac{d\lambda}{d\mu^2} = \beta_\lambda(\lambda, y_t, g_s, \dots) = \frac{1}{16\pi^2} (12\lambda^2 + 6\lambda y_t^2 - 3y_t^4), \quad y_t = \sqrt{2} \frac{m_t}{v} \sim 1 \quad (2.13)$$

where y_t is the top-Yukawa coupling and is proportional to the top-quark mass m_t .

Because the top-Yukawa coupling is of order $\mathcal{O}(1)$, small variations in the value of the top-quark mass modify the evolution of the Higgs quartic coupling λ in a non-trivial way. If $\lambda(\mu)$ was to become negative at scales much below the Planck scale, $M_P \sim 10^{18} - 10^{19}$ GeV (see Fig. 2.6a), the Higgs field could tunnel from the current false vacuum state to the true, absolutely stable vacuum ground state. Current measurements seem to support the fact that the SM is in a metastable state, as shown in Fig. 2.6b. For the existentially anxious reader, a state-of-the art calculation of the EW vacuum decay rate can be found in Ref. [35].

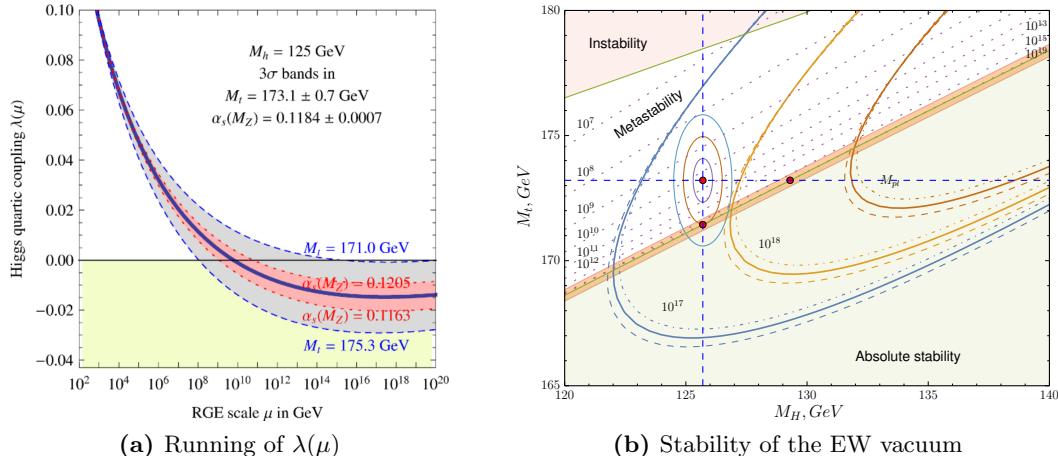


Figure 2.6: (a) The evolution of the Higgs quartic coupling λ can lead to negative values at high energy scales (below the Planck scale M_P). This in turn makes the EW vacuum potentially unstable. The running is highly dependent on the top-quark mass and α_s values [36]. (b) The SM point, in red, is plotted in the (m_h, m_t) phase-space with $1-, 2-$ and 3σ uncertainties. The pink dotted lines indicate contours where $\lambda(\mu) = 0$ for the indicated values of μ , and the parabolic curves where the beta-function $\beta_\lambda(\mu) = 0$ for chosen values of μ . The measured Higgs and top-quark masses point to a SM universe close to the metastable region [37].

423 2.4 Outstanding issues with the Standard Model

424 For all its successes, the SM is known to have some theoretical flaws. Below is a list of
 425 familiar shortcomings:

- 426 • **Massless neutrinos:** In the SM, neutrinos are naturally massless. Experi-
 427 ments [20] have shown that neutrinos can oscillate between the different fami-
 428 lies, and this requires a mixing of flavor states into mass eigenstates, similarly
 429 to the CKM mixing. Different mechanisms [38–40] were introduced to generate
 430 neutrino masses: a right-handed (so-called *sterile*) neutrino could exist, and not
 431 interact with matter (since no right-handed neutrino was ever observed), or neu-
 432 trinos could acquire a Majorana mass. Some R-parity violating supersymmetric
 433 (SUSY) models also produce neutrino masses [41, 42].
- 434 • **Gravity:** General relativity has yet to be quantized and incorporated into the SM
 435 under its current form, and a unified theory of all four interactions is still missing.
 436 As a first attempt, an exchange gravitational gauge boson can be introduced under
 437 the form of a spin-2 particle, called the graviton. The addition of corresponding
 438 terms to the SM Lagrangian spawns the apparition of UV divergences that cannot
 439 be handled by a finite number of counterterms [43–45], though, and the theory is
 440 not perturbatively renormalizable.
- 441 • **Dark matter:** The presence of dark matter in the Universe has been suggested
 442 from multiple cosmological observations [46–50]. Yet, the SM does not contain a
 443 good dark matter candidate particle. Some extensions of the SM, in particular
 444 SUSY, provide a heavy non-decaying particle (the lightest in the SUSY spectrum,
 445 called lightest supersymmetric particle) that turns out to be a good candidate.
- 446 • **Baryon asymmetry:** The SM predicts that matter and antimatter should have
 447 been produced almost symmetrically at the Big Bang. Yet baryons are observed
 448 to be in overwhelming excess over antibaryons in our part of the Universe [51, 52].
- 449 • **Hierarchy problem:** There is a manifest imbalance between the three unified
 450 forces of the SM and gravity, or between their respective mass scales. In particular,
 451 it is not clear why the Higgs boson mass is so small with respect to the Planck scale:
 452 basically, radiative corrections to the Higgs self-energy should blow up its mass, and
 453 the observed value of $m_h = 125$ GeV requires an incredible amount of fine-tuning to
 454 cancel radiative corrections. Again, SUSY models solve this problem by requiring
 455 every SM particle to have a supersymmetric partner which has the opposite spin-
 456 statistics: their contributions to the Higgs mass then cancel naturally [53].

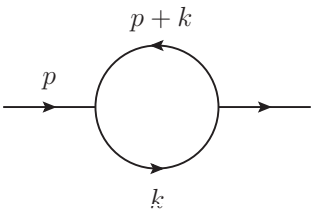
457 Although all model extensions of the SM have respective advantages over the current
 458 theory, none of the particles predicted by them has been observed at the LHC or any
 459 other experiment yet.

460 3 Higher-order perturbative calculations in 461 hadron-hadron collisions

462 The SM Lagrangian presented in the last chapter provides the Feynman rules to compute
 463 theoretical cross-sections. As will be explained in Section 3.1.3, the scattering amplitudes
 464 (at high-energies, for QCD) can be expanded to a perturbative series in the coupling
 465 constant: the interactions are represented by Feynman diagrams, and higher-order cor-
 466 rections generate loop diagrams that are most of the time divergent. Since the first
 467 successes of QFT in predicting basic energy spectrum properties and leading-order (LO)
 468 scattering amplitudes, there has always been a need for a more consistent framework in
 469 which higher-order corrections could be worked out. In this chapter, the important in-
 470 gredients used in most theoretical computations nowadays are summarized, in particular
 471 in the context of high-energy hadron-hadron collisions. Most of the traditional content
 472 presented here is adapted from Refs. [54–58].

473 3.1 Divergences in Quantum-Field Theory

474 Going beyond Feynman tree diagrams in the computation of scattering matrix-elements,
 475 one encounters two classes of divergences. Consider a one-loop scalar massless two-point
 476 function, where the internal loop-momentum is integrated over:

477 

$$I_2(p^2; 0, 0) = \int_{-\infty}^{\infty} \frac{d^4 k}{(2\pi)^4} \frac{1}{(k^2 + i\delta)((p+k)^2 + i\delta)} . \quad (3.1)$$

478 In the limit $|k| \rightarrow \infty$, the integral behaves as $I \propto \int \frac{dk k^3}{k^2 \cdot k^2} = \int \frac{dk}{k}$ which is logarithmi-
 479 cally divergent. The integral is also divergent when taking the limit $k \rightarrow 0$. These are
 480 called *ultraviolet*, respectively *infrared* divergences.

481 As a solution to the infinities conundrum, the above integral has to be treated by the
 482 introduction of a UV cutoff of some kind – this is a method called *regularization*, and
 483 by absorbing the regularized infinities in a consistent way through the *renormalization*
 484 of the Lagrangian bare couplings and masses.

485 3.1.1 Regularization

486 A first attempt at controlling UV divergences consists in the introduction of a high-
 487 momentum regulator $k^2 < \Lambda^2$. Then, the loop integral given in Eq. (3.1) behaves as

$$I_2(p^2; 0, 0) \propto \int_{\epsilon}^{\Lambda} \frac{dk}{k} \sim \log(\Lambda) , \quad (3.2)$$

and the integral diverges logarithmically in the cutoff Λ . This is typical of renormalizable theories. Now, obviously, any physical observable should not depend on the value of the arbitrary cutoff, and in practice it does not.¹ As a theoretical downside, the introduction of the cutoff breaks gauge-invariance. It also breaks translational invariance and makes it difficult to use Feynman parameters and the corresponding variable replacements $p \rightarrow p + k$.

A possible gauge-invariant regularization method is the so-called Pauli-Villars regularization: a much more massive particle is introduced and its contribution subtracted from the ordinary propagator, that is:

$$\int \frac{d^4k}{(2\pi)^4} \frac{1}{k^2 + i\delta} \rightarrow \int \frac{d^4k}{(2\pi)^4} \left(\frac{1}{k^2 + i\delta} - \frac{1}{k^2 - M^2 + i\delta} \right) . \quad (3.3)$$

The Pauli-Villars technique cannot be applied to QCD because it is not gauge-covariant, though. On the same stance, it introduces an unphysical field that violates the spin-statistics theorem (it amounts to a spurious scalar field with Fermi statistics). One of the preferred regularization methods nowadays is dimensional regularization. It was refined by 't Hooft and Veltman [60] to regularize any integral, is gauge-invariant and works for non-Abelian theories as well. The governing idea is that quantum-field theories in a smaller number of dimensions have a lesser superficial degree of divergence. The four dimensions of space-time are therefore analytically continued to $d = 4 - 2\epsilon$ dimensions, and the integral in Eq. (3.1) can be cast into the following form:

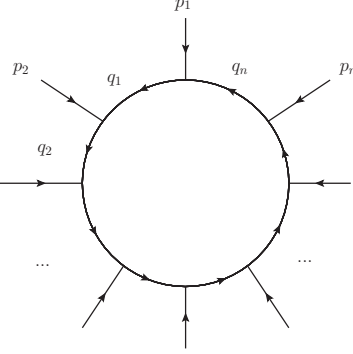
$$I_2(p^2; 0, 0) = \mu^{2\epsilon} \int \frac{d^d k}{(2\pi)^d} \frac{1}{(k^2 + i\delta)((p+k)^2 + i\delta)} , \quad (3.4)$$

where the renormalization scale μ is a dimensionful parameter needed to keep the integral dimensionless. Then the integral can be worked out by introducing Feynman parameters and Wick-rotating to give the analytical result

$$I_2(p^2; 0, 0) = \frac{1}{\epsilon} + \ln \frac{\mu^2}{-p^2 - i\delta} + 2 + \mathcal{O}(\epsilon) , \quad (3.5)$$

where the UV divergences now appear as (at most double, at one-loop) poles in the dimensional regulator ϵ . A general dimensionally-regularized one-loop scalar integral with n external legs has the form:

¹For a fun exercise of trying out different forms of cutoff (Gaussian, Dirac-delta,...), see Ref. [54] for the case of the vacuum polarization in the Casimir effect [59].

512 

$$I = \mu^{n-d/2} \int \frac{d^d k}{(2\pi)^d} \prod_{j=1}^n \frac{1}{(q_j^2 - m_j^2 + i\delta)} , \quad (3.6)$$

513 where the internal momenta $q_j = k + \sum_{i=1}^j p_i$ are expressed as a linear combination of
 514 the loop momentum k and the external momenta p_i . Systematic Feynman parameters
 515 can be found for the integral above, and generally it can be recast into the form

$$I = \Gamma(n - d/2) \prod_{i=1}^n \int_{0 \leq x_i \leq 1} dx_i \delta \left(1 - \sum_{j=1}^n x_j \right) \frac{\mathcal{U}^{n-d}(\vec{x})}{\mathcal{F}^{n-d/2}(\vec{x}, p_i \cdot p_j, m_i^2)} . \quad (3.7)$$

516 The x_1, \dots, x_n are the Feynman parameters, and \mathcal{U} , \mathcal{F} are the first, respectively
 517 second Symanzik polynomials.² Then, one needs only perform the integration over the
 518 Feynman parameters. Most importantly, all one-loop integrals can be reduced to a linear
 519 combination of a set of *master integrals* that are at most box-diagrams, which are all
 520 known analytically and implemented in integral libraries. Finally, for tensor integrals
 521 where the numerator of Eq. (3.6) contains Lorentz indices, there exist methods for their
 522 reduction to a set of scalar integrals, like the systematic Passarino-Veltman method [61]
 523 which uses a form factor expansion to factorize the indices. For the interested reader,
 524 Refs. [62–66] supply a comprehensive examination of various techniques for reducing and
 525 evaluating Feynman integrals.

526 Dimensional regularization has lots of benefits, and the algebra is quite straightforward.
 527 Its major disadvantage is that the Dirac algebra for fermions has to be analytically
 528 extended to $d = 4 - 2\epsilon$ space-time dimensions as well, which is not trivial. The Dirac
 529 matrices can be made to obey an analytically continued Clifford algebra

$$\{\gamma^\mu, \gamma^\nu\} = 2g^{\mu\nu} , \quad (3.8)$$

530 with a d -dimensional metric, $g^{\mu\nu}g_{\mu\nu} = d$, where it is but unclear what happens to the
 531 last Dirac matrix $\gamma_5 = i\gamma_0\gamma_1\gamma_2\gamma_3$. The different ways of treating γ_5 and the helicities of
 532 external and internal particle fields lead to different regularization schemes. Note that
 533 physical observables do not depend on the chosen scheme. In the dimensional reduction
 534 scheme (DRED) which is used for the predictions given in Chapters 6–11, the Dirac
 535 algebra is left to $d = 4$ dimensions, and the same holds for all external momenta and
 536 helicities. Only the internal momenta are analytically continued to d -dimensions.

²Eq. (3.7) can also be generalized to a Feynman integral for l loops, n external and m internal momenta.

537 **3.1.2 Renormalization**

538 As a way to treat the infinities arising from the UV region of integration, the bare param-
 539 eters of the Lagrangian are redefined to absorb the divergent contributions. Although
 540 this seems mathematically shaky, it is remarkable that the redefinition of a finite number
 541 of parameters allows for the treatment of divergences order-by-order and for all Feynman
 542 diagrams contributing to the amplitude of a renormalizable theory. In practice, renor-
 543 malization of the Lagrangian is achieved by rewriting the bare masses and couplings m_0
 544 and g_0 , as well as the fields themselves ψ_0 , as a physical (measurable) parameter and a
 545 counterterm

$$\begin{aligned} m_0 &= Z_m m = m + \delta m , \\ g_0 &= Z_g g = g + \delta g , \\ \psi_0 &= \sqrt{Z} \psi . \end{aligned} \tag{3.9}$$

546 The only requirement is that diagrams corresponding to the counterterms should can-
 547 cel UV divergences stemming from the bare Lagrangian. In principle, the procedure does
 548 not define how to handle the finite terms accompanying these diagrams: depending on
 549 the additional criteria, several renormalization schemes can be chosen (on-shell, MS, MS,
 550 or others). Here as well, the physical observables should be independent of the choice
 551 of scheme (the top-quark mass is a fringe example and will be discussed summarily in
 552 Chapter 6).

553 The physical parameters entering the Lagrangian, e.g. the masses and couplings m, g ,
 554 have to be determined by experiment. By definition, they are measured at a given energy
 555 scale. Colloquially, a renormalization starting point is chosen: the couplings/masses are
 556 then said to *run* with the scale at which they are defined. Notably, the renormalized
 557 field theory runs according to the Callan-Symanzik [67–69] equation, which governs the
 558 dependence of the n -point correlation functions on the model's parameters by asking
 559 that the bare Green's functions $G_0^{(n)}(x_1, \dots, x_n; m_0, g_0)$ do not depend on the variations
 560 given in Eq. (3.9):

$$\left(m \frac{\partial}{\partial m} + \beta(g) \frac{\partial}{\partial g} + n\gamma \right) G^{(n)}(x_1, \dots, x_n; m, g) = 0 , \tag{3.10}$$

561 where the β -function of the theory is defined as $\beta(g) = \frac{m}{\delta m} \delta g$, and the anomalous
 562 dimension is given by $\gamma = \frac{m}{\delta m} \frac{\delta \sqrt{Z}}{\sqrt{Z}}$. Eq. (3.10) is an example of a broad class of evolution
 563 equations called renormalization group equations (RGE).

564 **3.1.3 Perturbative expansion of Quantum Chromodynamics**

565 From the running of the strong coupling constant given by the QCD β -function,

$$\mu_R^2 \frac{\partial \alpha_s}{\partial \mu_R^2} = \beta(\alpha_s) = - (b_0 \alpha_s^2 + b_1 \alpha_s^3 + \dots) , \tag{3.11}$$

3.1 Divergences in Quantum-Field Theory

one sees that because of the negative sign in Eq. (3.11), the strong coupling $\alpha_s(\mu_R^2)$ becomes smaller at higher scales μ_R^2 . This running is manifest in Fig. 3.1, which shows measurements of the strong coupling α_s at different energy scales Q , in agreement with the QCD theory prediction. Thus, with the measured value of the strong coupling at intermediate scales $\alpha_s(M_Z) \approx 0.118$, the interactions at high-energy hadron colliders can be treated perturbatively in α_s . For any process cross-section $\sigma_{ab \rightarrow X}$, where a, b , and X are freely propagating initial-, respectively final-states, one can expand the cross-section in a Taylor series,

$$\hat{\sigma}_{ab \rightarrow X} = \alpha_s^k(\mu_R^2) (\hat{\sigma}_{\text{LO}}(p_i, p_f; \mu_R^2) + \alpha_s(\mu_R^2) \hat{\sigma}_{\text{NLO}}(p_i, p_f; \mu_R^2) + \mathcal{O}(\alpha_s^2(\mu_R^2))) . \quad (3.12)$$

At each order in the strong coupling α_s , the cross-section can be computed and will depend on the choice of the renormalization scale. Usually it is chosen close to the expected momentum exchange Q^2 . The systematic uncertainty related to the arbitrary choice of the scale is then estimated by varying the renormalization scale by factors of $\frac{1}{2}$ and 2.

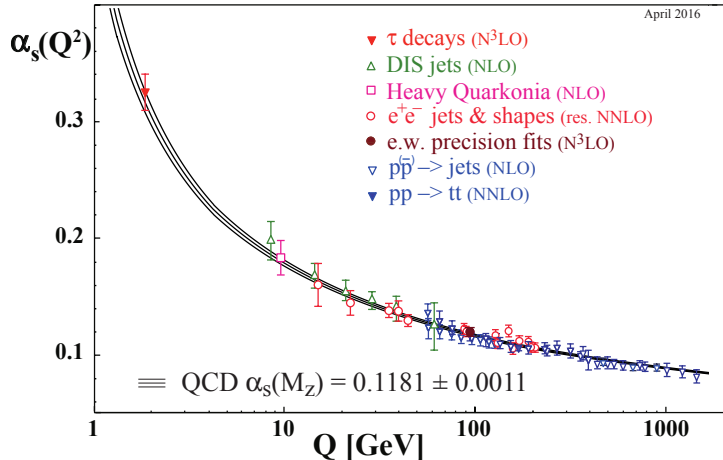


Figure 3.1: Various measurements of the strong coupling $\alpha_s(Q^2)$ at different energy scales Q show the running behavior typical of QCD, with a coupling strength that becomes smaller at higher energies, and a Landau pole at the hadronization scale $Q = \Lambda \sim 1 \text{ GeV}$. Figure taken from Ref. [1].

The accuracy of a computation is given by the truncation order of the perturbative series in Eq. (3.12). In certain regions of phase-space, though, large prefactors can be introduced at all orders, when two far-away scales Q and q are involved. This usually spawns the appearance of large logarithms of the form $\ln^n(Q^2/q^2)$, which have to be resummed to a given *logarithmic* accuracy across all orders. Some details will be given in Section 4.2.

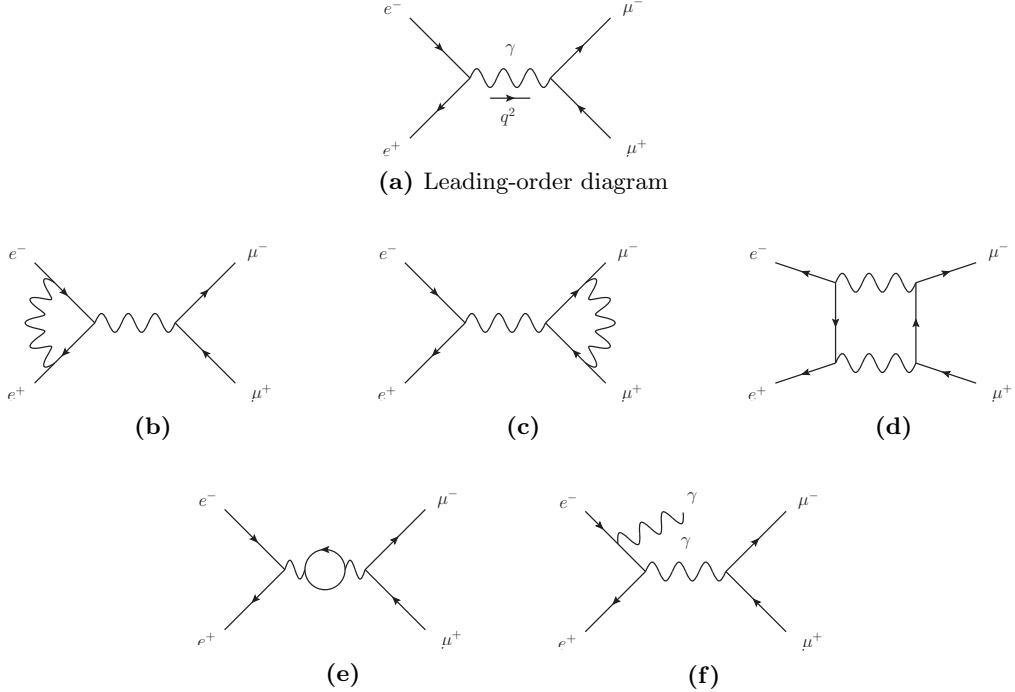
585 **3.2 Infrared divergences**


Figure 3.2: Feynman diagrams for $e^+e^- \rightarrow \mu^+\mu^-$. (a) The only leading-order diagram, with a photon in the s -channel, (b-e) virtual one-loop corrections and (f) a real-emission diagram.

586 Starting from an example, let us consider the case of QED higher-order corrections to
 587 $e^+e^- \rightarrow \mu^+\mu^-$ annihilation. Feynman diagrams up to $\mathcal{O}(\alpha^3)$ are shown in Fig. 3.2. At
 588 leading-order, the cross-section is given by

$$\sigma_{\text{LO}} = \int_{\Phi} d\Phi |\mathcal{M}_0|^2 = \frac{4\pi\alpha^2}{3q^2}, \quad (3.13)$$

589 where the squared amplitude $|\mathcal{M}_0|^2$ has to be integrated over the phase-space Φ , and
 590 q^2 is the momentum carried by the exchanged photon. Let us assume the UV divergences
 591 have been handled by the introduction of appropriate counterterms. That is, the UV
 592 divergences stemming from the loop momentum integration from diagrams (b) and (c)
 593 in Fig. 3.2 have been taken care of by renormalizing the electron charge and the muon
 594 charge, respectively. Diagram (e) is also UV divergent but is nothing else than vacuum
 595 polarization in QED (thus, it has no impact on any observable), while diagram (d) has
 596 no UV divergence. Computing the amplitude, one realizes there is also an IR divergence
 597 coming from the massless photon propagator in the loops.

598 First, the IR divergence needs regularizing. The simplest way to do that is to give the
 599 photon a small, non-zero mass, $m_\gamma > 0$, and to take the limit $m_\gamma \rightarrow 0$ at the end of the

3.3 The factorization theorem

600 calculation. Computing the virtual contribution, $\sigma_V \propto (\mathcal{M}_V^\dagger \mathcal{M}_0 + \text{h.c.})$, one arrives
601 at the result

$$\sigma_V = \frac{2}{3} \pi^2 \frac{\alpha^3}{q^2} \left(\frac{\pi^2}{5} - \frac{7}{2} - \ln^2 \left(\frac{m_\gamma^2}{q^2} \right) - 3 \ln \left(\frac{m_\gamma^2}{q^2} \right) \right). \quad (3.14)$$

602 The IR divergence is still present but it is explicit in $\ln(m_\gamma)$.³ For the perturbative
603 expansion to be consistent, real-emission diagrams of $\mathcal{O}(\alpha^3)$ have to be included, that
604 is diagrams of the sort pictured in Fig. 3.2f, where a photon is radiated either from the
605 initial- or the final-state. Doing so, one gets a contribution of the form $\sigma_R \propto |\mathcal{M}_R|^2$:

$$\sigma_R = \frac{2}{3} \pi^2 \frac{\alpha^3}{q^2} \left(-\frac{\pi^2}{5} + 5 + \ln^2 \left(\frac{m_\gamma^2}{q^2} \right) + 3 \ln \left(\frac{m_\gamma^2}{q^2} \right) \right). \quad (3.15)$$

606 Combining the different contributions to the cross-section, the IR divergences can-
607 cancel between the virtual one-loop and the real-emission matrix-elements to give a finite
608 correction to the leading-order cross-section:

$$\sigma_{\text{NLO}} = \sigma_{\text{LO}} + \sigma_V + \sigma_R = \sigma_{\text{LO}} \left(1 + \frac{3}{4\pi} \alpha \right). \quad (3.16)$$

609 This behavior is symptomatic of IR divergences and falls under the purview of the
610 Kinoshita–Lee–Nauenberg (KLN) theorem, which states that sufficiently inclusive ob-
611 servables are always IR-finite.

612 Although the cancellation of IR divergences is ensured by the KLN theorem, it is
613 non-trivial to realize it numerically (for example in the context of a Monte-Carlo event
614 generator). Section 4.1.2 will briefly develop this point.

615 3.3 The factorization theorem

616 The collision of composite states like the protons used at LHC implies interactions of
617 highly non-perturbative objects. It is not clear at first how to handle these theoretically:
618 color confinement does not allow for free quarks or gluons to be observed, thus the
619 initial-state in hadron colliders cannot a priori be defined perturbatively. At high-energy,
620 though, the interaction with the highest momentum exchange takes place over time scales
621 that are far smaller than the typical time scale at which the proton's constituents interact
622 among themselves. The description of such a collision can therefore be *factorized* in long-
623 and short-distance (or short- and long-time scale) physics: a hard collision of two freely
624 propagating partons, and non-perturbative interactions within hadrons. Mathematically,
625 the cross-section $\sigma_{pp \rightarrow X}$ for the production of a state X from the collision of two protons
626 can be written as

³The divergent terms are called Sudakov double logarithms and are systemic of collinear/soft emission (see Chapter 4).

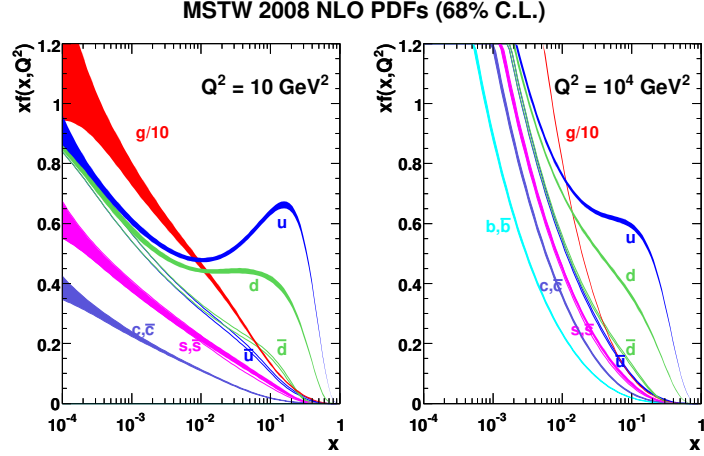


Figure 3.3: The MSTW 2008 NLO proton PDFs [70] as a function of the parent proton’s momentum fraction x at resolution scales $Q^2 = 10 \text{ GeV}^2$ (left), $Q^2 = 10^4 \text{ GeV}^2$ (right).

$$\sigma_{pp \rightarrow X} = \sum_{ab} \int dx_a f_{a/p}(x_a, \mu_F^2) \int dx_b f_{b/p}(x_b, \mu_F^2) \cdot \hat{\sigma}_{ab \rightarrow X}(x_a p_1, x_b p_2; \mu_F^2), \quad (3.17)$$

where a and b are possible constituents of the parent protons (sea or valence quarks and gluons), $f_{a/p}$, $f_{b/p}$ are encoding the non-perturbative origin of the partons in the parent protons, and $\hat{\sigma}_{ab \rightarrow X}$ is the cross-section for the production of the final-state X from the collision of the free partons a and b , the latter of which can now be computed perturbatively in QCD. Eq. (3.17) is called the *factorization theorem* of Quantum Chromodynamics, and sets the basis for all cross-section predictions at LHC. The functions $f_{a/p}$, $f_{b/p}$, which are called *parton distribution functions* (PDF), depend on the momentum fraction ξ_a , ξ_b carried away by the parton from the parent proton, and on the resolution scale Q^2 . Crudely said, the partonic content of the protons depends on the scale at which they are resolved.⁴ The PDFs by definition cannot be computed perturbatively in QCD, but they can be measured from experimental data. As a matter of fact, a precise measurement of the proton’s PDF is crucial, and constitutes one of the main sources of uncertainty in theoretical predictions at the LHC. Fig. 3.3 depicts the measurement of the proton PDFs by the MSTW collaboration from a global fit of hard-scattering data [70].

⁴The PDFs also obey an evolution equation similar to the RGE called DGLAP equation: this evolution runs from a central scale choice, namely the *factorization scale* μ_F .

642 4 Monte-Carlo (MC) event generators

643 To be able to compare a theory prediction for hadron colliders to an experimental mea-
 644 surement released by e.g. the ATLAS experiment, theorists and experimentalists meet
 645 on a common ground: the cross-section σ . The cross-section can be inclusive, and rep-
 646 presents the total number of events for a given process after applying cuts and correcting
 647 for the detector acceptance, or it can be a differential cross-section with respect to some
 648 kinematic variable $d\sigma/d\mathcal{O}$, where $\mathcal{O} = n_{\text{jets}}, m_{t\bar{t}}, \dots$ is any event observable. On one
 649 side, the theorists need to compute a cross-section from a QFT starting point, namely
 650 the Lagrangian: at the most basic level, this means implementing Fermi's golden rule
 651 (Eq. (4.1)). On the other side, experimentalists have to count events and correct for
 652 detector acceptance and resolution (Eq. (4.2)):

$$\sigma = \frac{1}{4E_a E_b v} \int \prod_f \left(\frac{d^3 p_f}{(2\pi)^3} \frac{1}{2E_f} \right) |\mathcal{M}_{fi}|^2 (2\pi)^4 \delta^4(p_a + p_b - \sum_f p_f), \quad (4.1)$$

$$\sigma = \frac{N_{\text{events}}}{\epsilon \cdot \mathcal{L}_{\text{int}}}, \quad (4.2)$$

653 where E_a and E_b are the energies of the incoming particles a and b , the constant
 654 $v = |\vec{v}_a - \vec{v}_b|$ is given by the relative 3-velocities of the particles in the beam and p_f , E_f
 655 are the 3-momenta and energies of all final states. As a matter of fact, the infinitesimal
 656 volume element above is relativistically invariant. Ultimately, the relativistic matrix-
 657 element squared $|\mathcal{M}_{fi}|^2$ has to be integrated over the whole phase-space while enforcing
 658 4-momentum conservation. Experimentally, in Eq. (4.2), the cross-section is equal to
 659 the event count, corrected for phase-space acceptance, detector resolution and normal-
 660 ized by the integrated luminosity \mathcal{L}_{int} . For the case of differential distributions, the
 661 formula becomes more complicated, as binned events migrate depending on the detector
 662 resolution. The discussion of this case is postponed to Chapter 8.

663 There are two issues with the picture at hand. First, the matrix-element for a given
 664 process can typically be computed only up to $\mathcal{O}(\text{few})$ external legs. Because the mul-
 665 tiplicity of final-state particles in a collider experiment like the LHC is of the order
 666 $\mathcal{O}(10^2 - 10^3)$, it is in practice impossible to calculate such amplitudes. Second, the
 667 perturbative expansion and the factorization presented in Chapter 3 break down when
 668 colored particles are produced with small energies. In particular, around energy scales
 669 where free final-state partons fall in the realm of non-perturbative interactions, they
 670 hadronize to form the observable colorless bound states demanded by color confinement.
 671 Therefore, the structure of the whole collision has to be broken down into pieces across
 672 the several scales involved, and the theoretical treatment of each piece is valid only in

4 Monte-Carlo (MC) event generators

these subdomains and subjected to different levels of approximation. The theory community developed the necessary ingredients to improve the description of each stage and assembled them into mostly-automated programs called *Monte-Carlo (MC) event generators*.

MC event generators basically simulate the particle collisions as they would happen at the interaction points of an experiment like ATLAS or CMS. The MC program has to match multi-scale physics to simulate a collision, taking into account non-perturbative (PDF and quark fragmentation, hadron decay, underlying event, proton beam remnants) as well as perturbative (matrix-element and parton-shower matching) phenomena, as shown in Fig. 4.1.

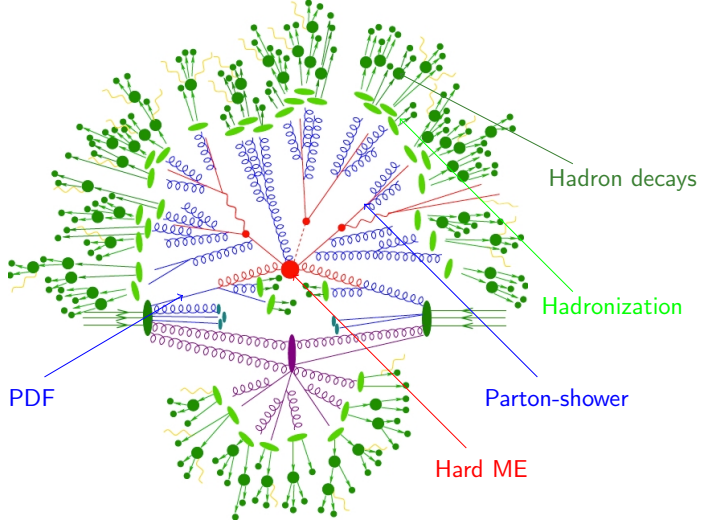


Figure 4.1: A typical MC event. Figure adapted from Ref. [71].

Under the hood of any Monte-Carlo program, the ingredients are essentially the same:

- **Monte-Carlo integrator:** The phase-space is sampled, usually with the help of an adaptive Monte-Carlo integration algorithm, to numerically perform the integral given in Eq. (4.1). As a notable example, the `Cuba` library [72] implements four multi-dimensional integration algorithms: `Vegas` [73], `Divonne` [74], `Suave` [72, 75] and `Cuhre` [76] (although `Cuhre` is deterministic and not properly a MC integrator).
- **PDFs:** There is an extensive amount of PDF measurements varying in the used datasets, theoretical precision, combination strategy, handling of α_s , or flavor thresholds. The `LHAPDF 6` package [77] interpolates PDF values from discrete measurement points in the (x, Q^2) phase-space and can be interfaced to the MC generator.

- **Hard matrix-element:** The core of the calculation is the computation of the matrix-element \mathcal{M}_{fi} . It determines the theoretical accuracy of the prediction to a given order in α_s . More details are given in Section 4.1.
- **Parton shower:** As stated above, the high-multiplicity final-state is evolved from the few-parton hard matrix-element through subsequent radiative emission by a parton-shower algorithm. These routines base on first-principles QCD (and QED), but contain inherent approximations and parametric degrees of freedom that generate an uncertainty associated with the choice of algorithm. Section 4.2 will expand on the topic.
- **Hadronization and hadron decay:** Once the shower evolution is brought down to energies of the order of the hadronization scale (of order $\mathcal{O}(1 \text{ GeV})$), the free partons bind to form colorless states. This is handled by a model on the only assumption that it should describe data to the best possible extent. Commonly, these models have a certain number of free parameters that are *tuned* to data. In Section 4.3, the Lund string and the cluster model are briefly detailed.
- **Multiple partonic interaction and underlying event:** Especially at small momentum fractions, it is possible that more than one parton from the same parent proton contribute to the interaction. The description of this phenomenon is also mostly based on MC modeling and has to be tuned to experimental data.

4.1 Matrix-element providers

The first programs for generating the matrix-element \mathcal{M}_{fi} needed in Eq. (4.1) were highly specialized. They would handle one specific process and would be mostly analytically hard-coded. At some point, authors from the theory community started to make their code available and the corresponding libraries would be assembled into multi-processes packages. This is the example of the MCFM [78], VBFNLO [79–81] and BlackHat [82] packages. Nowadays, after a paradigm shift, the computation of the hard process matrix-element is decidedly automatized at one-loop level: programs like MADLOOP [83–86], OPENLOOPS [87, 88], GoSam [89, 90], RECOLA [91, 92] and HELAC-NLO [93] can be interfaced directly to most MC generators and provide the amplitude given any phase-space point, while other programs focus on specific processes, as for example NJET [94], which calculates multijet amplitudes at NLO in massless QCD, VBFNLO for vector-boson fusion in a number of processes, or HJETS++ [95] for Higgs boson production in association with one or more jets in the high-energy limit. The program GoSam-2.0 is used in all subsequent NLO computations, thus its mode of operation is detailed in the next section.

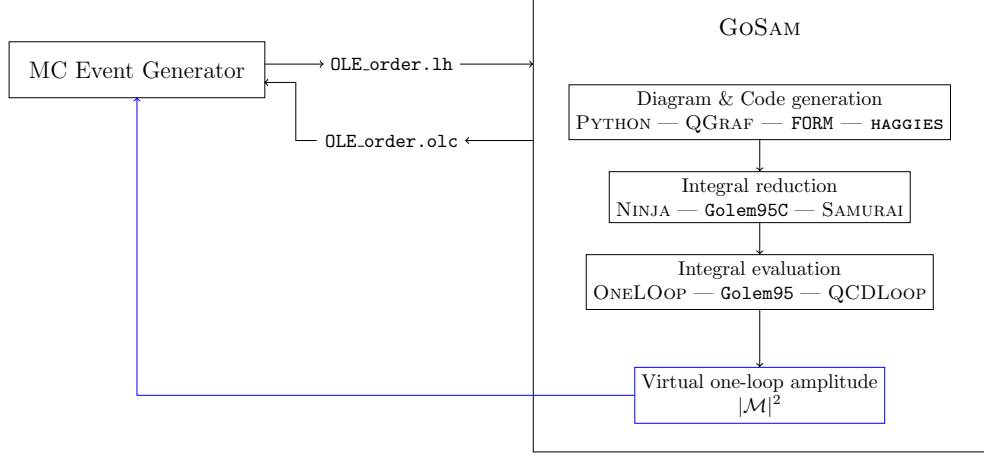


Figure 4.2: GoSAM relies on external packages to compute virtual one-loop amplitudes. Feynman diagrams are generated by QGRAF, and fortran code containing the terms relevant to each diagram is automatically written out by FORM. The various integral families are then reduced and the basis integrals evaluated using external libraries.

729 4.1.1 GoSam: MC interfacing of one-loop amplitudes

730 GoSAM is a general-purpose package that computes one-loop amplitudes automatically
 731 and interfaces to any MC generator, provided it supports the Binoth-Les Houches Accord
 732 (BLHA1 [96] or BLHA2 [97]) format. The workflow of GoSAM is shown in Fig. 4.2.

733 Any process can be defined in the GoSAM input card, where only incoming and
 734 outgoing particles as well as the desired order in α, α_s for the generation of the Feynman
 735 diagrams have to be given. The PYTHON `gosam.py` executable is then called and a series
 736 of external packages handle the different steps of the computation: QGRAF [98] generates
 737 the Feynman diagrams, and filters for vertices or propagators can be applied, as well as
 738 manual removal of diagrams. Then, FORM [99] code containing the relevant expressions
 739 is generated automatically for all diagrams and helicities. Integral reduction is operated
 740 by any of three programs, namely NINJA [100], Golem95C [101, 102] or SAMURAI [103].
 741 Finally, the evaluation of the set of basis integrals is performed using one of the three
 742 external integral libraries QCDLOOP [104], ONELOOP [105] or Golem95C.

743 On a higher level, in compliance with BLHA, the MC generator produces an order
 744 file `OLE.order.1h` containing the subprocesses to be computed by GoSAM. The latter is
 745 called and generates routines for all subprocesses. After checking the order file, GoSAM
 746 validates the order and returns a contract file `OLE.order.olc`. The generated libraries
 747 for all helicities are linked, and common functions are written in a `matrix.f90` file to be
 748 called by the MC generator. The physics parameters, like particle masses and couplings,
 749 can be set by an external call to the `OLP_Option` function. Then, for a set of 4-momenta
 750 $(p_i)_{i=1,\dots,n}$, the matrix-element is provided by calling the `OLP_EvalSubProcess({p_i})`
 751 function, which returns the full one-loop amplitude coefficients $c_{(-2)}, c_{(-1)}$ and c_0 (double,
 752 single pole and finite terms) as given in the Laurent series

$$\text{Re}\{\mathcal{M}^{(0)}\mathcal{M}_{\text{virt}}^{(1)}\} = g_1^{n_1} \dots g_q^{n_q} \frac{\alpha_s}{2\pi} \frac{(4\pi)^\epsilon}{\Gamma(1-\epsilon)} \left(\frac{c_{(-2)}}{\epsilon^2} + \frac{c_{(-1)}}{\epsilon} + c_0 + \mathcal{O}(\epsilon) \right), \quad (4.3)$$

where $g_i^{n_i}$ are the coupling constants appearing in the tree-level matrix-element. GoSAM is a very flexible package, and allows high-level control over the various subtleties of higher-order computations (e.g. choice of regularization scheme, renormalization counterterms, and so on). A rescue system for phase-space points that are numerically badly behaved can be activated, and the amplitude for these is recomputed either in quadruple precision or with a different method.

4.1.2 Infrared divergence cancellation

Having acquired the virtual contribution to the amplitude, one has to combine the Born, virtual and real-emission contributions together. As was shown in Section 3.2, the singularities appearing in both virtual loop calculations and in soft/collinear configurations of real emissions should combine to give finite quantities for any IR-safe observable.¹ Although this is analytically true, in the case of MC computations, the different contributions are first sampled over different phase-spaces, and only then combined. Symbolically, for the NLO cross-section σ^{NLO} :

$$\sigma^{\text{NLO}} = \int_{\Phi_m} d\sigma^B + \int_{\Phi_m} d\sigma^V + \int_{\Phi_{m+1}} d\sigma^R, \quad (4.4)$$

where $d\sigma^B$, $d\sigma^V$ and $d\sigma^R$ are the Born, virtual and real contributions. Note that the singularities in virtual and real contributions only cancel after integration. Numerically, the cancellation of IR divergences is thus non-trivial. At NLO, there are two kinds of algorithms to implement IR divergence cancellation: phase-space slicing and subtraction methods. The Catani-Seymour (CS) [106] and Frixione-Kunzst-Signer (FKS) [107, 108] automatized subtraction of IR divergences are mostly used nowadays in NLO MC generators. The CS algorithm is outlined below and is used in all calculations present in Chapters 6–10, while the PowHEG framework in Chapter 11 uses the FKS scheme.

Consider the addition of a subtraction term $d\sigma^S$ which approximates the ($d = 4 - 2\epsilon$ regularized) real contribution and reproduces its IR singularity pattern in d dimensions:

$$d\sigma^V + d\sigma^R = d\sigma^V + d\sigma^S + (d\sigma^R - d\sigma^S). \quad (4.5)$$

Then, the ($d = 4$)-dimension limit can be taken directly for the integration of the real-emission and the local counterterm cancels the divergence in the phase-space integrand. The total NLO cross-section then takes the form:

$$\sigma^{\text{NLO}} = \int_{\Phi_m} d\sigma^B + \int_{\Phi_m} \left(d\sigma^V + \int_{\Phi_1} d\sigma^S \right)_{\epsilon=0} + \int_{\Phi_{m+1}} (d\sigma^R|_{\epsilon=0} - d\sigma^S|_{\epsilon=0}), \quad (4.6)$$

¹Generally, at NLO, regularized poles appear either as double poles (soft and collinear), or single poles (soft, collinear, or UV).

4 Monte-Carlo (MC) event generators

780 where all integrals are now separately finite. The CS dipole formalism is a factorization
 781 framework that allows the automatic generation of the subtraction term $d\sigma^S$. Universal
 782 dipole factors are introduced for any process, and setting the subtraction term to

$$d\sigma^S = \sum_{\text{dipoles}} d\sigma^B \otimes dV_{\text{dip}}, \quad (4.7)$$

$$\int_{\Phi_{m+1}} d\sigma^S = \sum_{\text{dipoles}} \int_{\Phi_m} d\sigma^B \otimes \int_{\Phi_1} dV_{\text{dip}} =: \int_{\Phi_m} d\sigma^B \otimes \mathbf{I} \quad (4.8)$$

783 allows one to compute the cross-section σ^{NLO} of any process:

$$\int_{\Phi_m} d\sigma^B + \int_{\Phi_m} (d\sigma^V + d\sigma^B \otimes \mathbf{I})|_{\epsilon=0} + \int_{\Phi_{m+1}} \left(d\sigma^R|_{\epsilon=0} - \sum_{\text{dipoles}} d\sigma^B \otimes dV_{\text{dip}}|_{\epsilon=0} \right) \quad (4.9)$$

784 with \mathbf{I} the integrated CS insertion operator. The universal dipole factors are obtained
 785 by considering the soft/collinear limits of a one-emission matrix-element with respect to
 786 the Born configuration:

$$|\mathcal{M}_{m+1}|^2 = \sum_{k \neq i,j} \mathcal{D}_{ij,k}(p_1, \dots, p_{m+1}) + (\text{regular in } p_i \cdot p_j \rightarrow 0) \quad (4.10)$$

$$= - \sum_{k \neq i,j} \frac{1}{2p_i \cdot p_j} \mathcal{M}_m^\dagger(i, j \rightarrow \tilde{i}\tilde{j}, \tilde{k}) \left(\frac{\mathbf{T}_k \cdot \mathbf{T}_{ij}}{\mathbf{T}_{ij}^2} \mathbf{V}_{ij,k} \right) \mathcal{M}_m(i, j \rightarrow \tilde{i}\tilde{j}, \tilde{k}) \\ + (\text{regular in } p_i \cdot p_j \rightarrow 0) \quad (4.11)$$

787 where the singular terms are collected in the dipoles $D_{ij,k}$. The \mathbf{T}_i are the generators of
 788 the color algebra and \mathcal{M}_m is a general matrix-element corresponding to an m -particle
 789 final-state, $\mathcal{M}_m = |1, \dots, m\rangle$. Then Eq. (4.11) states that the matrix-element corre-
 790 sponding to an $(m+1)$ -particle final-state factorizes into dipole factors $\mathbf{V}_{ij,k}$ convo-
 791 luted with an underlying Born configuration where partons i and j are assembled into
 792 one parton $(\tilde{i}\tilde{j})$ (the so-called *emitter*), and parton \tilde{k} (the *spectator*) absorbs the residual
 793 4-momentum. The formulae for the universal dipoles $\mathbf{V}_{ij,k}$ are very closely related to
 794 the Altarelli-Parisi splitting functions, see Section 4.2.

795 In the case of the presence of initial-state hadrons like at the LHC, Eq. (4.11) is
 796 modified and an additional dipole term has to be added in Eq. (4.8), $dV_{\text{dip}} \rightarrow dV_{\text{dip}} +$
 797 dV'_{dip} . Eq. (4.8) then becomes

$$\int_{\Phi_{m+1}} d\sigma^S = \int_{\Phi_m} d\sigma^B \otimes \mathbf{I} + \int_0^1 dx \int_{\Phi_m} d\sigma_B(xp) \otimes (\mathbf{P} + \mathbf{K})(x), \quad (4.12)$$

798 where xp is the proton momentum fraction carried away by the parton, and \mathbf{P}, \mathbf{K} are
 799 insertion operators appearing from the convolution with the PDF.

4.2 Parton-shower models

4.2.1 Altarelli-Parisi splitting functions

Parts of the following section are adapted from Ref. [109]. Inherently, the few-parton, high-energy final-state generated by the hard process matrix-element further produces both QCD and QED radiation. The parton-shower algorithm evolves partons from the collision scale Q^2 , letting them radiate new partons (quarks and gluons), to a cutoff scale Q_{\min}^2 that is set around the hadronization scale. At that point, the shower terminates and the final-state is passed on to the hadronization model. Schematically, the simplest shower algorithms are based on the so-called Dokshitzer–Gribov–Lipatov–Altarelli–Parisi (DGLAP) kernels [110–112] for $1 \rightarrow 2$ collinear particle splitting $P_{a \rightarrow bc}$, as given in Fig. 4.3.

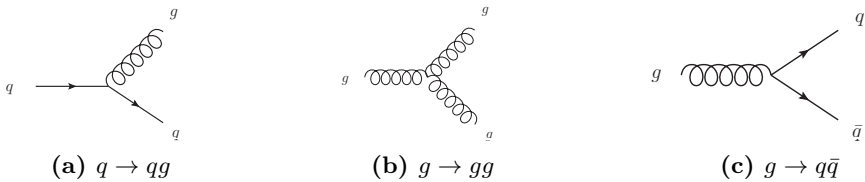


Figure 4.3: The QCD vertices for $1 \rightarrow 2$ splittings allow to calculate the leading-order kernels appearing in the DGLAP evolution equation.

The (unregularized) LO kernels can be computed from the QCD interaction vertices as:

$$P_{q \rightarrow qg}(z) = C_F \frac{1+z^2}{1-z}, \quad (4.13)$$

$$P_{g \rightarrow gg}(z) = 2C_A \left(\frac{1-z}{z} + z(1-z) + \frac{z}{1-z} \right), \quad (4.14)$$

$$P_{g \rightarrow q\bar{q}}(z) = T_R(1 - 2z(1-z)). \quad (4.15)$$

with z , $0 \leq z \leq 1$, the longitudinal momentum fraction of the parent parton a . Notice the undefined behavior of $P_{q \rightarrow qg}$ and $P_{g \rightarrow gg}$ for $z \rightarrow 1$: the splitting functions can be regularized from general constraints to:

$$P_{q \rightarrow qg}(z) = C_F \left(\frac{1+z^2}{(1-z)_+} + \frac{3}{2} \delta(z-1) \right), \quad (4.16)$$

$$P_{g \rightarrow gg}(z) = 2C_A \left(\frac{1-z}{z} + z(1-z) + \frac{z}{(1-z)_+} + \left(\frac{11}{12} - \frac{1}{3} \frac{T_R}{C_A} \right) \delta(z-1) \right), \quad (4.17)$$

$$P_{g \rightarrow q\bar{q}}(z) = T_R(1 - 2z(1-z)). \quad (4.18)$$

The factor $(1-z)^{-1}$ is regularized in being interpreted as a plus-distribution $(1-z)_+^{-1}$ such that for any test function $f(z)$ sufficiently regular at $z=0, z=1$,

4 Monte-Carlo (MC) event generators

$$\int_0^1 \frac{dz f(z)}{(1-z)_+} = \int_0^1 \frac{f(z) - f(1)}{1-z} . \quad (4.19)$$

818 The master equation governing the evolution of the collinear splitting of a parton a
 819 from a scale q^2 to a scale $q^2 + dq^2$ is then given by

$$dP_{a \rightarrow bc} = \frac{dq^2}{q^2} \frac{\alpha_s}{2\pi} P_{a \rightarrow bc}(z) dz , \quad (4.20)$$

820 where q^2 is an arbitrary strong-ordered evolution variable. It can be the azimuthal
 821 angle of emission $E_a^2 \theta^2$, or the particle's virtuality m^2 , or the transverse momentum
 822 p_T^2 . Different shower algorithms implement different choices of the evolution variable.
 823 This will be of importance when considering parton-shower related uncertainties, see
 824 Chapters 7 and 11.

825 4.2.2 The Sudakov form factor

826 Going from the one-emission to the multiple-emission case, and using broad assump-
 827 tions², the probability of no-emission between scales Q^2 and Q_{\max}^2 is given by the *Sudakov*
 828 *form factor*:

$$dP_{a \rightarrow bc}(z) = \frac{dq^2}{q^2} \frac{\alpha_s}{2\pi} P_{a \rightarrow bc}(z) dz \times \exp \left(- \sum_b \int_{Q^2}^{Q_{\max}^2} \frac{dq'^2}{q'^2} \int \frac{\alpha_s}{2\pi} P_{a \rightarrow bc}(z') dz' \right) . \quad (4.21)$$

829 As explained in Section 3.1.3, the perturbative expansion of the cross-section in α_s can
 830 suffer from large enhancements in the soft/collinear regions of phase-space. In general,
 831 double logarithms of the form $\alpha_s^n \log^{2n}(Q^2/q^2)$ appear when a soft particle is emitted, or
 832 when it becomes collinear to one of the incoming partons. Here, q^2 is the scale describing
 833 the soft/collinear emission, and Q^2 is the global scale of the process. Generally, this tower
 834 of large logarithms can be analytically resummed to all orders in α_s . Instead, the parton
 835 shower algorithm offers the possibility of resumming soft and collinear contributions
 836 within the Monte-Carlo framework. Nowadays, most parton showers only guarantee
 837 leading-logarithmic (LL) accuracy, although recent studies [113] have found differences
 838 at LL (subleading number of colors N_C), and NLL (leading- N_C) between parton-showers
 839 and analytic resummations.

840 4.2.3 Parton-shower matching

841 The shower algorithm should respect the theoretical accuracy of the hard matrix-element,
 842 and at the same time conserve the logarithmic accuracy of the parton-shower resumma-
 843 tion in their respective limits. In particular, the cross-section after showering should

²Namely that the time between emissions can be sliced, and unitarity as well as multiplicativity (meaning the shower has no memory of past emissions) hold.

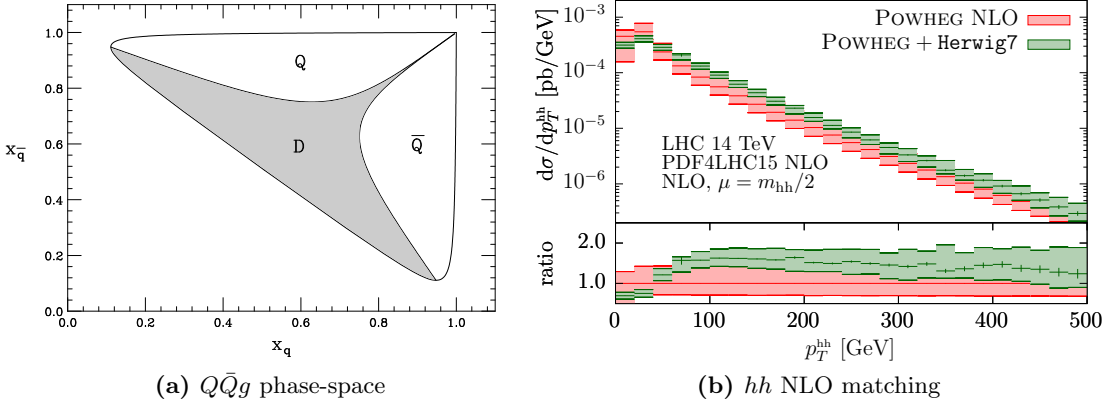


Figure 4.4: (a) Phase-space for a heavy-quark pair emitting a gluon, depicted as a function of the Dalitz plot variables ($x_Q, x_{\bar{Q}}$). Figure adapted from Ref. [118]. (b) The transverse momentum p_T^{hh} of the Higgs pair system in di-Higgs production is compared for the fixed-order NLO prediction to a parton-shower matched calculation.

844 be identical to the fixed-order cross-section. Also, kinematic configurations that belong both to the hard matrix-element and the parton-shower final-states should not be
 845 double-counted. This whole procedure is called *matching*.
 846

847 At NLO, the matching of the parton-shower algorithm to the fixed-order matrix-
 848 element handles both these issues. Roughly said, it interpolates between the two kine-
 849 matic regions where the hard matrix-element, respectively the parton-shower, generate
 850 their respective dominant contributions. As an example, the phase-space for the pro-
 851 duction of two heavy quarks and one gluon-emission $Q\bar{Q}g$ is given in Fig. 4.4a. The
 852 soft/collinear emission regions (where $x_Q \rightarrow 1$ or $x_{\bar{Q}} \rightarrow 1$, with $x_j = 2p \cdot q_j/p^2$, and p
 853 is the initial center-of-mass 4-momentum) can be covered by the parton-shower while
 854 the dead region (shaded) describes a hard gluon-emission (matrix-element). In a cor-
 855 rect matching, these regions should not overlap. An illustration of this fact is shown in
 856 Fig. 4.4b for the case of $gg \rightarrow hh$ production, where a fixed-order NLO calculation is
 857 matched to the **Herwig7** [114, 115] parton-shower. There, the parton-shower correctly
 858 reproduces the NLO computation at high-transverse momentum and softens the low-
 859 momentum region (Sudakov suppression). Among the various matching procedures that
 860 keep in line with the above criteria, the subtractive MC@NLO [116] and the multiplicative
 861 Powheg [117] schemes are among the most used ones.

862 As examples of available parton-shower algorithms mostly used by the physics commu-
 863 nity, the **Pythia 8** [119, 120] and **Herwig7** codes implement a p_T -ordering, respectively
 864 an angular-ordering in the choice of the evolution variable. **Herwig** also uses a dipole
 865 shower as an alternative algorithm (which is based on a Catani-Seymour dipole formula-
 866 tion of $2 \rightarrow 3$ splitting kernels). The **Sherpa** [121] generator implements two alternative
 867 parton-shower algorithms based on variations of the CS dipoles.

868 4.3 Hadronization

869 Once particles have been showered down to the hadronization scale, the hadronization
 870 model takes over. By far, the two most used hadronization models are the Lund string
 871 model and the cluster model.

872 4.3.1 Lund string model

873 The Lund string model [122] is based on the principle of quark color confinement. When
 874 two quarks are separated by a distance r , the potential takes the form:

$$U(r) = -\frac{4}{3} \frac{\alpha_s}{r} + \kappa r, \quad (4.22)$$

875 and the linear confinement contribution dominates for larger distances, with $\kappa \sim$
 876 1 GeV/fm. In analogy to a classical elastic potential, the field lines build up a stretched
 877 *string*. When the distance between a quark-pair increases, the string tension grows
 878 until the string breaks: the freed energy creates another quark-antiquark pair appearing
 879 from the vacuum. The creation of the quark-pair happens with a Gaussian probability
 880 (similarly to quantum tunnelling) in the quark transverse mass $m_T^2 = m^2 + p_T^2$. From
 881 Lorentz invariance, causality and left-right symmetry, the fragmentation function $f(z)$
 882 can be constrained and fixes the longitudinal momentum fraction z carried away by the
 883 created hadron:

$$\mathcal{P} \propto \exp\left(-\frac{\sigma m_T^2}{\kappa}\right), \quad f(z) \propto \frac{(1-z)^a}{z} \exp\left(-\frac{bm_T^2}{z}\right). \quad (4.23)$$

884 The Lund string model is implemented in the **Pythia 8** generator and the main pa-
 885 rameters a, b, σ are determined by tuning to data. For the more complex case of baryons,
 886 the three quarks can be pictured in a quark-diquark frame. Finally, the gluons appear
 887 as kinks on strings. For more details and improvements to the model, see the **Pythia**
 888 manual [123].

889 4.3.2 Cluster model

890 Instead of building on color confinement, the cluster model [124, 125] makes the as-
 891 sumption that gluons can be viewed as carrying color and anticolor and behaving as a
 892 $q\bar{q}$ pair. Color singlets usually obey a mass spectrum that peaks at low mass due to
 893 the property of preconfinement of the parton shower [126], i.e. they are closer to one
 894 another in phase-space. The model then clusters these color singlets together and splits
 895 them per the following procedure: if a cluster of mass M , with parton constituents of
 896 masses m_1, m_2 , satisfies

$$M^{C_{\text{pow}}} > C_{\text{max}}^{C_{\text{pow}}} + (m_1 + m_2)^{C_{\text{pow}}}, \quad (4.24)$$

897 the algorithm splits it and the masses get redistributed. To split a cluster, the model
 898 pops a $q\bar{q}$ pair from the vacuum and forms two new clusters with one original parton
 899 each, and masses distributed according to

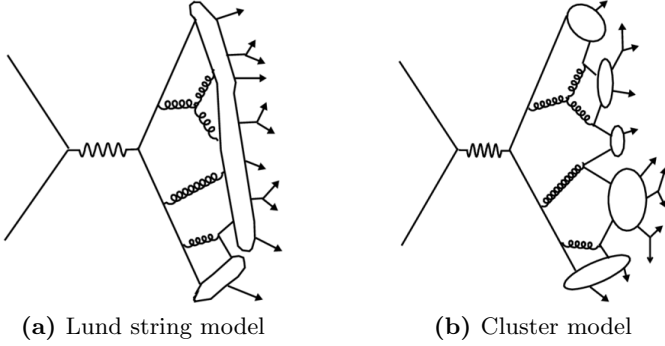


Figure 4.5: A pictorial representation of both hadronization models. (a) In the Lund model, the potential energy from the color field between two quarks increases linearly with the distance, like in a string. When a string breaks, a new quark-antiquark pair is created. (b) The cluster model groups color-connected partons together into clusters and lets them decay isotropically.

$$M_{1,2} = m_{1,2} + (M - m_{1,2} - m_q) \mathcal{R}_{1,2}^{P_{\text{split}}}, \quad (4.25)$$

with $\mathcal{R}_{1,2} \in [0, 1]$ two random numbers. Again, the parameters C_{pow} , C_{max} and P_{split} have to be tuned to data.

Notice that the cluster model does not propagate any spin information: the hadronized clusters therefore decay isotropically. Historically, the cluster model was implemented in the `Herwig` event generator. Fig. 4.5 summarizes the conceptual differences between the Lund string and the cluster model.

As a concluding remark, the MC event generators represent the basis of a large fraction of experimental measurements. They are quite complex systems whose constituents are all inter-correlated: the different pieces interact and the matching between all appearing physical scales is not always explicit at the end of the simulation. Typically, the parton-shower output influences the hadronization tune, and it is in general difficult to disentangle their respective contributions. As such, variations in the MC setup are linked to large uncertainties which should, in principle, be taken into account with their full correlations.

914 5 The LHC and the ATLAS detector

915 The Large Hadron Collider (LHC) is currently the most powerful particle accelerator
 916 worldwide and is located at the Centre Européen pour la Recherche Nucléaire (CERN)
 917 on the French-Swiss border, near Geneva. Historically, it replaced the Large Electron-
 918 Positron (LEP) collider after it was decommissioned in 2000, and is being housed in
 919 the same tunnel. In this chapter, the main working parts of the accelerator complex
 920 are briefly reviewed, and the structure of the ATLAS detector presented in more de-
 921 tail. A short overview of the trigger and data acquisition system, as well as the object
 922 reconstruction and MC simulation, will close the subject.

923 5.1 The Large Hadron Collider

924 The LHC's main collider ring [127–129] is installed in a circular tunnel of ~ 27 km
 925 circumference and a depth varying between 45 m and 170 m under ground level. It is
 926 designed to accelerate protons up to an energy of 7 TeV, reaching a design center-of-
 927 mass energy of 14 TeV at a peak luminosity of 10^{34} cm $^{-2}$ s $^{-1}$. As a side note, the LHC
 928 can also accelerate heavy ions, and in the past a few runs of lead-lead, proton-lead and
 929 xenon-xenon collisions have also given interesting complementary physics results.

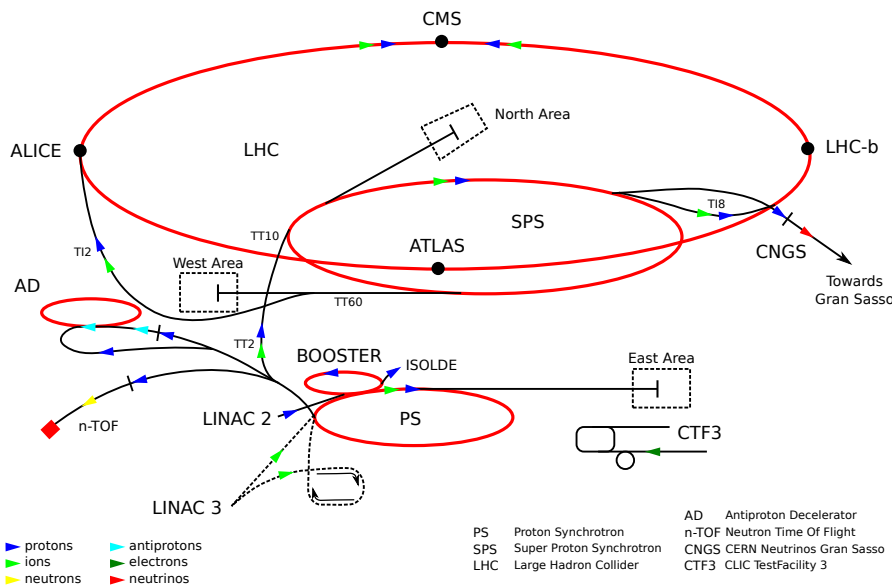


Figure 5.1: The LHC accelerator complex [130].

5 The LHC and the ATLAS detector

To accelerate protons to these high energies, a sequence of pre-accelerators boosts the proton beams before injecting them into the next link. A schematic of the full accelerator complex is presented in Fig. 5.1. Upon being produced and pre-collimated, the protons are accelerated to 50 MeV in the Linac2, then to 1.4 GeV in the Proton Synchrotron (PS) Booster, and to 26 GeV in the PS. Within the PS, the protons are collimated into 25 ns-spaced (7.5 m) bunches of around $1.15 \cdot 10^{11}$ protons per bunch. From there, the Super Proton Synchrotron (SPS) ramps up the energy to 450 GeV, and injects both beams in opposite directions into the LHC itself. After approximately 20 minutes of acceleration in the main LHC beampipe by 16 radiofrequency cavities, the proton bunches achieve the current energy of 6.5 TeV per beam.

Equipped with 1232 superconducting main dipole magnets, the LHC operates with magnetic fields of ~ 8.3 T to keep the proton bunches on their circular trajectory. The main dipole magnets are supplemented by higher-multipole magnets to correct for edge imperfections in the dipole field. Along the LHC beam path, 392 main quadrupole magnets are used to re-focus the proton beams.

Once at the nominal energy, the two circulating proton beams are brought to collision at four different interaction points, corresponding to the four biggest LHC experiments: ATLAS, CMS, ALICE and LHCb. Out of these, ATLAS and CMS are general-purpose detectors designed to discover higher-mass particles like the Higgs boson or possible supersymmetric resonances, as well as to produce high-precision measurements of particles like the top quark. On the other hand, ALICE is dedicated to studies of heavy-ion collisions and focuses on high-density QCD bound states, while LHCb is optimized to investigate heavy-flavor physics. From the start of Run II in 2015 until the Long Shutdown of December 2018, the LHC delivered a total integrated luminosity of 147 fb^{-1} at a maximal center-of-mass energy of 13 TeV and a peak luminosity of $2.1 \cdot 10^{34} \text{ cm}^{-2} \text{ s}^{-1}$, even surpassing the design value. The next section concentrates on the ATLAS detector substructure.

5.2 The ATLAS detector

A Toroidal LHC ApparatuS (ATLAS) [131] aims for high-energy precision measurements of the SM in all possible sectors: with the help of the enormous amount of data produced at LHC and the precision of the tracking detectors and calorimeters, it allows for measurements of particle masses and SM couplings (from the CKM matrix to the Higgs boson coupling to other particles, α_s measurements and PDF fits) or cross-section measurements, but also the observation of rare SM processes (like $t\bar{t}h$ production [132], light-by-light scattering [133] or $B_s^0 \rightarrow \mu^+ \mu^-$ decays [134]). These high-precision tests of the SM are intrinsically linked to searches for Beyond the SM (BSM) physics: higher-scale BSM particles participating in loop corrections to the SM can have an impact on the cross-sections or kinematic observables, and any observed deviation from the SM predictions would hint at New Physics at higher scales. In general, though, direct searches are employed to look for potential high-mass resonances.

The ATLAS detector, situated at the LHC beam interaction point 1 near Meyrin, Switzerland, has an onion-shell structure comprised of particle trackers, electromagnetic and hadronic calorimeters, and a muon detector: from inner to outer radii, the produced particles encounter the Inner Detector (ID), the Liquid Argon (LAr) and the Tile Calorimeter (TileCal), and finally the Muon Spectrometer (MS). The detector itself is 44 m long and has a diameter of 25 m, and weighs more than 7000 tons. Fig. 5.2 shows a sketch of the ATLAS detector. To bend the charged-particle tracks for momentum measurement, ATLAS relies on four magnets: a 2 T central solenoid [135] close to the interaction point, an 8-coil barrel toroid [136] that is cylindrically placed around the detector generating a peak magnetic field of 4 T, and two other 8-coil toroid magnets at the detector endcaps [137] which provide a peak magnetic field of 4 T on the superconductor (0.2 – 3.5 T in the bore). The geometry of the magnet coils is shown in Fig. 5.3.

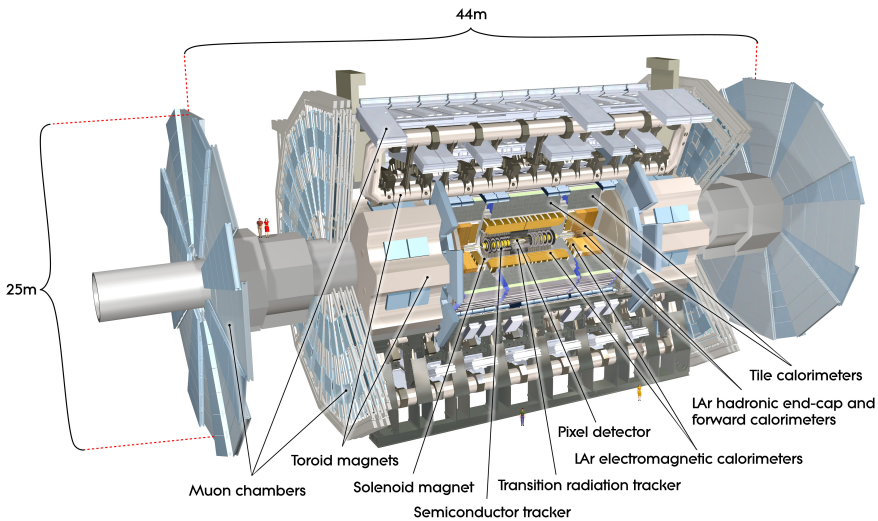


Figure 5.2: A cut-away view of the ATLAS detector. Figure from Ref. [131].

The ATLAS coordinate system is defined as right-handed and centered at the interaction point, with the beam axis chosen as the z -axis, the x -axis pointing towards the center of the LHC ring, and the y -axis pointing upwards.

5.2.1 The Inner Detector

Being the detector closest to the beampipe, the Inner Detector (ID) [138, 139] must fulfill several criteria for the reconstruction of charged-particles four-momenta, as well as for the identification of secondary vertices due to the decay of bottom-flavored hadrons or τ leptons, and for the measurement of the impact parameter. The ID is further divided into a silicon Pixel Detector [140], a Semiconductor Tracker (SCT) [141] and a Transition Radiation Tracker (TRT) [142, 143]. In Fig. 5.4, the structure of the ID is presented in a cut view along the beampipe (with the notable absence of the new insertable B -layer, or IBL [144, 145]).

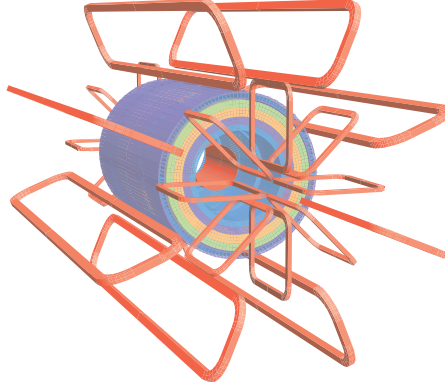


Figure 5.3: The geometry of the coils used to produce the magnetic field in the ATLAS detector. A solenoid magnet (2 T) is installed cylindrically around the beampipe, surrounded by a toroid magnet (4 T) and two endcap toroid magnets (4 T). Figure from Ref. [131].

The Pixel Detector has a total of $8.6 \cdot 10^7$ channels and is the device closest to the interaction point. Four concentric layers of silicon pixel detectors are laid out around the beam axis in so-called barrel layers. The innermost layer is called the insertable B -layer (IBL) and was installed during the first Long Shutdown. It is only 3.3 cm away from the nominal interaction region and improves measurements of (secondary) vertex positions. It was designed to work in a high-radiation environment. Three other layers are disposed concentrically around the beampipe, and additionally three pixel disks are mounted on each endcap. The Pixel Detector reaches a resolution of $\sim 10 \mu\text{m} \times 75 \mu\text{m}$ [146, 147] in the transverse, respectively longitudinal ($R - \phi, z$) directions.

At intermediate radius, the SCT is a silicon microstrip tracker and provides, using $6.2 \cdot 10^6$ readout channels, a measurement of the (R, ϕ, z) track points. Four SCT barrel layers are disposed at radii between 299 mm and 514 mm away from the beampipe, while 18 more planar discs are placed at the endcaps. The barrel modules have a resolution of $17 \mu\text{m} \times 570 \mu\text{m}$ [141, 148].

Finally, at the outer layer, the Transition Radiation Tracker is made of thin-walled straw tubes and gives information for distinguishing electrons from pions, as well as contributes to the transverse position measurement for a total of $3.5 \cdot 10^5$ readout channels. A straw tube is a 4 mm-diameter cylinder filled with gaseous xenon and a gold-plated tungsten wire strung through the center. With the inner tube wall (cathode) and the wire (anode) held at 1.5kV of voltage difference, a charged particle passing through ionizes the gas, and the freed electrons drift to the wire: the drift time can then be used to determine the distance from the anode. Moreover, electron identification succeeds by transition-radiation photons created between the straws and converted in the xenon gas. The probability of transition radiation is proportional to the relativistic γ -factor, which is usually higher for electrons and positrons. The TRT determines the transverse position at a resolution of $\sim 110 - 130 \mu\text{m}$ [149].

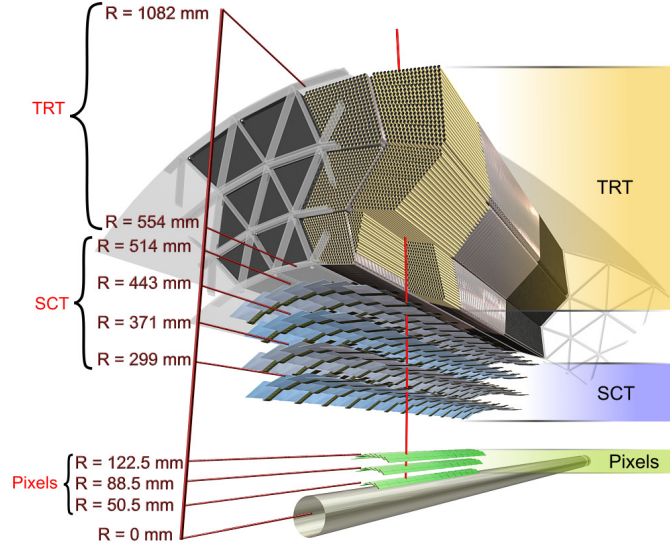


Figure 5.4: Cross-sectional view of the Inner Detector (ID). The ID particle tracker is made of the Pixel Detector, the microstrip Semiconductor Tracker (SCT), and the Transition Radiation Tracker (TRT). Figure from Ref. [131].

5.2.2 Calorimeters

Calorimeters mainly measure the energy deposited by the particles, but they also contribute to position measurements and particle identification as well as to the measurement of the missing transverse energy. ATLAS uses so-called sampling calorimeters with a *sandwich* structure. The detectors are made from alternating layers of high-density passive absorbers (Pb, Fe, Cu, ...) and active material (scintillating plastic, liquid argon, Si, ...) producing a detectable signal. The energy measurement is a destructive process: the incoming particle initiates secondary showers, and all produced particles deposit energy and radiate further until the total initial energy is absorbed. These energetic showers have different topologies depending on the type of incoming particle, namely whether they are leptonic (and photonic) or hadronic.

A passing electron/positron or a photon produces an electromagnetic (EM) shower in the absorber mainly through bremsstrahlung and electron-positron pair creation. EM showers are characterized by a rapid energy loss. A given detector material is described by the radiation length X_0 , which is the distance after which the incoming particle has deposited $1/e$ of its total energy.

In comparison, charged and neutral hadrons generate further hadronic activity by inelastic nuclear reactions through spallation and excitation. The secondary neutral mesons also generate additional EM shower activity. Furthermore, hadronic showers are generally wider than EM ones, and hadronic calorimeters are correspondingly much bulkier. They are characterized by the nuclear absorption length λ_a , for which 95% of the total energy is absorbed in a cylinder of radius λ_a . In ATLAS, both the EM and the hadronic calorimeters are found between the ID and the muon spectrometer.

5 The LHC and the ATLAS detector

5.2.2.1 The Liquid Argon (LAr) Calorimeter

Fig. 5.5 depicts the Liquid Argon (LAr) calorimeters [150] in yellow, which are closest to the ID and enveloped by the Tile Calorimeter. The LAr calorimeters contain both EM and hadronic detectors. The LAr calorimeters function as a system of alternating lead/stainless steel absorbers and electrodes measuring the signal drift-time, with the whole system immersed in liquid argon which plays the role of active medium.

The electromagnetic barrel (EMB, $|\eta| < 1.475$) and endcap (EMEC, $1.375 < |\eta| < 3.2$) calorimeters use the same absorber material and geometry. In the forward region (FCal) at rapidities $3.1 < |\eta| < 4.9$, a copper-based absorber covers EM activity while a tungsten module provides measurement of hadronic energy deposition. Finally, a hadronic LAr calorimeter is also placed at the endcaps (HEC) and complements readings from the Tile Calorimeter. The EM calorimeters have an energy resolution of $\sigma_E/E = 10\%/\sqrt{E} + 0.7\%$, while the FCAL subdetector fares more poorly with a resolution of $\sigma_E/E = 100\%/\sqrt{E} + 10\%$. Finally, the hadronic HEC subdetector reaches an energy resolution of $\sigma_E/E = 50\%/\sqrt{E} + 3\%$ [151].

5.2.2.2 The Tile Calorimeter (TileCal)

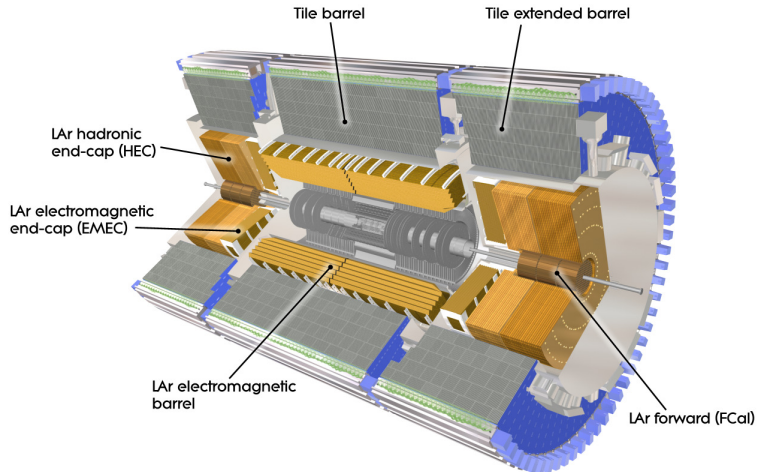


Figure 5.5: The ATLAS calorimetry system is composed of the inner Liquid Argon calorimeter (yellow) and the outer Tile Calorimeter (gray). Figure from Ref. [131].

The central and two extended barrel regions are covered by the TileCal [152], which is cylindrically disposed around the beampipe (see Fig. 5.5) and is made of iron plate absorbers and plastic scintillators as the active medium. The scintillating light created by hadronic energy deposition is wavelength-shifted and led to photomultiplier tubes that amplify the signal. The TileCal has a total energy resolution of $\sigma_E/E = 50\%/\sqrt{E} + 3\%$ for single pions [153].

5.2.3 The Muon Spectrometer

At the outmost layer of the ATLAS detector, the MS [154] is designed to deliver high-precision measurements of the muons' transverse momentum. It uses four different techniques to trigger and detect the produced muons: resistive-plate chambers (RPC) [155], cathode strip chambers (CSC) [156], monitored drift tubes (MDT) [157] and thin-gap chambers (TGC) [158], shown in Fig. 5.6. The muon tracks are bent by three air-core toroid magnets for a rapidity-dependent bending power between 1 – 7.5 Tm. This amounts to a resolution of $\sim 10\%$ in the transverse momentum of high-energy muons at around 1 TeV. Both the RPCs and the TGCs are used as a first-level trigger on well-resolved, high- p_T muons in the barrel region, respectively the endcaps. On the other hand, the MDTs which are laid out in the barrel and endcap regions, and the CSCs in the forward region, measure the position of the incoming muons in the bending plane.

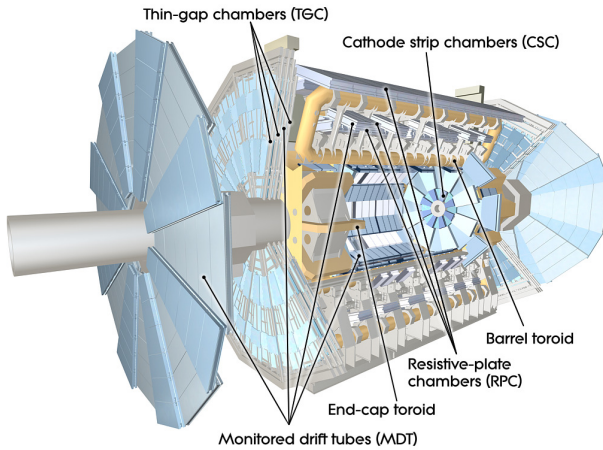


Figure 5.6: The ATLAS muon spectrometer. Figure from Ref. [131].

5.2.4 Trigger and Data acquisition

The collision rate at high-energy collider experiments like ATLAS poses enormous computing and storage requirements. At the LHC, the proton-bunch crossing-rate at the current luminosity towers at a monumental 40 MHz. With a data content of ~ 1.6 MB per event, the storage of all events would produce ~ 60 TB per second. Thus the event rate needs to be reduced to an affordable storage and readout rate. The ATLAS trigger and data acquisition system [159, 160] lowers the stored event rate using certain quality criteria from the detectors. The trigger system is organized in three sublevels:

- **Level 1:** The first layer triggers at the hardware level already, and uses both calorimetry information (cluster energy sum / isolation criteria) and data from the muon trigger chambers to reduce the event rate from 40 MHz to ~ 75 kHz. It also identifies regions-of-interest (ROI) characterized by specific signatures deemed physically relevant.

5 The LHC and the ATLAS detector

- 1090 • **Level 2:** At the software level, the Level 2 Trigger uses the ROIs identified by
1091 Level 1 and combines information from all subdetectors to focus on the physics
1092 objects. The event rate is then reduced from 75 kHz to ~ 1 kHz.
- 1093 • **Event Filter:** The full events are analyzed offline and the Level 2 selection is
1094 refined by the Event Filter (EF), which can also perform full event reconstruction
1095 at this stage. Accepted events are then stored permanently on disk at a rate of
1096 ~ 200 Hz for an acceptable total storage rate of around 300 MB per second.

1097 Since Run II, the ATLAS software trigger comprises a single high-level trigger (HLT)
1098 farm, instead of the separate Level 2 and EF trigger levels, reducing the Level 1 total
1099 event rate from 100 kHz to 1 – 1.5 kHz. The raw data is then stored first in the
1100 central CERN data center. These sites make up the so-called Tier-0 system. The LHC
1101 Computing Grid is composed of several levels (tiers). After the central CERN data
1102 center at Tier-0, the data is redistributed to 13 other computer storage and analysis
1103 sites forming the Tier-1, which store and process the raw data into refined formats
1104 and distributes it along to Tier-2 computer sites (university/institute clusters). Tier-3
1105 sites are composed of local computers for analysis purposes. Mostly, analysers use pre-
1106 processed data that simplifies the description of physics objects.

1107 5.2.4.1 Data formats

1108 From the raw data saved on-site to the final format available to analysts, several levels of
1109 data processing and reconstruction are implemented to derive a meaningful identification
1110 of physics objects that can be used as such in an analysis. Below are presented the
1111 successive file formats and their content:

- 1112 • **RAW:** The raw data from the trigger output are stored as primary information
1113 from the subdetectors: these complete events contain useless or redundant information
1114 and metadata for the final analyses.
- 1115 • **ESD:** The detector output present in the RAW events is fed to the reconstruction
1116 algorithm, and all the information needed for particle identification, track fitting,
1117 jet calibration is summarized in so-called Event Summary Data (ESD) files.
- 1118 • **xAOD:** More information is pruned away, and only the physics objects (electrons,
1119 muons, jets, MET, ...) are summarized in containers and saved as ROOT files
1120 called Analysis Object Data (xAOD).
- 1121 • **DxAOD:** The xAOD files are further reduced to analysis-dependent (Top, Higgs,
1122 SUSY ...) event subsets, the derived AODs (DxAOD). The goal is to reduce
1123 file size and analysis computing times. Derived AODs are produced by either
1124 removing uninteresting events (so-called *skimming*), eliminating entire variables
1125 or object collections from all events (*slimming*), or removing particular objects in
1126 some events (*thinning*). Analyses handle directly the derived xAOD files as input.

1127 **5.2.4.2 MC simulation and event reconstruction**

1128 Common MC event generation was explained in Chapter 4. In the following, a *parton-*
 1129 *level* event is defined as the set of particles (with their well-defined 4-momenta) produced
 1130 by the hard-scattering matrix-element or by the parton-shower algorithm applied to
 1131 the hard collision, but before hadronization. Both cases will be explicitly discerned
 1132 when necessary. Such parton-level events are unphysical since they do not obey color
 1133 confinement. The output of a full-fledged MC program after hadronization is a collection
 1134 of events at *particle-level*: this is usually the point of comparison between theory and
 1135 experiment. Finally, accounting for the further evolution of particles in the magnetic
 1136 field of a specific experiment, as well as geometric acceptance and detection efficiencies,
 1137 defines measurable events at *detector-level*. Fig. 5.7 illustrates the event level definitions.
 1138 The full process of producing sets of events at detector-level from the theory input will
 1139 be referred to as MC simulation.

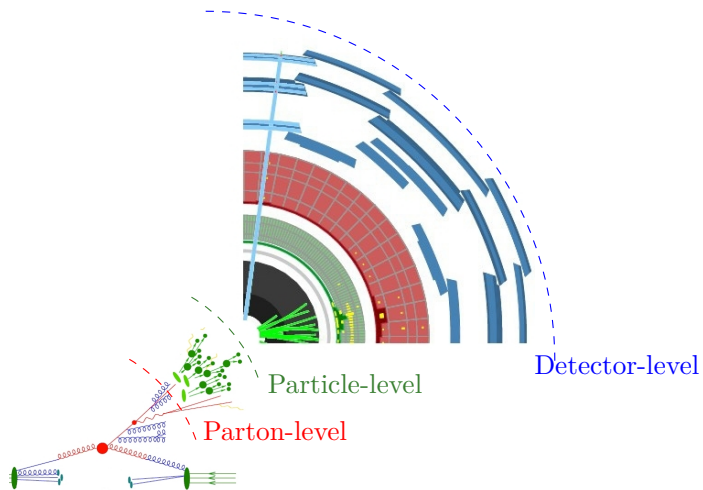


Figure 5.7: Definition of event levels: parton-level after the hard collision (and including parton-showering), particle-level after hadronization and detector-level after the evolution in the ATLAS magnetic field, digitization and reconstruction.

1140 In the ATLAS experiment, this production chain is implemented in the **Athena** frame-
 1141 work, and comprises several steps outlined in Fig. 5.8. The event output at each stage
 1142 is identified by a tag. For a given process, the first step consists of basic MC produc-
 1143 tion using the programs available on the market (SHERPA, Herwig7, Pythia8, and so
 1144 on). The **AthGeneration** subpackage handles the interfacing of public MC programs in
 1145 the ATLAS infrastructure, so as to ensure the use of common parameters, like particle
 1146 masses and decay widths, and to facilitate reproducibility. From job option scripts at
 1147 the user-level, the interface writes the standard input cards readable by the MC pro-
 1148 grams, and launches the event generation itself. The intermediate output at parton-level
 1149 (from the hard ME) is saved as Les Houches Event (LHE) files, and the generation of
 1150 fully-showered and hadronized particle-level events (**EVNT/e-tag**) is referred to as **evgen**.

5 The LHC and the ATLAS detector

1151 Next, the simulation of events from particle- to detector-level happens in two phases:
 1152 `simul` (**s/a**-tags) and `reco` (**r**-tag). The actual simulation (the evolution of the particles
 1153 in the ATLAS magnetic field and the generation of the detector response) is handled
 1154 by the GEANT4 [161] program: it contains the whole detector geometry and reproduces
 1155 the particle hits in the subdetectors, accounting for detection efficiency. Because of
 1156 the enormous computing time needed to produce hits from the hundreds of particles
 1157 at play, an alternative is to parametrize the detector response without running a full
 1158 event simulation (so-called ATLFAST [162] simulation). The output of the `simul` step is
 1159 a HITS file. Then, as happens with the real data in the `reco` stage, signals simulated
 1160 in the subdetectors are digitized, and the physics objects reconstructed to produce the
 1161 xAOD format mentioned above. DxAOEs derivations can be constructed for the latter
 1162 and serve as input to the analyses, like the MC event sets which will be introduced in
 1163 Chapter 9.

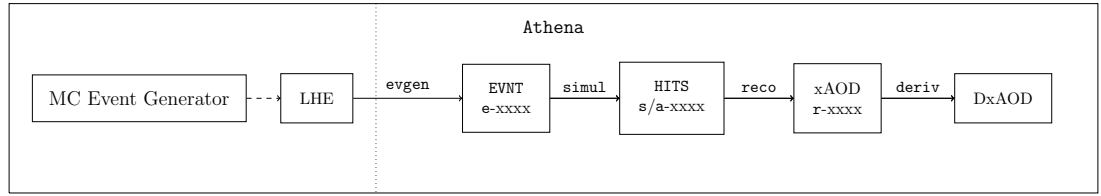


Figure 5.8: The `Athena` workflow for MC event generation and simulation.

1164 Without entering into much detail, trigger and reconstruction algorithms for elec-
 1165 trons and photons [163], muons [164], jets and MET [153, 165] mostly use information
 1166 from calorimeter energy clusters matched to one or several tracks identified in the Inner
 1167 Detector. The Level-2 trigger algorithm is applied online, but it matches closely the of-
 1168 fine reconstruction procedure. More about the exact trigger cut definitions and object
 1169 selection can be found in Ref. [166].

1170 For electrons and photons at the Level-1 trigger, a minimal transverse energy require-
 1171 ment is used and a veto can be applied on the activity in the hadronic calorimeter (VH)
 1172 behind the identified cluster in the EM calorimeter. At the Level-2 trigger, precision
 1173 tracks from the Inner Detector are extrapolated to the EM calorimeter and have to match
 1174 an identified cluster within $(\Delta\eta, \Delta\phi) = (0.05, 0.05)$. A multivariate algorithm [167] is
 1175 used for calibrating the measured cluster energy. Then, electrons are identified with
 1176 a likelihood (LH) discriminant that defines three working points: `Loose`, `Medium` and
 1177 `Tight`. This multivariate likelihood depends on variables characterizing the topologies
 1178 of EM showers in the calorimeter. Identification (ID) efficiency factors can then be deter-
 1179 mined from comparisons of MC simulations against data standard candles: for example,
 1180 lepton ID efficiencies are calibrated with the help of $J/\psi \rightarrow ll$, Drell-Yan $Z \rightarrow ll$ or
 1181 diphoton events. The latter also serve for calibrating energy/momentum scale and res-
 1182 olution factors (which correct, respectively quantify the systematic uncertainty on the
 1183 measured 4-momenta).

5.2 The ATLAS detector

Muons are reconstructed with a minimal requirement on the transverse momentum, as well as a possible loose isolation criterion. The total transverse momentum sum of all tracks in a $\Delta R = 0.2$ cone around the muon should not exceed 12% of the muon p_T . For high- p_T muons, no isolation criterion is applied.

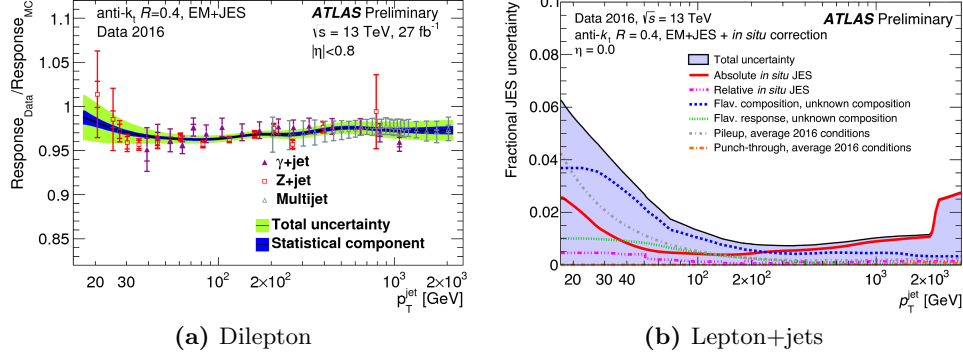


Figure 5.9: (a) Jet energy scale (JES) for three different in-situ calibrations and (b) JES uncertainty at $\sqrt{s} = 13$ TeV as a function of the jet p_T . Figures from Ref. [168].

Finally, for jet reconstruction the anti- k_T jet algorithm [169] is applied (with a distance parameter $R = 0.4$ for small- R jets) to topological clusters identified in the calorimeter. These topo-clusters are reconstructed from the full set of calorimeter clusters. The determination of jet energy scale (JES) factors and uncertainties is more complicated than for e.g. leptons, and comprises several steps: in particular, a MC-based calibration is followed by *in situ* energy calibration.¹ Especially for the case of the ATLAS top-quark mass analysis in the lepton+jets channel (which is not covered in this work), the jet- and b -jet energy scale systematics dominate the total measurement uncertainty. The p_T -dependent JES and its uncertainty are shown for good measure in Fig. 5.9. For a comprehensive study of jet reconstruction and associated uncertainties, the reader is referred to Ref. [170]. The exact object definitions and trigger cuts used by the ATLAS analysis presented in Chapter 9 will be recapitulated in due time.

¹This type of energy calibration uses events where a well-known reference object recoils against one measured jet, e.g. $Z(\rightarrow \ell\ell) + j$ or $\gamma + j$.

1200

Part II

1201

Top-Quark Mass Determinations

6 Theoretical predictions for $t\bar{t}$ final-states

The top-quark pairs created e.g. at the LHC are not observable *per se*: the top quark has a short lifetime of $\sim 0.5 \cdot 10^{-24}$ s. Thus the only directly measurable quantities are the kinematic properties of their decay products. The top quark has a decay branching ratio of 99.8% for $t \rightarrow W^+ b$, $\bar{t} \rightarrow W^- \bar{b}$. So, the final-state contains two b -jets that can be experimentally tagged, and depends only on the decay mode of the W bosons. In the case of top-quark pair production, both W bosons can decay either hadronically or leptonically, with branching ratios $\Gamma(W \rightarrow q\bar{q}') = 0.67$, $\Gamma(W \rightarrow \ell\nu_\ell) = 0.33$: the final-state can either be dileptonic, monoleptonic (lepton+jets) or all-hadronic, and the top-quark properties must then be reconstructed from the measured final-states. Fig. 6.1 depicts the topology of the three decay channels and Table 6.1 gives an overview of their respective cross-sections, advantages and disadvantages.

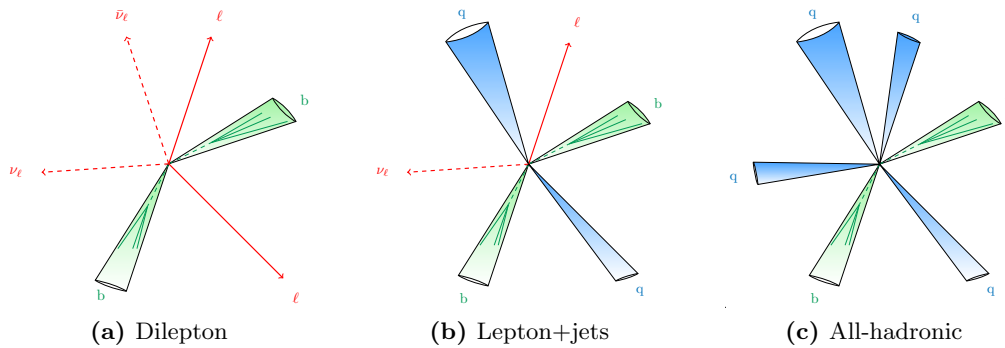


Figure 6.1: Topologies for $t\bar{t}$ events are either stemming from (a) dileptonic, (b) monoleptonic or (c) all-hadronic decays.

A precise computation for the top-quark pair production cross-section and differential observables is paramount for the extraction of top-quark properties. Most theoretical systematic uncertainties are well under control and have been the subject of various studies in the last few years [180–183]. In this chapter, the different theoretical descriptions of $pp \rightarrow t\bar{t}$ production are first reviewed, the most important issues are summarized and their potential impact on the extraction of top-quark properties from data are discussed, with a special focus on the top-quark observables. To do so in a realistic and quantitative way, an analysis close to the ATLAS 8 TeV top-quark mass extraction in the dilepton channel [184] is set up. The dilepton channel is the cleanest decay mode for an experimental measurement of the top-quark mass with the possibility of requiring two high-momentum leptons whose momenta are well-reconstructed. It has the advantage of a small background (coming mainly from fake leptons, diboson and Z +jets production)

6 Theoretical predictions for $t\bar{t}$ final-states

Final-state X	dilepton (w. $\tau^+\tau^-$)	$\ell+$ jets (w. $\tau+j$)	all-hadronic	all channels
$\Gamma(t\bar{t} \rightarrow X) [\%]$	10.89	44.02	44.89	100.0
$\sigma_{\text{NNLO}} [\text{pb}]$	27.42	110.82	113.02	$251.76^{+2.54\%}_{-3.44\%}$
Advantages	Clean signature	Full reconstruction	Largest BR	
Drawbacks	No full reconstruction	Jet-scale uncertainties	QCD background	
References	[171–173],[174, 175]	[172, 176],[5]	[177],[178]	

Table 6.1: For the three decay channels in $t\bar{t}$ production, the branching ratios and inclusive theoretical cross-sections at QCD NNLO+NNLL were computed with the Top++ program [179] for a top-quark mass of $m_t = 172.5$ GeV and the MSTW2008NNLO68cl PDF set. Advantages and drawbacks of (any) top-quark measurement in said channel are given. References for ATLAS measurements of the top-quark mass in particular are also laid out for each subchannel for the top-quark pole mass (in black), and for the MC mass (in blue) from template fits.

and a clean signature, but suffers from the small branching fraction ($\Gamma \sim 4.8\%$ for e/μ in the final-state). Cross-sections for all considered theoretical descriptions of $t\bar{t}$ final-states are given at the end of the chapter for the fiducial cuts employed in the analysis.

6.1 The narrow-width approximation (NWA)

Considering the intermediate state $W^+W^-b\bar{b}$, it makes sense at first to approximate it and examine only on-shell, doubly-resonant top-quark diagrams: the cross-section contribution stemming from non-resonant diagrams is expected to be of the order of $\mathcal{O}(\Gamma_t/m_t) \leq 1\%$, and usually neglecting other contributions is fine. This description is called the *narrow-width approximation* (NWA), and it builds on the limit $\Gamma_t \rightarrow 0$, where the top-quark propagator can then be written as

$$\lim_{\Gamma_t \rightarrow 0} \frac{1}{(p^2 - m_t^2) + m_t^2 \Gamma_t^2} = \frac{\pi}{m_t \Gamma_t} \delta(p^2 - m_t^2) + \mathcal{O}\left(\frac{\Gamma_t}{m_t}\right). \quad (6.1)$$

That is, top-quark production and decay entirely factorize, i.e.:

$$\begin{aligned} \mathcal{M}_{pp \rightarrow W^+W^-b\bar{b}} &= \mathcal{M}_{pp \rightarrow t\bar{t} \rightarrow W^+W^-b\bar{b}}^{\text{NWA}} + \mathcal{O}(\Gamma_t/m_t) \\ &= \mathcal{P}_{pp \rightarrow t\bar{t}} \otimes \mathcal{D}_{t \rightarrow W^+b} \otimes \mathcal{D}_{\bar{t} \rightarrow W^-\bar{b}} + \mathcal{O}(\Gamma_t/m_t), \end{aligned} \quad (6.2)$$

where \mathcal{P} denotes the $t\bar{t}$ production and \mathcal{D} the top-quark decay dynamics, and the spin correlations are correctly taken into account as indicated by the symbol \otimes . The corresponding three LO Feynman diagrams, as well as a few examples of one-loop diagrams for $gg \rightarrow t\bar{t}$ production, are shown in Fig. 6.2. Nowadays, most of the theoretical predictions used for the extraction of top-quark properties in experimental analyses rely on NLO matrix-elements for top-quark pair production only. The top-quark decay and all subsequent radiation is left to the MC generator, with the approximations it entails: particle

6.1 The narrow-width approximation (NWA)

decay usually only has LO accuracy, spin correlations (in particular in the parton-shower) were only recently implemented, and resummation is as good as the shower algorithm's accuracy. Even so, there exists a number of more complete MC implementations for $t\bar{t}$ production in the NWA: the effects of NLO corrections to both production and decay were investigated in the POWHEG-BOX-v2 [17–19] framework called `ttb_NLO_dec` [185]. The `Herwig7.1` MC generator supports a new multijet merging algorithm adapted to $t\bar{t}$ production at NLO [186], and finally the `SHERPA` generator allows for the matching of the CS shower to production of $t\bar{t}$ associated with 1-, 2- and 3-jets at NLO [187, 188].

Furthermore, some dedicated calculations have appeared over the years. In particular, QCD NNLO corrections for $t\bar{t}$ production have been calculated for differential distributions [189–191], and combined with NLO EW corrections [192]. For a review of NLO EW effects, see Refs. [193–195]. Leaving corrections in top-quark pair production and considering now the top-quark decay, it was later shown that higher-order corrections to the top-quark decay have a measurable impact on differential distributions in certain regions of phase-space. NLO radiative corrections to the top-quark decays were computed [196–198] and completed by NNLO QCD corrections [199, 200], NNLL resummation and other improvements above higher-order corrections in α_s [201–206]. Within the NWA, the calculation of QCD NNLO + NNLL' (soft-gluon and small-mass resummation) corrections for differential distributions was combined with NLO EW corrections and is the most complete fixed-order calculation up-to-date [207].

For the results shown in Section 6.5 in the NWA, the top-quark pair production is described at NLO QCD and factorizes from the top-quark decay. Furthermore, only the $e\mu$ dilepton channel is considered, that is $pp \rightarrow (e^+\nu_e)(\mu^-\bar{\nu}_\mu)b\bar{b}$ production for the analysis presented in Chapter 7. The top-quark decay accuracy is handled in three different ways:

- (1) Top-quark decay at LO is realized in the fixed-order `SHERPA` setup, as in Ref. [208] (referred to as $\textbf{NLO}_{\text{NWA}}^{\text{LOdec}}$ from now on).
- (2) The top-quark decay at NLO is computed in Ref. [197], and is shortly described below ($\textbf{NLO}_{\text{NWA}}^{\text{NLOdec}}$).
- (3) The top-quark decay is handled by the parton-shower, namely through the `SHERPA` CSS shower (\textbf{NLO}_{PS}).

Briefly, the $\textbf{NLO}_{\text{NWA}}^{\text{NLOdec}}$ calculation in the NWA is based on the following formula [197] where top-quark pair production and decay factorize. Taking the perturbative expansion of Eq. (6.2) to NLO gives

$$\begin{aligned} \mathcal{M}_{ij \rightarrow t\bar{t} \rightarrow b\bar{b}2\ell2\nu}^{\text{NWA, NLO}} = & \mathcal{P}_{ij \rightarrow t\bar{t}}^{\text{LO}} \otimes \mathcal{D}_{t \rightarrow b\ell^+\nu}^{\text{LO}} \otimes \mathcal{D}_{\bar{t} \rightarrow \bar{b}\ell^-\bar{\nu}}^{\text{LO}} + \mathcal{P}_{ij \rightarrow t\bar{t}}^{\delta\text{NLO}} \otimes \mathcal{D}_{t \rightarrow b\ell^+\nu}^{\text{LO}} \otimes \mathcal{D}_{\bar{t} \rightarrow \bar{b}\ell^-\bar{\nu}}^{\text{LO}} \\ & + \mathcal{P}_{ij \rightarrow t\bar{t}}^{\text{LO}} \otimes \left(\mathcal{D}_{t \rightarrow b\ell^+\nu}^{\delta\text{NLO}} \otimes \mathcal{D}_{\bar{t} \rightarrow \bar{b}\ell^-\bar{\nu}}^{\text{LO}} + \mathcal{D}_{t \rightarrow b\ell^+\nu}^{\text{LO}} \otimes \mathcal{D}_{\bar{t} \rightarrow \bar{b}\ell^-\bar{\nu}}^{\delta\text{NLO}} \right), \end{aligned} \quad (6.3)$$

where LO (δNLO) represent the LO (NLO) contributions to the $t\bar{t}$ production and top-quark decays, respectively.¹

¹The product $\mathcal{P}^{\delta\text{NLO}} \otimes \mathcal{D}^{\delta\text{NLO}}$ is formally of higher order.

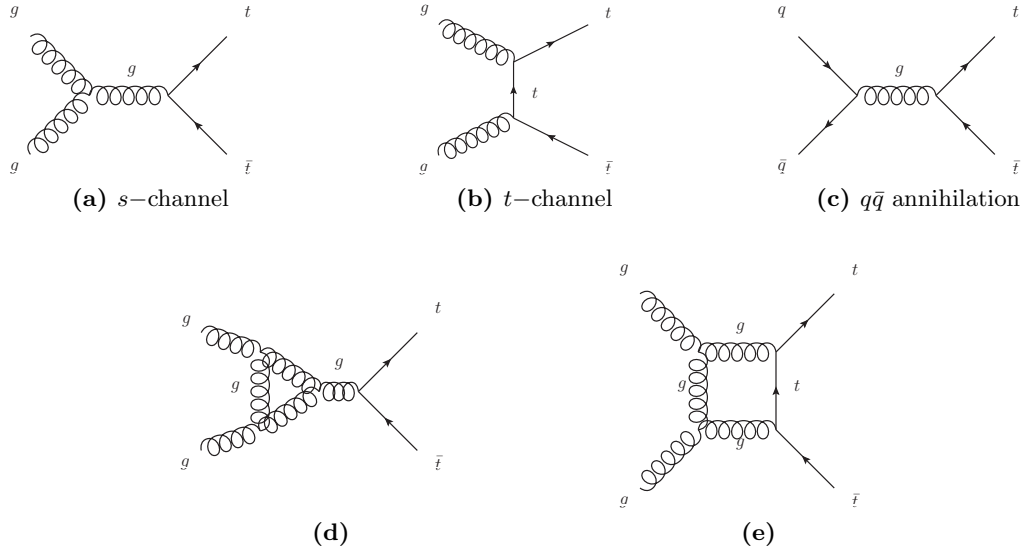


Figure 6.2: (a-c) Leading-order diagrams for $t\bar{t}$ production and (d-e) two examples of NLO QCD one-loop diagrams for $gg \rightarrow t\bar{t}$

As mentioned above, the NWA is expected to be precise enough for most calculations and yet, NLO and off-shell effects in the top-quark decay can have an important impact on sensitive regions of phase-space. In practice, experimental analyses do account for part of the non-doubly-resonant contributions: they include single-top quark production in the signal, since it contributes to the same final-state at NLO, or they subtract it consistently as background. To take care of the interference between $t\bar{t}$ and single-top diagrams, this is generally accomplished with the help of a diagram subtraction (DS) or diagram removal (DR) scheme [209]. This procedure is not entirely free of quirks and violates gauge-invariance. To get an entirely consistent theoretical prediction, it is therefore preferable to produce the full intermediate state $pp \rightarrow W^+W^-b\bar{b}$, which contains the complete set of Feynman diagrams at NLO.

6.2 $W^+W^-b\bar{b}$ production: review of existing calculations

In this section, the setup used for calculating NLO QCD corrections to the $pp \rightarrow W^+W^-b\bar{b}$ process is described, which is computationally more demanding than $pp \rightarrow t\bar{t}$ production in the NWA. The full calculation at NLO contains all doubly-resonant top-quark diagrams, but also non-doubly resonant as well as non-factorizing contributions. Fig. 6.3 illustrates some of the additional Feynman diagrams.

At LO, the full $W^+W^-b\bar{b}$ final-state including the non-resonant diagrams has been computed in Refs. [208, 210–212]. In general, the calculation of NLO corrections poses some technical problems because of the existence of b -quarks in both initial- and final-state. In the 5-flavor scheme (5FNS), where b -quarks are treated as massless, collinear

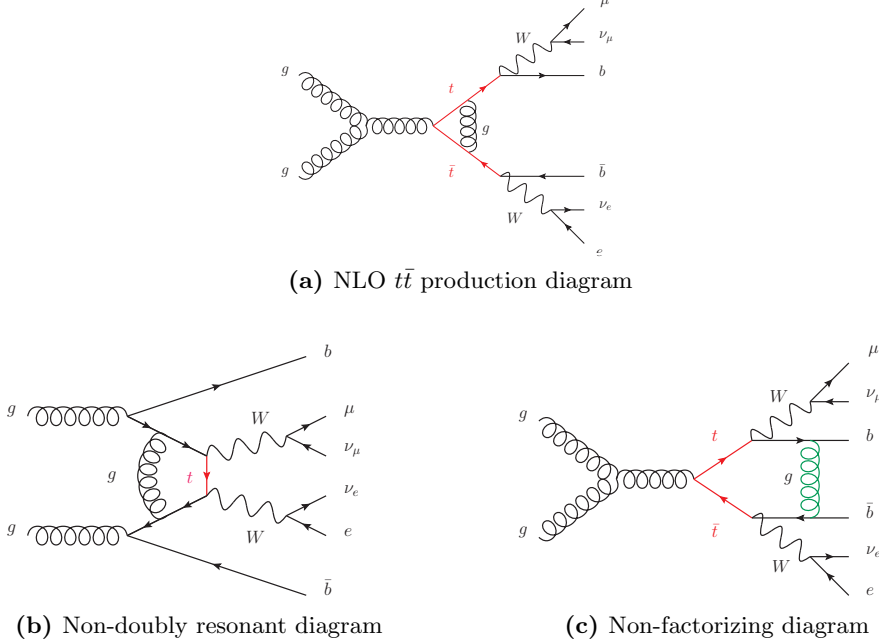


Figure 6.3: One-loop diagrams for $pp \rightarrow W^+W^-b\bar{b}$ production contain (a) NLO corrections to standard NWA $t\bar{t}$ production, but also (b) diagrams with one or no top-quark propagators and (c) resonant diagrams with non-factorizing legs

1301 $g \rightarrow b\bar{b}$ splittings contribute to the final-state and the corresponding IR divergence has
 1302 to be handled. Considering massive b -quarks (4FNS) has the advantage of allowing any
 1303 phase space restrictions on the b -quarks without endangering infrared safety, and thus
 1304 allows to consider exclusive 0, 1- and 2-jet bins for $pp \rightarrow (e^+\nu_e)(\mu^-\bar{\nu}_\mu)b\bar{b}$ in the same
 1305 setup. On the other hand, massive b -quarks are accompanied by an additional mass scale
 1306 to the one-loop integrals and thus renders the integral evaluation less straightforward.
 1307 In Refs. [213, 214], NLO calculations in the 4FNS have been performed.

1308 Often, the $W^+W^-b\bar{b}$ prediction differs from the NWA in phase-space regions accessible
 1309 only at NLO or sensitive to the top-quark decay kinematics. In Ref. [208], particular
 1310 emphasis has been put on the impact of the non-factorizing contributions on the top
 1311 quark mass measurements in the dilepton channel. Recently the calculation of the NLO
 1312 QCD corrections to $W^+W^-b\bar{b}$ production with full off-shell effects has also been achieved
 1313 in the lepton+jets channel [215].

1314 6.3 $W^+W^-b\bar{b}$ calculation setup at NLO QCD

1315 The calculation (along results for top-quark mass determinations) was published in
 1316 Ref. [216] and is analogous to the one described in Ref. [217]. The NLO QCD cor-
 1317 rections to the $pp \rightarrow W^+W^-b\bar{b} \rightarrow (e^+\nu_e)(\mu^-\bar{\nu}_\mu)b\bar{b}$ process are computed, i.e. up to
 1318 $\mathcal{O}(\alpha_s^2\alpha^2)$, in the 5FNS. This means that interference from (massless) b -quarks in the

6 Theoretical predictions for $t\bar{t}$ final-states

initial-state is taken into account. Top-quark finite width effects are fully included. The complex mass scheme is used to incorporate the width in a gauge-invariant way, where the top-quark mass is replaced by a complex number μ_t :

$$\mu_t^2 = m_t^2 - im_t\Gamma_t . \quad (6.4)$$

The W and intermediate Z bosons also acquire a complex mass. Note that only resonant W boson diagrams are taken into account: non-resonant contributions and finite- W -width effects were found to be small compared to top-quark effects [218]. The calculation is realized at parton-level within the SHERPA v2.2.3 framework,² where tree-level and real amplitudes are computed by the SHERPA matrix-element generators COMIX [220–222] and AMEGIC [223]. The one-loop amplitudes are compiled by GoSam and linked to SHERPA via the BLHA interface. Finally, the IR divergences are subtracted with the help of the Catani-Seymour dipole formalism as automated in SHERPA.

There are 334 diagrams contributing to the $q\bar{q} \rightarrow W^+W^-b\bar{b}$ virtual corrections, where q are the light quarks u, d, s, c , and 1068 diagrams contributing to $gg \rightarrow W^+W^-b\bar{b}$. Additionally, because of the b -quarks present in the initial-state, 668 one-loop diagrams contribute to $b\bar{b} \rightarrow W^+W^-b\bar{b}$.

In the results presented in Chapters 7 and 8, the full $pp \rightarrow W^+W^-b\bar{b} \rightarrow (e^+\nu_e)(\mu^-\bar{\nu}_\mu)b\bar{b}$ QCD NLO prediction is compared with various $t\bar{t}$ predictions in the NWA. To disentangle the effects from production and decay corrections (as well as extra radiation in a parton-shower resummed approximation), the four theoretical descriptions considered in the next chapter are summarized again for completeness:

- 1339 **NLO_{full}**: full NLO corrections to $pp \rightarrow W^+W^-b\bar{b}$ with leptonic W -decays,
- 1340 **NLO_{NWA}^{NLOdec}**: NLO $t\bar{t}$ production \otimes NLO decay,
- 1341 **NLO_{NWA}^{LOdec}**: NLO $t\bar{t}$ production \otimes LO decay,
- 1342 **NLO_{PS}**: NLO $t\bar{t}$ production+shower \otimes decay via parton showering.

Note that the three first theoretical descriptions are not matched to a parton-shower at all. The PDF4LHC15_nlo_30_pdfas sets [224] are interfaced to SHERPA via LHAPDF and events are produced at a center-of-mass energy of $\sqrt{s} = 13$ TeV. The central top-quark mass was set to $m_t = 172.5$ GeV and the G_μ –electroweak scheme was used with the following numerical values:

$$G_\mu = 1.16637 \cdot 10^{-5} \text{ GeV}^{-2}, \quad M_W = 80.385 \text{ GeV}, \quad M_Z = 91.1876 \text{ GeV}, \quad (6.5)$$

$$\begin{aligned} \Gamma_t^{\text{LO}} &= 1.4806 \text{ GeV}, & \Gamma_t^{\text{NLO}} &= 1.3535 \text{ GeV}, \\ \Gamma_W^{\text{LO}} &= 2.0454 \text{ GeV}, & \Gamma_W^{\text{NLO}} &= 2.1155 \text{ GeV}, \\ \Gamma_Z &= 2.4952 \text{ GeV}, \end{aligned} \quad (6.6)$$

where the LO (NLO) widths were used for the LO (NLO) decays, respectively.

²A patched version [219] was used for the CSS shower, with the correct eikonal expressions for radiating off massive top quarks (relevant only for the NLO_{PS} description).

1349 6.4 Event requirements

1350 To give a more quantitative assessment of the difference between these predictions with
 1351 respect to the extracted top-quark mass, an analysis that is similar to the ATLAS top-
 1352 quark mass measurement in the dilepton channel at 8 TeV [184] is considered, where the
 1353 trigger cuts on leptons and jets are adapted to the ATLAS 13 TeV standards. For details
 1354 of the analysis, the reader is referred to Chapter 7. The following event requirements
 1355 are applied:

- 1356 • the number of b -jets $n_{b,\text{jets}} = 2$ with $p_T^{\text{jet}} > 25 \text{ GeV}$ and $|\eta^{\text{jet}}| < 2.5$. Jets are
 1357 clustered with anti- k_T [169] as implemented in `FastJet` [225, 226] using a jet
 1358 distance parameter of $R = 0.4$. In the analysis, a jet is defined as b -jet if it
 1359 contains a B -hadron (or its decay products).
- 1360 • exactly two oppositely charged leptons which fulfill $p_T^\mu > 28 \text{ GeV}$, $|\eta^\mu| < 2.5$ for
 1361 muons and $p_T^e > 28 \text{ GeV}$, $|\eta^e| < 2.47$ for electrons excluding the crack region
 1362 $1.37 < |\eta^e| < 1.52$ between barrel and endcap EM calorimeters. For charged
 1363 leptons a separation of $\Delta R(\ell, \text{jet}) > 0.4$ to any jet is required: otherwise, the event
 1364 is vetoed entirely.
- 1365 • $p_T^{\ell b} > 120 \text{ GeV}$. Using the same lepton- b -jet assignments as for $m_{\ell b}$, the value of
 1366 $p_T^{\ell b}$ is defined as the average transverse momentum of both lepton- b -jet systems.

1367 The central scales are set to $\mu_R = \mu_F = m_t$. The scale variation bands are obtained
 1368 by varying $\mu_{R,F} = c_{R,F} m_t$, with $(c_R, c_F) \in \{(0.5, 0.5), (2, 2)\}$.³

In the NWA parton-shower results, the central scale was also compared to a dynamic scale called $\mu_{t\bar{t}}$. The latter is a “color-flow inspired” QCD scale suggested in Ref. [227]. For the Mandelstam invariants s , t and u , the dynamic scale is given by

$$\mu_{t\bar{t}}^2(q\bar{q} \rightarrow t\bar{t}) = 2 p_q p_t = m_t^2 - t , \quad (6.7)$$

$$\mu_{t\bar{t}}^2(\bar{q}q \rightarrow t\bar{t}) = 2 p_q p_t = m_t^2 - u , \quad (6.8)$$

$$\mu_{t\bar{t}}^2(gg \rightarrow t\bar{t}) = \begin{cases} m_t^2 - t & \text{with weight } w_1 \propto \frac{u-m_t^2}{t-m_t^2} + \frac{m_t^2}{m_t^2-t} \left\{ \frac{4t}{t-m_t^2} + \frac{m_t^2}{s} \right\} \\ m_t^2 - u & \text{with weight } w_2 \propto \frac{t-m_t^2}{u-m_t^2} + \frac{m_t^2}{m_t^2-u} \left\{ \frac{4u}{u-m_t^2} + \frac{m_t^2}{s} \right\} , \end{cases} \quad (6.9)$$

1369 the value of $\mu_{t\bar{t}}$ being chosen with a probability proportional to the two weights w_1, w_2 .

³Also, 7-point variations were considered but the simultaneous variations are identical to their envelope.

1370 6.5 Total cross-section results

1371 The fiducial cross-sections after applying the aforementioned cuts are given in Table 6.2
 1372 for all considered predictions, where production at LO accuracy is also added for com-
 1373 pleteness. The renormalization and factorization scale uncertainties are given in percent.

	X=LO [fb]	X=NLO [fb]
\mathbf{X}_{full}	$(739.5 \pm 0.3)^{+31.5\%}_{-22.4\%}$	$(914 \pm 3)^{+2.1\%}_{-7.6\%}$
$\mathbf{X}_{\text{NWA}}^{\text{LOdec}}$	$(727.3 \pm 0.2)^{+31.4\%}_{-22.3\%}$	$(1029 \pm 1)^{+10.4\%}_{-11.5\%}$
$\mathbf{X}_{\text{NWA}}^{\text{NLOdec}}$	-	$(905 \pm 1)^{+2.3\%}_{-7.7\%}$
$\mathbf{X}_{\text{PS}}, \mu = m_t$	$(637.7 \pm 0.9)^{+29.7\%}_{-21.0\%}$	$(886 \pm 1)^{+8.5\%}_{-9.3\%}$
$\mathbf{X}_{\text{PS}}, \mu = \mu_{t\bar{t}}$	$(499.7 \pm 0.7)^{+27.6\%}_{-19.3\%}$	$(805.2 \pm 0.9)^{+12.3\%}_{-10.9\%}$

Table 6.2: Cross-sections for all predictions at LO, respectively NLO in production, where the top-quark mass $m_t = 172.5$ GeV. The uncertainty stemming from MC integration is given in parentheses, and scale variation uncertainties are shown in percent.

1374 While the cross-sections for NLO_{full} and $\text{NLO}_{\text{NWA}}^{\text{NLOdec}}$ agree with each other within
 1375 expectations, the $\text{NLO}_{\text{NWA}}^{\text{LOdec}}$ cross-section is about 13% higher than the latter. The
 1376 NLO_{PS} cross-section, in comparison, is smaller because of the softening of b -jets which
 1377 leads to a higher rejection rate when taking jet requirements into account. The $\mu_{t\bar{t}}$
 1378 scale is larger than the central scale m_t , thus the even smaller cross-section for this
 1379 scale choice. Notice also the reduction in the renormalization and factorization scale
 1380 uncertainties when including NLO corrections to the top-quark decay. Usually, rather
 1381 than total inclusive cross-sections, the most sensitive top-quark mass measurements
 1382 rely on differential distributions, where mostly the distributions for $t\bar{t}$ final-states are
 1383 MC-generated and *fitted* to extract the top-quark mass (see the full explanation of
 1384 the method in Chapter 7). One caveat of considering differential distributions is that
 1385 the measured top-quark mass is rather represented by the MC input top-quark mass
 1386 parameter m_t^{MC} , instead of the top-quark pole mass (or any other QFT-defined mass)
 1387 measured in inclusive $t\bar{t}$ measurements.

1388 Leaving the difference between heavy-quark mass schemes aside, the exact procedure
 1389 used in current ATLAS analyses for measuring the MC top-quark mass is explained
 1390 in the next chapter, along with quantitative comparisons of the theoretical predictions
 1391 outlined above.

¹³⁹² 7 NWA versus $W^+W^-b\bar{b}$: Top-quark mass ¹³⁹³ uncertainties at parton-level

¹³⁹⁴ This chapter shall investigate quantitatively the effect of using the different theoretical
¹³⁹⁵ predictions presented above in a top-quark mass extraction. The measurement method
¹³⁹⁶ is based on the ATLAS 8 TeV analysis in the dilepton channel [184], where the ATLAS
¹³⁹⁷ cuts are adapted to the 13 TeV center-of-mass energy. This chapter first introduces
¹³⁹⁸ the template fit method that was used in the experimental measurement. After a short
¹³⁹⁹ discussion of important features of the considered observables, the results for the fit of
¹⁴⁰⁰ the top-quark mass and its dependence on the different theoretical descriptions of the
¹⁴⁰¹ $t\bar{t}$ dilepton final-state are laid out.

¹⁴⁰² 7.1 The template fit method

¹⁴⁰³ In the dilepton channel, the top-quark momenta cannot be fully reconstructed in the
¹⁴⁰⁴ experiment because of the two-particle spectrum spread given by the neutrinos from both
¹⁴⁰⁵ W -decays. One successful method is to use a differential distribution that is sensitive
¹⁴⁰⁶ to the top-quark mass instead and which can be defined without having to properly
¹⁴⁰⁷ reconstruct the top-quark intermediate states. The procedure is the following:

- ¹⁴⁰⁸ • Choose a distribution that is sensitive to the theoretical top-quark mass: for ex-
¹⁴⁰⁹ ample, the average invariant mass of the lepton- b -jet system $m_{\ell b}$ (which make up
¹⁴¹⁰ the visible top-quark decay products) is chosen as a function of the top-quark mass
¹⁴¹¹ set in the MC event generator.
- ¹⁴¹² • Generate distributions for different input top-quark masses m_t^{in} . These are called
¹⁴¹³ *template* distributions.
- ¹⁴¹⁴ • Individually fit the template distributions simulated for the input masses m_t^{in} with
¹⁴¹⁵ an appropriate function. Considering the simple example of a Gaussian fit, this
¹⁴¹⁶ gives:

$$\mathcal{G}(A, \mu, \sigma; m_t^{\text{in}}) = A(m_t^{\text{in}}) \exp \left(-\frac{(\mu(m_t^{\text{in}}) - m_t^{\text{in}})^2}{2\sigma^2(m_t^{\text{in}})} \right), \quad (7.1)$$

¹⁴¹⁷ where the parameters A, μ, σ are fit to the distributions generated for each input
¹⁴¹⁸ mass.

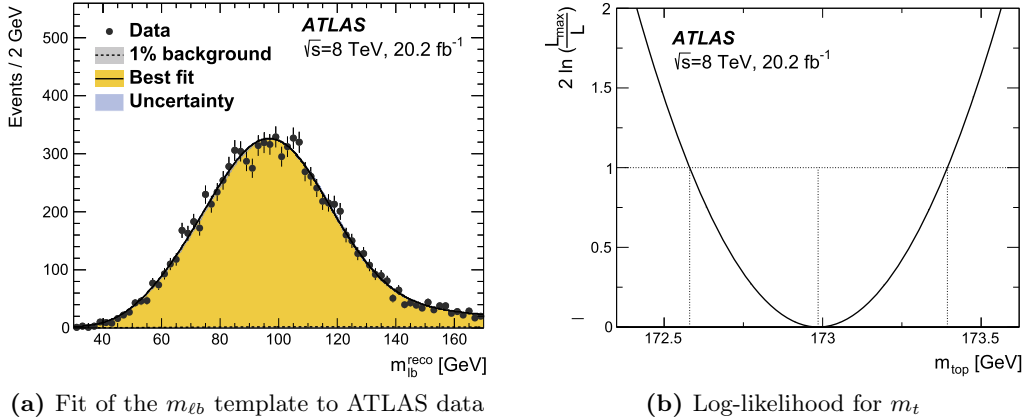


Figure 7.1: (a) The ATLAS 8 TeV analysis generates template distributions for m_{lb} for different input top-quark masses. These are fitted by a suitable function which parameters are expressed as linearly-dependent functions of m_t . (b) The likelihood function for m_t is then maximized in an unbinned fit to the measured m_{lb} distribution to extract the top-quark mass (Figures from Ref. [184]).

1419 This step is called *calibration* in the following paragraphs, and the functions for each
 1420 of the input top-quark masses are called calibration functions. The dependence of the
 1421 parameters on m_t^{in} is assumed to be linear, a fact that is checked against the MC
 1422 prediction. Once it is confirmed, the linear dependence is imposed (in this example,
 1423 $A(m_t^{\text{in}}) = a + b \cdot m_t^{\text{in}}$ with a and b fixed, and analogously for $\mu(m_t^{\text{in}})$, $\sigma(m_t^{\text{in}})$). The
 1424 underlying linear parameters are then kept constant, and the only free parameter is the
 1425 extracted top-quark mass $m_t = m_t^{\text{out}}$ to be measured. This function can then be used
 1426 directly in an unbinned likelihood fit to the distribution measured in experimental data,
 1427 as shown in Fig. 7.1 as an illustration from the ATLAS 8 TeV measurement.

1428 For a satisfying modeling of the m_{lb} distribution, the sum of a Gaussian and a Landau
 1429 distribution is used in the analysis. In practice, the overall normalization factor is fit
 1430 to the measured cross-section after cuts are applied. In the rest of this chapter, the
 1431 extraction is repeated from a custom analysis implemented in Rivet [228] similar to the
 1432 one performed by ATLAS, for the four different theoretical setups presented in Chapter 6
 1433 at parton-level (at particle-level for the parton-showered $t\bar{t}$ results). Different observables
 1434 are also compared in addition to m_{lb} .

1435 7.2 Definition of the observables

1436 The results presented in the rest of this chapter were published in Ref. [216]. The reader
 1437 is referred to the latter for details that are omitted in the following. A list of observables
 1438 is studied that should in principle be maximally sensitive to the top-quark mass while
 1439 minimally sensitive to theoretical systematic uncertainties (that is, including differences
 1440 between NWA and full $W^+W^-b\bar{b}$ predictions):

7.2 Definition of the observables

- $m_{\ell b}$ – the invariant mass of the two lepton- and b -jet systems

$$m_{\ell b}^2 = (p_\ell + p_b)^2. \quad (7.2)$$

Since both top quarks decay leptonically and there is no possibility to determine the charge of the b -jets experimentally, there is an ambiguity in the assignment of the lepton and b -jet to the two top quarks. Here, the same criterion is used as in the ATLAS analysis: the two possible pairs for the lepton- b -jet system ($\ell^+ b_1, \ell^- b_2$) are tried out, and the pairing that minimizes the sum of the two $m_{\ell b}$ values per event is chosen. The final value is set to the average of both $m_{\ell b}$ values.

- m_{T2} – following Refs. [229, 230] in the case of the final-state $(e^+\nu_e)(\mu^-\bar{\nu}_\mu)b\bar{b}$, the definition of this variable is given by

$$m_{T2}^2 = \min_{p_T^{\nu_1} + p_T^{\nu_2} = p_T^{\text{miss}}} \left[\max \left\{ m_T^2 \left(p_T^{(\ell^+ b_1)}, p_T^{\nu_1} \right), m_T^2 \left(p_T^{(\ell^- b_2)}, p_T^{\nu_2} \right) \right\} \right]. \quad (7.3)$$

The same pairing as for $m_{\ell b}$ is chosen for the lepton and b -jet systems, and the transverse mass is defined as

$$m_T^2 \left(p_T^{(\ell b_i)}, p_T^{\nu_i} \right) = m_{(\ell b_i)}^2 + 2 \left(E_T^{(\ell b_i)} E_T^{\nu_i} - p_T^{(\ell b_i)} p_T^{\nu_i} \right), \quad (7.4)$$

with $E_T = \sqrt{|p_T|^2 + m^2}$ and $m_{\nu_i} = 0$.

- $E_T^{\Delta R}$ – the lepton transverse energy weighted by the angular distance to the corresponding b -jet

$$E_T^{\Delta R} = \frac{1}{2} \left(E_T^{l_1} \Delta R(l_1, b_1) + E_T^{l_2} \Delta R(l_2, b_2) \right), \quad (7.5)$$

where again the above $m_{\ell b}$ criterion is used.

- $m_{\ell\ell}$ – the invariant mass of the two-lepton system.

For the NLO_{NWA}^{LOdec}, NLO_{NWA}^{NLOdec} and NLO_{full} calculations, only the parton-level is considered, including the decay products from the W bosons. The b -jets are identified with the b -quarks in that case. For the NLO_{PS} prediction, the cuts and observables are defined on the parton-level output of the shower algorithm, before any hadronization but with the full-particle final-state. Sets of MC samples were produced for input top-quark masses

$$m_t \in \{165.0, 172.5, 180.0\} [\text{GeV}]. \quad (7.6)$$

The dependence on the input top-quark mass m_t is shown for all four observables in Fig. 7.2. Whereas $m_{\ell b}$ and m_{T2} are the most sensitive to m_t with a ratio to the central choice of the order $\mathcal{O}(2-3)$ for the considered masses, the dependence of the $E_T^{\Delta R}$ and $m_{\ell\ell}$ observables on the top-quark mass is rather weak.

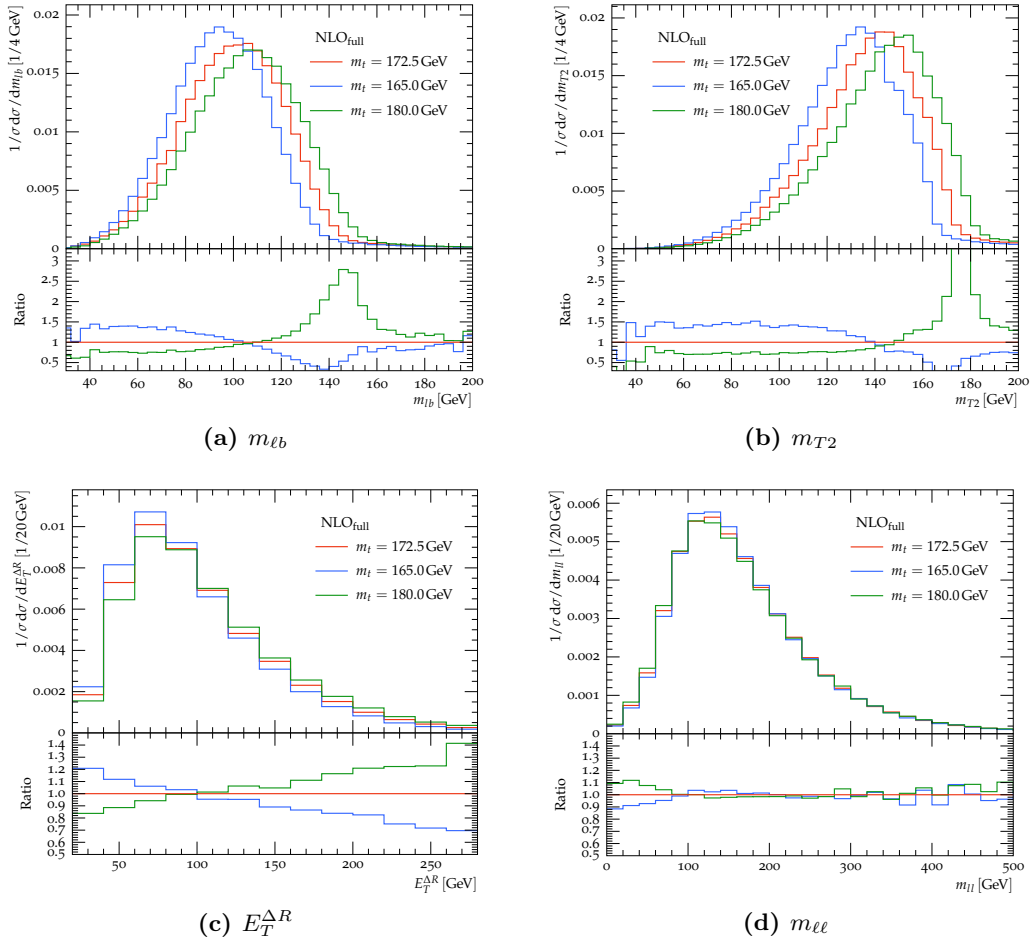


Figure 7.2: Differential observables are shown for three different top-mass points chosen symmetrically around $m_t = 172.5 \text{ GeV}$ for the full $W^+W^-b\bar{b}$ NLO prediction. While the (a) m_{llb} and the (b) m_{T2} observables show the highest top-mass dependence, the observables (c) $E_T^{\Delta R}$ and (d) m_{lll} are not sensitive enough to the top-mass to be considered for the template fit.

1467 7.3 Comparison of the different theoretical descriptions

1468 The normalized differential cross-section for the m_{llb} observable is outlined in Fig. 7.3
 1469 for the four theoretical predictions presented in Chapter 6. The ratio to the complete
 1470 $W^+W^-b\bar{b}$ NLO_{full} calculation is shown, where the latter's scale uncertainties are
 1471 represented by gray bands in the plot. Note that the m_{llb} distribution has a sharp kinematic
 1472 edge at $m_{llb}^{\text{edge}} = \sqrt{m_t^2 - m_W^2} \sim 153 \text{ GeV}$. Beyond the kinematic edge, the bins
 1473 are only populated by wrong lepton- b -jet pairing, additional radiation from the initial-
 1474 state clustered along the lepton- b -jet system, and non-resonant contributions. The LO
 1475 cross-section for $t\bar{t}$ production vanishes in this phase-space region. Thus, because NLO

7.3 Comparison of the different theoretical descriptions

corrections represent the first non-trivial order contributing to this region, differences between the theoretical descriptions considered here are expected to be sizeable around and above this kinematic edge. On the other hand, as seen in Fig. 7.2, this region also displays the highest sensitivity to the top-quark mass.

In Fig. 7.3, all predictions for $m_{\ell b}$ agree within a few percent in the bulk of the distribution, $40 \text{ GeV} \leq m_{\ell b} \leq 140 \text{ GeV}$, except for $\text{NLO}_{\text{NWA}}^{\text{LOdec}}$. The latter introduces a positive slope around and above the peak with differences of $\mathcal{O}(-10\%)$ at small masses up to $+20\%$ at $\sim 140 \text{ GeV}$, effectively shifting the peak to higher values of $m_{\ell b}$. This translates into an artificially higher extracted mass for the top quark when using LO decay predictions. In contrast, $\text{NLO}_{\text{NWA}}^{\text{NLOdec}}$ is found within 4% of the NLO_{full} prediction for the bulk of the distribution, starting to differ above the kinematic edge and stagnating at -50% of the full prediction in the tail, as expected. Finally, for the NLO_{PS} case, the tail at high $m_{\ell b}$ -values is populated by the additional radiation from the parton-shower, and is driven closer to NLO_{full} while it mostly lies between $\text{NLO}_{\text{NWA}}^{\text{LOdec}}$ and $\text{NLO}_{\text{NWA}}^{\text{NLOdec}}$ in the rest of the distribution.

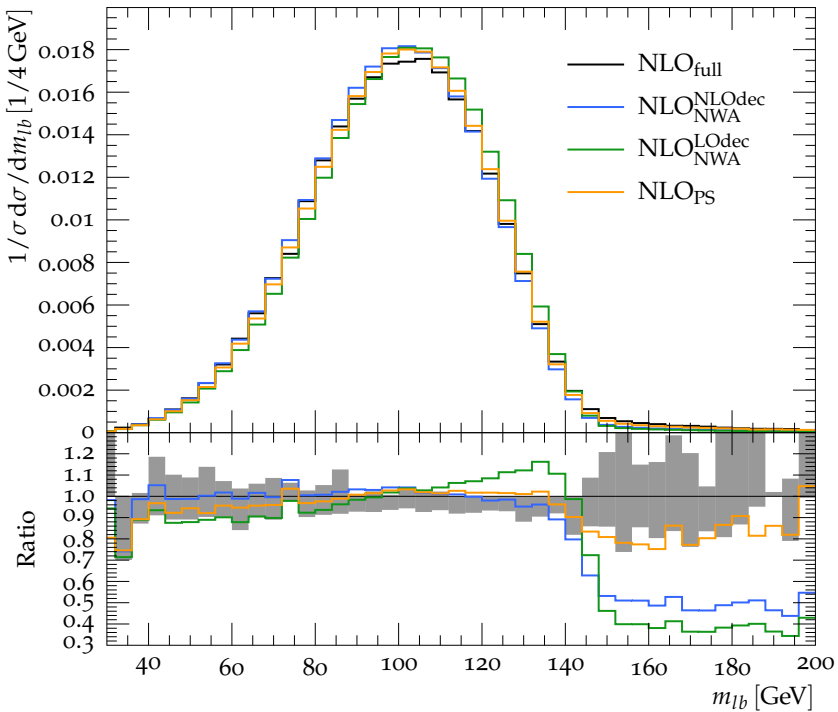


Figure 7.3: The normalized differential lepton- b -jet system invariant mass $m_{\ell b}$ is shown for all four theoretical predictions considered at 13 TeV, with their ratio to the NLO_{full} prediction. The gray band represents the latter's scale variation uncertainty.

Similar features can be observed for the normalized distribution of m_{T2} in Fig. 7.4 on a larger range up to the kinematic edge at $m_{T2}^{\text{edge}} = m_t$. In Figs. 7.5a and 7.5b, the normalized $E_T^{\Delta R}$ and $m_{\ell\ell}$ distributions show smaller differences between the theoretical predictions, with maximal deviations of $\mathcal{O}(10 - 12\%)$ in the regions of lowest cross-section. Since they are much less sensitive to the top-quark mass, though, they are not considered for the template fitting procedure in the results below.

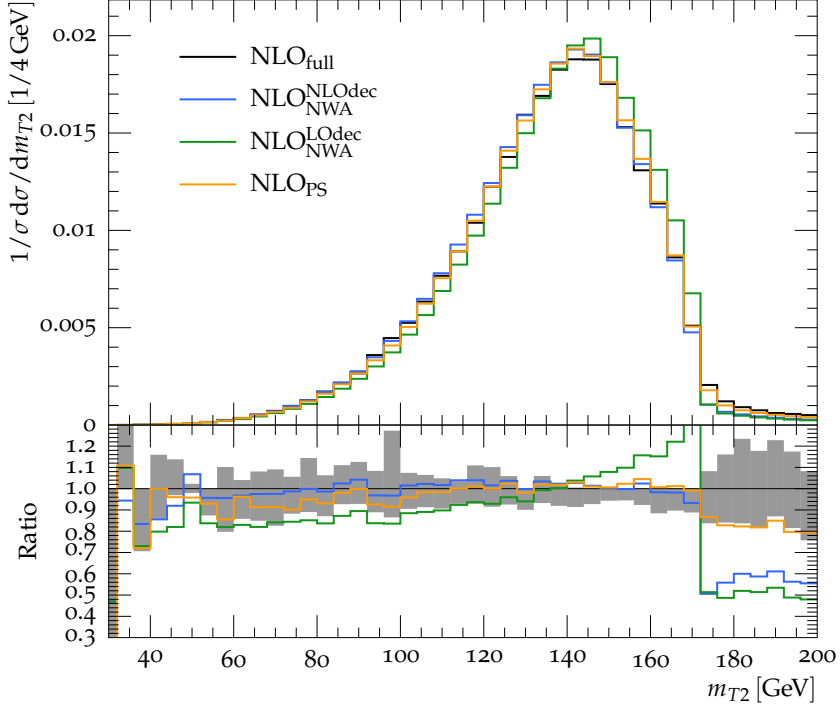


Figure 7.4: The normalized m_{T2} distribution is depicted for the four theoretical predictions, and shows a behavior similar to $m_{\ell b}$.

It is also enlightening to look at the scale dependence of the four theoretical descriptions for LO and NLO production. In Fig. 7.6a, the ratio of the $W^+W^-b\bar{b}$ prediction NLO_{full} to LO_{full} is shown for the $m_{\ell b}$ observable. Although large corrections are expected above the kinematic edge when going from LO to NLO in production, one finds unexpectedly important corrections in the low-mass region as well, where differences between both orders of accuracy in production are not covered by the scale uncertainties. In the NWA case shown in Fig. 7.6b, describing the top-quark decays at NLO also pushes the prediction out of the $\text{NLO}_{\text{NWA}}^{\text{LOdec}}$ scale uncertainties. The differences between the $\text{NLO}_{\text{NWA}}^{\text{LOdec}}$ and $\text{NLO}_{\text{NWA}}^{\text{NLOdec}}$, respectively NLO_{PS} are also not covered around the kinematic edge. In general, scale uncertainties in the NWA are shown to be misguidedly small in the tails of the $m_{\ell b}$ and m_{T2} distributions. The behavior of scale-varied predictions is depicted for m_{T2} , $E_T^{\Delta R}$ and $m_{\ell\ell}$ in Figs. 7.7–7.9.

Comparing the mass sensitivity in Fig. 7.2a and the systematic differences between predictions in Fig. 7.6a, the template fit strategy should be optimized to maximize the

7.3 Comparison of the different theoretical descriptions

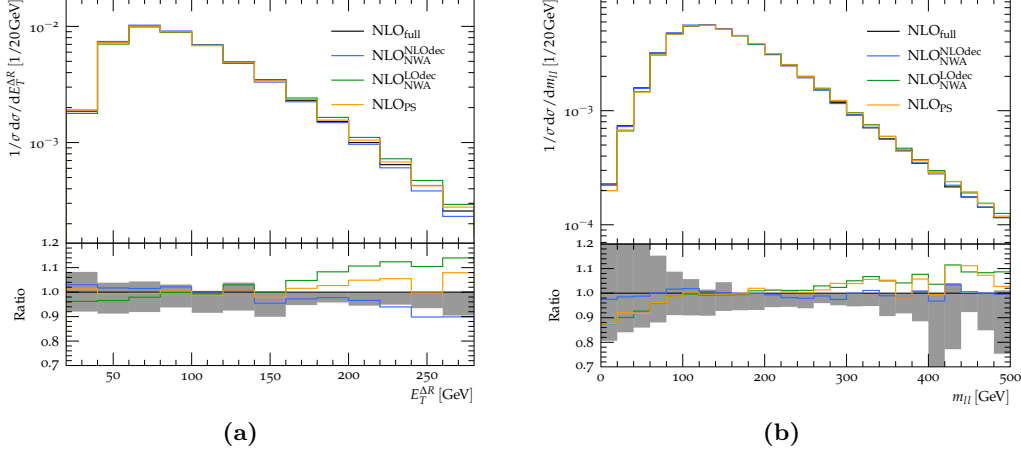


Figure 7.5: The normalized differential cross-sections for the (a) $E_T^{\Delta R}$ and (b) $m_{\ell\ell}$ distributions with all four theoretical predictions.

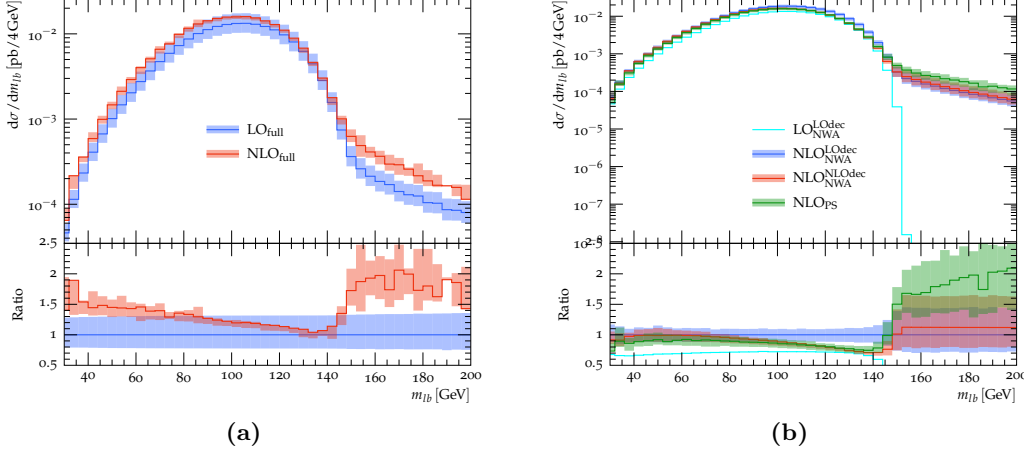


Figure 7.6: Results including scale variation bands for m_{lb} , for (a) the LO_{full} and NLO_{full} calculations, (b) the calculations based on the NWA. The ratios with respect to (a) LO_{full} and (b) NLO_{NWA}^{LOdec} are also shown.

1511 top-quark mass sensitivity while keeping the systematic uncertainty associated to the
1512 theoretical predictions to a minimum. The fit range is chosen to be

$$40 \text{ GeV} \leq m_{lb} \leq 160 \text{ GeV}, \quad (7.7)$$

$$80 \text{ GeV} \leq m_{T2} \leq 180 \text{ GeV}.$$

1513 The exact dependence on the fit range was investigated, where the results were repro-
1514 duced once with a restricted range of $m_{lb} \leq 140$ GeV, and numerical values were found
1515 to be stable.

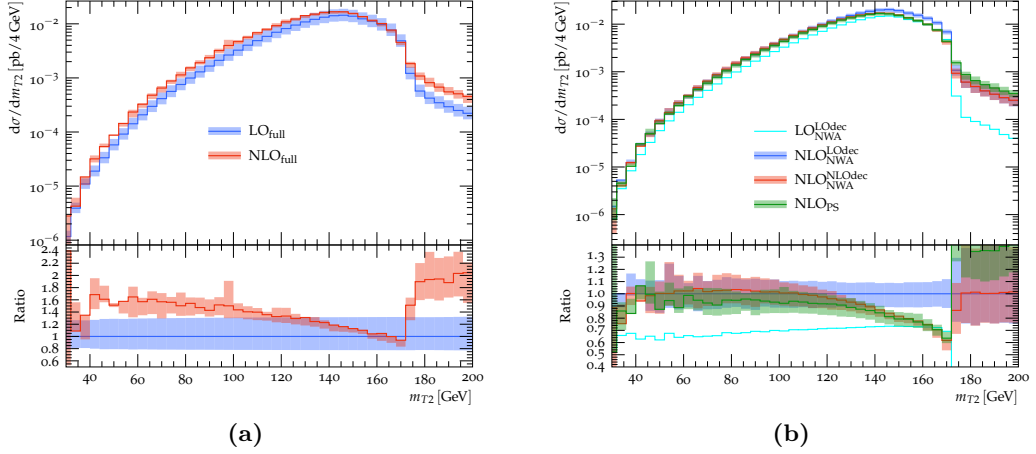


Figure 7.7: Results including scale variation bands for m_{T2} , for (a) the LO_{full} and NLO_{full} calculations, and (b) the calculations based on the NWA. The ratios are defined as in Fig. 7.6.

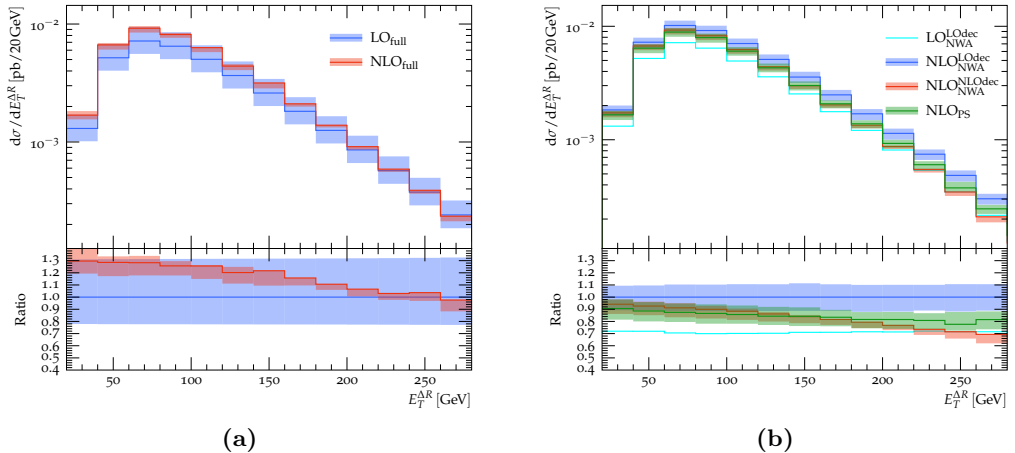


Figure 7.8: Results including scale variation bands for $E_T^{\Delta R}$ for (a) the LO_{full} and NLO_{full} calculations, and (b) the calculations based on the NWA. The ratios are defined as in Fig. 7.6.

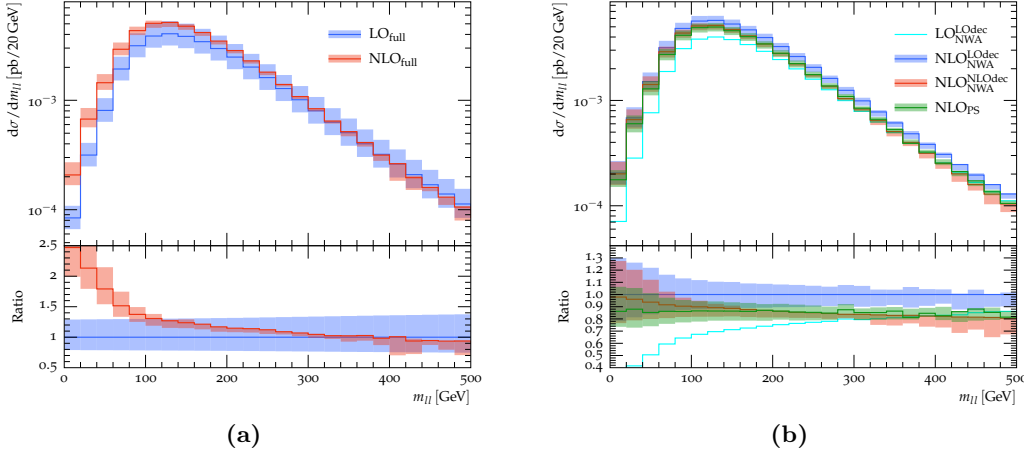


Figure 7.9: Results including scale variation bands for m_H , for (a) the LO_{full} and NLO_{full} calculations, and (b) the calculations based on the NWA. The ratios are defined as in Fig. 7.6.

1516 7.4 Template fit results

1517 After the qualitative discussion of differential results in the last section, reults from the
 1518 template fitting procedure are shown and numerical values compared for the extracted
 1519 top-quark mass from the different theoretical descriptions. To this effect, since no data
 1520 was available to compare to, the procedure outlined in Section 7.1 is adapted and the
 1521 following approach is applied to produce plots like the ones displayed in Fig. 7.10:

- 1522 • **Simulation :** The distributions for $m_{\ell b}$ and m_{T2} are produced at parton-level
 1523 with the three input top-quark masses m_t^{in} for all theoretical descriptions.
- 1524 • **Template calibration:** The template distributions produced in the first step are
 1525 individually fitted to the sum of a Gaussian and a Landau function. The theoretical
 1526 description used as a basis for the distribution is called the calibration set. In the
 1527 example of Fig. 7.10a, the calibration sets are described by the red/blue reference
 1528 points in the legend.
- 1529 • **Pseudo-data:** From the different theoretical descriptions, a subset of events is
 1530 drawn and labeled as *pseudo-data*. This sample corresponds to a luminosity of
 1531 50 fb^{-1} . In Fig. 7.10a, the theoretical description used for producing pseudo-data
 1532 is given at the top of the plot. In general, the pseudo-data set is drawn from the
 1533 more complete of the two predictions, which should be closer to real data. Pseudo-
 1534 experiments are performed by repeating the random drawing of the pseudo-data
 1535 1000 times from the subset of all events, for a given theory prediction.
- 1536 • **m_t extraction:** For each of the input top-quark masses m_t^{in} , an unbinned likeli-
 1537 hood fit is applied to the pseudo-data, using the corresponding calibration set, to
 1538 determine the extracted value of the top-quark mass m_t^{out} .

1539 The normalization of the histograms is chosen to reproduce the pseudo-data cross-
 1540 section in the fit range, so that the result of template fits only depend on differences in
 1541 the distribution shape. Looking again at Fig. 7.10a for reference, the red/blue points
 1542 indicate the offset of the extracted top-quark mass with respect to the MC input mass
 1543 $\Delta m_t^{\text{MC}} = m_t^{\text{out}} - m_t^{\text{in}}$. When using the calibration function generated from the same
 1544 theoretical prediction as used to produce the pseudo-data, the offset Δm_t should be close
 1545 to zero and serves as a cross-check that no systematic bias exists in the fitting procedure.
 1546 The error bars indicate the statistical uncertainty associated with the finite pseudo-data
 1547 sample. The results from the three mass points are then fitted to a constant, and the
 1548 numerical offset for Δm_t is given for each prediction in the legend, accompanied by its
 1549 statistical uncertainty. Finally, the systematic uncertainty bands are provided by fitting
 1550 the calibration set to the scale-varied pseudo-data.

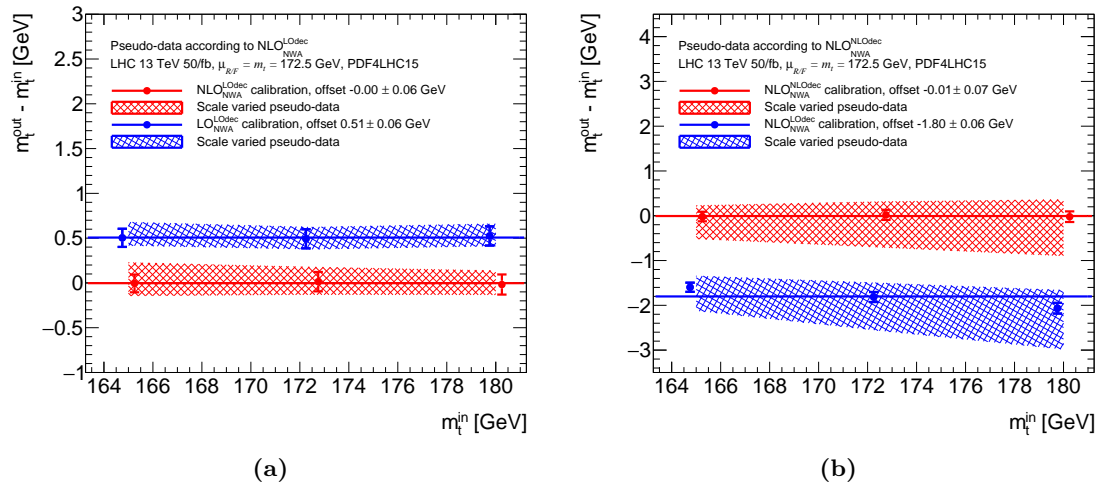


Figure 7.10: Pseudo-data is drawn according to (a) $\text{NLO}_{\text{NWA}}^{\text{LOdec}}$ and (b) $\text{NLO}_{\text{NWA}}^{\text{NLOdec}}$ for the three input top-quark masses, and the difference between the input mass and the template output is shown for each mass point. In each $m_{t\bar{b}}$ subplot, the calibration set from the same prediction (red) is used to show the absence of systematic bias in the template fit. The calibration set from (a) $\text{LO}_{\text{NWA}}^{\text{LOdec}}$ and (b) $\text{NLO}_{\text{NWA}}^{\text{LOdec}}$ yields an offset (blue) in the top-quark mass extracted from the theoretically more complete respective pseudo-data of (a) 0.51 GeV and (b) -1.80 GeV.

1551 Fig. 7.10a shows the offset between extracted and input top-quark masses when gen-
 1552 erating pseudo-data according to the $\text{NLO}_{\text{NWA}}^{\text{LOdec}}$ prediction, and using the calibration
 1553 function fitted from $\text{LO}_{\text{NWA}}^{\text{LOdec}}$ MC templates in blue. The offset in m_t produced by going
 1554 from LO to NLO in $t\bar{t}$ production amounts to 0.51 GeV. For comparison, Fig. 7.10b gives
 1555 the offset from fitting the $\text{NLO}_{\text{NWA}}^{\text{NLOdec}}$ pseudo-data with the $\text{NLO}_{\text{NWA}}^{\text{LOdec}}$ calibration func-
 1556 tion: higher-order corrections in the top-quark decay lead to a m_t -offset of -1.80 GeV.
 1557 Moreover, the NLO decay corrections in Fig. 7.10b lead to larger uncertainty bands, be-
 1558 cause the scale variations produce non-uniform shape differences. These results already

highlight the importance of higher-order corrections to the top-quark decay in a mass measurement based on $m_{\ell b}$.

Fig. 7.11 gives results for the extracted top-quark mass offsets when considering higher-order corrections in both production and decay, shown in Fig. 7.11a for the NWA case and in Fig. 7.11b for the full $W^+W^-b\bar{b}$ case. The factorization of production and decay in the NWA approximation yields an offset of -1.38 GeV, corresponding to the sum of the offsets in NLO production and decay shown in Fig. 7.10a, respectively Fig. 7.10b.

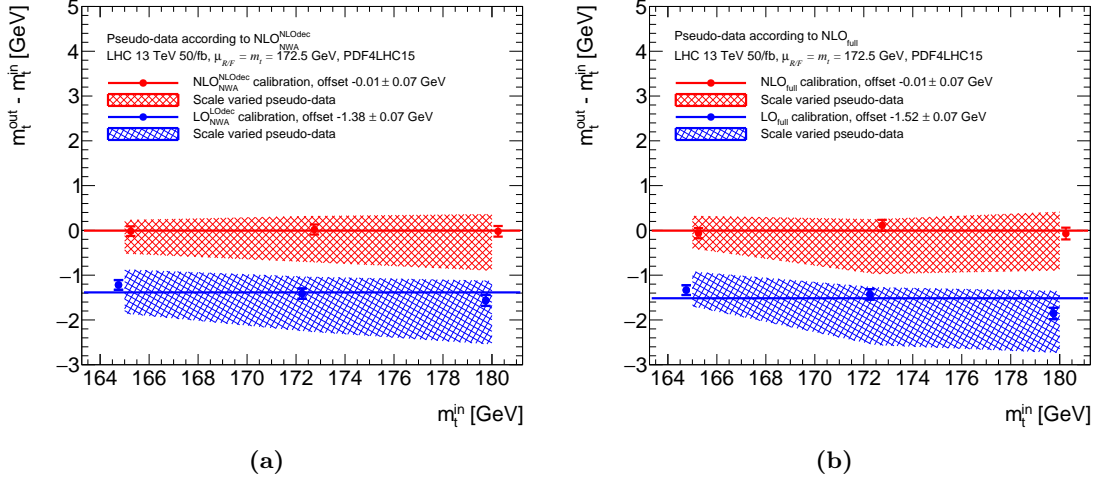


Figure 7.11: From fitting the $m_{\ell b}$ distribution, the offset for the extracted top-quark mass based on (a) $\text{NLO}_{\text{NWA}}^{\text{NLOdec}}$ and (b) $\text{NLO}_{\text{full}}^{\text{NLOdec}}$ pseudo-data underlines the effect of taking NLO contributions for production and decay into account.

Finally, the offsets in m_t produced when fitting the $\text{NLO}_{\text{full}}^{\text{NLOdec}}$ pseudo-data set with the calibration from the $\text{NLO}_{\text{NWA}}^{\text{NLOdec}}$ and the NLO_{PS} predictions are shown in Fig. 7.12a, respectively Fig. 7.12b. While $\text{NLO}_{\text{NWA}}^{\text{NLOdec}}$ still yields a sizeable offset of 0.83 GeV, the uncertainty bands now overlap. In the case of the NLO_{PS} calibration, the offset with respect to $\text{NLO}_{\text{full}}^{\text{NLOdec}}$ pseudo-data is compatible with zero within statistical uncertainties. Although the NLO_{PS} prediction does not describe the top-quark decay at NLO accuracy beyond the soft limit, it still largely reproduces the full $W^+W^-b\bar{b}$ description for the most part of the $m_{\ell b}$ fit range, as can be seen in Fig. 7.3. Further studies were performed to understand if the discrepancy between $\text{NLO}_{\text{NWA}}^{\text{NLOdec}}$ and NLO_{PS} originates in the parton-shower resummation. More details are given in Appendix A, where the parton-shower number of emissions in both the $t\bar{t}$ production and decay is gradually restricted, and offsets in m_t are compared to the $\text{NLO}_{\text{NWA}}^{\text{NLOdec}}$ prediction. Reducing the number of emissions to one in both production and decay showers moves the NLO_{PS} fitted m_t -value close to the $\text{NLO}_{\text{NWA}}^{\text{NLOdec}}$ prediction. It is the general softening of $m_{\ell b}$ around the kinematic edge, originating in the successive emissions from the parton-shower, that drives the top-quark mass fitted from the NLO_{PS} prediction towards the NLO_{full} value.

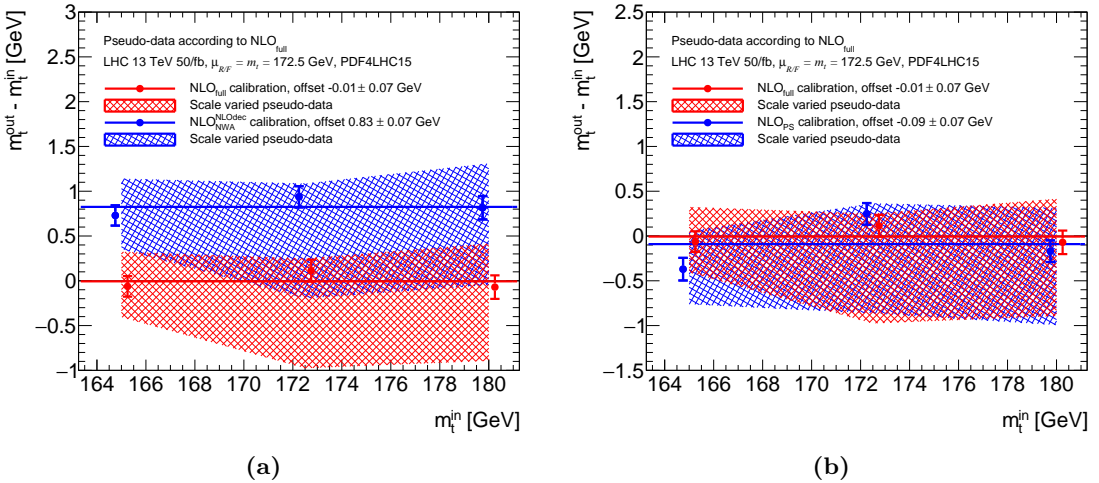


Figure 7.12: Top-quark mass offsets from m_{tb} for pseudo-data generated from the NLO_{full} prediction are reduced when considering the case of (a) NLO_{NWA}^{NLOdec} and (b) NLO_{PS} calibration functions.

Similar results are also shown for the m_{T2} distribution in Appendix A. The numerical offsets for all comparisons are summarized in Table 7.1, together with a combined χ^2 computed from both $m_{\ell b}$ and m_{T2} offsets for the same theoretical predictions. The value of χ^2 is defined as $\chi^2 = (o_1 - o_2)^2 / (u_1^2 + u_2^2)$, with $i = 1, 2 = m_{\ell b}, m_{T2}$ and $o_i \pm u_i$ are the corresponding offsets and their (uncorrelated) uncertainties. While almost all χ^2 values are consistent with zero, the comparison between $\text{NLO}_{\text{NWA}}^{\text{NLOdec}}$ and NLO_{PS} differs significantly: the m_{T2} estimator for the top-quark mass is simply less sensitive to differences between the two latter predictions.

In conclusion, while NWA predictions are not disallowed, this study shows that higher-order corrections to the top-quark decays are at least as important as corrections to $t\bar{t}$ production. The comparisons presented above suffer from a few shortcomings: in particular, further showering and hadronization effects, as well as detector efficiencies are expected to partly wash out the differences observed in the extracted top-quark mass. This is the subject of Chapter 9, which treats the topic in an even closer experimental setup with the help of a folding procedure in the ATLAS framework.

Pseudo-data	Calibration	Offset [GeV]		Figure		χ^2
		$m_{\ell b}$	m_{T2}	$m_{\ell b}$	m_{T2}	
NLO _{NWA} ^{LOdec}	LO _{NWA} ^{LOdec}	+0.51 ± 0.06	+0.48 ± 0.04	7.10a	A.4a	0.17
NLO _{NWA} ^{NLOdec}	NLO _{NWA} ^{LOdec}	-1.80 ± 0.06	-1.67 ± 0.04	7.10b	A.4b	3.25
NLO _{NWA} ^{NLOdec}	LO _{NWA} ^{LOdec}	-1.38 ± 0.07	-1.24 ± 0.05	7.11a	A.4c	2.65
NLOfull	LOfull	-1.52 ± 0.07	-1.62 ± 0.05	7.11b	A.4d	1.35
NLOfull	NLO _{NWA} ^{NLOdec}	+0.83 ± 0.07	+0.60 ± 0.06	7.12a	A.4e	6.22
NLOfull	NLO _{PS}	-0.09 ± 0.07	-0.07 ± 0.06	7.12b	A.4f	0.05
NLO _{PS}	NLO _{NWA} ^{LOdec}	-0.92 ± 0.07	-1.17 ± 0.05	A.3a	A.4g	8.45
NLO _{PS}	NLO _{NWA} ^{NLOdec}	+0.96 ± 0.07	+0.68 ± 0.05	A.3b	A.4h	10.59
NLO _{PS}	NLO _{PS} (μ_{tt})	-0.03 ± 0.07	+0.02 ± 0.05	A.5b	A.5d	0.34

Table 7.1: The offsets from the top-quark mass extraction are given in GeV for pairs of the considered theoretical descriptions, from which the pseudo-data is generated, respectively the calibration function produced. The results are given for both the $m_{\ell b}$ and m_{T2} distributions, along with the corresponding plot references (see also Appendix A). A χ^2 value is computed between offsets procured from fits of $m_{\ell b}$ and m_{T2} .

¹⁵⁹⁷ 8 Experimental resolution and bin migration¹⁵⁹⁸

¹⁵⁹⁹ In the following chapter, the results outlined in Chapter 7 are reproduced with full
¹⁶⁰⁰ particle-level predictions and the NLO_{full} calculation is compared to $t\bar{t}$ results in the
¹⁶⁰¹ ATLAS Athena framework at detector-level. To study the extracted values of the top-
¹⁶⁰² quark mass from reconstructed events in a fast-simulation style, all distributions are
¹⁶⁰³ folded from particle-level to detector-level in a custom implementation. Top-quark mass
¹⁶⁰⁴ determinations focus entirely on the dilepton channel in this chapter, but the folding
¹⁶⁰⁵ setup can be used in all decay channels.

¹⁶⁰⁶ 8.1 Inverse problems

¹⁶⁰⁷ Usually, to compare experimentally measured cross-sections to a theoretical prediction,
¹⁶⁰⁸ background contributions are first subtracted from data, and the corresponding signal
¹⁶⁰⁹ distributions are unfolded to particle-level so that available measurements can be di-
¹⁶¹⁰ rectly compared by theorists to their own predictions. The unfolding procedure is a
¹⁶¹¹ particular example of so-called inverse problems: having a true distribution $f(x)$ for
¹⁶¹² some observable Ω , $x \in [\Omega_{\min}, \Omega_{\max}]$, the measured distribution $g(y)$ is given by the
¹⁶¹³ Fredholm integral equation:

$$g(y) = \int_{\Omega_{\min}}^{\Omega_{\max}} K(x, y)f(x)dx, \quad (8.1)$$

¹⁶¹⁴ where the kernel $K(x, y)$ is a continuous function. For binned results, discretizing
¹⁶¹⁵ Eq. (8.1) gives a linear equation for \mathbf{x} , \mathbf{y} the n -, respectively m -bin histograms corre-
¹⁶¹⁶ sponding to the true, respectively the measured distribution:

$$y_j = \sum_{i=1}^n A_{ij}x_i, \quad j \in \{1, \dots, m\}, \quad (8.2)$$

¹⁶¹⁷ where \mathbf{A} is the bin migration matrix. The problem of inverting Eq. (8.2), that is to
¹⁶¹⁸ uncover the true distribution \mathbf{x} of an observable Ω from the measured signal distribution
¹⁶¹⁹ \mathbf{y} , is the foundation of unfolding procedures. Because noise in the measured function
¹⁶²⁰ can lead to instabilities in the inversion of the response matrix \mathbf{A} , the procedure has
¹⁶²¹ to be regularized. There are two distinct unfolding methods: direct unfolding proce-
¹⁶²² dures, which usually implement some regularization parameter for a smooth inversion
¹⁶²³ of Eq. (8.2), and iterative methods. For a short review of unfolding methods in particle
¹⁶²⁴ physics, see Ref. [231].

Conversely, instead of unfolding the data to particle-level, the chosen strategy for the 13 TeV ATLAS top-quark mass analysis in both lepton+jets and dilepton channels is to produce the distribution templates and perform the likelihood fit only at detector-level, for several reasons. In particular, the top-quark mass extraction in the lepton+jets channel suffers mostly from jet and b -jet energy scale uncertainties (see Section 5.2.4). To try and reduce the latter, the lepton+jets analysis contains a 3D-fit where the template parametrization depends on the top-quark mass m_t and both the jet and b -jet energy scale factors (JSF and b -JSF). All three parameters are then simultaneously measured from a fit to data. It is therefore simpler to simulate all samples up to detector-level, and directly perform the fit of all three parameters without having to handle a 3D-unfolding. This procedure also avoids numerical instabilities inherent to the chosen unfolding algorithm. The main disadvantage of the direct method lies in the computing time: indeed, all MC samples (m_t -varied central predictions, systematics-varied samples, and background) have to be simulated up to detector-level. Instead, a complementary alternative is proposed with the use of direct folding, as in Eq. (8.2), to provide distributions at detector-level from the samples generated at particle-level. Thus, the costly ATLAS simulation is avoided and one can quickly quantify effects of systematic uncertainties on e.g. the extracted top-quark mass.

8.2 Folding setup in ATLAS

Considering the results of Chapter 7, the goal is to use the folding setup in ATLAS to estimate the uncertainty in using the incomplete $t\bar{t}$ prediction instead of a full parton-showered $W^+W^-b\bar{b}$ event set. It is clear that simulating all MC samples from particle-to detector-level is time-consuming: with one theoretical central prediction (for example POWHEG + Pythia8) and one parameter for the template fit (e.g. the top-quark mass m_t), one has to produce and simulate as many samples as top-quark mass points.

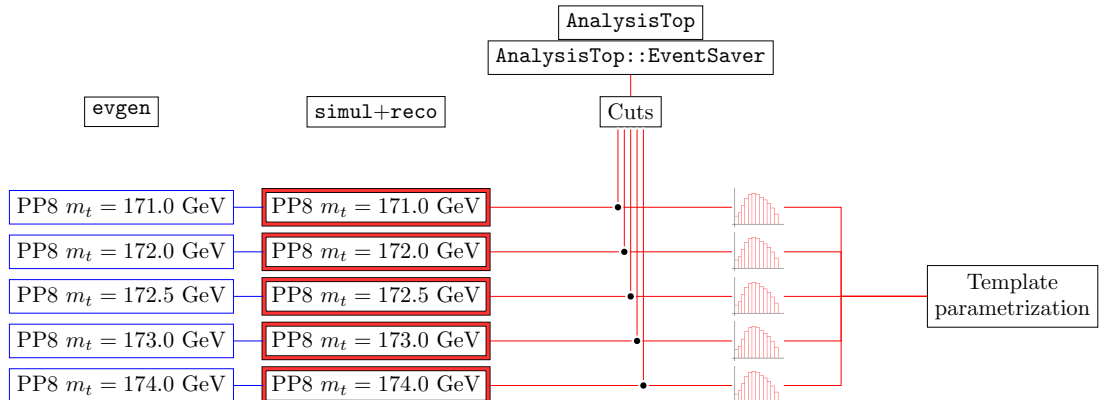


Figure 8.1: The workflow for a template fit of the central prediction POWHEG+Pythia8 (PP8) and five top-quark mass points.

Fig. 8.1 illustrates the current analysis workflow for five top-quark mass points. Each of the samples is produced at particle-level first (`evgen` in blue on the far left) and has to be simulated (`simul+reco` in red). In the ATLAS 13 TeV analysis, all samples entering the template fit parametrization are fast-simulated with the ATLFAST [162] package. A custom event saver from the `AnalysisTop` package applies the cuts outlined in Section 8.4 and saves histograms for control purposes, as well as the final observables entering the top-quark mass fit. Histograms of the $m_{\ell b}$ distribution for all individual mass points are then fed to the template parametrization.

To estimate systematic uncertainties, MC variation samples currently go through the same routine. For example, MC samples with variations of radiative parameters (e.g. `hdamp` in POWHEG, or `Pythia8` versus `Herwig7` for the shower algorithm) are also simulated and parametrized, and the result of the template fit is taken as a systematic uncertainty on the central sample for the extracted top-quark mass. For a swifter evaluation of the associated systematics, histograms of variation samples (e.g. `hdamp_var` and `shower_var`, or $W^+W^-b\bar{b}$) are directly folded from particle- to detector-level, and the output in the template fit is used for an estimate of the systematic uncertainty on the extracted top-quark mass.

A simple version of Eq. (8.2) is introduced, where pure bin migration is implemented by a right stochastic matrix \mathbf{A} , and the detector efficiencies are represented by two bin-by-bin probability vectors ϵ^{eff} and f^{acc} :

$$\mathcal{R}_i = \frac{1}{f_i^{\text{acc}}} A_{ij} \times \left(\mathcal{P}_j \epsilon_j^{\text{eff}} \right), \quad (8.3)$$

where \mathcal{R}_i is the number of events at detector-level in bin i (for an arbitrary differential distribution), and \mathcal{P}_j is the number of events at particle-level in bin j . The migration matrix A_{ij} is the probability for an event in bin j at particle-level to move to bin i at detector-level, provided the event is reconstructed. Finally, the efficiency ϵ_j^{eff} is the probability for an event in bin j at particle-level to be reconstructed in the detector, and f_i^{acc} the probability of an event in bin i at detector-level to stem from a fake signal (i.e. it has no existing counterpart at particle-level). The migration matrices and detector efficiencies only encode the experimental resolution simulated by ATLFAST.

This alternative procedure is depicted in Fig. 8.2. The central POWHEG+`Pythia8` (PP8) sample is simulated once: histograms at both detector-level (in red) and particle-level (in blue) are fed to the custom folding package (green nodes). The `build.py` script produces the migration matrices and detector efficiencies defined above. In principle, for a given top-quark mass, pure theoretical uncertainties can then be estimated by applying the migration matrices and efficiencies from the central sample to variation samples, since detector effects do not depend on the MC theory variations themselves. The `upfold.py` script implements Eq. (8.3) and generates folded detector-level histograms from the particle-level of MC-varied samples, and writes them out for future use in the template fit. Moreover, consistency and statistical cross-checks are performed by a `tests.py` script. Now, in addition to the usual systematic variations, an estimate is computed for the uncertainty stemming from the non-resonant and non-factorizing diagrams in the full $W^+W^-b\bar{b}$ calculation.

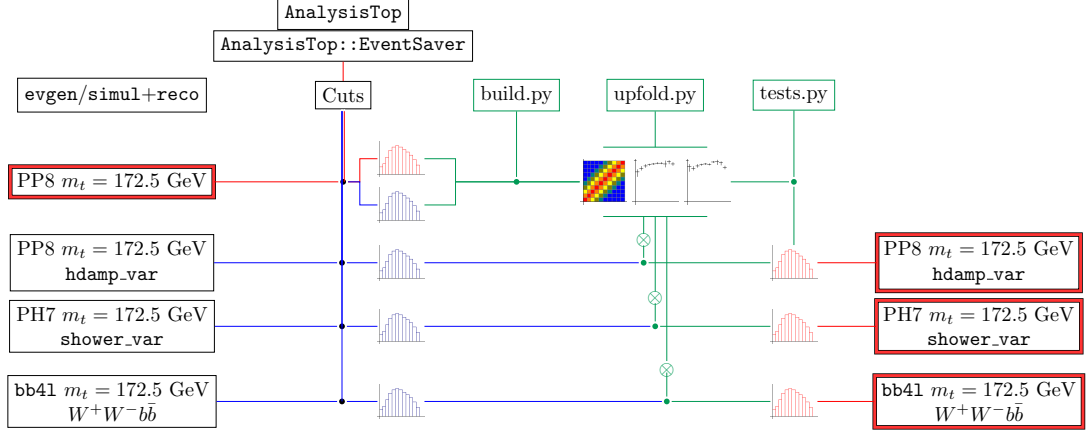


Figure 8.2: The folding package builds migration matrices and efficiency histograms from the simulated detector- and the particle-level of a central sample, for example Powheg + Pythia8 with $m_t = 172.5$ GeV. They are used to fold particle-level histograms from MC-varied samples to detector-level.

1691 8.3 Theoretical descriptions and MC samples

1692 The MC derivation samples (DxAOD) used for all subsequent studies were produced
 1693 officially by ATLAS during the MC16a campaign (optimized to describe the 2015/2016
 1694 data) and are summarized in Table 8.1. The nominal samples for NLO $t\bar{t}$ in the NWA
 1695 are generated by Powheg (for the matrix-element) and parton-showered with Pythia8
 1696 for five different mass points.¹ These samples are simulated to detector-level with the
 1697 ATLFAST algorithm, but a cross-check is done with respect to the full GEANT4 simulation
 1698 for one mass point. To be able to have a fairer comparison of the full $W^+W^-b\bar{b}$ prediction
 1699 to the $t\bar{t}$ NWA description, the single-top Wt channel (with diagram-removal) is added
 1700 to the $t\bar{t}$ sample. Finally, in order to generate $W^+W^-b\bar{b}$ predictions at particle-level,
 1701 the following setup is used:

- 1702 • **Parton-level production:** The full dilepton final-state $(e^+\nu_e)(\mu^-\bar{\nu}_\mu)b\bar{b}$ events
 1703 are produced at parton-level with a local installation of the bb4l generator in
 1704 Powheg-BOX-RES. They are generated outside of Athena since the implemen-
 1705 tation of the bb4l program has not been validated yet. LHE files are written out
 1706 by Powheg for later showering.
- 1707 • **Particle-level production:** The Herwig7.1.3 parton-shower is applied in Athena
 1708 to the parton-level events produced with bb4l. Hadronization is also handled in
 1709 Herwig by the cluster model.
- 1710 • **Analysis pre-step:** The Athena MC simulation step produces a so-called event
 1711 (EVNT) file containing the particle information and kinematics. To be able to run

¹Samples with nine top-quark mass points were officially produced, but only the same mass points as for $W^+W^-b\bar{b}$ samples are used in this study.

8.3 Theoretical descriptions and MC samples

Sample DSID	Generator (ME + PS/Had)	m_t [GeV]	Simulation tags
NLO $t\bar{t}$ (NWA)			
411053	POWHEG+Pythia8	171	e6696_a875_r9364_p3629
411054	POWHEG+Pythia8	172	e6696_a875_r9364_p3629
410472	POWHEG+Pythia8	172.5	e6348_a875_r9364_p3629
411057	POWHEG+Pythia8	173	e6696_a875_r9364_p3629
411058	POWHEG+Pythia8	174	e6696_a875_r9364_p3629
NLO $W^+W^-b\bar{b}$			
999991	bb4l+Herwig7	171	—
999992	bb4l+Herwig7	172	—
999995	bb4l+Herwig7	172.5	—
999993	bb4l+Herwig7	173	—
999994	bb4l+Herwig7	174	—
NLO single-top W^-t (DR)			
411109	POWHEG+Pythia8	171	e6852_a875_r9364_p3629
411111	POWHEG+Pythia8	172	e6852_a875_r9364_p3629
410646	POWHEG+Pythia8	172.5	e6552_a875_r9364_p3629
411117	POWHEG+Pythia8	173	e6852_a875_r9364_p3629
411119	POWHEG+Pythia8	174	e6852_a875_r9364_p3629
NLO single-top $W^+\bar{t}$ (DR)			
411110	POWHEG+Pythia8	171	e6852_a875_r9364_p3629
411112	POWHEG+Pythia8	172	e6852_a875_r9364_p3629
410647	POWHEG+Pythia8	172.5	e6552_a875_r9364_p3629
411118	POWHEG+Pythia8	173	e6852_a875_r9364_p3629
411120	POWHEG+Pythia8	174	e6852_a875_r9364_p3629
$t\bar{t}$ variation samples			
410472	POWHEG+Pythia8	172.5	e6348_s3126_r9364_p3629
410482	POWHEG+Pythia8 $h_{\text{damp}}^{\text{up}}$	172.5	e6454_a875_r9364_p3629
410558	POWHEG+Herwig7.0.4	172.5	e6366_a875_r9364_p3629

Table 8.1: Summary of the MC derivations used as input to the top-quark mass analysis.

the `AnalysisTop` routine on the sample, one needs to transform it to a DxAOD derivation format. The truth information is propagated to the derivation-level by running the `Reco_tf.py` script in `Athena` with `Truth1` level, which means the derivation output basically contains thinned MC truth information.

For first studies, predictions for five mass points are generated both for the $t\bar{t}$ NWA and the $W^+W^-b\bar{b}$ configurations (as well as for single-top Wt samples):

$$m_t \in \{171, 172, 172.5, 173, 174\} \text{ [GeV]} . \quad (8.4)$$

1718 8.4 The AnalysisTop setup

1719 In the Athena framework, the `AnalysisTop` package contains all the ingredients that are
 1720 useful for general top-quark measurements. It is regularly updated with respect to latest
 1721 calibration methods and numerical results, and serves as an interface between detector
 1722 quantities and the final derivations. In this case, except when explicitly stated otherwise,
 1723 the version used is `AnalysisTop 21.2.61`. Within the latter, some slightly modified
 1724 version of the `TopMass_13TeV_FrMu` ATLAS analysis at 13 TeV is set up. As mentioned
 1725 earlier, the code executes both lepton+jets and dilepton routines simultaneously. The
 1726 various MC samples were presented above, and the following cuts are applied:

- 1727 • Two oppositely charged leptons with exactly one electron and one muon which fulfill $p_T^\ell > 28$ GeV. For reconstructed events, the lepton criteria for passing the trigger requirements are taken from the Top Trigger Group recommendation. These depend on the luminosity and are different for 2015 and 2016 data. They are set to:

```
1732 HLT_e24_lhmedium_L1EM20VH HLT_e60_lhmedium HLT_e120_lhloose
1733 HLT_mu20_iloose_L1MU15 HLT_mu50
```

1734 for the 2015 data, respectively for the 2016 data:

```
1735 HLT_e26_lhtight_nod0_ivarloose HLT_e60_lhmedium_nod0
1736 HLT_e140_lhloose_nod0 HLT_mu26_ivarmedium HLT_mu50 .
```

1737 The reader is referred back to Section 5.2.4 for definitions of the trigger cuts and
 1738 reconstruction algorithms.

- 1739 • $H_T = \sum_i p_{T,i} > 120$ GeV with H_T the event's total transverse momentum.
- 1740 • $n_{\text{jets}} \geq 2$ for the total number of jets with $p_T^{\text{jet}} > 25$ GeV.
- 1741 • exactly two b -jets, $n_{b,\text{jets}} = 2$ with $p_T^{\text{jet}} > 25$ GeV. For reconstructed events, a 70%
 1742 b -tagging working point is chosen for the MV2c10 [232, 233] b -tagging algorithm.
 1743 A b -jet is defined within particle-level events using the `JET_N_GHOST` criterion in
 1744 `AnalysisTop`, for which a jet is b -tagged if it contains a B -hadron.
- 1745 • $m_{\ell\ell} > 15$ GeV for the invariant mass of the two-lepton system.

9 Determination of the top-quark mass at detector-level

The simulated $t\bar{t}$ NWA predictions are compared at particle- and detector-level for control distributions, as well as for the $m_{\ell b}$ histogram which enters the template fit for the top-quark mass determination. Migration matrices and detector efficiencies derived from those samples are also plotted. After some simple cross-checks of the setup, the $W^+W^-b\bar{b}$ folded results and template parametrization are presented, along with numerical comparisons of both theoretical descriptions for the extraction of the top-quark mass. All results shown here are preliminary and should be taken with a grain of salt.

9.1 Differential results at particle- and detector-level

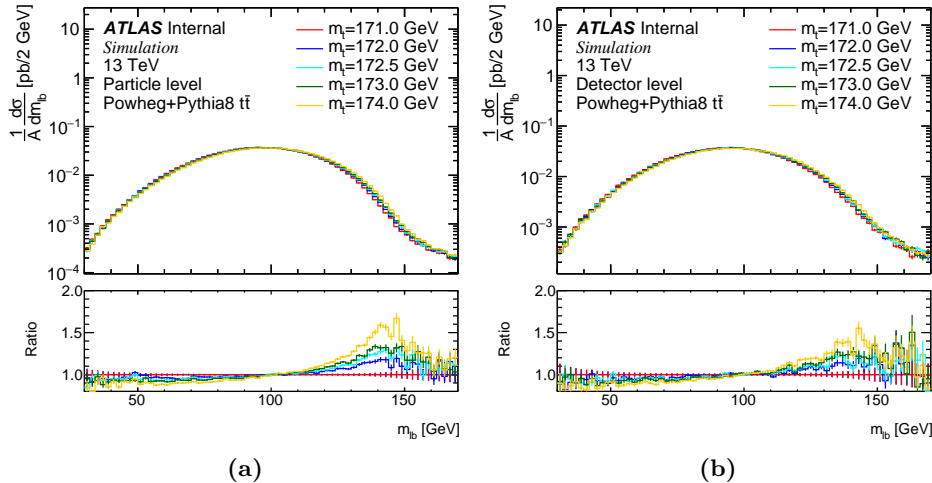


Figure 9.1: The normalized $m_{\ell b}$ distribution from the PP8 $t\bar{t}$ NWA predictions is shown for five top-quark mass points at (a) particle-level and (b) detector-level.

In Fig. 9.1, distributions of the $m_{\ell b}$ observable are shown for the five different MC top-quark mass points generated from the $t\bar{t}$ NWA predictions produced by POWHEG matched to Pythia8 (PP8). In all plots, the distributions are arbitrarily normalized since, as in Chapter 7, only shape differences matter in the template fit. In this case, the distributions are normalized so that their integral in the plot range $m_{\ell b} \in [30 \text{ GeV}, 170 \text{ GeV}]$ equals one. The ratio is shown to the prediction with the

9 Determination of the top-quark mass at detector-level

central top-quark mass, and error bars indicate MC statistical uncertainties. The predictions are shown at particle-level in Fig. 9.1a and at detector-level in Fig. 9.1b. Already, the sensitivity to the input top-quark mass decreases visibly when comparing the particle- and detector-levels. Fig. 9.2a gives the particle-level $m_{\ell b}$ distribution for the full $W^+W^-b\bar{b}$ prediction at NLO QCD, again as a function of the five input top-quark masses, while Fig. 9.2b shows differences between both $t\bar{t}$ and $W^+W^-b\bar{b}$ computations for an input top-quark mass of $m_t = 172.5$ GeV. In general, the $m_{\ell b}$ distribution from the $W^+W^-b\bar{b}$ sample is shifted towards smaller top-quark masses, as was the case in Chapter 7.

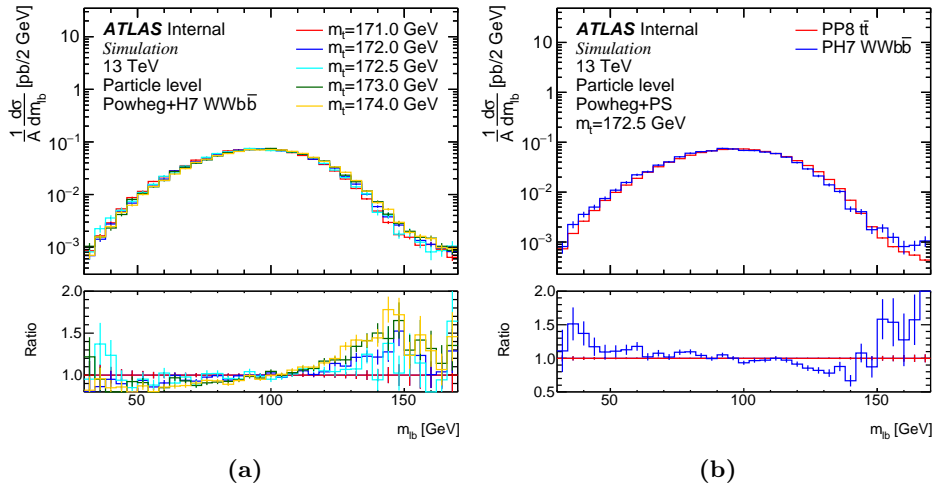


Figure 9.2: The normalized $m_{\ell b}$ distribution is given for the generated $W^+W^-b\bar{b}$ events with (a) the five different input top-quark masses and (b) for $m_t = 172.5$ GeV and compared to $t\bar{t}$ at the same mass point.

Now, as stated above, the $W^+W^-b\bar{b}$ predictions are to be folded from particle- to detector-level using the $t\bar{t}$ migration matrices. Before jumping to the final results, a few control observables are used to reconstruct the migration matrices and efficiencies. Histograms are pictured at particle- and detector-level for the $t\bar{t}$ sample at $m_t = 172.5$ GeV. In Fig. 9.3a, the distribution of the angular separation between both leptons $\Delta R_{\ell\ell}$ is shown. The total number of events simply corresponds to the full MC sample. The migration matrix \mathbf{A}_{ij} is pictured in Fig. 9.3b. For distributions relying on well-reconstructed objects, like $\Delta R_{\ell\ell}$, the migration matrix is extremely diagonal. The efficiency ϵ^{eff} and fake rate f^{acc} are displayed in Fig. 9.3c and Fig. 9.3d, respectively. The overall efficiency is small with an average of $\sim 26\%$ coming from the reconstruction trigger cuts at detector-level, which do not exist at particle-level.

9.1 Differential results at particle- and detector-level

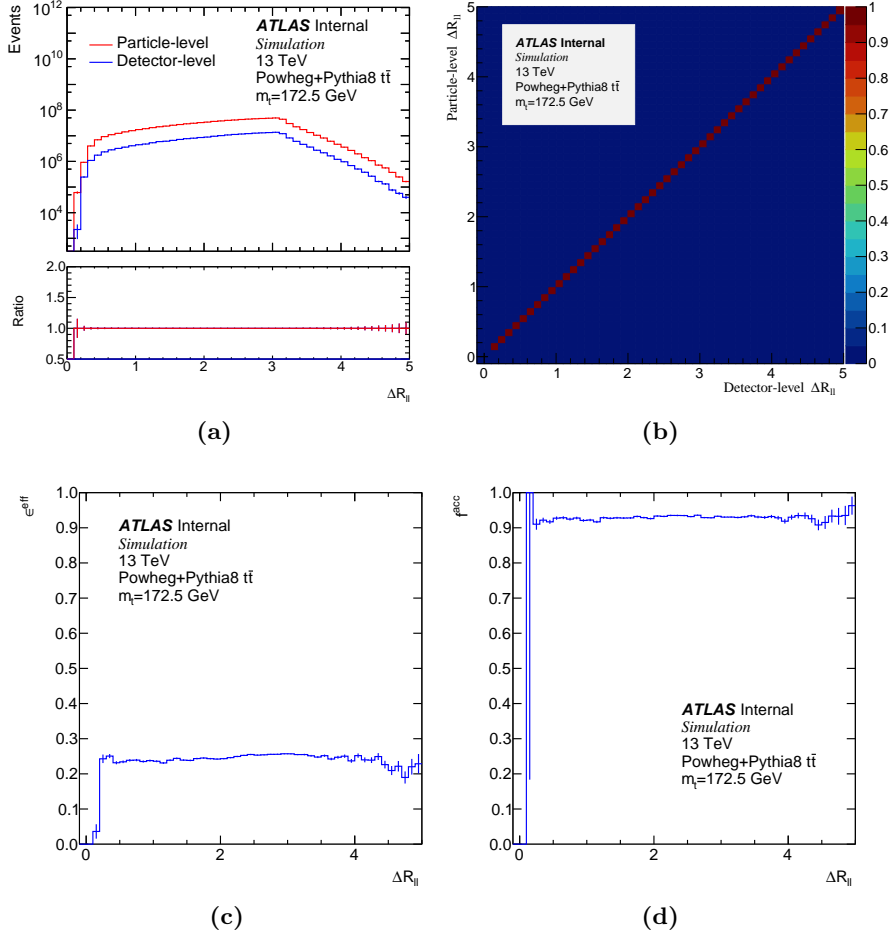


Figure 9.3: The angular separation between both leptons $\Delta R_{\ell\ell}$ for the PP8 $t\bar{t}$ sample at $m_t = 172.5$ GeV. (a) Differential distributions at particle- and detector-level, (b) migration matrix \mathbf{A}_{ij} , (c) efficiency ϵ^{eff} and (d) fake rate f^{acc} as defined in Eq. (8.3).

9 Determination of the top-quark mass at detector-level

Switching to jets, which are generally less well-behaved objects under reconstruction, Fig. 9.4 gives histograms and migration ingredients for the number of jets n_{jets} . Already there is some migration to the next bins (and next-to-next bins for higher jet multiplicities). While for $\Delta R_{\ell\ell}$, both the efficiency and the fake rate were almost constant, Fig. 9.4d underlines some bin-dependence of the fake rate for the number of reconstructed jets.

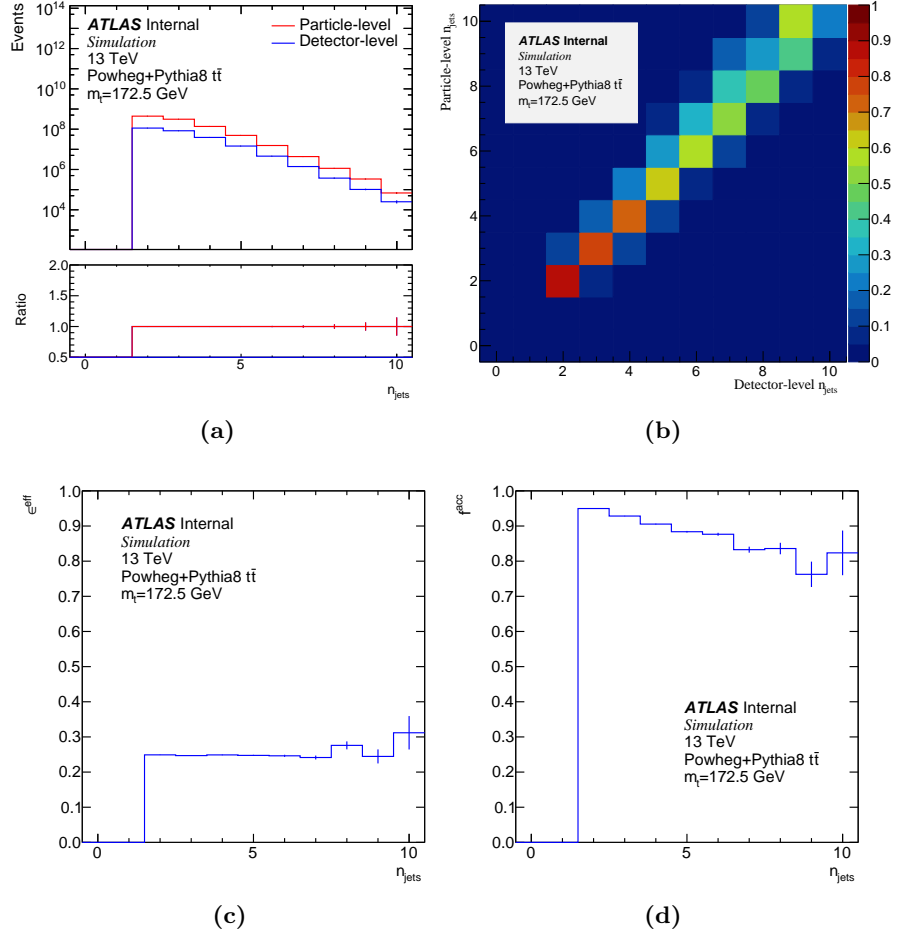


Figure 9.4: The number of jets n_{jets} for the PP8 $t\bar{t}$ sample at $m_t = 172.5 \text{ GeV}$. (a) Differential distributions at particle- and detector-level, (b) migration matrix \mathbf{A}_{ij} , (c) efficiency ϵ_{eff} and (d) fake rate f_{acc} as defined in Eq. (8.3).

Finally, for the $m_{\ell b}$ distribution, the same quantities are shown in Fig. 9.5. Here, the migration ingredients were rebinned for better visibility. Correct reconstruction is harder, and mostly depends on the pairing of the lepton- and b -jet systems, which might not be the same at particle- than at detector-level. The efficiency is highest below the kinematic edge, which corresponds to well-separated, on-shell top-quark pairs.

9.1 Differential results at particle- and detector-level

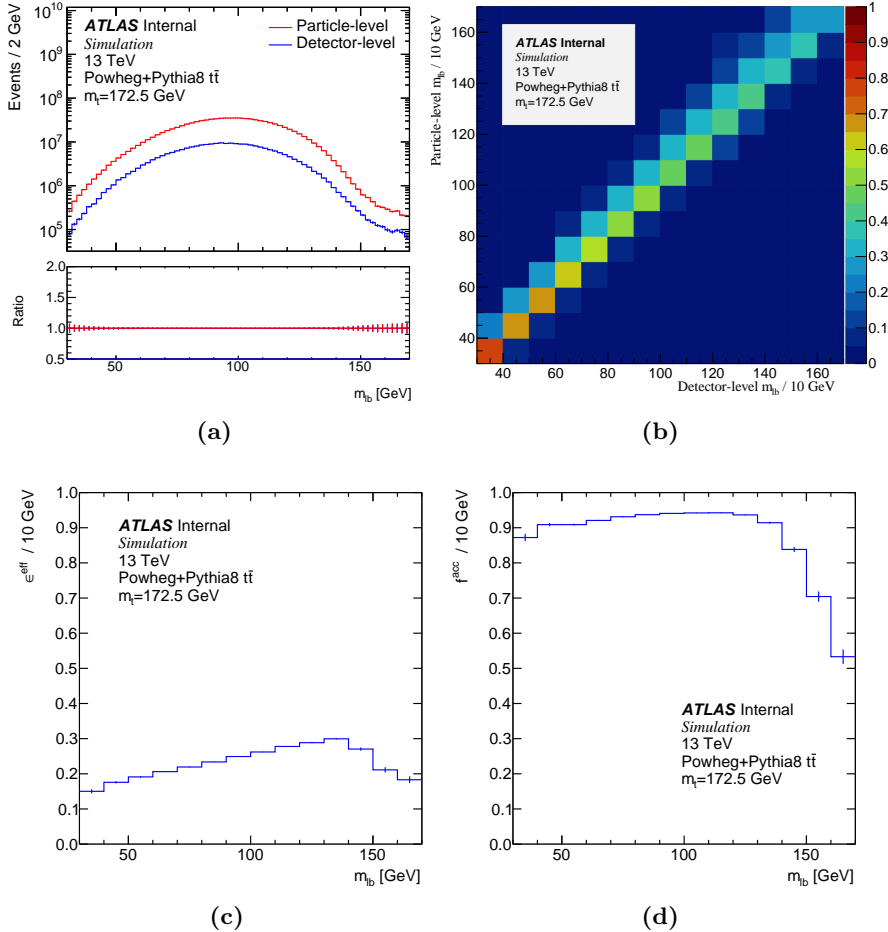
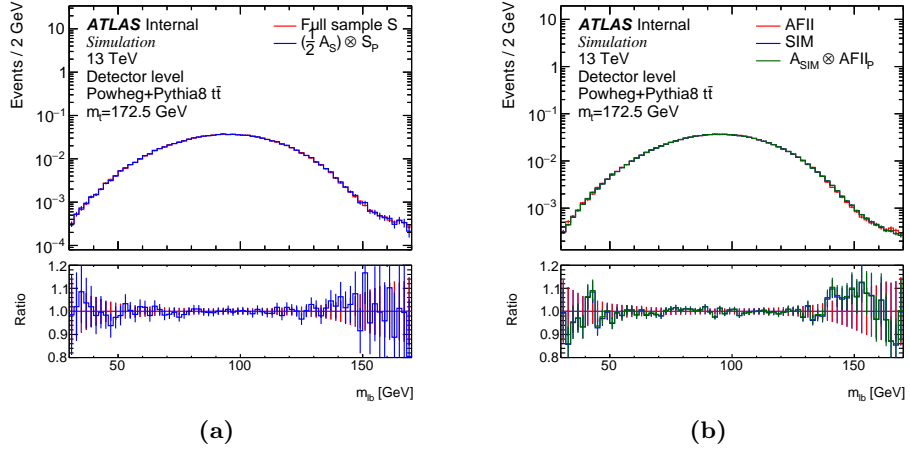


Figure 9.5: The lepton- b -jet invariant mass m_{lb} for the PP8 $t\bar{t}$ sample at $m_t = 172.5$ GeV. (a) Differential distributions at particle- and detector-level, (b) migration matrix \mathbf{A}_{ij} , (c) efficiency ϵ^{eff} and (d) fake rate f^{acc} as defined in Eq. (8.3).

1793 9.2 Statistical and systematic cross-checks

1794 To ensure that statistical uncertainties are propagated correctly from particle-level to
 1795 detector-level during the folding procedure, only half of the sample for the $t\bar{t}$ prediction
 1796 at $m_t = 172.5$ GeV is used to derive migration matrices and efficiencies. The fold-
 1797 ing ingredients from this reduced sample, called symbolically $\frac{1}{2}A_S$, are then applied
 1798 to the particle-level sample S_P with full statistics. The $m_{\ell b}$ distribution obtained at
 1799 detector-level (folded from the subset sample) is compared to the simulated detector-
 1800 level distribution with full statistics S in Fig. 9.6a. The differences between both are
 1801 covered by the statistical uncertainties with no significant bias. In Fig. 9.6b, the $m_{\ell b}$
 1802 distribution is compared at detector-level for both the GEANT4 (SIM) and the ATLFast
 1803 (AFII) algorithms. Although some structure in the distribution tail seems to indicate a
 1804 softer spectrum for ATLFast than for the full simulation, both distributions still agree
 1805 within statistical uncertainties.



1806 **Figure 9.6:** Migration ingredients from one sample are used to fold another sample's particle-
 1807 level $m_{\ell b}$ distribution for statistical and systematic cross-checks. (a) A statistical
 1808 subset is used to derive migration ingredients $\frac{1}{2}A_S$ and fold the full sample S_P . (b)
 1809 Same for the GEANT4 (SIM) and ATLFast (AFII) simulated samples.

1810 In the following, migration ingredients are consistently chosen to use the same input
 1811 top-quark mass as the sample to be folded. Still, the input top-quark mass does not
 1812 produce any systematic bias in the folded distributions: in Fig. 9.7a, the migration ingre-
 1813 dients from the $m_t = 174$ GeV sample are used to fold the $m_t = 171$ GeV prediction to
 1814 detector-level. The folded and simulated distributions for $m_t = 171$ GeV agree perfectly.
 1815 The same should be true of any theoretical MC variation. Usually, the h_{damp} parameter
 1816 in POWHEG, which regulates the amount of hard radiation, is taken as such a variation.
 1817 The central value is chosen as equal to the top-quark mass, $h_{\text{damp}} = m_t =: h_1$. The
 1818 variation sample uses $h_{\text{damp}} = 2m_t =: h_2$. Folding the varied sample at particle-level
 1819 $h_{2,P}$ with the migration ingredients A_{h_1} from the central sample leads to good agree-
 1820 ment at detector-level, as shown in Fig. 9.7b. Finally, a comparison is made between

9.2 Statistical and systematic cross-checks

both Pythia8 and Herwig7 parton-showers at particle-level in Fig. 9.8a. The fact that Pythia8 produces harder radiation than Herwig7 is well-known (see Chapter 11 for the case of Higgs pair production). The effect on the top-quark mass was investigated in the POWHEG-BOX-RES framework recently [234], where offsets in the position of the peak of the W - b -jet system of up to 1 GeV were underlined. In the dilepton case, the parton-shower differences do lead to important offsets at particle-level. Once detector effects are taken into account, though, the discrepancy is much less pronounced, as shown in Fig. 9.8b.

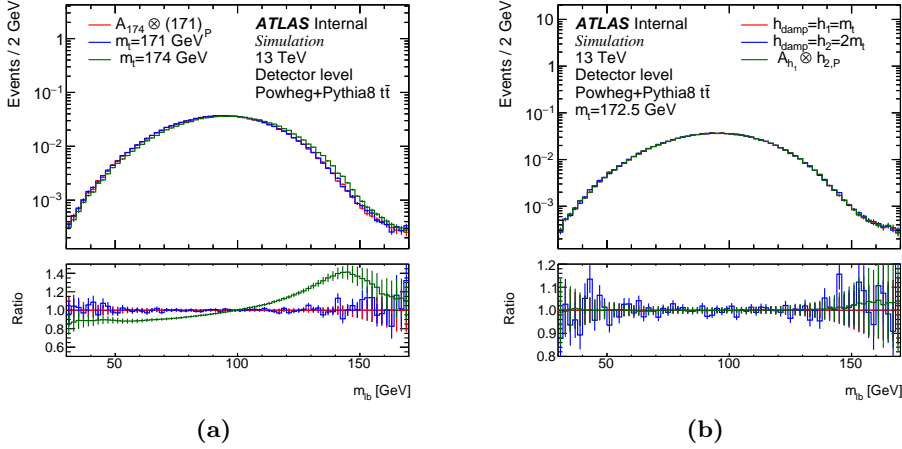


Figure 9.7: (a) Same as Fig. 9.6 for the $m_t = 174$ GeV sample folding of the $m_t = 171$ GeV prediction, and (b) for the central and varied values of the h_{damp} parameter.

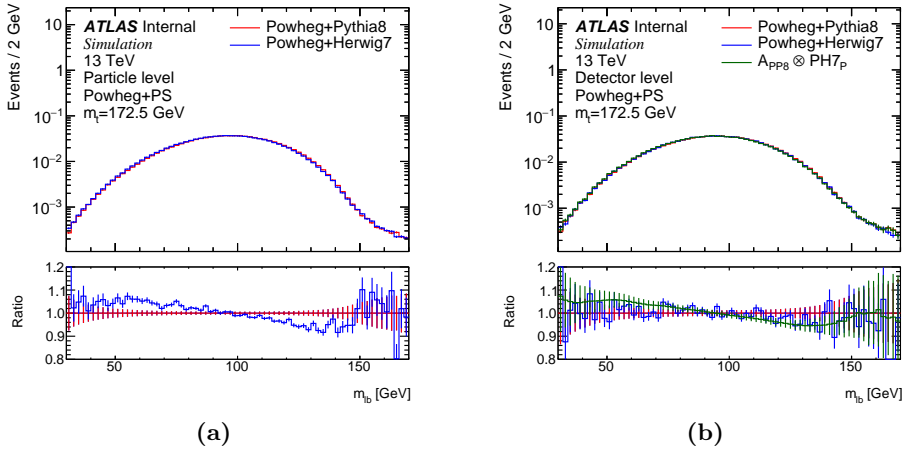


Figure 9.8: (a) The Pythia8 (PP8) and Herwig7 (PH7) parton>Showered samples are compared at particle-level for a fixed top-quark mass $m_t = 172.5$ GeV. (b) Same as Fig. 9.6 for the PP8 and PH7 samples.

1825 9.3 Folded results and template parametrization

1826 In Fig. 9.9a, the normalized $m_{\ell b}$ distribution is shown for the signal ($t\bar{t}$ and single-top
 1827 in the Wt channel) and the $W^+W^-b\bar{b}$ prediction at particle-level for an input top-quark
 1828 mass $m_t = 172.5$ GeV. The migration ingredients \mathbf{A}_{ij} , ϵ^{eff} and f^{acc} from the central
 1829 $t\bar{t}$ sample are used to fold the $W^+W^-b\bar{b}$ prediction generated with `bb4l`. The same
 1830 samples are then compared at detector-level in Fig. 9.9.

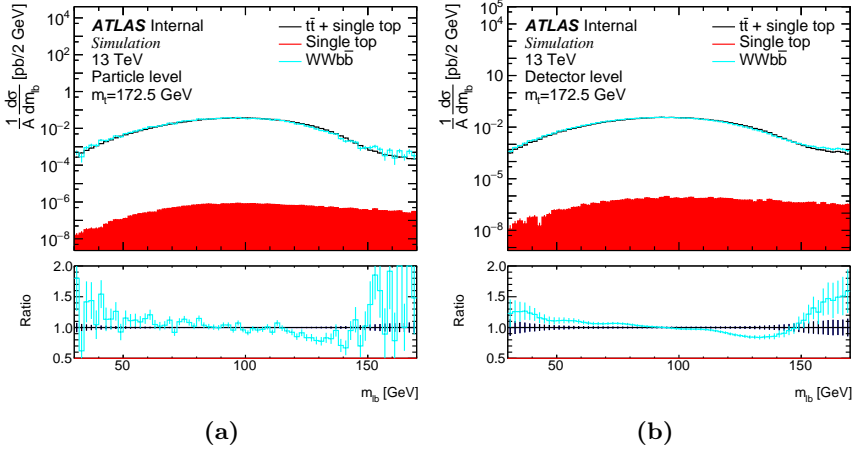


Figure 9.9: The normalized $m_{\ell b}$ distribution is shown for the $t\bar{t}$ plus single-top samples, as
 well as the $W^+W^-b\bar{b}$ prediction, at (a) particle-level and (b) detector-level, where
 $W^+W^-b\bar{b}$ is folded with the central PP8 $t\bar{t}$ migration matrix.

1831 The $m_{\ell b}$ template distributions for all five input top-quark masses are parametrized
 1832 separately. In this case, a sum of three Gaussian distributions is used for a total of
 1833 nine parameters. Fig. 9.10 shows the $m_{\ell b}$ distribution from the MC samples and the
 1834 fitted functions. As a side note, the fit is performed with MINUIT [235] within the
 1835 `AnalysisTop` framework. The fit range is chosen to be $m_{\ell b} \in [40$ GeV, 148 GeV], and
 1836 the chosen functions satisfactorily describe the distribution in the fit range.

1837 The linear dependence of the functional parameters on the top-quark mass is then
 1838 fixed, and the mass itself left as the only free parameter. The approximately linear
 1839 dependence of the different functional parameters on the input top-quark mass is shown
 1840 in Appendix B.

1841 9.4 Numerical result for top-quark mass uncertainties

1842 Similarly to Chapter 7, the calibration functions from the $t\bar{t}$ plus single-top samples
 1843 are used to fit pseudo-data drawn from the $W^+W^-b\bar{b}$ samples. The template fit to
 1844 pseudo-data gives an offset in the extracted top-quark mass.

9.4 Numerical result for top-quark mass uncertainties

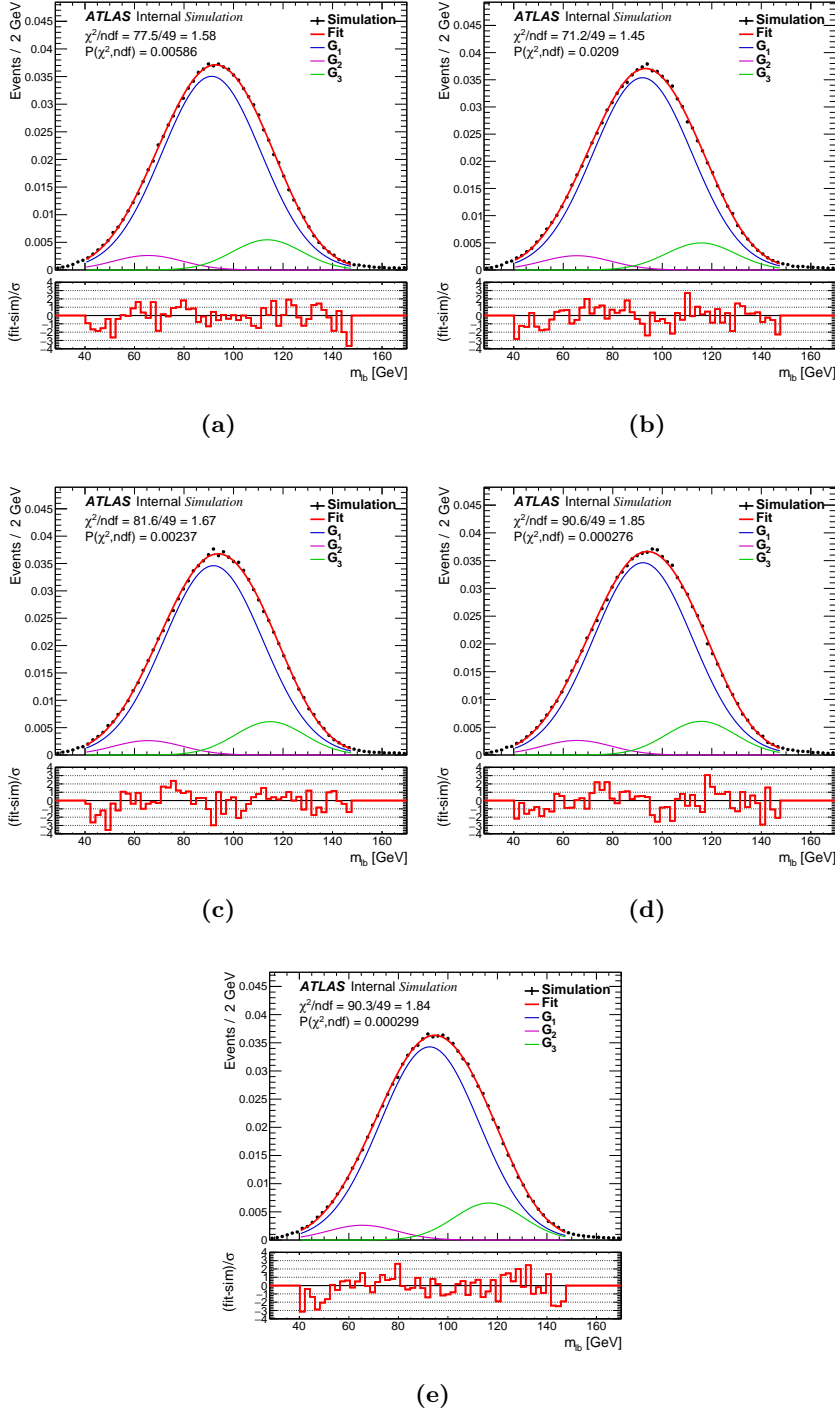


Figure 9.10: The m_{lb} distribution for the $t\bar{t}$ plus single-top samples are fitted to the sum of three Gaussian functions for m_t = (a) 171 GeV, (b) 172 GeV, (c) 172.5 GeV, (d) 173 GeV and (e) 174 GeV.

1845

Part III

1846

Top-Quark Mass Effects in Higgs Pair Production

1847

1848 10 Top-mass dependence in Higgs pair 1849 production at NLO

1850 The top-quark mass also has substantial effects in the Higgs sector. After the discovery
 1851 of the Higgs boson by both ATLAS [236] and CMS [237] experiments in 2012, which was
 1852 the crowning completion of one of LHC’s foremost goals, the experimental community
 1853 set to measure its properties to further test if it was compatible with the SM predicted
 1854 Higgs boson. As of today, some of the Higgs boson properties are very well-measured (as
 1855 for the example of its mass, spin, or couplings to heavier fermions and gauge bosons).
 1856 Still, because of lower branching ratios and irreducible backgrounds, the measurement
 1857 of the Higgs boson couplings to light fermions, as well as the Higgs self-coupling, is
 1858 still accompanied by large uncertainties of the order of $\mathcal{O}(100\%)$ in the case of the
 1859 trilinear self-coupling. This leaves room for New Physics to appear. The latest ATLAS
 1860 constraint on the Higgs boson self-coupling, in ratio to its predicted value from the
 1861 SM $c_{hhh} = \lambda/\lambda_{SM}$, is $-5.0 \leq c_{hhh} \leq 12.1$ [16] at 95% confidence level (CL), from a
 1862 combination of three searches for the hh final-states $b\bar{b}b\bar{b}$, $b\bar{b}\tau^+\tau^-$ and $b\bar{b}\gamma\gamma$. These limits
 1863 assume the other Higgs couplings to be SM-like. In the future, with the accumulation
 1864 of statistics at high-luminosity (HL)-LHC, the experimental bounds are expected to
 1865 improve, and the measurement of differential distributions (with a small number of total
 1866 events) is even conceivable. In the rest of this chapter, the theoretical standpoint of
 1867 hh production is reviewed, and the way New Physics can strongly affect this process is
 1868 presented in the framework of a non-linear EFT.

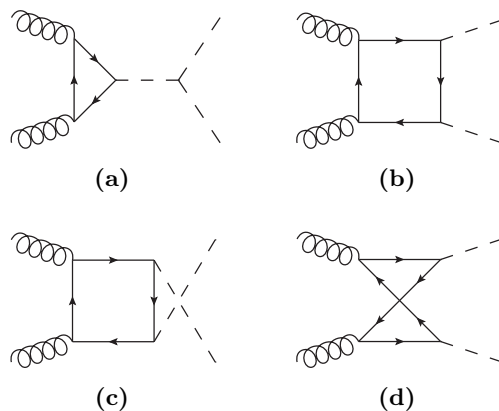


Figure 10.1: (a-d) LO Feynman diagrams for hh production by gluon-fusion.

10.1 Theoretical descriptions of hh production

At the LHC, Higgs bosons (and in particular Higgs boson pairs, which are considered in the next chapters) are produced mainly via a top-quark loop. Fig. 10.1 displays the LO Feynman diagrams for di-Higgs production in gluon-fusion: diagrams that contain the Higgs self-coupling λ are called *triangle-like* (as in Fig. 10.1a), and diagrams that do not *box-like* (as in Figs 10.1b–10.1d).¹ Because $gg \rightarrow hh$ production is loop-induced, NLO corrections start at two-loop order already and pose a challenge to compute. The matrix-element for $g(p_1, \mu, a) + g(p_2, \nu, b) \rightarrow h(p_3) + h(p_4)$ production decomposes into two form factors (with p_i the 4-momenta, Greek letters for the Lorentz indices and roman letters for the color indices):

$$\mathcal{M}_{ab}^{\mu\nu} = \frac{\alpha_s}{8\pi v^2} \delta_{ab} \epsilon_\mu \epsilon_\nu (F_1(\hat{s}, \hat{t}, m_h^2, m_t^2, d) T_1^{\mu\nu} + F_2(\hat{s}, \hat{t}, m_h^2, m_t^2, d) T_2^{\mu\nu}), \quad (10.1)$$

where the Lorentz structure is contained in the tensors T_1 , T_2 and the functions F_1 , F_2 depend on four physical scales altogether (two kinematic invariants and both particle mass scales, as well as on the analytically-continued dimension d). Finally, the first form factor can be further split into a contribution stemming only from triangle-like diagrams, respectively only box-like diagrams:

$$F_1 = F_\Delta + F_\square, \quad (10.2)$$

and the box diagrams contribute to both F_\square and F_2 . Historically, the LO one-loop total cross-section has been known analytically for a long time [238], and the triangular form factor given in Eq. (10.2), for $\tau = 4m_t^2/\hat{s}$, takes the form

$$F_\Delta = \frac{6m_h^2 \lambda \hat{s}}{\hat{s} - m_h^2} \tau (1 + (1 - \tau)f(\tau)), \quad (10.3)$$

$$f(\tau) := \begin{cases} \arcsin^2(\frac{1}{\sqrt{\tau}}) & \tau \geq 1 \\ -\frac{1}{4} \left(\log\left(\frac{1+\sqrt{1-\tau}}{1-\sqrt{1-\tau}}\right) - i\pi \right)^2 & \tau < 1. \end{cases}$$

The triangle diagrams can be reduced to single Higgs production and subsequent attachment of the triple Higgs vertex, where all the NLO integrals (massive two-loop up to three-point) have been computed with the full top-mass dependence [239–241]. The two-loop massive four-point integrals to $gg \rightarrow hh$ are known analytically only partly [242–244]. Some computations exist with expansions in given kinematic limits (large top-quark mass [242], top-quark threshold [245], small Higgs transverse momentum [246], and high-energy expansion [247, 248]). In the following, only the heavy-top limit $m_t \rightarrow \infty$ is considered, without any expansion in $1/m_t^{2n}$, as well as several approximations that include part of the full-theory result at NLO QCD.

¹At two-loop level, some diagrams do not contain the coupling λ but have triangular topologies, see e.g. the last diagram in Fig. 10.4.

1896 **10.1.1 Approximations in the heavy-top limit ($m_t \rightarrow \infty$)**

1897 To circumvent the direct computation of the difficult NLO QCD corrections to $gg \rightarrow hh$,
 1898 one neat approach that was applied successfully in Higgs production (as well as in a
 1899 whole collection of other processes) is to collapse one top-quark loop to an effective
 1900 coupling between gluons and Higgs bosons within a so-called Effective Field Theory
 1901 (EFT). This is the so-called heavy-top limit (HTL). EFTs are usually employed to
 1902 describe physics entering at a higher-scale than the typical scales of the process at
 1903 hand. In an agnostic approach, one assumes nothing about new particles and instead
 1904 computes effective couplings between known particles, that are only indirectly affected
 1905 by more massive particles. Their exact degrees of freedom are thus integrated out of
 1906 the calculation. This was for example the basic framework of the Fermi theory before
 1907 W and Z bosons were discovered, where one assumes a 4-particle interaction vertex
 1908 between fermions coupling with strength G_F . In the case of di-Higgs production, the
 1909 top-quark degrees of freedom are integrated out and an effective coupling between gluons
 1910 and Higgs bosons is introduced. There exist different consistent formulations of a theory
 1911 with effective coupling vertices between gluons and Higgs bosons: usually, one introduces
 1912 higher-dimension contact operators into the SM Lagrangian, with an EFT expansion in
 1913 the New Physics scale $1/\Lambda$.² Another EFT formulation will be introduced in Section 10.2.

1914 In the next Sections, comparisons are shown between predictions for the full theory
 1915 at QCD NLO and various approximations based on the heavy-top limit for variations of
 1916 the Higgs couplings.³ In order of increasing accuracy, these are:

- 1917 • **Pure HTL:** all top-quark loops are shrunk to an effective vertex between gluons
 1918 and Higgs bosons. At LO, the form factors given in Eqs. (10.1), (10.3), for $\tau \rightarrow \infty$,
 1919 reduce to

$$F_{\Delta} \rightarrow \frac{3m_h^2 \lambda}{\hat{s} - m_h^2} \left(\frac{4}{3} \hat{s} \right) , \quad (10.5)$$

$$F_{\square} \rightarrow -\frac{4}{3} \hat{s} , \quad (10.6)$$

$$F_2 \rightarrow 0 . \quad (10.7)$$

1920 At NLO, they are at most given by one-loop diagrams.

- 1921 • **Born-improved HTL:** the virtual and real contributions are calculated within
 1922 HTL, but reweighted on an event-by-event basis with the ratio of the full-theory
 1923 Born to the HTL Born contribution,

$$d\sigma_{V,R}^{B,i} = d\sigma_{V,R}^{\text{HTL}} \frac{d\sigma_B^{\text{FT}}}{d\sigma_B^{\text{HTL}}} . \quad (10.8)$$

²Mostly, nowadays, analyses consider only dimension-6 operators, because the only dimension-5 operator violates lepton number conservation.

³In the SM case, there are already important differences between the considered approximations [249].

- **FT_{approx}** : the same prescription as given in Eq. (10.8) is applied for the virtual contribution, but the real-emission matrix-element is computed in the full theory (these are at most one-loop diagrams).
- **Full theory**: the real and two-loop virtual contributions are computed with full m_t -dependence.

10.1.2 Two-loop contribution in the SM

The first full computation of NLO QCD corrections to $gg \rightarrow hh$ production in the SM was presented in Ref. [249]. All BSM results shown in Sections 10.3 and 11.2 are based on two-loop amplitudes calculated numerically for the SM.

As a brief description of the calculation, the two-loop contribution to the SM amplitude was generated by an extended version of GoSAM called GoSAM-2LOOP. The reduction to master integrals was operated with REDUZE 2 [250] as far as possible, and the integral evaluation performed with the help of sector decomposition in SECDEC 3 [251–253]. In particular, the integration itself was implemented within a rank-one lattice quasi-Monte-Carlo rule (QMC) that is described in more detail in Refs. [254, 255]. The Higgs and the top-quark mass are fixed, so that the integrals depend only on the two kinematic invariants \hat{s} and \hat{t} .⁴

Examples of the SM two-loop Feynman diagrams are given in the first, third and last rows of Fig. 10.4. The amplitude was calculated for a pre-sampled set of 5372 phase-space points in (\hat{s}, \hat{t}) at 14 TeV and 1343 points at 100 TeV. IR subtraction was performed within the CS dipole formalism, where for the gg channel, the insertion operator **I** is given by

$$\mathbf{I}_{gg} = \frac{\alpha_s}{2\pi} \frac{(4\pi)^\epsilon}{\Gamma(1-\epsilon)} \left(\frac{\mu_R^2}{2p_1 \cdot p_2} \right)^\epsilon \cdot 2 \left(\frac{C_A}{\epsilon^2} + \frac{\beta_0}{2\epsilon} - C_A \frac{\pi^2}{3} + \frac{\beta_0}{2} + K_g \right), \quad (10.9)$$

with $\beta_0 = \frac{11}{6}C_A - \frac{2}{3}T_R N_f$ and $K_g = \left(\frac{67}{18} - \frac{\pi^2}{6} \right) C_A - \frac{10}{9}T_R N_f$. As a side note, the IR singular pattern is the same between the SM and the BSM case presented below. When inserting the CS operator into the Born term, see Eq. (4.8), the poles from the virtual contribution should cancel. To get the correct finite terms, thus, the Born has to be expanded up to $\mathcal{O}(\epsilon^2)$. The explicit cancellation of poles in ϵ is checked numerically.

10.2 The Electroweak Chiral Lagrangian

Regarding variations of the Higgs couplings, one class of extensions of the SM called the Electroweak Chiral Lagrangian (EWChL) [257, 258] is considered. The latter framework is a non-linear realization of an EFT which will be described in some detail below. The EWChL, to leading-order, is given as

⁴The top-quark mass is renormalized on-shell. Dependence of the numerical results on the top-mass scheme are investigated in Ref. [256].

$$\begin{aligned}
 \mathcal{L}_2 = & -\frac{1}{2}\langle G_{\mu\nu}G^{\mu\nu}\rangle - \frac{1}{2}\langle W_{\mu\nu}W^{\mu\nu}\rangle - \frac{1}{4}B_{\mu\nu}B^{\mu\nu} + \sum_{\psi=q_L,l_L,u_R,d_R,e_R} \bar{\psi}iD\psi \\
 & + \frac{v^2}{4} \langle D_\mu U^\dagger D^\mu U \rangle (1 + F_U(h)) + \frac{1}{2}\partial_\mu h \partial^\mu h - V(h) \\
 & - v \left[\bar{q}_L \left(Y_u + \sum_{n=1}^{\infty} Y_u^{(n)} \left(\frac{h}{v} \right)^n \right) UP_+ q_R + \bar{q}_L \left(Y_d + \sum_{n=1}^{\infty} Y_d^{(n)} \left(\frac{h}{v} \right)^n \right) UP_- q_R \right. \\
 & \left. + \bar{l}_L \left(Y_e + \sum_{n=1}^{\infty} Y_e^{(n)} \left(\frac{h}{v} \right)^n \right) UP_- l_R + \text{h.c.} \right], \tag{10.10}
 \end{aligned}$$

where $U = \exp(2i\phi^a T^a/v)$ is the Goldstone matrix and contains the electroweak Goldstone fields ϕ^a , and T^a are the generators of $SU(2)_L$. Here, $P_\pm = 1/2 \pm T_3$ are the chiral projection operators, and the Higgs sector is characterized by an order-by-order expansion in the Higgs EW singlet h , given by the functions

$$F_U(h) = \sum_{n=1}^{\infty} f_{U,n} \left(\frac{h}{v} \right)^n, \quad V(h) = v^4 \sum_{n=2}^{\infty} f_{V,n} \left(\frac{h}{v} \right)^n. \tag{10.11}$$

The coefficients $f_{U,n}$, $V_{U,n}$ and $Y_{u,d,e}^{(n)}$ are in principle free parameters and can be of $\mathcal{O}(1)$. The SM case is retrieved when

$$f_{U,1} = 2, \quad f_{U,2} = 1, \quad f_{V,2} = f_{V,3} = \frac{m_h^2}{2v^2}, \quad f_{V,4} = \frac{m_h^2}{8v^2}, \quad Y_f^{(1)} = Y_f. \tag{10.12}$$

Now, this Lagrangian is structured not in terms of canonical dimensions for the quantum fields and couplings, but rather in terms of *chiral* dimensions (as in the case of the chiral EFT of pions in QCD). The chiral dimension assigned to fields, derivatives and couplings are

$$d_\chi(A_\mu, \varphi, h) = 0, \quad d_\chi(\partial, \bar{\psi}\psi, g, y) = 1, \tag{10.13}$$

with A_μ being any gauge field, g representing any of the SM gauge couplings, and y any weak coupling (like the Yukawa couplings). The ordering in the chiral dimension d_χ is equivalent to counting the number of loops L , $d_\chi = 2L + 2$. In summary, the NLO (in α_s) QCD corrections to hh production stem from one-loop diagrams in the leading (in d_χ) EWChL \mathcal{L}_2 and from tree diagrams in the next-to leading part \mathcal{L}_4 . All of these contributions are of chiral dimension $d_\chi = 4$. Then, in the Higgs sector, the effective Lagrangian reduces to

$$\mathcal{L} \supset \underbrace{-m_t \left(c_t \frac{h}{v} + c_{tt} \frac{h^2}{v^2} \right) \bar{t}t}_{\mathcal{L}_2} - c_{hhh} \frac{m_h^2}{2v} h^3 + \underbrace{\frac{\alpha_s}{8\pi} \left(c_{ggh} \frac{h}{v} + c_{gggh} \frac{h^2}{v^2} \right) G_{\mu\nu}^a G^{a,\mu\nu}}_{\mathcal{L}_4}. \tag{10.14}$$

1973 The EWChL introduces five anomalous couplings to the SM and the corresponding
 1974 LO Feynman diagrams are given in Fig. 10.2.

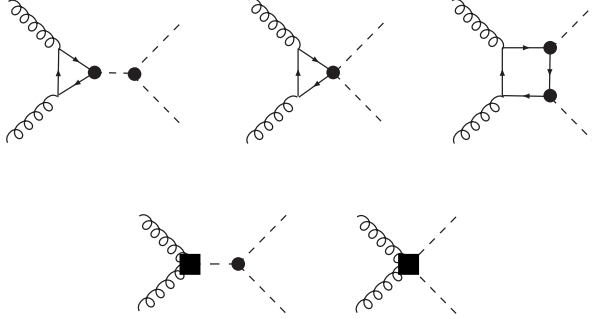


Figure 10.2: LO diagrams for the various terms from the EWChL Lagrangian. Both vertices from \mathcal{L}_2 (black dots) and local contact terms from \mathcal{L}_4 (black squares) contribute.

1975 Diagrams that are of higher chiral dimension (or do not belong to $\mathcal{O}(\alpha_s^4 \alpha^2)$) are sys-
 1976 tematically neglected, like the ones given in Fig. 10.3. The full virtual amplitude is then
 1977 given by two-loop contributions (Fig. 10.4), one-loop diagrams that contain one effective
 1978 coupling from \mathcal{L}_4 (Fig. 10.5), and one tree-diagram containing exactly two effective
 1979 vertices between gluons and Higgs bosons (Fig. 10.6). Note that all two-loop diagrams
 1980 with non-SM values of the Higgs couplings can be retrieved from their SM counterparts
 1981 by rescaling at amplitude-level:

$$\begin{aligned} \mathcal{M}_V(\Delta_1) &\rightarrow \mathcal{M}_V^{\text{SM}}(\Delta_1) \cdot c_t c_{hh} && (1^{\text{st}} \text{ row in Fig. 10.4}) \\ \mathcal{M}_V(\Delta_2) &\rightarrow \mathcal{M}_V^{\text{SM}}(\Delta_1) \cdot \frac{\hat{s} - m_h^2}{3m_h^2} c_{tt} && (2^{\text{nd}} \text{ row in Fig. 10.4}) \\ \mathcal{M}_V(\square) &\rightarrow \mathcal{M}_V^{\text{SM}}(\square) \cdot c_t^2 && (3^{\text{rd}}, 4^{\text{th}} \text{ rows in Fig. 10.4}), \end{aligned}$$

1982 where $\mathcal{M}_V(\Delta_1)$ are the triangle diagrams from the 1st row of Fig. 10.4, $\mathcal{M}_V(\Delta_2)$ from
 1983 the 2nd row (given by the corresponding diagrams from the 1st row where the s -channel
 1984 Higgs propagator gets pinched), and $\mathcal{M}_V(\square)$ are the box-diagrams from the 3rd row.
 1985 Accordingly, the amplitudes computed in Ref. [249] are used for the pre-sampled set of
 1986 phase-space points and are simply rescaled.

1987 Finally, real-emission diagrams contain five-point one-loop diagrams with SM-like
 1988 topologies, as well as tree diagrams carrying one effective coupling between gluons and
 1989 Higgs bosons from \mathcal{L}_4 (Fig. 10.7).

1990 10.3 Total cross-sections for BSM benchmark points

1991 All results for total and differential cross-sections presented in this chapter can be found
 1992 in Ref. [259]. To summarize, all HTL contributions were computed analytically with

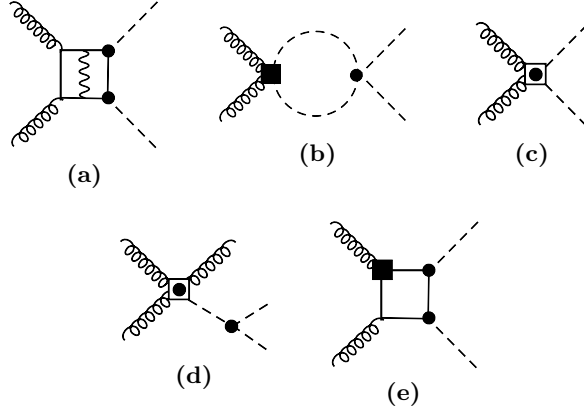


Figure 10.3: (a-d) Diagrams that do not scale like α_s^4 are consistently neglected. (e) The chromomagnetic operator $Q_{ttG} = c_t g_s \bar{t}_L \sigma_{\mu\nu} G^{\mu\nu} t_R$ only contributes at two-loop order at least ($d_\chi = 6$).

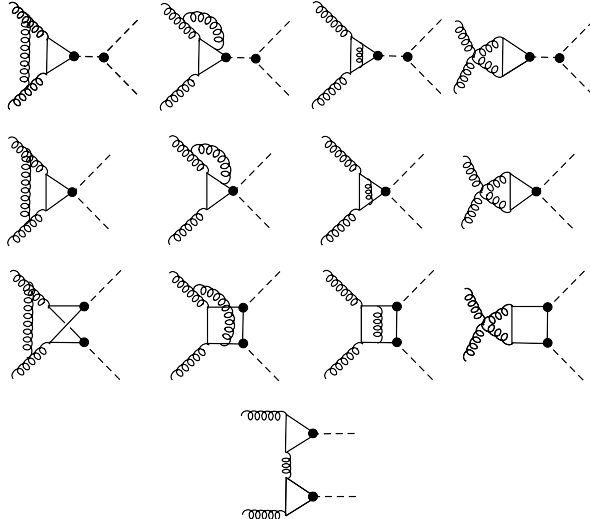


Figure 10.4: Two-loop diagrams generated by the EWChL at NLO QCD. They can all be computed by rescaling from the corresponding SM diagrams (see text).

1993 FORM. In FT_{approx} and in the full theory predictions, the real radiation is provided by
 1994 GoSAM. A Universal FeynRules Output (UFO) model [260] for the EWChL was pro-
 1995 duced with FEYNRULES [261, 262] and interfaced to GoSAM to produce all tree and
 1996 one-loop diagrams. The various parts are assembled into a C++ code which performs the
 1997 phase-space integration with VEGAS as interfaced through the CUBA package.

1998 The results shown below are produced at a center-of-mass energy of $\sqrt{s} = 14$ TeV,
 1999 where the PDF4LHC15_nlo_100_pdfs is used and interfaced through LHAPDF. The cor-
 2000 responding value of $\alpha_s(\mu)$, with $\alpha_s(m_Z) = 0.118$, is consistently employed throughout

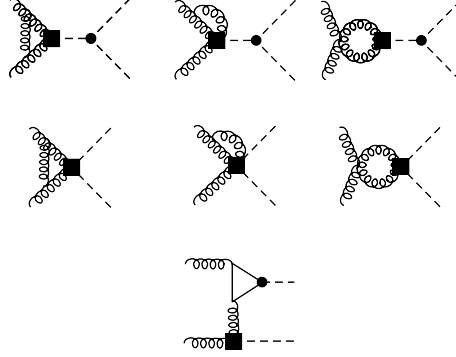


Figure 10.5: One-loop virtual contributions at NLO QCD: these diagrams contain exactly one effective contact coupling from \mathcal{L}_4 .

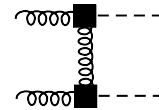


Figure 10.6: Tree diagram at NLO QCD containing exactly two effective couplings from \mathcal{L}_4 .

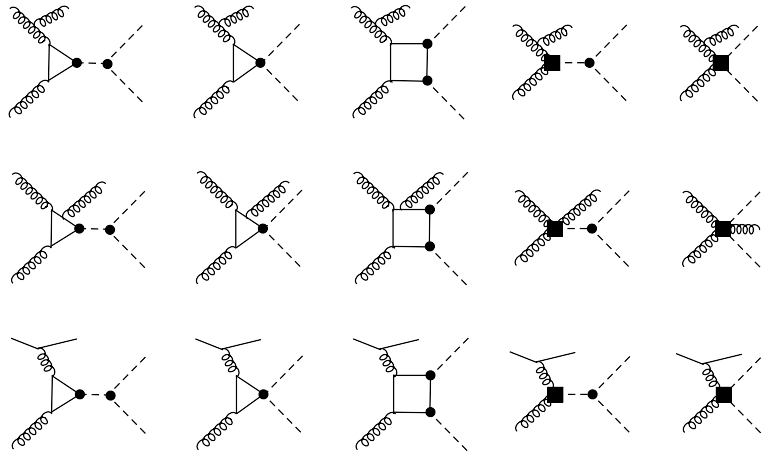


Figure 10.7: Real-emission contributions that are either one-loop diagrams without effective contact coupling, or tree diagrams with exactly one such coupling.

the calculation. The Higgs boson and top-quark masses are set to $m_h = 125$ GeV and $m_t = 173$ GeV, as the two-loop amplitudes were computed with these values, and both their widths are set to zero. Finally, the renormalization and factorization scales are set to $\mu_R = \mu_F = \mu_0 = m_{hh}/2$ and uncertainties are estimated according to 7-point scale variations $\mu_{R,F} = c_{R,F}\mu_0$ with $(c_R, c_F) \in \{0.5, 1, 2\} \times \{0.5, 1, 2\} \setminus \{(0.5, 2), (2, 0.5)\}$.

10.3 Total cross-sections for BSM benchmark points

To characterize the 5-dimensional BSM space, the set of Higgs coupling variations used in the following part is based mostly on the definition of benchmark (BM) points presented in Ref. [263]. There, the BSM space is scanned for different values of the Higgs anomalous couplings and clustered into blocks that manifest a similar behavior in differential distributions. The set of BM points is defined in Table 10.1, and the total cross-sections, K -factors and uncertainties are shown in Table 10.2.

First, looking at Table 10.2, the NLO cross-sections can become quite sizeable depending on the BM point considered (of $\mathcal{O}(100)$ times the SM cross-section), and some are even excluded considering recent bounds on hh production from experimental limits. With the ATLAS current limit [16] on the observed non-resonant hh production cross-section of 220 fb at 95% CL, several BM points would indeed be excluded already. Second, the full m_t -dependent NLO corrections are important, with K -factors between 1.66 and 2.34, and are accompanied by large scale uncertainties of $\mathcal{O}(15 - 20\%)$ (similarly to single Higgs production at NLO QCD [264, 265]). Finally, the K -factors themselves depend substantially on the considered BSM point. This is also illustrated in Fig. 10.8, where only one parameter is varied at a time. In fact, studies realized in the heavy-top limit suggest the K -factors's dependence on the different couplings to be quite small [266] (of $\mathcal{O}(5\%)$ or less for all considered coupling variations). Once full top-quark loop corrections are taken into account, though, the K -factors for c_{hhh} , c_{tt} and c_t vary by more than 30% (55% for c_{tt}). Later on, in Section 10.4, it will be shown that this feature is especially prominent around the top-quark pair $2m_t$ threshold when considering differential distributions.

BM	c_{hhh}	c_t	c_{tt}	c_{ggh}	c_{gggh}
1	7.5	1.0	-1.0	0.0	0.0
2	1.0	1.0	0.5	$-\frac{1.6}{3}$	-0.2
3	1.0	1.0	-1.5	0.0	$\frac{0.8}{3}$
4	-3.5	1.5	-3.0	0.0	0.0
5	1.0	1.0	0.0	$\frac{1.6}{3}$	$\frac{1.0}{3}$
6	2.4	1.0	0.0	$\frac{0.4}{3}$	$\frac{0.2}{3}$
7	5.0	1.0	0.0	$\frac{0.4}{3}$	$\frac{0.2}{3}$
8a	1.0	1.0	0.5	$\frac{0.8}{3}$	0.0
9	1.0	1.0	1.0	-0.4	-0.2
10	10.0	1.5	-1.0	0.0	0.0
11	2.4	1.0	0.0	$\frac{2.0}{3}$	$\frac{1.0}{3}$
12	15.0	1.0	1.0	0.0	0.0
SM	1.0	1.0	0.0	0.0	0.0

Table 10.1: Different BM points in the 5-dimensional Higgs coupling space are analyzed below at inclusive, respectively differential cross-section level.

Furthermore, the ratio of the cross-section to the SM can be parametrized [263, 267] in terms of the anomalous Higgs couplings: the cross-section ratio is expressed as a polynomial whose coefficients correspond to all squared/interference terms from the various diagrams. At LO, this gives 15 possible combinations:

10 Top-mass dependence in Higgs pair production at NLO

BM	σ_{NLO} [fb]	K -factor	scale uncertainties [%]	stat. uncertainties [%]	$\frac{\sigma_{\text{NLO}}}{\sigma_{\text{NLO,SM}}}$
B_1	194.89	1.88	$^{+19}_{-15}$	1.6	5.915
B_2	14.55	1.88	$^{+5}_{-13}$	0.56	0.4416
B_3	1047.37	1.98	$^{+21}_{-16}$	0.15	31.79
B_4	8922.75	1.98	$^{+19}_{-16}$	0.39	270.8
B_5	59.325	1.83	$^{+4}_{-15}$	0.36	1.801
B_6	24.69	1.89	$^{+2}_{-11}$	2.1	0.7495
B_7	169.41	2.07	$^{+9}_{-12}$	2.2	5.142
B_{8a}	41.70	2.34	$^{+6}_{-9}$	0.63	1.266
B_9	146.00	2.30	$^{+22}_{-16}$	0.31	4.431
B_{10}	575.86	2.00	$^{+17}_{-14}$	3.2	17.48
B_{11}	174.70	1.92	$^{+24}_{-8}$	1.2	5.303
B_{12}	3618.53	2.07	$^{+16}_{-15}$	1.2	109.83
SM	32.95	1.66	$^{+14}_{-13}$	0.1	1

Table 10.2: The total cross-sections for the considered BSM BM points, with their respective K -factors, scale and (MC) statistical uncertainties, as well as the ratio to the SM cross-section $\sigma_{\text{NLO,SM}} = 32.95$ fb.

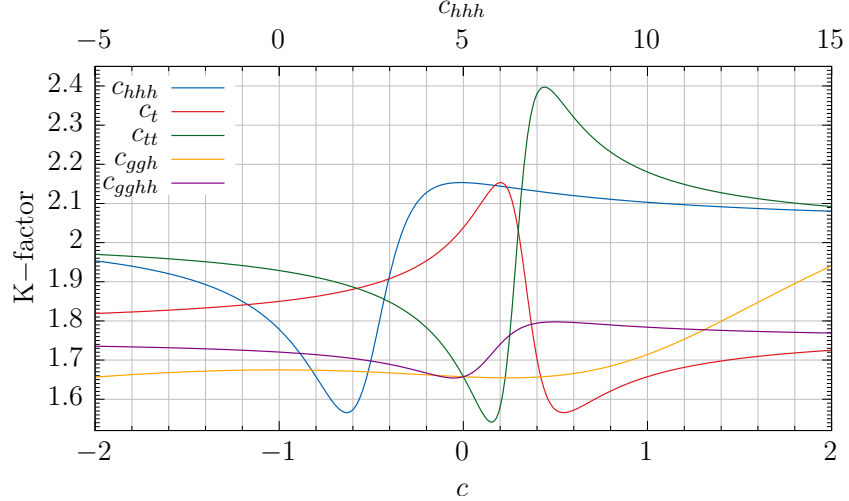


Figure 10.8: The K -factor is shown as a function of c_{hhh} on the top axis, and of the other couplings on the lower axis.

$$\begin{aligned}
 \sigma/\sigma_{SM} = & A_1 c_t^4 + A_2 c_{tt}^2 + A_3 c_t^2 c_{hhh}^2 + A_4 c_{ggh}^2 c_{hhh}^2 + A_5 c_{gghh}^2 + A_6 c_{tt} c_t^2 \\
 & + A_7 c_t^3 c_{hhh} + A_8 c_{tt} c_t c_{hhh} + A_9 c_{tt} c_{ggh} c_{hhh} + A_{10} c_{tt} c_{gghh} \\
 & + A_{11} c_t^2 c_{ggh} c_{hhh} + A_{12} c_t^2 c_{gghh} + A_{13} c_t c_{hhh}^2 c_{ggh} \\
 & + A_{14} c_t c_{hhh} c_{gghh} + A_{15} c_{ggh} c_{hhh} c_{gghh}. \tag{10.15}
 \end{aligned}$$

10.3 Total cross-sections for BSM benchmark points

2032 The coefficients A_1 to A_{15} are corrected at NLO, and 8 new coefficients appear from
 2033 genuine NLO diagrams:

$$\Delta\sigma/\sigma_{SM} = A_{16} c_t^3 c_{ggh} + A_{17} c_t c_{tt} c_{ggh} + A_{18} c_t c_{ggh}^2 c_{hhh} + A_{19} c_t c_{ggh} c_{gghh} \\ + A_{20} c_t^2 c_{ggh}^2 + A_{21} c_{tt} c_{ggh}^2 + A_{22} c_{ggh}^3 c_{hhh} + A_{23} c_{ggh}^2 c_{gghh}. \quad (10.16)$$

2034 These coefficients can be determined by dedicated event generation runs for a set of
 2035 the 5-dimensional parameter space, and by projecting out a system of equations, or
 2036 by a simple fit of the polynomial in Eq. (10.16) to the calculated set of cross-sections.
 2037 The results for the NLO coefficients A_1 to A_{23} at $\sqrt{s} = 14$ TeV are given in Table C.1.
 2038 Interestingly, once the cross-section coefficients are computed, the parametrization given
 2039 in Eqs. (10.15), (10.16) yields the cross-section for any point of the BSM space. This
 2040 for example allows to produce iso-contour plots where curves represent configurations in
 2041 the BSM space which lead to the same cross-section, see Figs. 10.9, 10.10, 10.11. In the
 2042 latter, two BSM couplings are simultaneously varied (within bounds still approximately
 2043 allowed by experimental measurements), and iso-curves for the ratio to the SM cross-
 2044 section at LO (red), respectively NLO (black), are shown.

2045 The cross-section iso-curves are given for c_{tt} against c_{gghh} in Fig. 10.9a, respectively
 2046 against c_{ggh} in Fig. 10.9b. In both cases, the cross-section varies sizeably with respect
 2047 to the SM value, and is generally more sensitive to changes in c_{tt} . The NLO corrections
 2048 to hh introduce important shifts in the iso-curves (reflected by the large K -factors).
 2049 Fig. 10.10 shows iso-contours for variations of c_{hhh} versus c_{ggh} , respectively c_{tt} . Again,
 2050 the curves are much more dependent on c_{hhh} than on the Higgs contact coupling, as
 2051 exhibited by Fig. 10.10a. In comparison, the dependence of the cross-section on c_{hhh}
 2052 and c_{tt} is large, with ratios to the SM cross-section going up to a factor $\mathcal{O}(\sim 100)$.
 2053 Finally, iso-contours are also plotted for simultaneous variations of c_t versus c_{tt} and c_{hhh}
 2054 in Fig. 10.11.

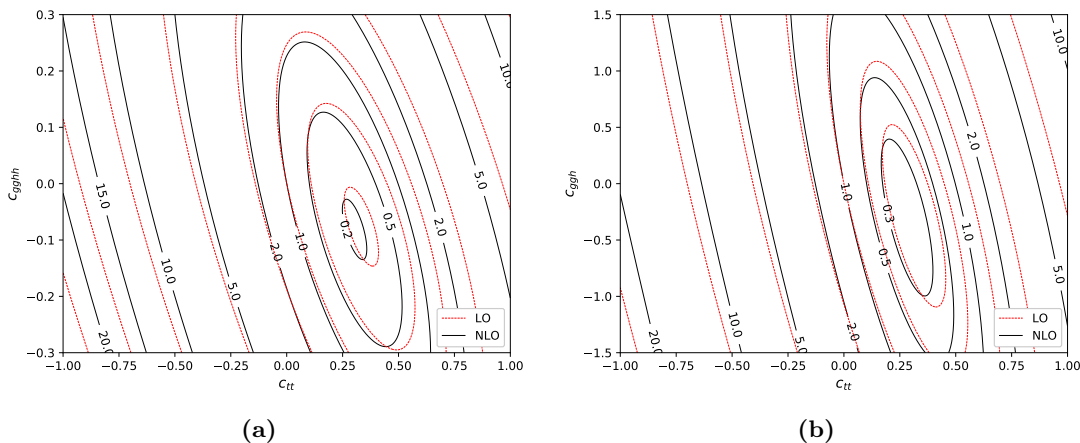


Figure 10.9: Iso-contours of σ/σ_{SM} : (a) c_{gghh} and (b) c_{ggh} versus c_{tt} .

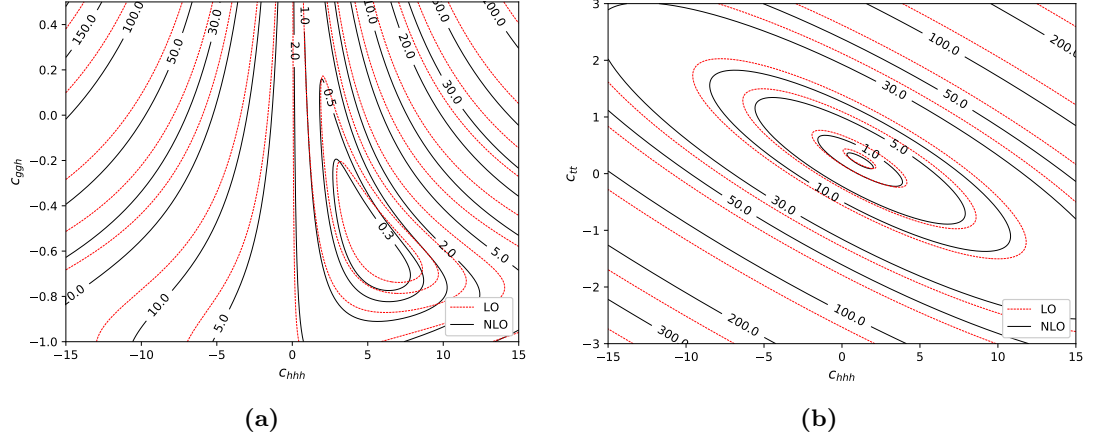


Figure 10.10: Iso-contours of σ/σ_{SM} : (a) c_{gg} and (b) c_{tt} versus c_{hh} .

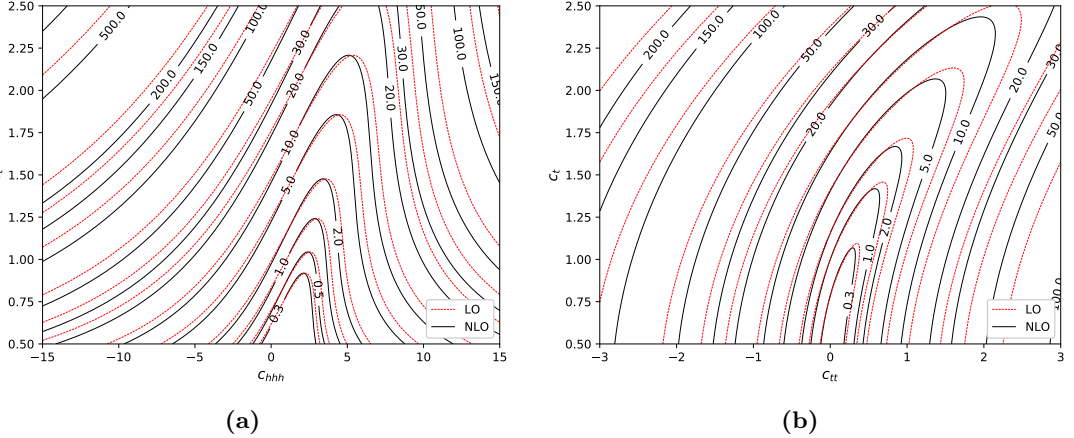


Figure 10.11: Iso-contours of σ/σ_{SM} : (a) c_t versus c_{hh} and (b) c_t versus c_{tt} .

2055 10.4 Differential cross-sections and HTL approximations

2056 Next, differential cross-sections are compared for the various approximations laid out in
 2057 Section 10.1.1. Distributions are shown for the invariant mass of the Higgs boson pair
 2058 system m_{hh} and the transverse momentum of one (any) Higgs $p_{T,h}$, for a subset of the
 2059 BM points defined in Table 10.2.

2060 In Fig. 10.12, both distributions are displayed for the BM point 6: the SM distri-
 2061 butions are plotted against the the BSM Born-improved, FT_{approx} and full predictions,
 2062 respectively, both at LO and NLO. While the B_6 total cross-section is similar to the SM
 2063 value for all considered NLO approximations, the interference pattern between triangle-
 2064 and box-like diagrams is very different. The m_{hh} observable in Fig. 10.12a manifests a

dip around $m_{hh} = 370$ GeV,⁵ which would be a characteristic sign of BSM physics at the differential level. As a matter of fact, the chosen value of $c_{hhh} = 2.4$ corresponds approximately to a maximal destructive interference between triangle- and box-like contributions when the other couplings are kept fixed at their SM values. Secondly, the differential K -factor shown in the first ratio plot (in red), which is found to be relatively flat in the usual HTL approximations, varies by more than 70% for the full m_t -dependent NLO prediction. Finally, while both the Born-improved and FT_{approx} descriptions show the largest difference to the full NLO calculation around the top-quark pair threshold (see the purple and green curves in the second ratio plot), they describe the tail of the m_{hh} distribution rather well. The same considerations apply to the $p_{T,h}$ distribution plotted in Fig. 10.12b.

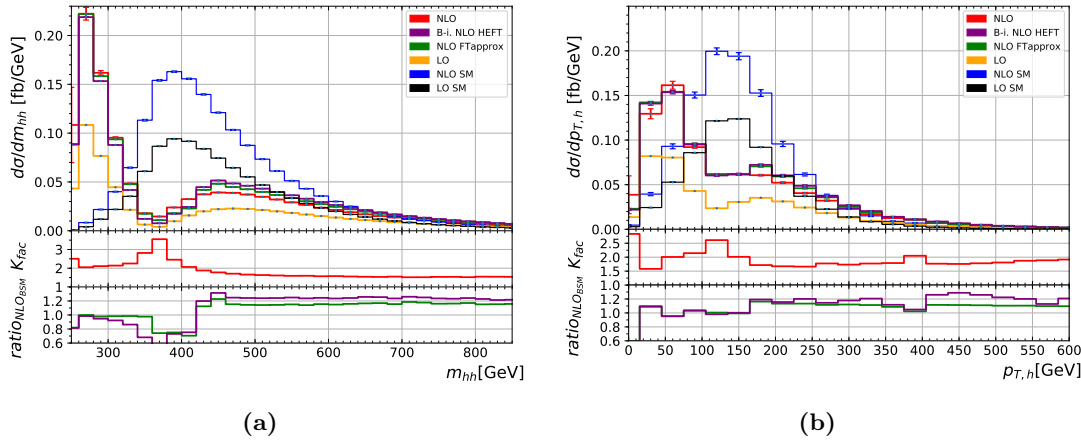


Figure 10.12: (a) Higgs boson pair invariant mass and (b) Higgs transverse momentum for BM point 6 ($c_{hhh} = 2.4, c_t = 1, c_{tt} = 0, c_{ggh} = 2/15, c_{gghh} = 1/15$) with all considered hh production approximations.

The same differential distributions are plotted for the BM point 9 in Fig. 10.13, which is characterized by SM values for c_{hhh}, c_t and non-zero values of c_{tt} and gluon-Higgs couplings c_{ggh}, c_{gghh} . In this case, the cross-section is much larger than the SM value. The anomalous gluon-Higgs coupling values also enhance the tail of both distributions (the dependence of the c_{gghh} term grows proportionally to the invariant \hat{s} in the limit $\hat{s} \rightarrow \infty$). Both NLO approximations fall short of describing the full prediction around the top-quark pair threshold and in the middle-range part of the m_{hh} distribution.

Renormalization and factorization scale uncertainties are given along the central prediction for the BM point 5 in Fig. 10.14. This BM point is one example where, contrary to the SM case, the envelope is not given by the two most extreme scale variations $c_{R,F} \in \{(0.5, 0.5), (2, 2)\}$, which both give downwards deviations. As for the SM point, the NLO BM prediction is not covered by the LO scale uncertainties. All BM points not shown here are given in Appendix C for completeness.

⁵The LO pure HTL amplitude vanishes at $m_{hh} = 429$ GeV.

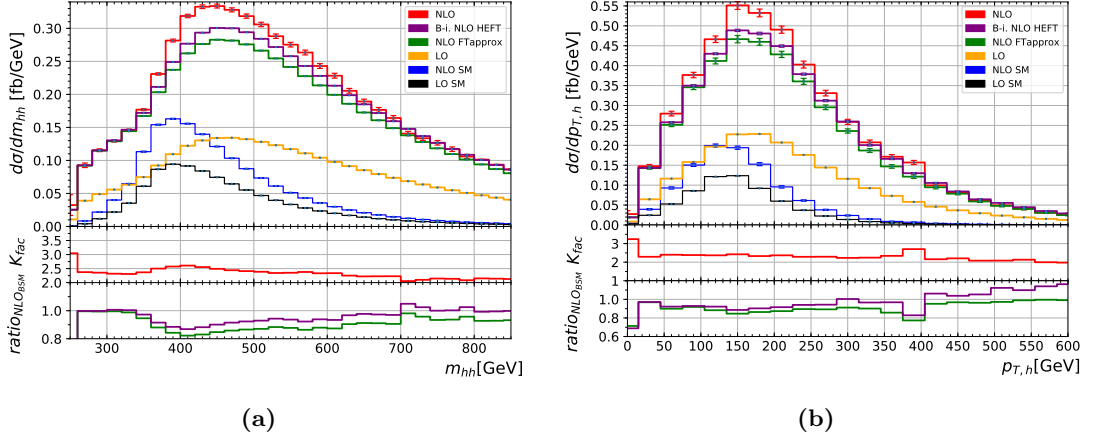


Figure 10.13: (a) Higgs boson pair invariant mass and (b) Higgs transverse momentum for BM point 9 ($c_{hhh} = 1, c_t = 1, c_{tt} = 1, c_{ggh} = -0.4, c_{gggh} = -0.2$).

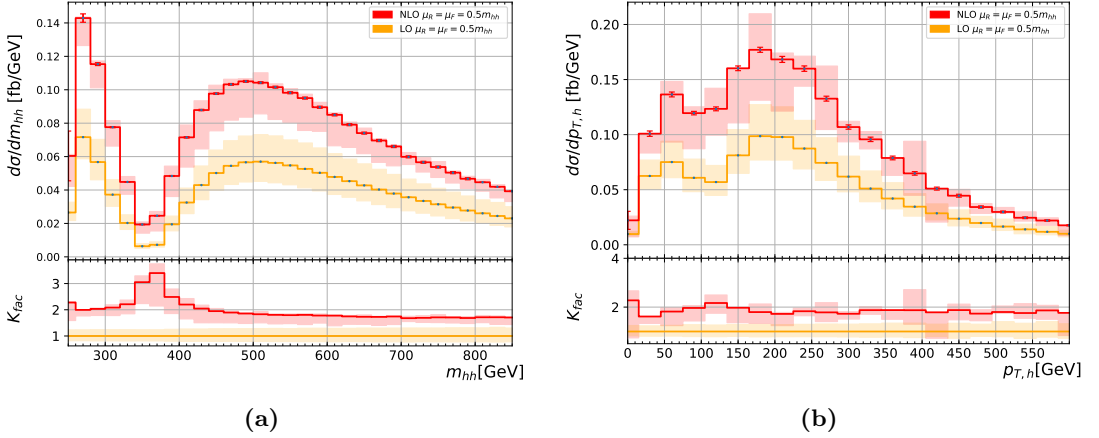


Figure 10.14: The (a) m_{hh} and (b) $p_{T,h}$ distributions for BM point 5 ($c_{hhh} = 1, c_t = 1, c_{tt} = 0, c_{ggh} = 8/15, c_{gggh} = 1/3$), along with μ_R/μ_F scale uncertainties.

Note that both BM points 5 and 9 assume values of c_{ggh} that are already excluded by CMS for $c_t = 1$ [268]. Generally, the full m_t -dependent NLO prediction introduces a high dependence of the K -factor on both the anomalous Higgs couplings and at the differential level in distribution bins. For some BM points, the Born-improved and FT_{approx} approximations fare rather poorly and should be replaced by the full theory prediction when comparing to experimentally measured cross-sections, for maximal exclusion limits on anomalous couplings. In particular, it should help identify updated BM points in the BSM space of anomalous Higgs couplings. In this prospect, part of the EWChL setup presented above is incorporated into a MC event generator available to experimentalists.

2099 11 Variations of the triple Higgs-coupling 2100 and parton-shower effects

2101 Having considered the extension of the SM through the EWChL and the effects of the
 2102 full NLO QCD corrections due to the top-quark loops in hh production, its implementa-
 2103 tion in a full-fledged MC event generator is presented. Numerical results and differential
 2104 distributions are given in more detail in Ref. [269]. A version of the m_t -dependent predic-
 2105 tion at NLO was already implemented in the case of the SM in the POWHEG-BOX-V2
 2106 package `UserProcesses-V2/ggHH`. It is extended to allow for variations of both the Higgs
 2107 boson trilinear self-coupling λ and the top-Higgs Yukawa coupling y_t : the result is a pub-
 2108 lic MC generator that permits full particle-level production. In particular, Higgs bosons
 2109 are allowed to decay, and the fixed-order calculation can be matched to a parton-shower
 2110 and hadronization package. In this chapter, the working mode of the POWHEG-BOX
 2111 MC generator is briefly presented. The interfacing of the two-loop contribution to hh
 2112 production (including the aforementioned coupling variations) is explained, and NLO
 2113 cross-sections at $\sqrt{s} = 13, 14, 27$ TeV, as well as differential distributions at $\sqrt{s} = 14$ TeV
 2114 are shown. Finally, the matching of the fixed-order NLO calculation to a parton-shower
 2115 is studied in more depth, and shower-related systematic uncertainties are estimated.

2116 11.1 The Powheg-BOX framework

2117 The POWHEG-BOX framework [17–19] is a `fortran` MC event generator skeleton that
 2118 handles MC integration and event production for any arbitrary NLO process, suppos-
 2119 ing the user grants the few necessary input ingredients for the calculation, namely a
 2120 parametrization of phase-space and the different contributions to the amplitude. The
 2121 POWHEG-BOX also constitutes a repository of previously calculated processes which are
 2122 made publicly available. In the following, the second version of the program POWHEG-
 2123 BOX-V2 is used. The POWHEG formalism bases on the following formula for the hardest
 2124 emission:

$$d\sigma_{\text{NLO}} = d\Phi_m \bar{B}(\Phi_m) \left(\Delta(p_{T,\min}, \mu^2) + \int_{p_{T,\min}} d\Phi_1 \Delta(p_T, \mu^2) \frac{R(\Phi_{m+1})}{B(\Phi_m)} \Theta(\mu^2 - p_T) \right), \quad (11.1)$$

2125 where $p_{T,\min}$ is the parton-shower IR cutoff, μ^2 is the shower starting scale, B and R are
 2126 the Born and the real-emission matrix-elements, and \bar{B} represents the Born underlying
 2127 configuration. Note that in general, the transverse momentum could be replaced by
 2128 any other shower evolution variable. The function Δ is the Sudakov form factor (see

2129 Section 4.2.2) yielding the probability of no-emission above a given scale. In the POWHEG
 2130 notation,

$$\Delta(t_0, t) = \exp \left(- \int d\Phi_1 \frac{R(\Phi_{m+1}) \Theta(t - t_0)}{B(\Phi_m)} \right). \quad (11.2)$$

2131 For more details, the reader is referred to Ref. [18]. The workflow is quite simple and
 2132 separates into four stages:

- 2133 • An importance sampling grid for the integration is determined: if run in parallel
 2134 mode, POWHEG generates importance sampling grids for each seed and subse-
 2135 quently combines them into one and stores the result in a `pwgxgrid.dat` file.
- 2136 • The integration is performed, and an upper bounding envelope is determined for
 2137 the underlying Born kinematics cross-section \bar{B} and stored into a `pwggrid.dat`
 2138 file.
- 2139 • The upper bound for the normalization of the radiation function $R(\Phi_{m+1})/B(\Phi_m)$
 2140 is found, and stored into a `pwgubound.dat` file.
- 2141 • Events can be generated in the LHE format, and run in parallel. Files `pwgevents.lhe`
 2142 are produced and can then be fed to a parton-shower algorithm later on.

2143 11.2 Interfacing two-loop contributions

2144 The grid of the amplitude at pre-sampled PS points used for producing the results of
 2145 Chapter 10 is stored and has to be interfaced to POWHEG. First, the program has
 2146 to be able to call the virtual amplitude at any phase-space point (without having to
 2147 recompute the expensive two-loop integrals for any possible kinematics (\hat{s}, \hat{t})). In the
 2148 SM `ggHH` program [270], this is handled by setting up a Python interface that interpolates
 2149 the 2-dimensional grid: first, the (\hat{s}, \hat{t}) phase-space is re-parametrized into new variables
 2150 (x, c_θ) to produce an almost uniform distribution of phase-space points. This is achieved
 2151 by choosing

$$x = f(\beta(\hat{s})), \quad c_\theta = |\cos(\theta)| = \left| \frac{\hat{s} + 2\hat{t} - 2m_h^2}{\hat{s}\beta(\hat{s})} \right|, \quad \beta = \sqrt{1 - \frac{4m_h^2}{\hat{s}}} \quad (11.3)$$

2152 with f any monotonic function. In this case, $f(\beta(\hat{s}))$ is chosen to be the cumulative
 2153 distribution function of the phase-space points generated in Ref. [249]. A uniform grid in
 2154 the (x, c_θ) space is generated, and the result at each point is set by linearly interpolating
 2155 the amplitude using the neighboring points computed by `SECDEC`. The amplitude at
 2156 any phase-space points is then interpolated using the Clough-Tougher scheme in `SciPy`,
 2157 which allows for a high numerical stability. For details on the grid performance and
 2158 caveats, the reader is referred to Ref. [270?].

11.3 Total and differential cross-sections at fixed-order

2159 The implementation of variations of the Higgs trilinear self-coupling λ bases on a
 2160 simple observation: at all orders (in QCD), the full amplitude for di-Higgs production
 2161 is a second-order polynomial in λ ,

$$M_\lambda \equiv |\mathcal{M}_\lambda|^2 = A + B \lambda + C \lambda^2. \quad (11.4)$$

2162 Thus knowing the amplitude for three values of λ allows to interpolate the matrix-
 2163 element to any other arbitrary value. In this case, grids of the virtual amplitudes are
 2164 produced for $\lambda \in \{-1, 0, 1\}$. Before starting the POWHEG run, the three grids are
 2165 combined to a new grid containing the virtual amplitude for the user-given value of the
 2166 Higgs self-coupling by simple Lagrange interpolation,

$$M_\lambda = M_{\lambda=0} (1 - \lambda^2) + \frac{M_{\lambda=1}}{2} (\lambda + \lambda^2) + \frac{M_{\lambda=-1}}{2} (-\lambda + \lambda^2), \quad (11.5)$$

2167 where the uncertainties on the three amplitudes are added in quadrature. This grid is
 2168 then further propagated to the Clough-Tougher interpolation routine. Note that in the
 2169 BSM case, points at 100 TeV are also included in the grid to further improve statistics
 2170 at higher center-of-mass energies, and by extension, in distribution tails. On the other
 2171 hand, because BSM distributions differ in shape from the SM case (for example, see
 2172 Fig. 11.2), phase-space regions that could well be populated for certain values of the
 2173 anomalous couplings are not always well-sampled by the SM grid.

2174 11.3 Total and differential cross-sections at fixed-order

2175 The PDF4LHC15_nlo_30_pdfas set is used and interfaced to POWHEG-BOX-V2 through
 2176 LHAPDF. Jets are clustered by the anti- k_T algorithm [169] as implemented in **FastJet**,
 2177 with a jet distance parameter of $R = 0.4$ and a minimum transverse momentum $p_{T,\min}^{\text{jet}} =$
 2178 20 GeV. Otherwise, the same setup presented in Section 10.3 is used for the next results.
 2179 Note that the nomenclature is different, with respect to Chapter 10, for variations of
 2180 the Higgs trilinear coupling and the top-Higgs Yukawa coupling: the Higgs self-coupling
 2181 ratio to the SM value, formerly called c_{hh} , is replaced by κ_λ (in reference to the widely-
 2182 used experimental κ framework), and the top-Higgs Yukawa coupling ratio c_t is now
 2183 named y_t .

2184 Total cross-sections for various values of $\kappa_\lambda = \lambda/\lambda_{\text{SM}}$ were computed for $\sqrt{s} = 13, 14$
 2185 and 27 TeV and are displayed in Table 11.1. Note again that the cross-section has a
 2186 minimum around $\kappa_\lambda \sim 2.4$, for which the interference between triangle- and box-like
 2187 diagrams is at its most destructive. The K -factor is plotted in Fig. 11.1 as a function
 2188 of the Higgs self-coupling, this time ranging over the full, not yet excluded region for κ_λ .

2189 The distribution of the invariant mass of the Higgs boson pair hh is shown for the
 2190 considered values of κ_λ in Fig. 11.2 with their respective scale uncertainties. For values
 2191 of κ_λ that lead to minimal cross-section, the interference pattern is well-recognizable
 2192 with a dip around $m_{hh} \sim 350$ GeV, near the top-pair threshold. For greater values of

11 Variations of the triple Higgs-coupling and parton-shower effects

$\lambda_{\text{BSM}}/\lambda_{\text{SM}}$	$\sigma_{\text{NLO}}@13\text{TeV} [\text{fb}]$	$\sigma_{\text{NLO}}@14\text{TeV} [\text{fb}]$	$\sigma_{\text{NLO}}@27\text{TeV} [\text{fb}]$	K-factor@14TeV
-1	$116.71^{+16.4\%}_{-14.3\%}$	$136.91^{+16.4\%}_{-13.9\%}$	504.9	1.86
0	$62.51^{+15.8\%}_{-13.7\%}$	$73.64^{+15.4\%}_{-13.4\%}$	275.29	1.79
1	$27.84^{+11.6\%}_{-12.9\%}$	$32.88^{+13.5\%}_{-12.5\%}$	$127.7^{+11.5\%}_{-10.4\%}$	1.66
2	$12.42^{+13.1\%}_{-12.0\%}$	$14.75^{+12.0\%}_{-11.8\%}$	59.10	1.56
2.4	$11.65^{+13.9\%}_{-12.7\%}$	$13.79^{+13.5\%}_{-12.5\%}$	53.67	1.65
3	$16.28^{+16.2\%}_{-15.3\%}$	$19.07^{+17.1\%}_{-14.1\%}$	69.84	1.90
5	$81.74^{+20.0\%}_{-15.6\%}$	$95.22^{+19.7\%}_{-11.5\%}$	330.61	2.14

Table 11.1: The cross-sections for di-Higgs production at full NLO QCD are given for $\sqrt{s} = 13, 14$ and 27 TeV with scale uncertainties for several values of $\kappa_\lambda = \lambda/\lambda_{\text{SM}}$.

2193 $|\kappa_\lambda|$, this dip completely disappears and the enhanced triangle-like contribution tends
2194 to populate the lower m_{hh} -region. A similar behavior is observed for the transverse
2195 momentum of one (any) Higgs boson, as presented in Fig. 11.3, although the effect is
2196 partly washed out.

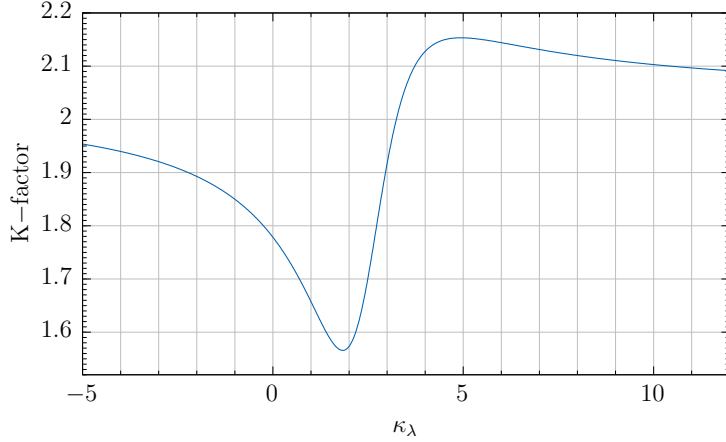


Figure 11.1: The full-theory NLO QCD K -factor is plotted as a function of the trilinear Higgs self-coupling κ_λ .

2197 Furthermore, variations of the top-Higgs Yukawa coupling y_t can be recovered by a
2198 trick: allowing for y_t variations changes Eq. (11.4) into

$$|\mathcal{M}|^2 = y_t^4 \left[\mathcal{M}_B \mathcal{M}_B^* + \frac{\lambda}{y_t} (\mathcal{M}_B \mathcal{M}_T^* + \mathcal{M}_T \mathcal{M}_B^*) + \frac{\lambda^2}{y_t^2} \mathcal{M}_T \mathcal{M}_T^* \right], \quad (11.6)$$

2199 where \mathcal{M}_B is the box- and \mathcal{M}_T is the triangle contribution, and only the ratio $\frac{\lambda}{y_t}$
2200 appears up to an overall factor. So, it suffices to generate events with the value of λ

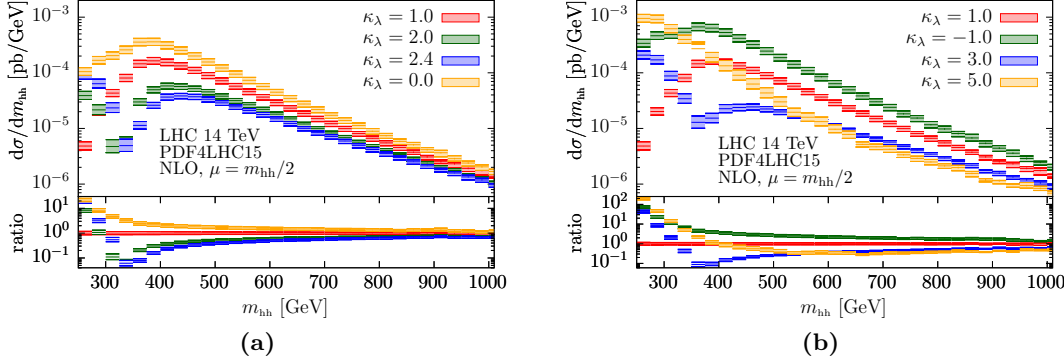


Figure 11.2: The Higgs boson pair invariant mass distributions for different values of κ_λ are given at $\sqrt{s} = 14$ TeV.

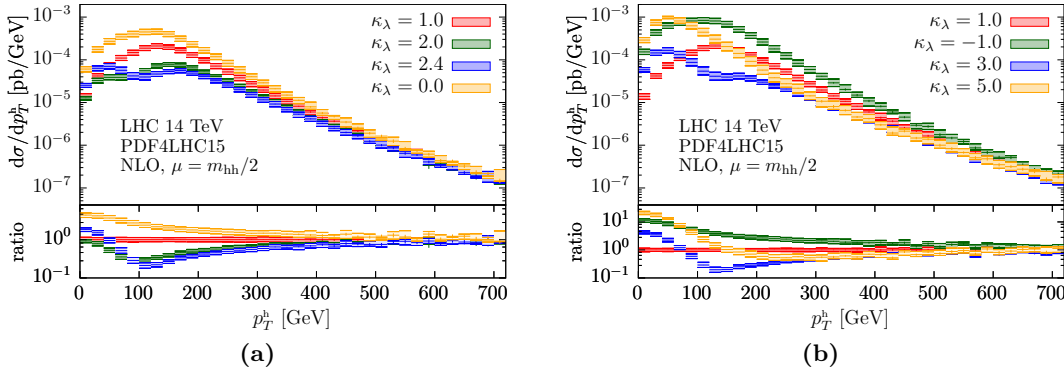


Figure 11.3: The transverse momentum of one (any) Higgs boson is shown for several values of κ_λ at $\sqrt{s} = 14$ TeV.

2201 corresponding to the desired value of the ratio $\frac{\lambda}{y_t}$, and finally rescale all results by y_t^4 .
 2202 For example, to produce results for $\kappa_\lambda = 1$, $y_t = 0.8$, the cross-section is given by

$$d\sigma_{\text{NLO}}(\kappa_\lambda = 1, y_t = 0.8) = (0.8)^4 \cdot d\sigma_{\text{NLO}}\left(y_t = 1, \kappa_\lambda = \frac{1}{0.8} = 1.25\right). \quad (11.7)$$

2203 Both m_{hh} and p_T^h distributions are displayed for y_t -values close to the currently ex-
 2204 cluded region in Fig. 11.4.

2205 11.4 Parton-shower matched predictions at NLO

2206 To be used by experimentalists for full simulation, the fixed-order calculation is matched
 2207 to a parton-shower (whose final-state can also be hadronized later on) within POWHEG.
 2208 In the fourth generation stage presented above, POWHEG generates full parton-level

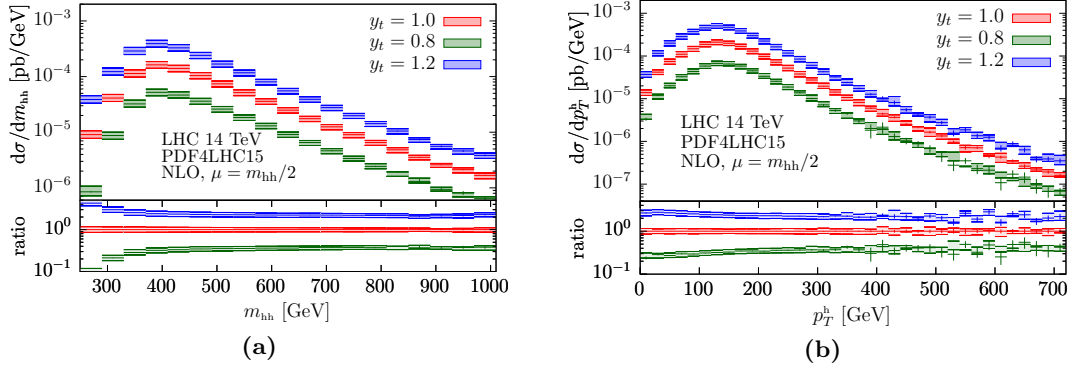


Figure 11.4: (a) The invariant mass of the Higgs boson pair system and (b) the transverse momentum of one Higgs boson are shown for three values of y_t . The procedure for generating y_t -varied events is explained in the text.

events and stores them in LHE files. These can then be used as input to most modern parton-shower programs. For this purpose, two different parton-shower programs are employed, namely **Pythia 8.235** and **Herwig7.1.4**. Additionally, both the angular-ordered (so called \tilde{q}) and the dipole shower algorithms present in **Herwig** are applied. The interfacing of both programs to POWHEG is mostly automatized: the standard **UserHooks** based on the **main31** LHE showering routine from **Pythia** are used to set the shower p_T definitions and vetoes (see Appendix D). For **Herwig7**, a process-independent interface library is present since revision **r3591** of the POWHEG-BOX-V2 which sets the **LHEReader** class and handles the **Herwig** output for the event analysis. Finally, in both showers, the tunes are left to their default values. Note that the Sudakov form factor is automatically included by POWHEG when producing LHE files. The POWHEG h_{damp} parameter is kept fixed throughout the next section and set to $h_{\text{damp}} = 250$ GeV.

In Fig. 11.5a, the transverse momentum of one (any) Higgs boson p_T^h is shown for the fixed-order NLO prediction, as well as the matched predictions to the three different shower algorithms: **Pythia 8** (PP8), and both the angular-ordered \tilde{q} shower (PH7- \tilde{q}) and the dipole shower (PH7-dipole) from **Herwig**. For variables that are inclusive in the additional radiation, like p_T^h , all predictions are very much identical. In the case of variables that are sensitive to real emission, like the angular distance of both Higgs bosons $\Delta R^{hh} = \sqrt{(\eta_1 - \eta_2)^2 + (\phi_1 - \phi_2)^2}$ shown in Fig. 11.5b, the showered predictions differ from the NLO calculation. There, the Sudakov exponent effectively resums radiation around $\Delta R^{hh} = \pi$, where the Higgs bosons are close to a back-to-back configuration. In addition, the parton-shower starts populating the region $\Delta R^{hh} < \pi$. Also, differences between the **Pythia** and **Herwig** parton-showers are already visible: while both **Herwig** showers produce very similar results, **Pythia** overshoots their prediction by $\sim 50\%$.

The differences between both parton-shower programs become more obvious when considering the transverse momentum of the Higgs boson pair system p_T^{hh} , displayed in Fig. 11.6 for two values of the Higgs trilinear coupling $\kappa_\lambda = 1$, $\kappa_\lambda = 2.4$. In that case, both **Pythia** and **Herwig** agree at low transverse momentum, until they start to deviate

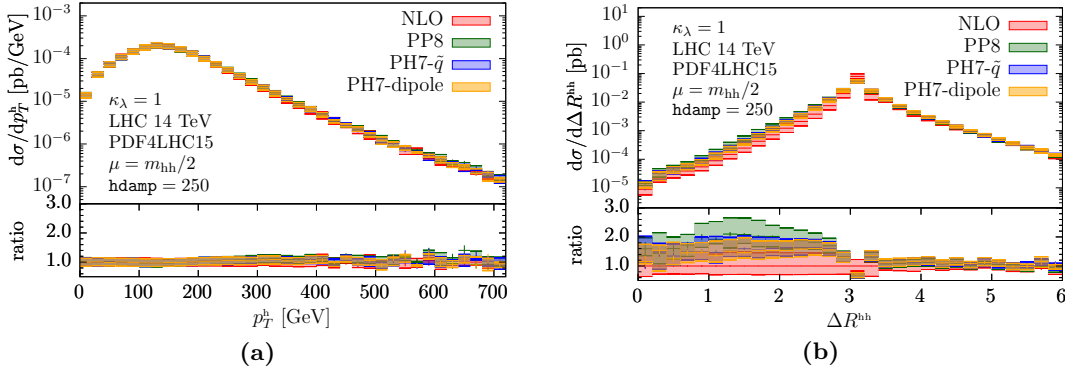


Figure 11.5: For the SM case $\kappa_\lambda = 1$, (a) the transverse momentum of one Higgs boson, and (b) the angular distance between both Higgs bosons are shown for the fixed-order NLO case, as well as for the three different parton-shower algorithms. The parton-level events from **POWHEG** are matched to **Pythia 8** (PP8), and to both the angular-ordered \tilde{q} -shower (PH7- \tilde{q}) and the dipole shower (PH7-dipole) from **Herwig7**.

at $p_T^{hh} \sim 100$ GeV already. Then, while both **Herwig** showers correctly reproduce the hard NLO emission in the high- p_T^{hh} region, the **Pythia** parton-shower produces much harder radiation and its ratio to the fixed-order prediction stagnates at ~ 2 over the remaining range. The harder spectrum from **Pythia** was found to be due to too hard sub-leading jets produced solely in the shower [271] as compared to the older **Pythia 6** parton-shower in di-Higgs production. In other processes, like $t\bar{t}$ production, sizeable differences between **Pythia** and **Herwig** had also already been observed [272].

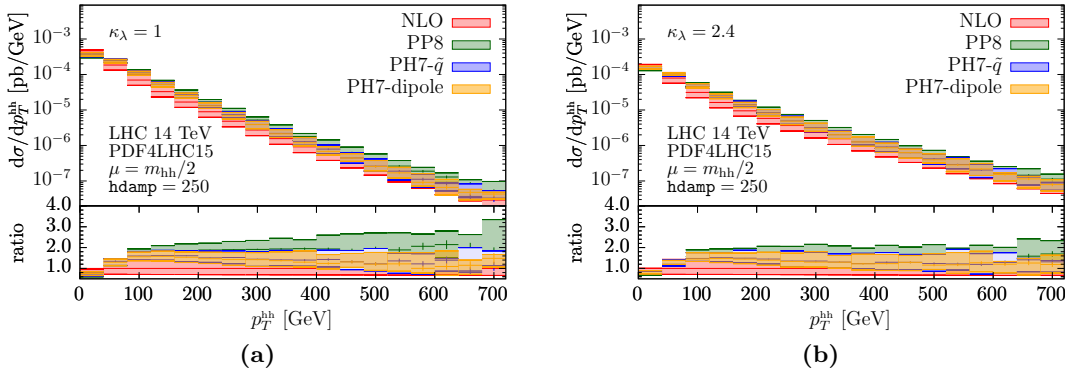


Figure 11.6: The NLO fixed-order prediction is compared to results from the three parton-shower algorithms with respect to the transverse momentum of the Higgs boson pair system p_T^{hh} for (a) $\kappa_\lambda = 1$ and (b) $\kappa_\lambda = 2.4$.

As a way to estimate shower-matching uncertainties, the maximal transverse momentum allowed for shower emissions can be set in **Herwig** by varying the so-called hard scale

2246 μ_Q . The parameter `HardScaleFactor` is varied to $c_Q = 0.5$, $c_Q = 2$ and applied on the
 2247 central hard shower scale separately for the up- and down-variations of the renormalization
 2248 and factorization scales $\mu_{R,F}$. In Fig. 11.7, the result is presented for the di-Higgs
 2249 transverse momentum p_T^{hh} and the angular separation between the Higgs bosons ΔR^{hh} .
 2250 The shower scale variations add to the renormalization/factorizations scale uncertainties,
 2251 bringing their common envelope to a corresponding 50% – 100% overall systematic
 2252 uncertainty in the far- p_T^{hh} region of the distribution. The differences between the
 2253 central `Pythia` and `Herwig` predictions are then partly covered by the hard shower scale
 2254 variations.

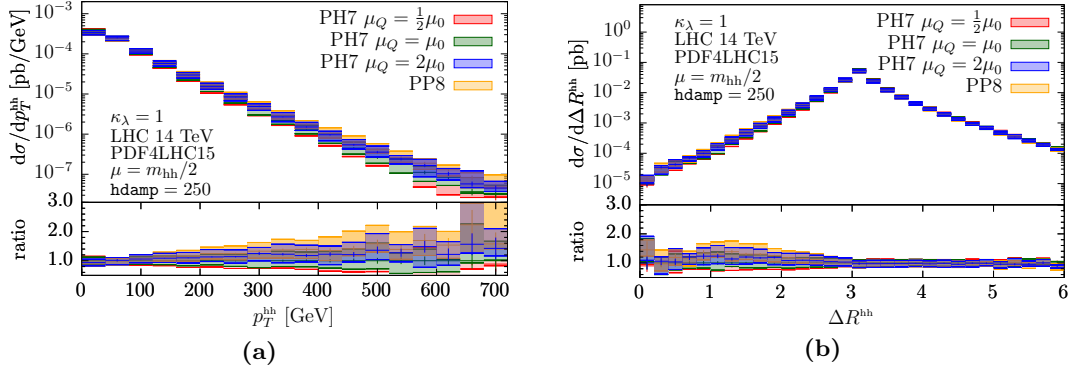


Figure 11.7: (a) The di-Higgs transverse momentum p_T^{hh} and (b) the angular separation ΔR^{hh} between the Higgs bosons are shown for variations of the `Herwig` hard shower scale, which regulates the maximal allowed transverse momentum of shower emissions. The hard scale $\mu_Q = c_Q\mu_0$ is varied by $c_Q \in \{\frac{1}{2}, 2\}$ with respect to the default scale μ_0 .

2255 All in all, considering both scale and parton-shower uncertainties, the Higgs pair
 2256 process underlines the necessity of computing higher-order corrections in both fixed-order
 2257 and resummation accuracy. In the future, it will be informative to study parton-shower
 2258 (as well as other non-perturbative, e.g. hadronization) modeling effects in loop-induced
 2259 color singlet production and try and reduce the sizeable associated uncertainties.

2260 12 Conclusion and Outlook

2261 A precise determination of the top-quark mass is argued to be important for several
2262 reasons: its value is used in global electroweak fits, and it largely affects the running
2263 of the Higgs quartic coupling and thus the stability of the SM vacuum. Nowadays,
2264 experimental measurements have reduced the top-quark mass uncertainty to the point
2265 where new questions have to be asked. In particular:

- 2266 • Are the theoretical descriptions of the $t\bar{t}$ final-state used in MC simulations for
2267 experimental analyses good enough?
- 2268 • Do the uncertainties correctly cover the unknown higher-order corrections and
2269 other neglected contributions?
- 2270 • What is the exact nature of the measured MC top-quark mass, and how does it
2271 relate to other mass schemes?

2272 The answer to these questions requires a lot of effort from both the experimental
2273 and theoretical sides. One specific assumption made in most $t\bar{t}$ analyses relies on the
2274 factorization of top-quark pair production and decay: such a treatment is called the
2275 narrow-width approximation (NWA). In automatized particle-level MC event generators,
2276 this description usually contains NLO QCD production of a $t\bar{t}$ pair and LO decay of the
2277 top quarks. The full parton-level final-state is then handed over to the parton-shower
2278 and hadronization algorithms. It was shown that for certain observables, higher-order
2279 and off-shell effects can lead to important differences. Specifically, NLO QCD corrections
2280 to the top-quark decay can have sizeable effects on the kinematics of its decay products.

2281 To reach a quantifiable answer to the first and second questions stated above, the
2282 determination of the top-quark mass in the dilepton channel is taken as an example.
2283 Experimentally, the template fit method provides an extraction of the MC top-quark
2284 mass. Following the same procedure, template distributions for $pp \rightarrow (e^+\nu_e)(\mu^-\bar{\nu}_\mu)b\bar{b}$
2285 are produced at $\sqrt{s} = 13$ TeV using four different theoretical descriptions of the final-
2286 state at parton-level. Starting from top-quark pair production at NLO QCD, three
2287 different levels of accuracy for the top-quark decay are investigated: LO, respectively
2288 NLO QCD, as well as decay by a parton-shower. Finally, these three NWA predictions
2289 are compared to a $W^+W^-b\bar{b}$ calculation at parton-level. The latter contains Feynman
2290 diagrams that are not present in the NWA, namely diagrams with top-quark legs that
2291 do not factorize, and diagrams with zero or one top-quark propagator only.

12 Conclusion and Outlook

2292 In an implementation similar to the ATLAS analysis, distributions of the lepton and
2293 b -jet invariant mass $m_{\ell b}$ are parametrized separately for a set of MC input top-quark
2294 masses. Once the parameters are fixed, only the top-quark mass is left as a free quantity
2295 to be determined by a fit to data. To compare the different calculations two-by-two,
2296 the parametrization from one theoretical prediction is used in an unbinned likelihood
2297 fit to pseudo-data drawn from another prediction. The offsets outlined in the extracted
2298 top-quark mass represent the systematic uncertainty accompanying the use of the in-
2299 complete set of diagrams. It is shown that NLO corrections to the top-quark decay in
2300 the NWA have an important effect on the extracted top-quark mass. In fact, the offset
2301 in the top-quark mass is opposite in sign and higher in absolute value than from NLO
2302 corrections to $t\bar{t}$ production. When comparing the NLO top-quark decay to the full
2303 $W^+W^-b\bar{b}$ computation, the offset is reduced to (0.83 ± 0.07) GeV. More importantly,
2304 the offset in the extracted top-quark mass stemming from renormalization/factorization
2305 scale variations now overlap. These comparisons suggest that the scale uncertainties in
2306 $t\bar{t}$ production with LO top-quark decay are underestimated. While the NLO corrections
2307 to the top-quark decay describe correctly the emission of a hard jet from the final-state,
2308 the parton-shower is formally of LO accuracy in QCD. Yet, because it produces addi-
2309 tional radiation as the parton-level is fully-showered down to hadronization scales, it
2310 comes close to the top-quark mass extracted from $W^+W^-b\bar{b}$ samples, with an offset of
2311 (-0.09 ± 0.07) GeV.

2312 The studies presented above suffer from two complications: first, they were realized at
2313 parton-level, and it is unclear if the bias in the extracted top-quark mass is as important
2314 at detector-level. Second, they only compared pure $t\bar{t}$ predictions to the full $W^+W^-b\bar{b}$
2315 computation, while usually single-top production in the Wt channel is also included in
2316 the signal. As a first attempt at curing both issues, a setup implemented in the ATLAS
2317 **Athena** framework is presented, where particle-level distributions can be folded up to
2318 detector-level. Bin migration matrices and detector efficiencies are derived from simu-
2319 lated $t\bar{t}$ samples produced at five different top-quark mass points. In parallel, $W^+W^-b\bar{b}$
2320 samples are generated using the **bb41** MC generator present in the POWHEG-BOX-RES
2321 framework, and matched to the **Herwig7** parton-shower. This time, the folding ingre-
2322 dients from the $t\bar{t}$ prediction are used to bring the $W^+W^-b\bar{b}$ distribution of $m_{\ell b}$ to
2323 detector-level. The same procedure of template parametrization and fit to pseudo-data
2324 is repeated at detector-level, and the templates from $t\bar{t}$ and single-top Wt are compared
2325 to the full $W^+W^-b\bar{b}$ calculation. This procedure is fast, and avoids the need to simulate
2326 all MC variation samples. In relation to the third question given above, the folding setup
2327 might be useful to compute an estimate of the top-quark mass IR-dependence on e.g.
2328 the shower cutoff scale Q_0 in **Herwig**: in turn, this would help shed some light on the
2329 controversial relations between different mass definitions.

2330 The top-quark mass also has sizeable theoretical effects in the computation of Higgs
2331 boson pair production in gluon-gluon fusion at the LHC. This process is important since
2332 it is the golden channel to experimentally constrain the trilinear Higgs self-coupling. At
2333 LO, Higgs pair production takes place via an intermediate top-quark loop. At NLO, the
2334 virtual contributions are thus of two-loop order and the Feynman integrals contain up to
2335 four mass scales. Only part of the integral families is known analytically at this point.

2336 Nevertheless, these integrals were recently evaluated numerically with the full top-quark
2337 mass dependence using sector decomposition. To allow for variations of the Higgs boson
2338 couplings to the QCD sector, a non-linear EFT framework is introduced under the form of
2339 the Electroweak Chiral Lagrangian (EWChL). At NLO in QCD, this class of extensions
2340 contains five couplings parametrizing variations from the SM: the Higgs-top Yukawa
2341 coupling c_t and the trilinear Higgs self-coupling c_{hhh} , as well as effective couplings for
2342 two-top-two-Higgs c_{tt} , gluon-gluon-Higgs c_{ggh} and two-gluons-two-Higgs c_{gghh} vertices.

2343 Basing on a grid of virtual two-loop amplitudes for pre-sampled phase-space points in
2344 the SM, cross-section results are presented for Higgs pair production at NLO QCD with
2345 full top-quark mass dependence in the EWChL framework. Both inclusive and differen-
2346 tial cross-sections are produced at $\sqrt{s} = 14$ TeV for several benchmark points character-
2347 izing the BSM parameter space. Inclusive cross-sections exhibit large K -factors up to
2348 $K \sim 2.34$ depending on the considered BM point. In particular, once the full top-quark
2349 loops are taken into account, a sizeable dependence of the K -factors on the top-quark
2350 couplings c_t and c_{tt} is underlined, as well as on the trilinear coupling c_{hhh} .

2351 Finally, a MC event generator is put forward for use by experimentalists in Higgs pair
2352 searches. Within the POWHEG-BOX-V2 framework, the MC generator `ggHH` for Higgs
2353 pair production in the SM at NLO QCD is extended with the possibility of varying
2354 the trilinear Higgs self-coupling and the Higgs-top Yukawa coupling. In this program,
2355 the hard NLO matrix-element can be matched to both `Pythia8` and `Herwig7` parton-
2356 showers. Some first studies suggest that there are large uncertainties associated to the
2357 parton-shower.

2358 [Some general comments on top-Higgs physics in the future]

2359 **Bibliography**

- 2360 [1] PARTICLE DATA GROUP collaboration, *Review of Particle Physics*, *Phys. Rev. D*
2361 **98** (2018) 030001.
- 2362 [2] CDF collaboration, *Observation of Top Quark Production in $\bar{p}p$ Collisions with*
2363 *the Collider Detector at Fermilab*, *Phys. Rev. Lett.* **74** (1995) 2626–2631.
- 2364 [3] D0 collaboration, *Observation of the top quark*, *Phys. Rev. Lett.* **74** (1995)
2365 2632–2637.
- 2366 [4] “LHC Top Working Group.”
2367 <https://twiki.cern.ch/twiki/bin/view/LHCPhysics/LHCTopWG>.
- 2368 [5] ATLAS collaboration, *Measurement of the top quark mass in the $t\bar{t} \rightarrow$*
- 2369 *lepton+jets channel from $\sqrt{s} = 8$ TeV ATLAS data and combination with*
2370 *previous results*, *Submitted to: Eur. Phys. J.* (2018) [arXiv:1810.01772].
- 2371 [6] CMS collaboration, *Measurement of the top quark mass using proton-proton data*
2372 *at $\sqrt{s} = 7$ and 8 TeV*, *Phys. Rev.* **D93** (2016) 072004 [arXiv:1509.04044].
- 2373 [7] P. Marquard, A.V. Smirnov, V.A. Smirnov et al., *Quark Mass Relations to*
2374 *Four-Loop Order in Perturbative QCD*, *Phys. Rev. Lett.* **114** (2015) 142002
2375 [arXiv:1502.01030].
- 2376 [8] M. Beneke and V.M. Braun, *Heavy quark effective theory beyond perturbation*
2377 *theory: Renormalons, the pole mass and the residual mass term*, *Nucl. Phys.*
2378 **B426** (1994) 301–343 [arXiv:hep-ph/9402364].
- 2379 [9] I.I.Y. Bigi, M.A. Shifman, N.G. Uraltsev et al., *The Pole mass of the heavy*
2380 *quark. Perturbation theory and beyond*, *Phys. Rev.* **D50** (1994) 2234–2246
2381 [arXiv:hep-ph/9402360].
- 2382 [10] M. Beneke, *More on ambiguities in the pole mass*, *Phys. Lett.* **B344** (1995)
2383 341–347 [arXiv:hep-ph/9408380].
- 2384 [11] A.H. Hoang, C. Lepenik and M. Preisser, *On the Light Massive Flavor*
2385 *Dependence of the Large Order Asymptotic Behavior and the Ambiguity of the*
2386 *Pole Mass*, *JHEP* **09** (2017) 099 [arXiv:1706.08526].
- 2387 [12] A.H. Hoang and I.W. Stewart, *Top Mass Measurements from Jets and the*
2388 *Tevatron Top-Quark Mass*, *Nucl. Phys. Proc. Suppl.* **185** (2008) 220–226
2389 [arXiv:0808.0222].

Bibliography

- 2390 [13] A.H. Hoang, S. Plätzer and D. Samitz, *On the Cutoff Dependence of the Quark
2391 Mass Parameter in Angular Ordered Parton Showers*, *JHEP* **10** (2018) 200
2392 [arXiv:1807.06617].
- 2393 [14] ATLAS collaboration, *Combined measurements of Higgs boson production and
2394 decay using up to 80 fb^{-1} of proton-proton collision data at $\sqrt{s} = 13 \text{ TeV}$
2395 collected with the ATLAS experiment*, Tech. Rep. ATLAS-CONF-2018-031,
2396 CERN, Geneva, Jul 2018.
- 2397 [15] CMS collaboration, *Combined measurements of the Higgs boson's couplings at
2398 $\sqrt{s} = 13 \text{ TeV}$* , Tech. Rep. CMS-PAS-HIG-17-031, CERN, Geneva, 2018.
- 2399 [16] ATLAS collaboration, *Combination of searches for Higgs boson pairs in pp
2400 collisions at 13 TeV with the ATLAS experiment.*, Tech. Rep.
2401 ATLAS-CONF-2018-043, CERN, Geneva, Sep 2018.
- 2402 [17] P. Nason, *A New method for combining NLO QCD with shower Monte Carlo
2403 algorithms*, *JHEP* **11** (2004) 040 [arXiv:hep-ph/0409146].
- 2404 [18] S. Frixione, P. Nason and C. Oleari, *Matching NLO QCD computations with
2405 Parton Shower simulations: the POWHEG method*, *JHEP* **11** (2007) 070
2406 [arXiv:0709.2092].
- 2407 [19] S. Alioli, P. Nason, C. Oleari et al., *A general framework for implementing NLO
2408 calculations in shower Monte Carlo programs: the POWHEG BOX*, *JHEP* **06**
2409 (2010) 043 [arXiv:1002.2581].
- 2410 [20] SUPER-KAMIOKANDE collaboration, *Evidence for oscillation of atmospheric
2411 neutrinos*, *Phys. Rev. Lett.* **81** (1998) 1562–1567.
- 2412 [21] S.L. Glashow, *The renormalizability of vector meson interactions*, *Nuclear
2413 Physics* **10** (1959) 107 – 117.
- 2414 [22] S. Weinberg, *A model of leptons*, *Phys. Rev. Lett.* **19** (1967) 1264–1266.
- 2415 [23] A. Salam and J.C. Ward, *Weak and electromagnetic interactions*, *Il Nuovo
2416 Cimento* **11** (1959) 568–577.
- 2417 [24] D.J. Gross and F. Wilczek, *Ultraviolet behavior of non-abelian gauge theories*,
2418 *Phys. Rev. Lett.* **30** (1973) 1343–1346.
- 2419 [25] H.D. Politzer, *Reliable perturbative results for strong interactions?*, *Phys. Rev.
2420 Lett.* **30** (1973) 1346–1349.
- 2421 [26] ATLAS collaboration, *Standard Model Summary Plots Spring 2019*, Tech. Rep.
2422 ATL-PHYS-PUB-2019-010, CERN, Geneva, Mar 2019.
- 2423 [27] F. Englert and R. Brout, *Broken symmetry and the mass of gauge vector mesons*,
2424 *Phys. Rev. Lett.* **13** (1964) 321–323.

- [2425] [28] P.W. Higgs, *Broken symmetries and the masses of gauge bosons*, *Phys. Rev. Lett.* **13** (1964) 508–509.
- [2426]
- [2427] [29] G.S. Guralnik, C.R. Hagen and T.W.B. Kibble, *Global conservation laws and massless particles*, *Phys. Rev. Lett.* **13** (1964) 585–587.
- [2428]
- [2429] [30] J. Bardeen, L.N. Cooper and J.R. Schrieffer, *Theory of superconductivity*, *Phys. Rev.* **108** (1957) 1175–1204.
- [2430]
- [2431] [31] T.D. Lee, *A Theory of Spontaneous T Violation*, *Phys. Rev. D* **8** (1973) 1226–1239.
- [2432]
- [2433] [32] S. Dimopoulos and H. Georgi, *Softly Broken Supersymmetry and SU(5)*, *Nucl. Phys.* **B193** (1981) 150–162.
- [2434]
- [2435] [33] LHC HIGGS CROSS SECTION WORKING GROUP collaboration, *Handbook of LHC Higgs Cross Sections: 4. Deciphering the Nature of the Higgs Sector*, [arXiv:1610.07922].
- [2436]
- [2437]
- [2438] [34] K.G. Chetyrkin and M.F. Zoller, *Three-loop β -functions for top-Yukawa and the Higgs self-interaction in the standard model*, *JHEP* **2012** (2012) 33.
- [2439]
- [2440] [35] S. Chigusa, T. Moroi and Y. Shoji, *State-of-the-Art Calculation of the Decay Rate of Electroweak Vacuum in the Standard Model*, *Phys. Rev. Lett.* **119** (2017) 211801.
- [2441]
- [2442]
- [2443] [36] G. Degrassi, S. Di Vita, J. Elias-Miró et al., *Higgs mass and vacuum stability in the Standard Model at NNLO*, *JHEP* **2012** (2012) 98.
- [2444]
- [2445] [37] A.V. Bednyakov, B.A. Kniehl, A.F. Pikelner et al., *Stability of the electroweak vacuum: Gauge independence and advanced precision*, *Phys. Rev. Lett.* **115** (2015) 201802.
- [2446]
- [2447]
- [2448] [38] J. Schechter and J.W.F. Valle, *Neutrino masses in $SU(2) \otimes U(1)$ theories*, *Phys. Rev. D* **22** (1980) 2227–2235.
- [2449]
- [2450] [39] T. Yanagida, *Horizontal Symmetry and Masses of Neutrinos*, *Progress of Theoretical Physics* **64** (1980) 1103–1105.
- [2451]
- [2452] [40] R.N. Mohapatra and G. Senjanovic, *Neutrino Mass and Spontaneous Parity Nonconservation*, *Phys. Rev. Lett.* **44** (1980) 912.
- [2453]
- [2454] [41] F. Borzumati, Y. Grossman, E. Nardi et al., *Neutrino masses and mixing in supersymmetric models without R parity*, *Phys. Lett.* **B384** (1996) 123–130 [arXiv:hep-ph/9606251].
- [2455]
- [2456]
- [2457] [42] N. Haba, M. Matsuda and M. Tanimoto, *Large neutrino flavor mixings and gauge mediated supersymmetry breaking scenario*, *Phys. Lett.* **B478** (2000) 351–357 [arXiv:hep-ph/9911511].
- [2458]
- [2459]

Bibliography

- 2460 [43] B.S. DeWitt, *Quantum Theory of Gravity. I. The Canonical Theory*, *Phys. Rev.*
2461 **160** (1967) 1113–1148.
- 2462 [44] B.S. DeWitt, *Quantum Theory of Gravity. II. The Manifestly Covariant Theory*,
2463 *Phys. Rev.* **162** (1967) 1195–1239.
- 2464 [45] B.S. DeWitt, *Quantum Theory of Gravity. III. Applications of the Covariant
2465 Theory*, *Phys. Rev.* **162** (1967) 1239–1256.
- 2466 [46] F. Zwicky, *Die Rotverschiebung von extragalaktischen Nebeln*, *Helvetica Physica
2467 Acta* **6** (1933) 110–127.
- 2468 [47] H.W. Babcock, *The rotation of the Andromeda Nebula*, *Lick Observatory Bulletin*
2469 **19** (1939) 41–51.
- 2470 [48] K.C. Freeman, *On the Disks of Spiral and S0 Galaxies*, **160** (1970) 811.
- 2471 [49] V.C. Rubin and W.K. Ford, Jr., *Rotation of the Andromeda Nebula from a
2472 Spectroscopic Survey of Emission Regions*, **159** (1970) 379.
- 2473 [50] K.G. Begeman, A.H. Broeils and R.H. Sanders, *Extended rotation curves of
2474 spiral galaxies - Dark haloes and modified dynamics*, **249** (1991) 523–537.
- 2475 [51] A.D. Sakharov, *Violation of CP Invariance, C asymmetry, and baryon
2476 asymmetry of the universe*, *Pisma Zh. Eksp. Teor. Fiz.* **5** (1967) 32–35.
- 2477 [52] PLANCK collaboration, *Planck 2013 results. XVI. Cosmological parameters*,
2478 *Astron. Astrophys.* **571** (2014) A16 [[arXiv:1303.5076](#)].
- 2479 [53] S. Weinberg, *Gauge Hierarchies*, *Phys. Lett.* **82B** (1979) 387–391.
- 2480 [54] M.D. Schwartz, *Quantum Field Theory and the Standard Model*. Cambridge
2481 University Press, 2014.
- 2482 [55] M.E. Peskin and D.V. Schroeder, *An Introduction to Quantum Field Theory*.
2483 Addison-Wesley, Reading, USA, 1995.
- 2484 [56] G. Isidori, *Lecture notes in Quantum Field Theory II*, Frühjahrsemester 2015.
- 2485 [57] G. Buchalla, *Lecture notes for Introduction to the SM*, Wintersemester 2008.
- 2486 [58] G. Heinrich, *Lecture notes for Colorful Loops: Introduction to Quantum
2487 Chromodynamics and Loop Calculations*, Sommersemester 2018.
- 2488 [59] H.B.G. Casimir, *On the Attraction Between Two Perfectly Conducting Plates*,
2489 *Indag. Math.* **10** (1948) 261–263.
- 2490 [60] G. 't Hooft and M. Veltman, *Regularization and renormalization of gauge fields*,
2491 *Nuclear Physics B* **44** (1972) 189 – 213.

- [61] G. Passarino and M. Veltman, *One-loop corrections for e^+e^- annihilation into $\mu^+\mu^-$ in the Weinberg model*, *Nuclear Physics B* **160** (1979) 151 – 207.
- [62] A. Denner and S. Dittmaier, *Reduction schemes for one-loop tensor integrals*, *Nucl. Phys.* **B734** (2006) 62–115 [arXiv:hep-ph/0509141].
- [63] T. Binoth, J.P. Guillet, G. Heinrich et al., *An algebraic/numerical formalism for one-loop multi-leg amplitudes*, *JHEP* **10** (2005) 015 [arXiv:hep-ph/0504267].
- [64] J.M. Campbell, E.W.N. Glover and D.J. Miller, *One loop tensor integrals in dimensional regularization*, *Nucl. Phys.* **B498** (1997) 397–442 [arXiv:hep-ph/9612413].
- [65] J. Fleischer, F. Jegerlehner and O.V. Tarasov, *Algebraic reduction of one loop Feynman graph amplitudes*, *Nucl. Phys.* **B566** (2000) 423–440 [arXiv:hep-ph/9907327].
- [66] A.I. Davydychev, *A Simple formula for reducing Feynman diagrams to scalar integrals*, *Phys. Lett.* **B263** (1991) 107–111.
- [67] C.G. Callan, *Broken scale invariance in scalar field theory*, *Phys. Rev. D* **2** (1970) 1541–1547.
- [68] K. Symanzik, *Small distance behaviour in field theory and power counting*, *Communications in Mathematical Physics* **18** (1970) 227–246.
- [69] K. Symanzik, *Small-distance-behaviour analysis and Wilson expansions*, *Communications in Mathematical Physics* **23** (1971) 49–86.
- [70] A.D. Martin, W.J. Stirling, R.S. Thorne et al., *Parton distributions for the LHC*, *The European Physical Journal C* **63** (2009) 189–285.
- [71] S. Hoeche, “SLAC Theoretical Physics, Monte-Carlo Simulations.” <https://theory.slac.stanford.edu/our-research/simulations>.
- [72] T. Hahn, *Cuba—a library for multidimensional numerical integration*, *Computer Physics Communications* **168** (2005) 78 – 95.
- [73] G.P. Lepage, *A new algorithm for adaptive multidimensional integration*, *Journal of Computational Physics* **27** (1978) 192 – 203.
- [74] J.H. Friedman and M.H. Wright, *A nested partitioning procedure for numerical multiple integration*, *ACM Trans. Math. Softw.* **7** (1981) 76–92.
- [75] W.H. Press and G.R. Farrar, *Recursive Stratified Sampling for Multidimensional Monte Carlo Integration*, *Computers in Physics* **4** (1990) 190–195.
- [76] J. Berntsen, T.O. Espelid and A. Genz, *An Adaptive Algorithm for the Approximate Calculation of Multiple Integrals*, *ACM Trans. Math. Softw.* **17** (1991) 437–451.

Bibliography

- 2527 [77] A. Buckley, J. Ferrando, S. Lloyd et al., *LHAPDF6: parton density access in the*
2528 *LHC precision era*, *The European Physical Journal C* **75** (2015) 132.
- 2529 [78] J.M. Campbell, R.K. Ellis and W.T. Giele, *A multi-threaded version of MCFM*,
2530 *The European Physical Journal C* **75** (2015) 246.
- 2531 [79] K. Arnold, M. Bähr, G. Bozzi et al., *VBFNLO: A parton level Monte Carlo for*
2532 *processes with electroweak bosons*, *Computer Physics Communications* **180**
2533 (2009) 1661 – 1670.
- 2534 [80] J. Baglio et al., *VBFNLO: A Parton Level Monte Carlo for Processes with*
2535 *Electroweak Bosons - Manual for Version 2.7.0*, [arXiv:1107.4038].
- 2536 [81] J. Baglio et al., *Release Note - VBFNLO 2.7.0*, [arXiv:1404.3940].
- 2537 [82] Z. Bern, L.J. Dixon, F. Febres Cordero et al., *The BlackHat Library for*
2538 *One-Loop Amplitudes*, *J. Phys. Conf. Ser.* **523** (2014) 012051 [arXiv:1310.2808].
- 2539 [83] V. Hirschi, R. Frederix, S. Frixione et al., *Automation of one-loop QCD*
2540 *corrections*, *JHEP* **05** (2011) 044 [arXiv:1103.0621].
- 2541 [84] V. Hirschi, *New developments in MadLoop*, [arXiv:1111.2708].
- 2542 [85] R. Pittau, *Status of MadLoop/aMC@NLO*, in *International Workshop on Future*
2543 *Linear Colliders (LCWS11) Granada, Spain, September 26-30, 2011*, 2012,
2544 [arXiv:1202.5781].
- 2545 [86] J. Alwall, R. Frederix, S. Frixione et al., *The automated computation of tree-level*
2546 *and next-to-leading order differential cross sections, and their matching to parton*
2547 *shower simulations*, *JHEP* **2014** (2014) 79.
- 2548 [87] F. Cascioli, P. Maierhöfer and S. Pozzorini, *Scattering amplitudes with open*
2549 *loops*, *Phys. Rev. Lett.* **108** (2012) 111601.
- 2550 [88] F. Buccioni, S. Pozzorini and M. Zoller, *On-the-fly reduction of open loops*, *The*
2551 *European Physical Journal C* **78** (2018) 70.
- 2552 [89] G. Cullen, N. Greiner, G. Heinrich et al., *Automated one-loop calculations with*
2553 *GoSam*, *The European Physical Journal C* **72** (2012) 1889.
- 2554 [90] G. Cullen, H. van Deurzen, N. Greiner et al., *GoSam-2.0: a tool for automated*
2555 *one-loop calculations within the Standard Model and beyond*, *The European*
2556 *Physical Journal C* **74** (2014) 3001.
- 2557 [91] S. Actis, A. Denner, L. Hofer et al., *Recursive generation of one-loop amplitudes*
2558 *in the Standard Model*, *JHEP* **04** (2013) 037 [arXiv:1211.6316].
- 2559 [92] S. Actis, A. Denner, L. Hofer et al., *RECOLA: REcursive Computation of*
2560 *One-Loop Amplitudes*, *Comput. Phys. Commun.* **214** (2017) 140–173
2561 [arXiv:1605.01090].

- [93] G. Bevilacqua, M. Czakon, M.V. Garzelli et al., *HELAC-NLO*, *Comput. Phys. Commun.* **184** (2013) 986–997 [[arXiv:1110.1499](#)].
- [94] S. Badger, B. Biedermann, P. Uwer et al., *Numerical evaluation of virtual corrections to multi-jet production in massless QCD*, *Computer Physics Communications* **184** (2013) 1981 – 1998.
- [95] F. Campanario, T.M. Figy, S. Plätzer et al., *Electroweak Higgs Boson Plus Three Jet Production at Next-to-Leading-Order QCD*, *Phys. Rev. Lett.* **111** (2013) 211802.
- [96] T. Binoth, F. Boudjema, G. Dissertori et al., *A proposal for a standard interface between Monte Carlo tools and one-loop programs*, *Computer Physics Communications* **181** (2010) 1612 – 1622.
- [97] S. Alioli, S. Badger, J. Bellm et al., *Update of the Binoth Les Houches Accord for a standard interface between Monte Carlo tools and one-loop programs*, *Computer Physics Communications* **185** (2014) 560 – 571.
- [98] P. Nogueira, *Automatic Feynman Graph Generation*, *Journal of Computational Physics* **105** (1993) 279 – 289.
- [99] J.A.M. Vermaasen, *New features of FORM*, [[arXiv:math-ph/0010025](#)].
- [100] T. Peraro, *Ninja: Automated integrand reduction via Laurent expansion for one-loop amplitudes*, *Computer Physics Communications* **185** (2014) 2771 – 2797.
- [101] G. Cullen, J.P. Guillet, G. Heinrich et al., *Golem95C: A library for one-loop integrals with complex masses*, *Computer Physics Communications* **182** (2011) 2276 – 2284.
- [102] J.P. Guillet, G. Heinrich and J.F. von Soden-Fraunhofen, *Tools for NLO automation: extension of the Golem95C integral library*, *Comput. Phys. Commun.* **185** (2014) 1828–1834 [[arXiv:1312.3887](#)].
- [103] P. Mastrolia, G. Ossola, T. Reiter et al., *Scattering Amplitudes from Unitarity-based Reduction Algorithm at the Integrand-level*, *JHEP* **08** (2010) 080 [[arXiv:1006.0710](#)].
- [104] R.K. Ellis and G. Zanderighi, *Scalar one-loop integrals for QCD*, *JHEP* **02** (2008) 002 [[arXiv:0712.1851](#)].
- [105] A. van Hameren, *Oneloop: For the evaluation of one-loop scalar functions*, *Computer Physics Communications* **182** (2011) 2427 – 2438.
- [106] S. Catani and M.H. Seymour, *A General algorithm for calculating jet cross-sections in NLO QCD*, *Nucl. Phys.* **B485** (1997) 291–419 [[arXiv:hep-ph/9605323](#)].

Bibliography

- 2597 [107] S. Frixione, Z. Kunszt and A. Signer, *Three jet cross-sections to next-to-leading*
2598 *order, Nucl. Phys.* **B467** (1996) 399–442 [[arXiv:hep-ph/9512328](#)].
- 2599 [108] S. Frixione, *A General approach to jet cross-sections in QCD, Nucl. Phys.* **B507**
2600 (1997) 295–314 [[arXiv:hep-ph/9706545](#)].
- 2601 [109] G. Salam, *ICTP-SAIFR School on QCD and LHC physics, Sao Paulo, Brazil,*
2602 July 2015.
- 2603 [110] G. Altarelli and G. Parisi, *Asymptotic Freedom in Parton Language, Nucl. Phys.*
2604 **B126** (1977) 298–318.
- 2605 [111] Y.L. Dokshitzer, *Calculation of the Structure Functions for Deep Inelastic*
2606 *Scattering and e^+e^- Annihilation by Perturbation Theory in Quantum*
2607 *Chromodynamics., Sov. Phys. JETP* **46** (1977) 641–653.
- 2608 [112] V.N. Gribov and L.N. Lipatov, *Deep inelastic ep scattering in perturbation*
2609 *theory, Sov. J. Nucl. Phys.* **15** (1972) 438–450.
- 2610 [113] M. Dasgupta, F.A. Dreyer, K. Hamilton et al., *Logarithmic accuracy of parton*
2611 *showers: a fixed-order study, JHEP* **09** (2018) 033 [[arXiv:1805.09327](#)].
- 2612 [114] M. Bahr et al., *Herwig++ Physics and Manual, Eur. Phys. J.* **C58** (2008)
2613 639–707 [[arXiv:0803.0883](#)].
- 2614 [115] J. Bellm et al., *Herwig 7.0/Herwig++ 3.0 release note, Eur. Phys. J.* **C76** (2016)
2615 196 [[arXiv:1512.01178](#)].
- 2616 [116] S. Frixione and B.R. Webber, *Matching NLO QCD computations and parton*
2617 *shower simulations, JHEP* **2002** (2002) 029–029.
- 2618 [117] S. Frixione, P. Nason and C. Oleari, *Matching NLO QCD computations with*
2619 *parton shower simulations: the POWHEG method, JHEP* **2007** (2007) 070–070.
- 2620 [118] S. Gieseke, P. Stephens and B. Webber, *New formalism for QCD parton showers,*
2621 *JHEP* **12** (2003) 045 [[arXiv:hep-ph/0310083](#)].
- 2622 [119] T. Sjostrand, S. Mrenna and P.Z. Skands, *PYTHIA 6.4 Physics and Manual,*
2623 *JHEP* **05** (2006) 026 [[arXiv:hep-ph/0603175](#)].
- 2624 [120] T. Sjostrand, S. Mrenna and P.Z. Skands, *A Brief Introduction to PYTHIA 8.1,*
2625 *Comput. Phys. Commun.* **178** (2008) 852–867 [[arXiv:0710.3820](#)].
- 2626 [121] T. Gleisberg, S. Hoeche, F. Krauss et al., *Event generation with SHERPA 1.1,*
2627 *JHEP* **02** (2009) 007 [[arXiv:0811.4622](#)].
- 2628 [122] B. Andersson, G. Gustafson, G. Ingelman et al., *Parton fragmentation and string*
2629 *dynamics, Physics Reports* **97** (1983) 31 – 145.

- 2630 [123] T. Sjöstrand, S. Ask, J.R. Christiansen et al., *An introduction to PYTHIA 8.2*,
2631 *Computer Physics Communications* **191** (2015) 159 – 177.
- 2632 [124] A. Kupco, *Cluster hadronization in HERWIG 5.9*, in *Monte Carlo generators for*
2633 *HERA physics. Proceedings, Workshop, Hamburg, Germany, 1998-1999*,
2634 292–300, 1998, [arXiv:[hep-ph/9906412](#)].
- 2635 [125] S. Gieseke, F. Loshaj and P. Kirchgässner, *Soft and diffractive scattering with the*
2636 *cluster model in Herwig*, *The European Physical Journal C* **77** (2017) 156.
- 2637 [126] D. Amati and G. Veneziano, *Preconfinement as a property of perturbative QCD*,
2638 *Physics Letters B* **83** (1979) 87–92.
- 2639 [127] O.S. Brüning, P. Collier, P. Lebrun et al., *LHC Design Report*, CERN Yellow
2640 Reports: Monographs. CERN, Geneva, 2004.
- 2641 [128] O. Buning, P. Collier, P. Lebrun et al., *LHC Design Report. 2. The LHC*
2642 *infrastructure and general services*, .
- 2643 [129] M. Benedikt, P. Collier, V. Mertens et al., *LHC Design Report. 3. The LHC*
2644 *injector chain*, .
- 2645 [130] “CERN Official Website.”
2646 <http://public.web.cern.ch/public/en/research/AccelComplex-en.html>.
- 2647 [131] ATLAS collaboration, *The ATLAS Experiment at the CERN Large Hadron*
2648 *Collider*, *JINST* **3** (2008) S08003.
- 2649 [132] ATLAS collaboration, *Observation of Higgs boson production in association with*
2650 *a top quark pair at the LHC with the ATLAS detector*, *Phys. Lett.* **B784** (2018)
2651 173–191 [arXiv:[1806.00425](#)].
- 2652 [133] ATLAS collaboration, *Observation of light-by-light scattering in ultraperipheral*
2653 *Pb+Pb collisions with the ATLAS detector*, .
- 2654 [134] ATLAS collaboration, *Study of the rare decays of B_s^0 and B^0 mesons into muon*
2655 *pairs using data collected during 2015 and 2016 with the ATLAS detector*,
2656 *Submitted to: JHEP* (2018) [arXiv:[1812.03017](#)].
- 2657 [135] M. Aleksa, F. Bergsma, P.A. Giudici et al., *Measurement of the ATLAS solenoid*
2658 *magnetic field*, .
- 2659 [136] ATLAS collaboration, *ATLAS barrel toroid: Technical design report*, .
- 2660 [137] ATLAS collaboration, *ATLAS end-cap toroids: Technical Design Report*,
2661 Technical Design Report ATLAS. CERN, Geneva, 1997.
- 2662 [138] ATLAS collaboration, *ATLAS inner detector: Technical design report. Vol. 2*, .

Bibliography

- 2663 [139] ATLAS collaboration, *ATLAS inner detector: Technical design report. Vol. 1*, .
- 2664 [140] ATLAS collaboration, *ATLAS pixel detector: Technical design report*, .
- 2665 [141] ATLAS collaboration, *Operation and performance of the ATLAS semiconductor*
2666 *tracker, JINST* **9** (2014) P08009 [[arXiv:1404.7473](#)].
- 2667 [142] ATLAS TRT collaboration, *The ATLAS transition radiation tracker*, in
2668 *Astroparticle, particle and space physics, detectors and medical physics*
2669 *applications. Proceedings, 8th Conference, ICATPP 2003, Como, Italy, October*
2670 *6-10, 2003*, 497–501, 2003, [[arXiv:hep-ex/0311058](#)], DOI.
- 2671 [143] A.S. Boldyrev et al., *The ATLAS transition radiation tracker, Instrum. Exp.*
2672 *Tech.* **55** (2012) 323–334.
- 2673 [144] F. Hügging, *The ATLAS Pixel Insertable B-layer (IBL)*, *Nuclear Instruments*
2674 *and Methods in Physics Research Section A: Accelerators, Spectrometers,*
2675 *Detectors and Associated Equipment* **650** (2011) 45 – 49.
- 2676 [145] A. La Rosa, *The ATLAS Insertable B-Layer: from construction to operation*,
2677 *JINST* **11** (2016) C12036 [[arXiv:1610.01994](#)].
- 2678 [146] H. Pernegger, *The Pixel Detector of the ATLAS Experiment for LHC Run-2*,
2679 *Tech. Rep. ATL-INDET-PROC-2015-001. 06*, CERN, Geneva, Feb 2015.
- 2680 [147] ATLAS collaboration, *The Upgraded Pixel Detector of the ATLAS Experiment*
2681 *for Run-2 at the LHC*, Tech. Rep. ATL-INDET-PROC-2016-009, CERN,
2682 Geneva, Nov 2016.
- 2683 [148] S. Viel et al., *Performance of silicon pixel detectors at small track incidence*
2684 *angles for the ATLAS Inner Tracker Upgrade*, *Nucl. Instrum. Meth.* **A831**
2685 (2016) 254–259.
- 2686 [149] ATLAS collaboration, *Performance of the ATLAS Transition Radiation Tracker*
2687 *in Run 1 of the LHC: tracker properties*, *JINST* **12** (2017) P05002
2688 [[arXiv:1702.06473](#)].
- 2689 [150] ATLAS collaboration, *ATLAS liquid-argon calorimeter: Technical Design*
2690 *Report*, Technical Design Report ATLAS. CERN, Geneva, 1996.
- 2691 [151] P. Strizenec, *Performance of the ATLAS liquid argon calorimeter after three*
2692 *years of LHC operation and plans for a future upgrade*, *Journal of*
2693 *Instrumentation* **9** (2014) C09007–C09007.
- 2694 [152] ATLAS collaboration, *ATLAS tile calorimeter: Technical Design Report*,
2695 *Technical Design Report ATLAS*. CERN, Geneva, 1996.
- 2696 [153] A. Hrynevich, *Performance of the ATLAS tile calorimeter*, *Journal of*
2697 *Instrumentation* **12** (2017) C06021–C06021.

- 2698 [154] ATLAS collaboration, *ATLAS muon spectrometer: Technical Design Report*,
2699 Technical Design Report ATLAS. CERN, Geneva, 1997.
- 2700 [155] D. Boscherini, *Performance and operation of the ATLAS Resistive Plate*
2701 *Chamber system in LHC Run-1*, *JINST* **9** (2014) C12039.
- 2702 [156] K. Nikolopoulos et al., *Cathode strip chambers in ATLAS : Installation,*
2703 *commissioning and in situ performance*, in *Proceedings, 2008 IEEE Nuclear*
2704 *Science Symposium*, 2819–2824, 2008.
- 2705 [157] M. Livan, *Monitored drift tubes in ATLAS, Nuclear Instruments and Methods in*
2706 *Physics Research Section A: Accelerators, Spectrometers, Detectors and*
2707 *Associated Equipment* **384** (1996) 214 – 218.
- 2708 [158] K. Nagai, *Thin gap chambers in ATLAS, Nuclear Instruments and Methods in*
2709 *Physics Research Section A: Accelerators, Spectrometers, Detectors and*
2710 *Associated Equipment* **384** (1996) 219 – 221.
- 2711 [159] ATLAS collaboration, *Performance of the ATLAS Trigger System in 2010*, *The*
2712 *European Physical Journal C* **72** (2012) 1849.
- 2713 [160] ATLAS collaboration, *The Run-2 ATLAS Trigger System*, *J. Phys. Conf. Ser.*
2714 **762** (2016) 012003.
- 2715 [161] GEANT4 collaboration, *GEANT4: A Simulation toolkit*, *Nucl. Instrum. Meth.*
2716 **A506** (2003) 250–303.
- 2717 [162] E. Richter-Was, D. Froidevaux and L. Poggioli, *ATLFAST 2.0 a fast simulation*
2718 *package for ATLAS*, .
- 2719 [163] ATLAS collaboration, *Electron reconstruction and identification in the ATLAS*
2720 *experiment using the 2015 and 2016 LHC proton-proton collision data at $\sqrt{s} =$*
2721 *13 TeV, Submitted to: Eur. Phys. J.* (2019) [arXiv:1902.04655].
- 2722 [164] ATLAS collaboration, *Muon reconstruction performance of the ATLAS detector*
2723 *in proton–proton collision data at $\sqrt{s} = 13$ TeV*, *Eur. Phys. J.* **C76** (2016) 292
2724 [arXiv:1603.05598].
- 2725 [165] ATLAS collaboration, *Performance of b-Jet Identification in the ATLAS*
2726 *Experiment*, *JINST* **11** (2016) P04008 [arXiv:1512.01094].
- 2727 [166] ATLAS collaboration, *Performance of the ATLAS Trigger System in 2015*, *Eur.*
2728 *Phys. J.* **C77** (2017) 317 [arXiv:1611.09661].
- 2729 [167] ATLAS collaboration, *Electron and photon energy calibration with the ATLAS*
2730 *detector using data collected in 2015 at $\sqrt{s} = 13$ TeV*, Tech. Rep.
2731 ATL-PHYS-PUB-2016-015, CERN, Geneva, Aug 2016.

Bibliography

- 2732 [168] ATLAS collaboration, *JES Plots for Moriond 2017*, Mar 2017.
2733 <https://atlas.web.cern.ch/Atlas/GROUPS/PHYSICS/PLOTS/JETM-2017-003/>.
- 2734 [169] M. Cacciari, G.P. Salam and G. Soyez, *The Anti- $k(t)$ jet clustering algorithm*,
2735 *JHEP* **04** (2008) 063 [[arXiv:0802.1189](https://arxiv.org/abs/0802.1189)].
- 2736 [170] ATLAS collaboration, *Jet energy measurement and its systematic uncertainty in*
2737 *proton-proton collisions at $\sqrt{s} = 7$ TeV with the ATLAS detector*, *Eur. Phys. J.*
2738 *C* **75** (2015) 17 [[arXiv:1406.0076](https://arxiv.org/abs/1406.0076)].
- 2739 [171] ATLAS collaboration, *Measurement of the top quark mass with the template*
2740 *method in the $t\bar{t} \rightarrow$ lepton + jets channel using ATLAS data*, *The European*
2741 *Physical Journal C* **72** (2012) 2046.
- 2742 [172] ATLAS collaboration, *Measurement of the top quark mass in the $t\bar{t} \rightarrow$*
2743 *lepton+jets and $t\bar{t} \rightarrow$ dilepton channels using $\sqrt{s} = 7$ TeV ATLAS data*, *The*
2744 *European Physical Journal C* **75** (2015) 330.
- 2745 [173] ATLAS collaboration, *Measurement of the $t\bar{t}$ production cross-section using $e\mu$*
2746 *events with b-tagged jets in pp collisions at $\sqrt{s} = 7$ and 8TeV with the ATLAS*
2747 *detector*, *The European Physical Journal C* **74** (2014) 3109.
- 2748 [174] ATLAS collaboration, *Measurement of the top quark mass in the $t\bar{t}$ dilepton*
2749 *channel from $\sqrt{s} = 8$ TeV ATLAS data*, *Physics Letters B* **761** (2016) 350 – 371.
- 2750 [175] ATLAS collaboration, *Measurement of lepton differential distributions and the*
2751 *top quark mass in $t\bar{t}$ production in pp collisions at $\sqrt{s} = 8$ TeV with the ATLAS*
2752 *detector*, *The European Physical Journal C* **77** (2017) 804.
- 2753 [176] ATLAS collaboration, *Determination of the top-quark pole mass using $t\bar{t} + 1$ -jet*
2754 *events collected with the ATLAS experiment in 7 TeV pp collisions*, *JHEP* **2015**
2755 (2015) 121.
- 2756 [177] ATLAS collaboration, *Measurement of the top-quark mass in the fully hadronic*
2757 *decay channel from ATLAS data at $\sqrt{s} = 7$ TeV*, *The European Physical Journal*
2758 *C* **75** (2015) 158.
- 2759 [178] ATLAS collaboration, *Top-quark mass measurement in the all-hadronic $t\bar{t}$ decay*
2760 *channel at $\sqrt{s} = 8$ TeV with the ATLAS detector*, *JHEP* **2017** (2017) 118.
- 2761 [179] M. Czakon and A. Mitov, *Top++: A Program for the Calculation of the*
2762 *Top-Pair Cross-Section at Hadron Colliders*, *Comput. Phys. Commun.* **185**
2763 (2014) 2930 [[arXiv:1112.5675](https://arxiv.org/abs/1112.5675)].
- 2764 [180] ATLAS collaboration, *Studies on top-quark Monte Carlo modelling for Top2016*,
2765 *Tech. Rep. ATL-PHYS-PUB-2016-020*, CERN, Geneva, Sep 2016.

- 2766 [181] ATLAS collaboration, *Studies on top-quark Monte Carlo modelling with Sherpa*
 2767 and MG5_aMC@NLO, Tech. Rep. ATL-PHYS-PUB-2017-007, CERN, Geneva,
 2768 May 2017.
- 2769 [182] ATLAS collaboration, *Investigation of systematic uncertainties on the*
 2770 *measurement of the top-quark mass using lepton transverse momenta*, Tech. Rep.
 2771 ATL-PHYS-PUB-2018-001, CERN, Geneva, Feb 2018.
- 2772 [183] ATLAS collaboration, *Improvements in $t\bar{t}$ modelling using NLO+PS Monte*
 2773 *Carlo generators for Run2*, Tech. Rep. ATL-PHYS-PUB-2018-009, CERN,
 2774 Geneva, Jul 2018.
- 2775 [184] ATLAS collaboration, *Measurement of the top quark mass in the $t\bar{t} \rightarrow$ dilepton*
 2776 *channel from $\sqrt{s} = 8$ TeV ATLAS data*, *Phys. Lett.* **B761** (2016) 350–371
 2777 [arXiv:1606.02179].
- 2778 [185] J.M. Campbell, R.K. Ellis, P. Nason et al., *Top-pair production and decay at*
 2779 *NLO matched with parton showers*, *JHEP* **04** (2015) 114 [arXiv:1412.1828].
- 2780 [186] J. Bellm, S. Gieseke and S. Plätzer, *Merging NLO Multi-jet Calculations with*
 2781 *Improved Unitarization*, *Eur. Phys. J.* **C78** (2018) 244 [arXiv:1705.06700].
- 2782 [187] S. Hoeche, F. Krauss, P. Maierhoefer et al., *Next-to-leading order QCD*
 2783 *predictions for top-quark pair production with up to two jets merged with a parton*
 2784 *shower*, *Phys. Lett.* **B748** (2015) 74–78 [arXiv:1402.6293].
- 2785 [188] S. Höche, P. Maierhöfer, N. Moretti et al., *Next-to-leading order QCD predictions*
 2786 *for top-quark pair production with up to three jets*, *Eur. Phys. J.* **C77** (2017) 145
 2787 [arXiv:1607.06934].
- 2788 [189] M. Czakon, D. Heymes and A. Mitov, *High-precision differential predictions for*
 2789 *top-quark pairs at the LHC*, *Phys. Rev. Lett.* **116** (2016) 082003
 2790 [arXiv:1511.00549].
- 2791 [190] M. Czakon, D. Heymes and A. Mitov, *Dynamical scales for multi-TeV top-pair*
 2792 *production at the LHC*, *JHEP* **04** (2017) 071 [arXiv:1606.03350].
- 2793 [191] M. Czakon, D. Heymes and A. Mitov, *fastNLO tables for NNLO top-quark pair*
 2794 *differential distributions*, [arXiv:1704.08551].
- 2795 [192] M. Czakon, D. Heymes, A. Mitov et al., *Top-pair production at the LHC through*
 2796 *NNLO QCD and NLO EW*, *JHEP* **10** (2017) 186 [arXiv:1705.04105].
- 2797 [193] W. Hollik and D. Pagani, *The electroweak contribution to the top quark*
 2798 *forward-backward asymmetry at the Tevatron*, *Phys. Rev.* **D84** (2011) 093003
 2799 [arXiv:1107.2606].

Bibliography

- 2800 [194] J.H. Kühn, A. Scharf and P. Uwer, *Weak Interactions in Top-Quark Pair*
2801 *Production at Hadron Colliders: An Update*, *Phys. Rev.* **D91** (2015) 014020
2802 [arXiv:1305.5773].
- 2803 [195] D. Pagani, I. Tsinikos and M. Zaro, *The impact of the photon PDF and*
2804 *electroweak corrections on $t\bar{t}$ distributions*, *Eur. Phys. J.* **C76** (2016) 479
2805 [arXiv:1606.01915].
- 2806 [196] W. Bernreuther, A. Brandenburg, Z.G. Si et al., *Top quark pair production and*
2807 *decay at hadron colliders*, *Nucl. Phys.* **B690** (2004) 81–137
2808 [arXiv:hep-ph/0403035].
- 2809 [197] K. Melnikov and M. Schulze, *NLO QCD corrections to top quark pair production*
2810 *and decay at hadron colliders*, *JHEP* **0908** (2009) 049 [arXiv:0907.3090].
- 2811 [198] J.M. Campbell and R.K. Ellis, *Top-quark processes at NLO in production and*
2812 *decay*, *J. Phys.* **G42** (2015) 015005 [arXiv:1204.1513].
- 2813 [199] M. Brucherseifer, F. Caola and K. Melnikov, $\mathcal{O}(\alpha_s^2)$ *corrections to*
2814 *fully-differential top quark decays*, *JHEP* **04** (2013) 059 [arXiv:1301.7133].
- 2815 [200] J. Gao and A.S. Papanastasiou, *Top-quark pair-production and decay at high*
2816 *precision*, *Phys. Rev.* **D96** (2017) 051501 [arXiv:1705.08903].
- 2817 [201] M. Beneke, P. Falgari, S. Klein et al., *Hadronic top-quark pair production with*
2818 *NNLL threshold resummation*, *Nucl. Phys.* **B855** (2012) 695–741
2819 [arXiv:1109.1536].
- 2820 [202] M. Cacciari, M. Czakon, M. Mangano et al., *Top-pair production at hadron*
2821 *colliders with next-to-next-to-leading logarithmic soft-gluon resummation*, *Phys.*
2822 *Lett.* **B710** (2012) 612–622 [arXiv:1111.5869].
- 2823 [203] A. Ferroglio, S. Marzani, B.D. Pecjak et al., *Boosted top production: factorization*
2824 *and resummation for single-particle inclusive distributions*, *JHEP* **01** (2014) 028
2825 [arXiv:1310.3836].
- 2826 [204] A. Broggio, A.S. Papanastasiou and A. Signer, *Renormalization-group improved*
2827 *fully differential cross sections for top pair production*, *JHEP* **10** (2014) 98
2828 [arXiv:1407.2532].
- 2829 [205] N. Kidonakis, *High-order threshold corrections for top-pair and single-top*
2830 *production*, in *Proceedings, Meeting of the APS Division of Particles and Fields*
2831 *(DPF 2015): Ann Arbor, Michigan, USA, 4–8 Aug 2015*, 2015,
2832 [arXiv:1509.07848].
- 2833 [206] B.D. Pecjak, D.J. Scott, X. Wang et al., *Resummed differential cross sections for*
2834 *top-quark pairs at the LHC*, *Phys. Rev. Lett.* **116** (2016) 202001
2835 [arXiv:1601.07020].

- 2836 [207] M.L. Czakon et al., *Top quark pair production at NNLO+NNLL' in QCD*
 2837 *combined with electroweak corrections*, in *11th International Workshop on Top*
 2838 *Quark Physics (TOP2018) Bad Neuenahr, Germany, September 16-21, 2018,*
 2839 *2019*, [arXiv:1901.08281].
- 2840 [208] G. Heinrich, A. Maier, R. Nisius et al., *NLO QCD corrections to $W^+W^-b\bar{b}$*
 2841 *production with leptonic decays in the light of top quark mass and asymmetry*
 2842 *measurements*, *JHEP* **1406** (2014) 158 [arXiv:1312.6659].
- 2843 [209] S. Frixione, E. Laenen, P. Motylinski et al., *Single-top hadroproduction in*
 2844 *association with a W boson*, *JHEP* **07** (2008) 029 [arXiv:0805.3067].
- 2845 [210] A. Denner, S. Dittmaier, S. Kallweit et al., *NLO QCD corrections to $WWbb$*
 2846 *production at hadron colliders*, *Phys. Rev. Lett.* **106** (2011) 052001
 2847 [arXiv:1012.3975].
- 2848 [211] A. Denner, S. Dittmaier, S. Kallweit et al., *NLO QCD corrections to off-shell*
 2849 *top-antitop production with leptonic decays at hadron colliders*, *JHEP* **10** (2012)
 2850 110 [arXiv:1207.5018].
- 2851 [212] G. Bevilacqua, M. Czakon, A. van Hameren et al., *Complete off-shell effects in*
 2852 *top quark pair hadroproduction with leptonic decay at next-to-leading order*,
 2853 *JHEP* **02** (2011) 083 [arXiv:1012.4230].
- 2854 [213] R. Frederix, *Top Quark Induced Backgrounds to Higgs Production in the*
 2855 *$WW^{(*)} \rightarrow ll\nu\nu$ Decay Channel at Next-to-Leading-Order in QCD*, *Phys. Rev.*
 2856 *Lett.* **112** (2014) 082002 [arXiv:1311.4893].
- 2857 [214] F. Cascioli, S. Kallweit, P. Maierhöfer et al., *A unified NLO description of*
 2858 *top-pair and associated Wt production*, *Eur. Phys. J.* **C74** (2014) 2783
 2859 [arXiv:1312.0546].
- 2860 [215] A. Denner and M. Pellen, *Off-shell production of top-antitop pairs in the*
 2861 *lepton+jets channel at NLO QCD*, *JHEP* **02** (2018) 013 [arXiv:1711.10359].
- 2862 [216] G. Heinrich, A. Maier, R. Nisius et al., *NLO and off-shell effects in top quark*
 2863 *mass determinations*, *JHEP* **07** (2018) 129 [arXiv:1709.08615].
- 2864 [217] G. Heinrich, A. Maier, R. Nisius et al., *NLO QCD corrections to $WWbb$*
 2865 *production with leptonic decays in the light of top quark mass and asymmetry*
 2866 *measurements*, *JHEP* **2014** (2014) 158.
- 2867 [218] A. Denner, S. Dittmaier, S. Kallweit et al., *NLO QCD corrections to off-shell*
 2868 *top-antitop production with leptonic decays at hadron colliders*, *JHEP* **2012**
 2869 (2012) 110.
- 2870 [219] S. Höche and J.C. Winter. Private communication.

Bibliography

- 2871 [220] C. Duhr, S. Hoeche and F. Maltoni, *Color-dressed recursive relations for*
2872 *multi-parton amplitudes*, *JHEP* **08** (2006) 062 [[arXiv:hep-ph/0607057](#)].
- 2873 [221] T. Gleisberg and S. Hoeche, *Comix, a new matrix element generator*, *JHEP* **12**
2874 (2008) 039 [[arXiv:0808.3674](#)].
- 2875 [222] T. Gleisberg, S. Hoeche, F. Krauss et al., *How to calculate colourful cross*
2876 *sections efficiently*, [[arXiv:0808.3672](#)].
- 2877 [223] F. Krauss, R. Kuhn and G. Soff, *AMEGIC++ 1.0: A Matrix element generator*
2878 *in C++*, *JHEP* **02** (2002) 044 [[arXiv:hep-ph/0109036](#)].
- 2879 [224] J. Butterworth et al., *PDF4LHC recommendations for LHC Run II*, *J. Phys.*
2880 **G43** (2016) 023001 [[arXiv:1510.03865](#)].
- 2881 [225] M. Cacciari and G.P. Salam, *Dispelling the N^3 myth for the k_t jet-finder*, *Phys.*
2882 *Lett.* **B641** (2006) 57–61 [[arXiv:hep-ph/0512210](#)].
- 2883 [226] M. Cacciari, G.P. Salam and G. Soyez, *FastJet User Manual*, *Eur. Phys. J.* **C72**
2884 (2012) 1896 [[arXiv:1111.6097](#)].
- 2885 [227] S. Höche, J. Huang, G. Luisoni et al., *Zero and one jet combined next-to-leading*
2886 *order analysis of the top quark forward-backward asymmetry*, *Phys. Rev.* **D88**
2887 (2013) 014040 [[arXiv:1306.2703](#)].
- 2888 [228] A. Buckley, J. Butterworth, L. Lönnblad et al., *Rivet user manual*, *Comput.*
2889 *Phys. Commun.* **184** (2013) 2803–2819 [[arXiv:1003.0694](#)].
- 2890 [229] C.G. Lester and D.J. Summers, *Measuring masses of semiinvisibly decaying*
2891 *particles pair produced at hadron colliders*, *Phys. Lett.* **B463** (1999) 99–103
2892 [[arXiv:hep-ph/9906349](#)].
- 2893 [230] A. Barr, C. Lester and P. Stephens, *$m(T2)$: The Truth behind the glamour*, *J.*
2894 *Phys.* **G29** (2003) 2343–2363 [[arXiv:hep-ph/0304226](#)].
- 2895 [231] V. Blobel, *An Unfolding method for high-energy physics experiments*, in *Advanced*
2896 *Statistical Techniques in Particle Physics. Proceedings, Conference, Durham,*
2897 *UK, March 18-22, 2002*, 258–267, 2002, [[arXiv:hep-ex/0208022](#)],
2898 <http://www.ippp.dur.ac.uk/Workshops/02/statistics/proceedings//blobel2.pdf>.
- 2899 [232] ATLAS collaboration, *Optimisation of the ATLAS b-tagging performance for the*
2900 *2016 LHC Run*, Tech. Rep. ATL-PHYS-PUB-2016-012, CERN, Geneva, Jun
2901 2016.
- 2902 [233] ATLAS collaboration, *Flavour tagging algorithms and performance at the*
2903 *ATLAS experiment*, Tech. Rep. ATL-PHYS-PROC-2016-105, CERN, Geneva,
2904 Aug 2016.

- 2905 [234] P. Nason, *The Top Quark Mass at the LHC*, in *Proceedings, Old and New Strong*
 2906 *Interactions from LHC to Future Colliders (LFC17): Trento, Italy, September*
 2907 *11-15, 2017*, 65–70, 2017, [[arXiv:1801.04826](#)].
- 2908 [235] F. James, *MINUIT Function Minimization and Error Analysis: Reference*
 2909 *Manual Version 94.1*, .
- 2910 [236] ATLAS collaboration, *Observation of a new particle in the search for the*
 2911 *Standard Model Higgs boson with the ATLAS detector at the LHC*, *Phys. Lett.* **B716** (2012) 1–29 [[arXiv:1207.7214](#)].
- 2913 [237] CMS collaboration, *Observation of a new boson at a mass of 125 GeV with the*
 2914 *CMS experiment at the LHC*, *Phys. Lett.* **B716** (2012) 30–61 [[arXiv:1207.7235](#)].
- 2915 [238] E.W.N. Glover and J.J. van der Bij, *Higgs Boson Pair Production via Gluon*
 2916 *Fusion*, *Nucl. Phys.* **B309** (1988) 282.
- 2917 [239] M. Spira, A. Djouadi, D. Graudenz et al., *Higgs boson production at the LHC*,
 2918 *Nucl. Phys.* **B453** (1995) 17–82 [[arXiv:hep-ph/9504378](#)].
- 2919 [240] R. Bonciani, A. Ferroglia, P. Mastrolia et al., *Two-loop $N(F)=1$ QED Bhabha*
 2920 *scattering differential cross section*, *Nucl. Phys.* **B701** (2004) 121–179
 2921 [[arXiv:hep-ph/0405275](#)].
- 2922 [241] C. Anastasiou, S. Beerli, S. Bucherer et al., *Two-loop amplitudes and master*
 2923 *integrals for the production of a Higgs boson via a massive quark and a*
 2924 *scalar-quark loop*, *JHEP* **01** (2007) 082 [[arXiv:hep-ph/0611236](#)].
- 2925 [242] G. Degrassi, P.P. Giardino and R. Gröber, *On the two-loop virtual QCD*
 2926 *corrections to Higgs boson pair production in the Standard Model*, *Eur. Phys. J.*
 2927 **C76** (2016) 411 [[arXiv:1603.00385](#)].
- 2928 [243] R. Bonciani, V. Del Duca, H. Frellesvig et al., *Next-to-leading order QCD*
 2929 *corrections to the decay width $H \rightarrow Z\gamma$* , *JHEP* **08** (2015) 108 [[arXiv:1505.00567](#)].
- 2930 [244] T. Gehrmann, S. Guns and D. Kara, *The rare decay $H \rightarrow Z\gamma$ in perturbative*
 2931 *QCD*, *JHEP* **09** (2015) 038 [[arXiv:1505.00561](#)].
- 2932 [245] R. Gröber, A. Maier and T. Rauh, *Reconstruction of top-quark mass effects in*
 2933 *Higgs pair production and other gluon-fusion processes*, *JHEP* **03** (2018) 020
 2934 [[arXiv:1709.07799](#)].
- 2935 [246] R. Bonciani, G. Degrassi, P.P. Giardino et al., *Analytical Method for*
 2936 *Next-to-Leading-Order QCD Corrections to Double-Higgs Production*, *Phys. Rev.*
 2937 *Lett.* **121** (2018) 162003 [[arXiv:1806.11564](#)].
- 2938 [247] G. Mishima, *High-Energy Expansion of Two-Loop Massive Four-Point Diagrams*,
 2939 *JHEP* **02** (2019) 080 [[arXiv:1812.04373](#)].

Bibliography

- 2940 [248] J. Davies, G. Mishima, M. Steinhauser et al., *Double Higgs boson production at*
2941 *NLO in the high-energy limit: complete analytic results*, *JHEP* **01** (2019) 176
2942 [[arXiv:1811.05489](#)].
- 2943 [249] S. Borowka, N. Greiner, G. Heinrich et al., *Full top quark mass dependence in*
2944 *Higgs boson pair production at NLO*, *JHEP* **10** (2016) 107 [[arXiv:1608.04798](#)].
- 2945 [250] A. von Manteuffel and C. Studerus, *Reduze 2 - Distributed Feynman Integral*
2946 *Reduction*, [[arXiv:1201.4330](#)].
- 2947 [251] J. Carter and G. Heinrich, *SecDec: A general program for sector decomposition*,
2948 *Comput. Phys. Commun.* **182** (2011) 1566–1581 [[arXiv:1011.5493](#)].
- 2949 [252] S. Borowka, J. Carter and G. Heinrich, *Numerical Evaluation of Multi-Loop*
2950 *Integrals for Arbitrary Kinematics with SecDec 2.0*, *Comput. Phys. Commun.*
2951 **184** (2013) 396–408 [[arXiv:1204.4152](#)].
- 2952 [253] S. Borowka, G. Heinrich, S.P. Jones et al., *SecDec-3.0: numerical evaluation of*
2953 *multi-scale integrals beyond one loop*, *Comput. Phys. Commun.* **196** (2015)
2954 470–491 [[arXiv:1502.06595](#)].
- 2955 [254] S.P. Jones, *Automation of 2-loop Amplitude Calculations*, *PoS LL2016* (2016)
2956 069 [[arXiv:1608.03846](#)].
- 2957 [255] S. Borowka, G. Heinrich, S. Jahn et al., *A GPU compatible quasi-Monte Carlo*
2958 *integrator interfaced to pySecDec*, *Comp. Phys. Comm.* (2018)
2959 [[arXiv:1811.11720](#)].
- 2960 [256] J. Baglio, F. Campanario, S. Glaus et al., *Gluon fusion into Higgs pairs at NLO*
2961 *QCD and the top mass scheme*, [[arXiv:1811.05692](#)].
- 2962 [257] G. Buchalla, O. Catà and C. Krause, *Complete Electroweak Chiral Lagrangian*
2963 *with a Light Higgs at NLO*, *Nucl. Phys.* **B880** (2014) 552–573 [[arXiv:1307.5017](#)].
- 2964 [258] G. Buchalla, O. Catá and C. Krause, *On the Power Counting in Effective Field*
2965 *Theories*, *Phys. Lett.* **B731** (2014) 80–86 [[arXiv:1312.5624](#)].
- 2966 [259] G. Buchalla, M. Capozi, A. Celis et al., *Higgs boson pair production in non-linear*
2967 *Effective Field Theory with full m_t -dependence at NLO QCD*, *JHEP* **09** (2018)
2968 057 [[arXiv:1806.05162](#)].
- 2969 [260] C. Degrande, C. Duhr, B. Fuks et al., *UFO - The Universal FeynRules Output*,
2970 *Comput. Phys. Commun.* **183** (2012) 1201–1214 [[arXiv:1108.2040](#)].
- 2971 [261] A. Alloul, N.D. Christensen, C. Degrande et al., *FeynRules 2.0 - A complete*
2972 *toolbox for tree-level phenomenology*, *Comput. Phys. Commun.* **185** (2014)
2973 2250–2300 [[arXiv:1310.1921](#)].

- 2974 [262] N.D. Christensen and C. Duhr, *FeynRules - Feynman rules made easy*, *Comput. Phys. Commun.* **180** (2009) 1614–1641 [[arXiv:0806.4194](#)].
- 2975
- 2976 [263] A. Carvalho, M. Dall’Osso, T. Dorigo et al., *Higgs Pair Production: Choosing Benchmarks With Cluster Analysis*, *JHEP* **04** (2016) 126 [[arXiv:1507.02245](#)].
- 2977
- 2978 [264] A. Djouadi, M. Spira and P. Zerwas, *Production of Higgs bosons in proton colliders. QCD corrections*, *Physics Letters B* **264** (1991) 440 – 446.
- 2979
- 2980 [265] S. Dawson, *Radiative corrections to Higgs boson production*, *Nucl. Phys.* **B359** (1991) 283–300.
- 2981
- 2982 [266] R. Grober, M. Muhlleitner, M. Spira et al., *NLO QCD Corrections to Higgs Pair Production including Dimension-6 Operators*, *JHEP* **09** (2015) 092 [[arXiv:1504.06577](#)].
- 2983
- 2984
- 2985 [267] A. Azatov, R. Contino, G. Panico et al., *Effective field theory analysis of double Higgs boson production via gluon fusion*, *Phys. Rev.* **D92** (2015) 035001 [[arXiv:1502.00539](#)].
- 2986
- 2987
- 2988 [268] CMS collaboration, *Measurement and interpretation of differential cross sections for Higgs boson production at $\sqrt{s} = 13$ TeV*, *Phys. Lett.* **B792** (2019) 369 [[arXiv:1812.06504](#)].
- 2989
- 2990
- 2991 [269] G. Heinrich, S.P. Jones, M. Kerner et al., *Probing the trilinear Higgs boson coupling in di-Higgs production at NLO QCD including parton shower effects*, [[arXiv:1903.08137](#)].
- 2992
- 2993
- 2994 [270] G. Heinrich, S.P. Jones, M. Kerner et al., *NLO predictions for Higgs boson pair production with full top quark mass dependence matched to parton showers*, *JHEP* **08** (2017) 088 [[arXiv:1703.09252](#)].
- 2995
- 2996
- 2997 [271] *Les Houches 2017: Physics at TeV Colliders Standard Model Working Group Report*, 2018.
- 2998
- 2999 [272] S. Ferrario Ravasio, T. Jezo, P. Nason et al., *A Theoretical Study of Top-Mass Measurements at the LHC Using NLO+PS Generators of Increasing Accuracy*, [[arXiv:1801.03944](#)].
- 3000
- 3001

3002 A Further template fit plots

3003 A better understanding of the discrepancy between the NLO_{full} prediction and the
 3004 $\text{NLO}_{\text{NWA}}^{\text{NLOdec}}$, respectively NLO_{PS} calculations is needed. Compared to the NLO_{full} pseudo-
 3005 data, the $\text{NLO}_{\text{NWA}}^{\text{NLOdec}}$ prediction leads to a rather large offset in the top-quark mass of
 3006 (0.83 ± 0.07) GeV. On the other hand, the NLO_{PS} prediction gives an offset to the
 3007 $W^+W^-b\bar{b}$ pseudo-data of only (-0.09 ± 0.07) GeV. New parton-showered predictions
 3008 $(n_{\max}^{\text{prod}}, n_{\max}^{\text{dec}})$ are produced where the shower is terminated after a certain number of
 3009 emissions n_{\max} in the $t\bar{t}$ production and decay showers. In Fig. A.1, the pseudo-data
 3010 from these predictions are compared to the full parton-shower and the $\text{NLO}_{\text{NWA}}^{\text{NLOdec}}$ cali-
 3011 bration function and pseudo-data. For each of the samples, the offset in m_t is given as
 3012 a colored bar (in blue for the $\text{NLO}_{\text{NWA}}^{\text{NLOdec}}$ calibration function, respectively in red when
 3013 using the NLO_{PS} calibration). Then, for only one allowed emission in both production
 3014 and decay showers, the top-quark mass offset between $\text{NLO}_{\text{PS}}^{(1,1)}$ and $\text{NLO}_{\text{NWA}}^{\text{NLOdec}}$ is re-
 3015 duced to (-0.11 ± 0.06) GeV. Thus, the additional radiation accounts for the observed
 3016 discrepancy in the offsets.

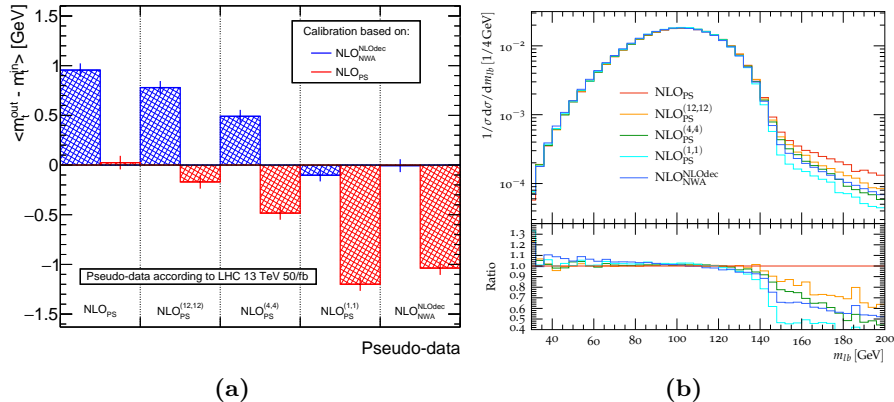


Figure A.1: (a) The offsets fitted from the $m_{t\bar{b}}$ distribution are shown for $\text{NLO}_{\text{PS}}^{(n_{\max}^{\text{prod}}, n_{\max}^{\text{dec}})}$ restricted-shower pseudo-data samples. (b) The normalized $m_{t\bar{b}}$ distribution is plotted for the mentioned predictions at $m_t = 172.5$ GeV.

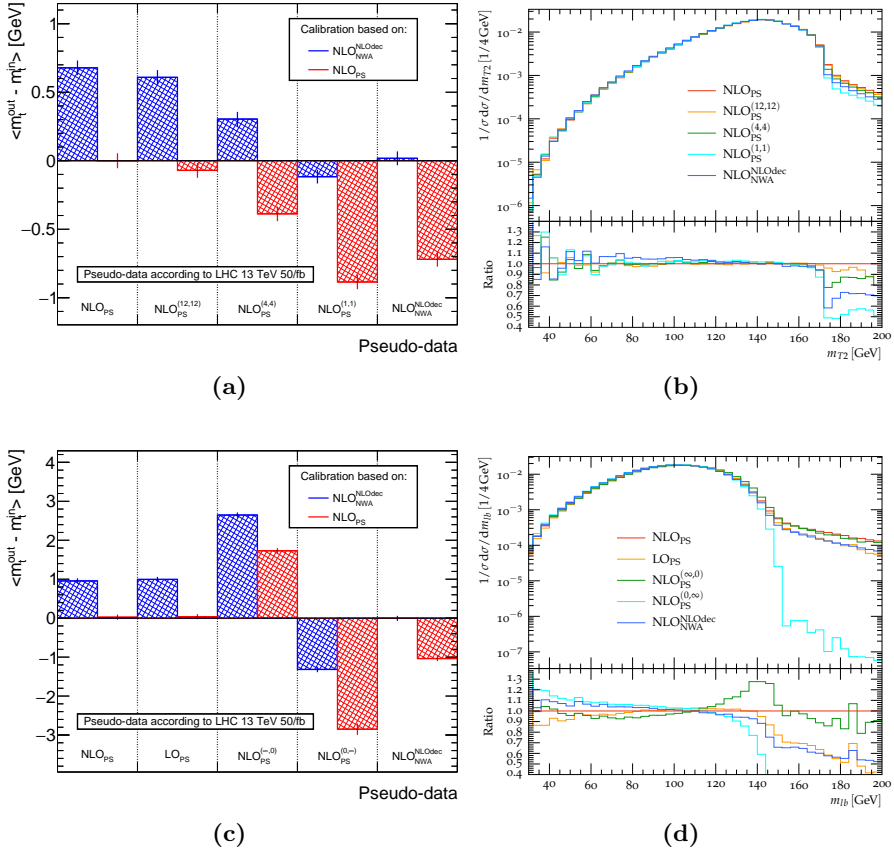


Figure A.2: (a-b) Same as A.1 for m_{T2} . (c-d) Same as Fig. A.1, but for the NLO_{PS} and LO_{PS} cases, as well as for pseudo-data sets generated by predictions where the decay shower, respectively the production shower are entirely deactivated.

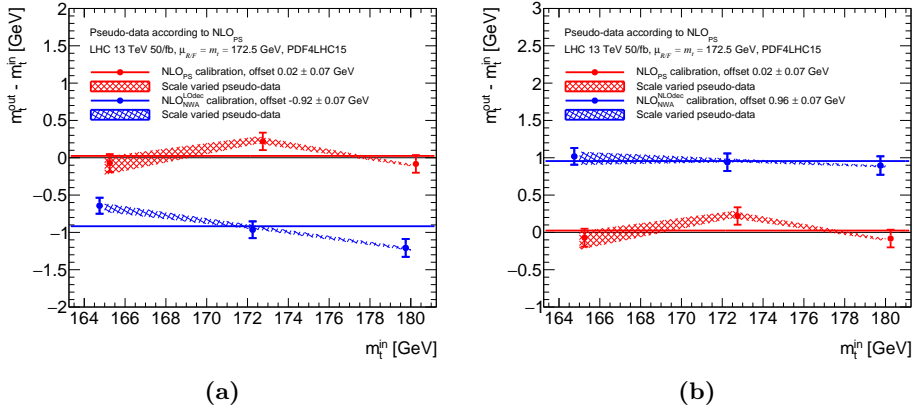


Figure A.3: Further band plots from $m_{\ell b}$ fitted pseudo-data sets.

A Further template fit plots

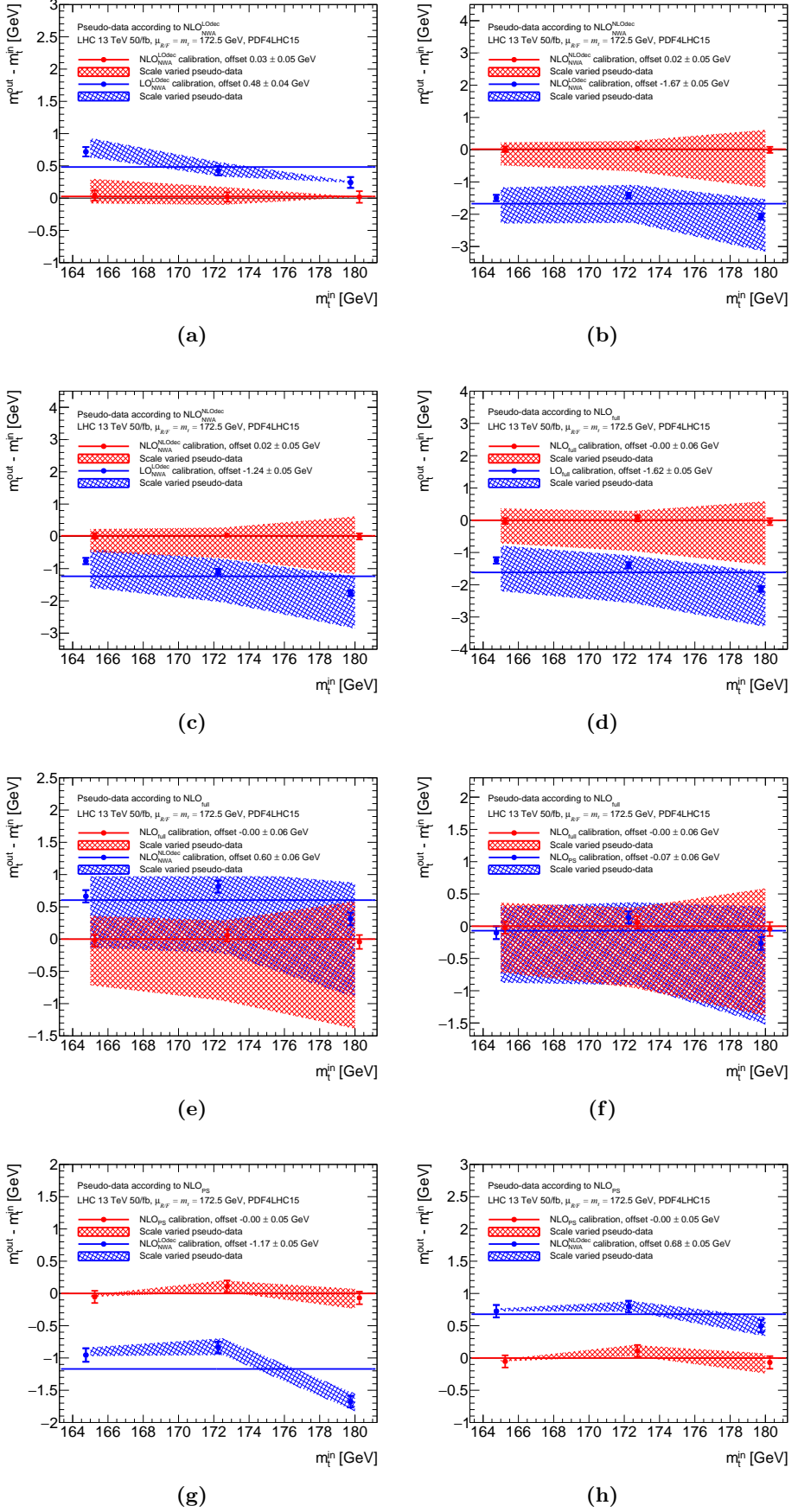


Figure A.4: Further band plots from m_{T2} fitted pseudo-data sets.

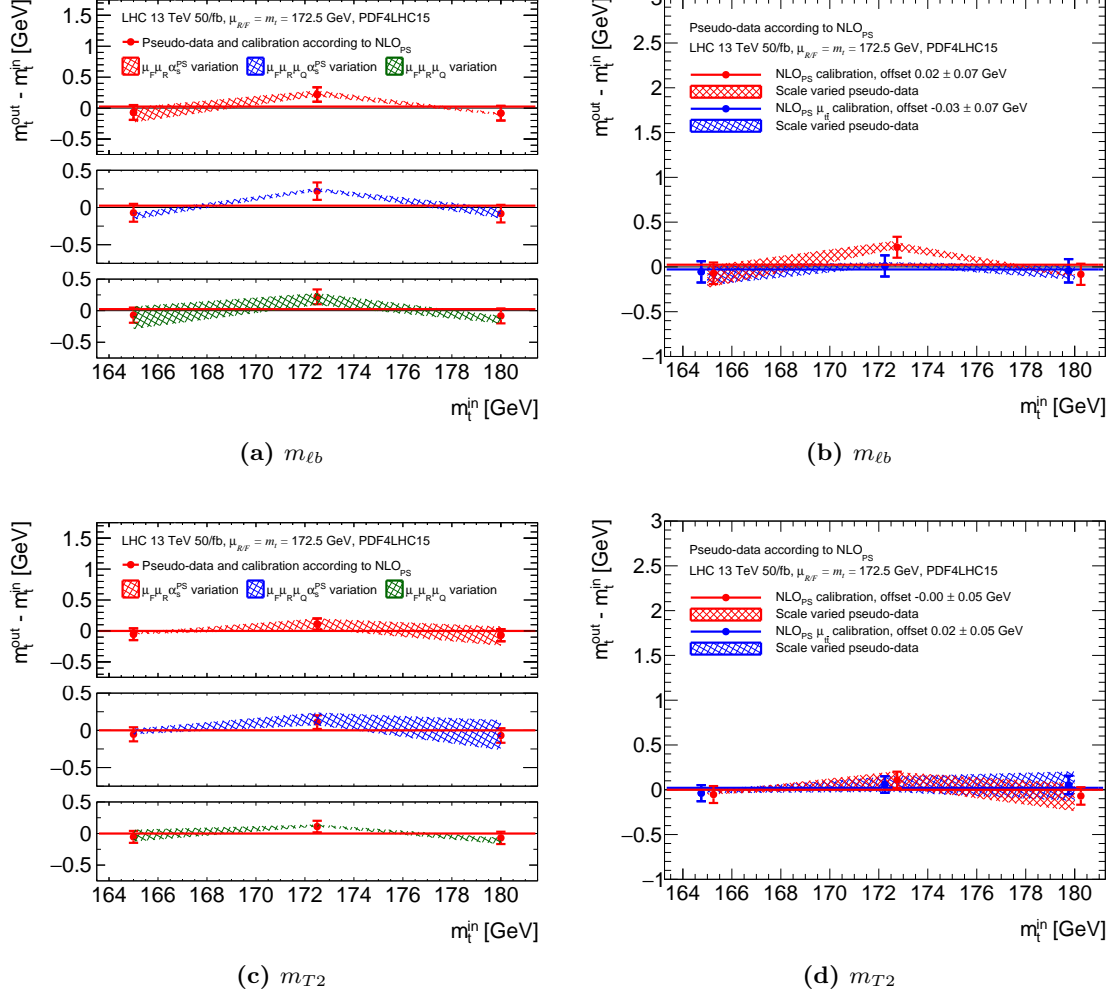


Figure A.5: Offsets from NLO_{PS} predictions comparing (a) different prescriptions for evaluating the shower scale uncertainties and (b) the two different central scale choices described in the text.

B Template fit parameters at detector-level

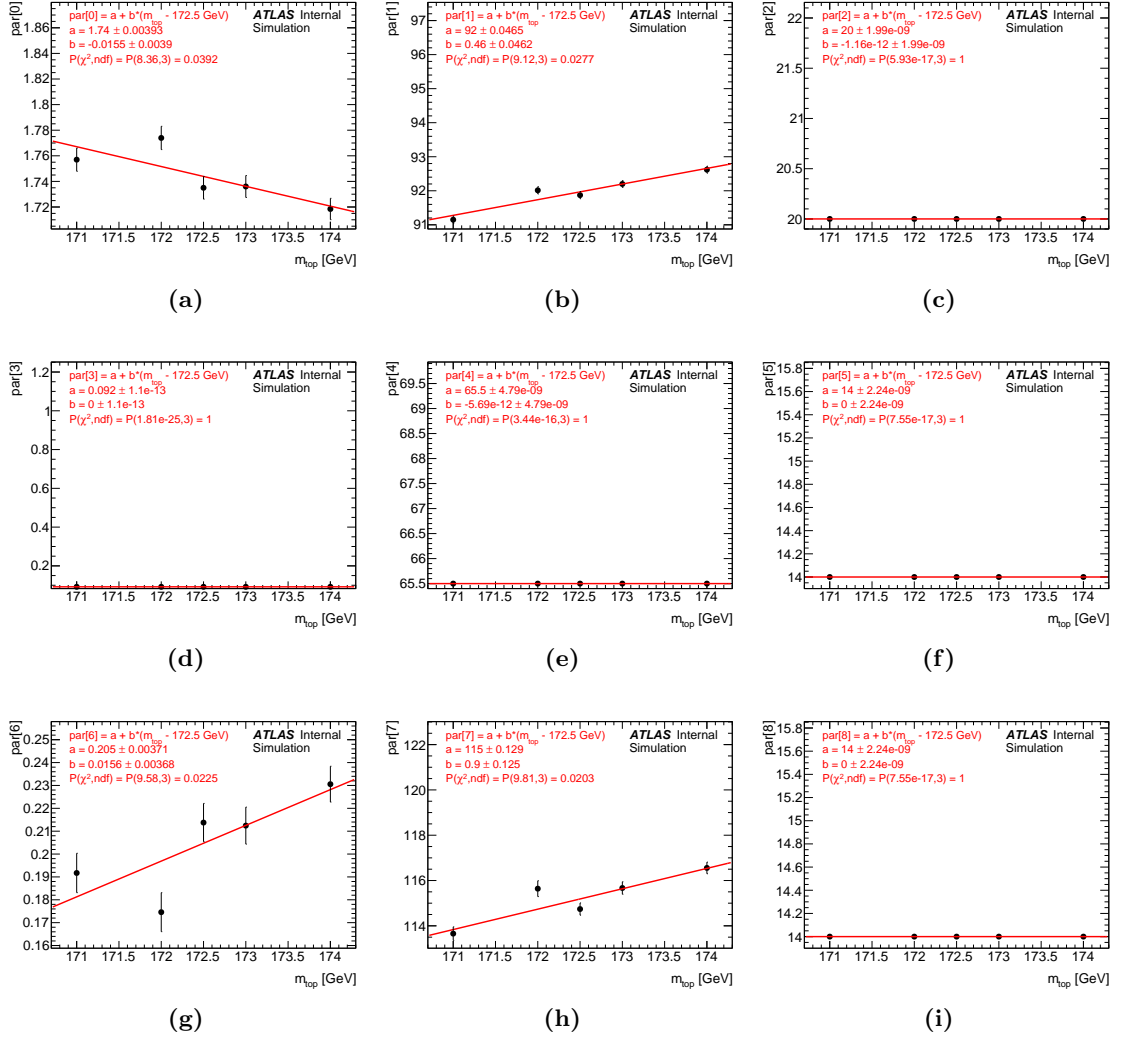


Figure B.1: The linear dependence of the nine functional fit parameters on the MC input top-quark mass, for the $t\bar{t}$ plus single-top samples at detector-level.

3018 C BSM benchmark points in hh production

3019 The coefficients A_i , $i = 1, \dots, 23$ (15) defined for the general expression of the NLO
 3020 (LO) cross-section as a function of the anomalous Higgs couplings in Eq. (10.16) are
 3021 shown in Table C.1, at 13 TeV at LHC. To compute these, the cross-section was calcu-
 3022 lated for different values of the couplings that were replaced in Eq. (10.16), thus giving
 3023 a system of equations that one can project out to extract the values of the coefficients
 3024 A_i .

3025 The LO and NLO coefficients for $\sqrt{s} = 13, 14$ and 27 TeV are available on the ARXIV
 3026 e-print of Ref. [259], as well as a Mathematica file explaining how to use them. These
 3027 can also be derived differentially for a fixed bin width. The differential coefficients can
 3028 also be downloaded for the m_{hh} distribution, with the binning shown in the histograms.

A_i	A_i^{LO}	ΔA_i^{LO}	A_i^{NLO}	ΔA_i^{NLO}
A_1	2.0806	0.0016	2.2339	0.0101
A_2	10.2011	0.0081	12.4598	0.0424
A_3	0.2781	0.0019	0.3422	0.0154
A_4	0.3140	0.0003	0.3468	0.0033
A_5	12.2731	0.0101	13.0087	0.0962
A_6	-8.4931	0.0089	-9.6455	0.0504
A_7	-1.3587	0.0015	-1.5755	0.0136
A_8	2.8025	0.0131	3.4385	0.0772
A_9	2.4802	0.0128	2.8669	0.0772
A_{10}	14.6908	0.0311	16.6912	0.1785
A_{11}	-1.1592	0.0031	-1.2529	0.0291
A_{12}	-5.5118	0.0131	-5.8122	0.1340
A_{13}	0.5605	0.0034	0.6497	0.0287
A_{14}	2.4798	0.0190	2.8593	0.1930
A_{15}	2.8943	0.0158	3.1448	0.1487
A_{16}			-0.008162	0.000225
A_{17}			0.020865	0.000399
A_{18}			0.016816	0.000783
A_{19}			0.029858	0.000829
A_{20}			-0.027025	0.000702
A_{21}			0.072692	0.001288
A_{22}			0.014523	0.000704
A_{23}			0.123291	0.006506

Table C.1: The coefficients defined in Eqs. (10.15), (10.16) are determined by computing cross-
 sections for a subset of parameters, and projecting out equations for the A_i 's. Statistical
 uncertainties are propagated from the cross-section level to the coefficient
 result, without correlations.

C BSM benchmark points in hh production

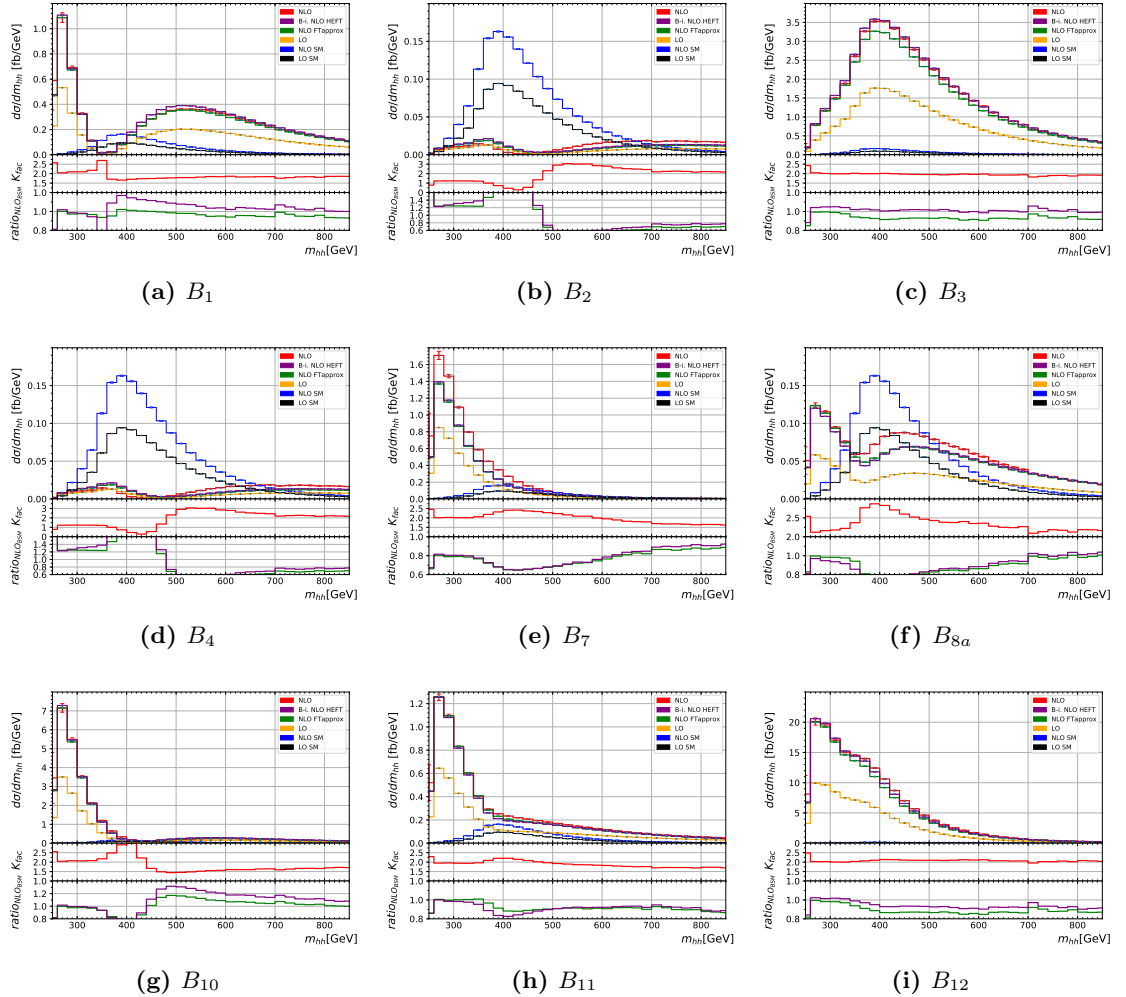


Figure C.1: The invariant mass of the Higgs boson pair m_{hh} is shown for the different benchmark points B_i , $i = 1, \dots, 12$ defined in Table 10.1 and not already shown in Chapter 10.

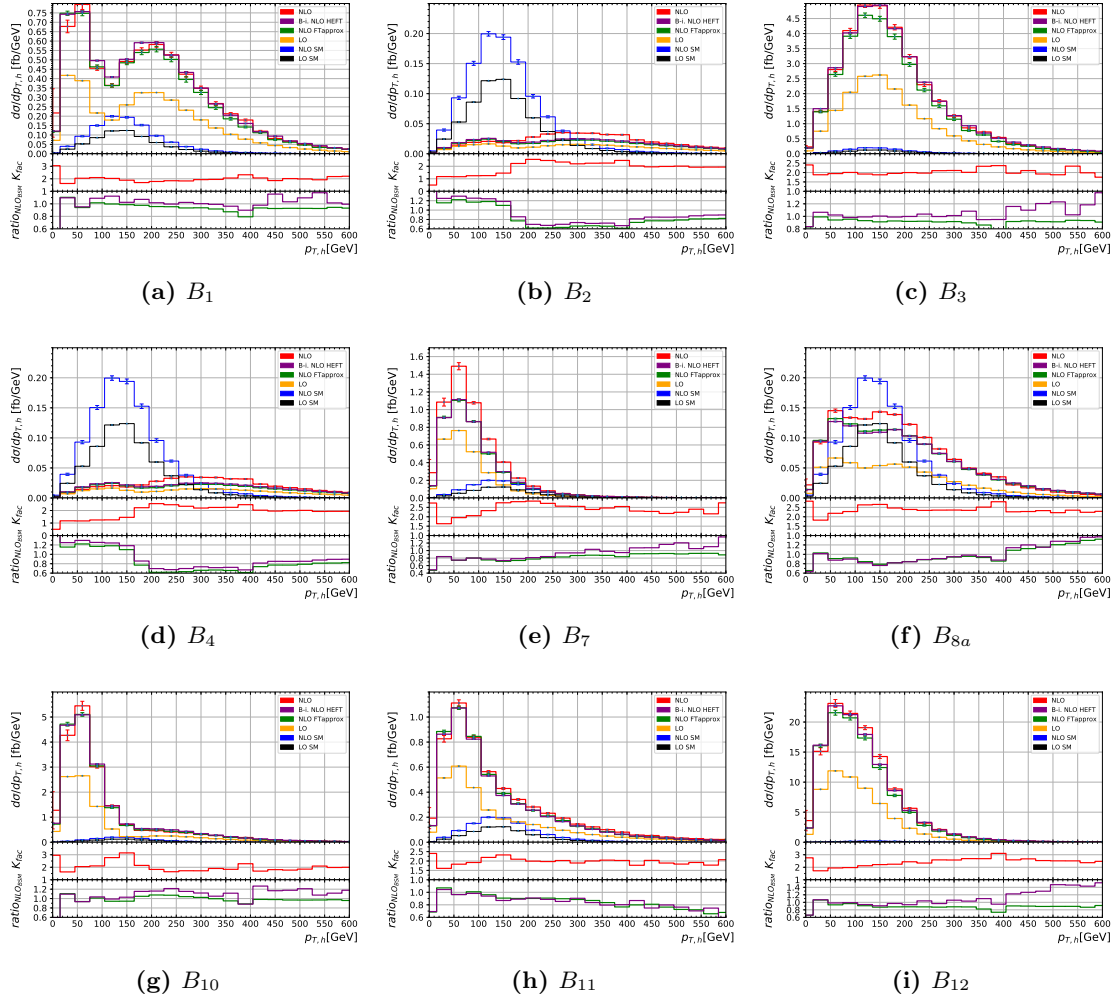


Figure C.2: The transverse momentum $p_{T,h}$ of one (any) Higgs boson is shown for the different benchmark points B_i , $i = 1, \dots, 12$ defined in Table 10.1 and not already shown in Chapter 10.

3029 D Hardness definitions in matching Powheg 3030 to Pythia

3031 The technical parameters for matching the **Pythia** 8 parton-shower to LHE files pro-
3032 duced by POWHEG are defined in a file called **main31.cmnd**, which bases on the LHE
3033 showering example from **Pythia**. There, several definitions for the additional radia-
3034 tion have to be set in order for the parton-shower to avoid double-counting regions of
3035 phase-space already covered by POWHEG. The following definitions are set:

- 3036 • The number of final-state particles in the Born process $gg \rightarrow hh$.

3037 **POWHEG:nFinal = 2**

- 3038 • The parton-shower vetoes emissions that have a transverse momentum higher than
3039 the hardest POWHEG emission, and checks the first three. A veto is applied if
3040 **pTemt > pThard** (see below).

3041 **POWHEG:veto = 1**

3042 **POWHEG:vetoCount = 3**

- 3043 • The **pTemt** and **pThard** scale definition is set: **pTemt** is set to the transverse mo-
3044 mentum of the radiated particle with respect to the emitting parton, and **pThard** is
3045 set to the **SCALUP** value read in the LHE event, and set by POWHEG. The definition
3046 of the emitted parton is chosen by **Pythia** for the final-state radiation.

3047 **POWHEG:pTemt = 0**

3048 **POWHEG:pThard = 0**

3049 **POWHEG:emitted = 0**

3050 **POWHEG:pTdef = 1**

3051 The hardness **pTdef** is defined by the transverse momentum p_T for initial-state
3052 radiation, and with the distance between radiator and emitted partons d_{ij} for
3053 final-state radiation corresponding to the POWHEG definition given by:

$$d_{ij} = \frac{m_{ij}^2 E_i E_j}{(E_i + E_j)^2} .$$

3054 Acknowledgments

3055 First and foremost, I am infinitely grateful to both my supervisors, Stefan Kluth on the
3056 ATLAS computing side, and Gudrun Heinrich in the phenomenology group, for actively
3057 following my progress and keeping me on the right track with always astute advice. I
3058 could not have done it without their considerate help and encouragement.

3059 I am much obliged to all my publication collaborators, past and present, for their
3060 hard work, spontaneity and for maintaining an ever enjoyable working atmosphere: G.
3061 Buchalla, A. Celis, M. Capozi, G. Heinrich, S. Jones, M. Kerner, G. Luisoni, R. Mah-
3062 bubani, A. Maier, R. Nisius, H. Rzehak, J. Schlenk, M. Schulze and J. Winter. I would
3063 also like to thank A. Knue and B. Pearson for their incredible understanding of all
3064 the tiny details of the ATLAS analysis. They are responsible for making the interface
3065 comprehensible, which probably saved me a lot of nightmarish headaches.

3066 Of course, there is no office without officemates: my appreciation goes to A. Knue, A.
3067 Verbitskyi, D. Britzger, F. Klimpel and S. Schulte from the ATLAS computing group,
3068 for the lively discussions and the enormous pleasure I had working with you.

3069 Much valued was the time spent with the people from Gudrun's phenomenology group:
3070 it is not always easy to move to a new city or meet entirely new people, and for the casual
3071 climate and the few Oktoberfest visits together, I am most grateful. Thanks to H. Bahl,
3072 M. Capozi, L. Chen, S. Hessenberger, S. Jahn, V. Papara, C. Pietsch, J. Schlenk, T.
3073 Zirke for making especially my first few months in Munich brighter.

3074 I am eternally indebted to all the excellent friends that made the time at the Institute
3075 seem relativistically short, in particular those living permanently in, or sporadically
3076 passing by Connollystrasse: E. Bertoldo, M. Capozi, N. Ferreiro, M. Mancuso and F.
3077 Putzolu, E. Vitagliano, F. Guescini.

3078 I cannot stress enough how much friends were important to my mental sanity: after
3079 the long hours and weekends of work, it was always good to know whom to count on for
3080 releasing the pressure. This also applies to all the people whose visits from Switzerland
3081 rekindled the spark during a weekend of partying. Lots and lots of thanks in particular
3082 to C. Crusem, B. Despond, M. Predikaka and K. Novoselc, A. Du Cos, A. Lichtlé, G.
3083 Mathys and C. Traveletti.

3084 To my girlfriend at the time, Marthe, I want to say how grateful I am for the moments
3085 we enjoyed together. The past two years were beautiful, and I am profoundly glad to
3086 have walked part of the path with you.

3087 Finally, I offer my last resounding thanks to my whole family, in particular to my
3088 parents and my siblings. Without my parents, I would never have a life nearly as
3089 exciting and vibrant as this one. Thank you for what I know sometimes amounted to
3090 difficult sacrifices, and for your unfaltering support. To my brother and sister, thank
3091 you for the frequent calls, the fun times in Gruyère, Munich or wherever halfway was,
3092 and generally for keeping me anchored in the normal world.